Abstract

Title of dissertation: FUNDAMENTAL UNDERSTANDING, PREDICTION AND VALIDATION OF ROTOR VIBRATORY LOADS IN STEADY LEVEL FLIGHT

Anubhav Datta, Doctor of Philosophy, 2004

Dissertation directed by: Professor Inderjit Chopra
Department of Aerospace Engineering

This work isolates the physics of aerodynamics and structural dynamics from the helicopter rotor aeromechanics problem, investigates them separately, identifies the prediction deficiencies in each, improves upon them, and couples them back together. The objective is to develop a comprehensive analysis capability for accurate and consistent prediction of rotor vibratory loads in steady level flight. The rotor vibratory loads are the dominant source of helicopter vibration. There are two critical vibration regimes for helicopters in steady level flight: (1) low speed transition and (2) high speed forward flight. The mechanism of rotor vibration at low speed transition is well understood - inter-twinning of blade tip vortices below the rotor disk. The mechanism of rotor vibration at high speed is not clear. The focus in this research is on high speed flight. The goal is to understand the key mechanisms involved and accurately model them.

Measured lift, chord force, pitching moment and damper force from the UH-60A Flight Test Program are used to predict, validate and refine the rotor structural dynamics. The prediction errors originate entirely from structural modeling. Once validated, the resultant blade deformations are used to predict and validate aerodynamics. Air loads are calculated using a table look up based unsteady lifting-line model and compared with predictions from a 3-dimensional unsteady CFD model. Both Navier-Stokes and Euler predictions are studied. By separating aerodynamics from structural dynamics, it is established that the advancing blade lift phase problem and the problem of vibratory air loads at high speed stem from inaccurate aerodynamic modeling, not structural dynamic modeling. Vibratory lift at high speed is caused by large elastic torsion deformations (-8 to -10 degrees near the tip) driven by pitching moments and wake interactions on the advancing blade. The dominant phenomenon at the outboard stations (86.5% R to 99% R) is the elastic torsion. Vibratory lift at these stations are dominantly 3/rev and arise from 2/rev elastic torsion. At the inboard stations (67.5% R and 77.5% R), the vibratory lift is impulsive in nature and is not captured by elastic torsion alone. An accurate rotor wake model is necessary in addition to accurate elastic torsion. Accurate elastic torsion requires accurate pitching moments. Lifting-line models, with airfoil tables, unsteady aerodynamics, near wake and far wake do not capture the unsteady transonic pitching moments at the outboard stations (86.5% R to 99% R). A 3-dimensional CFD analyses, both Navier-Stokes and Euler, significantly improve pitching moment predictions at the outboard stations.

The 3D Navier-Stokes CFD analysis is then consistently coupled with a rotor

comprehensive analysis to improve prediction of rotor vibratory loads at high speed. The CFD-comprehensive code coupling is achieved using a loose coupling methodology. The CFD analysis significantly improves section pitching moment prediction near the blade tip. because it captures the steady and unsteady 3D transonic effects. Accurate pitching moments drive elastic twist deformations which together with a refined rotor wake model generate the right vibratory airload harmonics at all radial stations. The flap bending moments, torsion bending moments and pitch link load predictions are significantly improved by CFD coupling.

FUNDAMENTAL UNDERSTANDING, PREDICTION AND VALIDATION OF ROTOR VIBRATORY LOADS IN STEADY-LEVEL FLIGHT

by

Anubhav Datta

Dissertation submitted to the Faculty of the Graduate School of the
University of Maryland, College Park in partial fulfillment
of the requirements for the degree of
Doctor of Philosophy
2004

Advisory Commmittee:

Professor Inderjit Chopra, Chair/Advisor
Professor Gordon Leishman
Associate Professor Roberto Celi
Associate Professor Norman Wereley
Professor Ricardo Nochetto

Dedicated to those, whose thoughts, ideas and creativity

have inspired me :

Johann Sebastian Bach

Sharath Chandra Chattyopadhay

Charles Darwin

Jean-Marie Deguignet

Jawaharlal Nehru

Pierre Auguste Renoir

Antoine-Marie-Roger de Saint-Exupery

Leo Tolstoy

Samuel Clemens (Mark Twain)

Acknowledgments

It would impossible to acknowledge everyone who have contributed to this work. This has been a collaborative research effort within and outside Maryland, with groups from NASA/Army at Ames and Langley, Sikorsky and Boeing. Nonetheless, I would like to acknowledge here, some of those who, directly or indirectly have contributed to the successful completion of this work, and in making the last six years a very enjoyable and intellectually stimulating experience.

Dr. Chopra has been my mentor. It was he, who proposed to resolve the enormously challenging problem of high speed rotor vibration as an systematic research effort within the Center of Excellence program. It gave us a head start in the subsequent NASA/Army Airloads Workshop involving key aeromechanics people from the industry, government and academia - a group he worked to bring together. A large share of the breakthrough, that has been achieved in the last five years, is due to him. He is an expert, far greater than I, on every topic that I have tried to investigate in this work. He has ignored my shortcomings, of which there are many, elevated my strengths, of which there are a few, gave me intellectual freedom and space in which I could cultivate them. I value greatly - his understanding of human aspiration, fascination for physical phenomenon and unsolved problems and encouragement for free thinking.

Dr. Baeder has been my second advisor. The use of CFD as a tool in my

research, is due entirely to him and my colleague, Dr. Sitaraman. I have used their analyses with great confidence and to immense benefit. Much of the ideas behind wake effects on airloads at high speed emerged out of discussions I have had with him.

I would like to thank Dr. Gordon Leishman for his insightful comments on my work and Dr. Celi and Dr. Wereley for their constructive criticisms. I express my gratitude to Dr. Nochetto and Dr. Balachandran for correcting my thesis and attending my defense at a very short notice in spite of their various commitments during that time.

I have had the opportunity to work closely with accomplished researchers like Prof. Marat Tishchenko of the Russian Academy of Sciences, Robert Ormiston of the Army AFDD and Frank Harris (previously with Bell) - whose idealism for research and vitality of ideas have enriched my own thought process immensely. I have also greatly appreciated their personal warmth and kindness.

I fondly remember Prof. Alfred Gessow, with whom I have shared design work as well as research ideas. His untimely demise has been a profound loss for the Rotorcraft Center. I would like to thank Dr. Nagaraj for his thoughtful comments. The perspectives of an accomplished designer is always of great value for a rotor analyst. Dr. Pines have given me sound and sincere advice on many occasions and I thank him for his thoughtfulness.

I would like to acknowledge Jim Duh and Shyi-Yaung Chen of Sikorsky who first successfully solved the full scale UH-60A Black Hawk structural response problem and laid the foundation for all subsequent air load activities; Bobby Mathews,

Frank Tarzanin and Ram Janakiram of Boeing; Charles Berezin and Alan Egolf of Sikorsky; Wayne Johnson, Joon Lim, Mark Potsdam, Hyeonsoo Yeo and Bill Bousman from NASA Ames and Army AFDD.

I am indebted to many of my colleagues in Maryland, in addition to Dr. Sitaraman of the CFD research group. Beatrice Roget has helped me understand the mathematical formulation of the structural dynamics problem and was instrumental in the development of the mechanical airloads solution. Jinwei Shen and Yang Mao have shown me how to use and understand the inner workings of UMARC. I would like to acknowledge some in the Rotorcraft Center with whom I have had useful interactions. Nikhil, Preston, Rendy, Greg Pugliese, Andy Bernhard, Kiran, Jayant, Jinsong, Lin liu, Carlos, Maria and Shreyas are to name a few. My laptop would have long stopped working without support from Shreyas, Sudarshan and Vishnu.

Avinandan and Arena have been a great source of support and happiness to me, in spite of the long distances separating us for much of these years. In times of trouble they have always been a perennial supply of cheer. Same for Sugato and Soma, whom I have known for twenty four and twelve years. Endless reservoirs of kindness and sound judgment, they both have always overlooked my drawbacks. I would like to thank Daniel Griffiths and Hyeonsoo Yeo for their valuable friendship over the years. I have spent many a times sharing my happiness and worries with them.

I want to take this opportunity to specially acknowledge Ms. Cecil Spiegel. Her dynamism of life, vigor of thought and independence of ideas, at eighty-nine years of age has been an inspiration to me. I thank her for being an understanding

friend and a kind and affectionate grandmother to me. I also like to thank Sylvia for her kindness and friendship.

The contribution of my aunt Swagata, whom I call mashimoni, are beyond what I can summarize in a few sentences. Nevertheless, this is an appropriate place to document my gratitude towards her. She and my uncle, Tapas, have been enthusiastic readers of my papers and articles, from Martian Rotorcraft to UH-60A Black Hawk, always supplying me with critical comments and suggestions - although they are electrical engineers and mathematician/computer scientists by profession.

There is nothing that I can write which would properly acknowledge the extent of my parents sacrifice and dedication to my education and research. My mother gave up her research interests in political science and her career as an accomplished classical dancer to raise me. My father gave up his academic career as a power system expert to provide me with the best possible educational opportunities. They taught me to think. They taught me not to accept anything without a critical, rational and educated thought process. I had only two toys, a cat and a lion, but volumes of encyclopaedea and tell me why's.

My parents are serious critics of whatever I write, though he is an electrical engineer and she a political science teacher by profession. They are probably the only two people who are waiting to read every word of my thesis outside my five committee members. Only they would not be as forgiving as my professors with the inaccuracies.

TABLE OF CONTENTS

LIST OF FIGURES

LIST OF TABLES

Chapter 1

Introduction

Prediction of helicopter rotor loads and vibration is a key thrust area within the field of rotor aeromechanics. Rotor aeromechanics covers a wide area of multi-disciplinary research, from aeroelastic response and stability, to vibration prediction and control, to unsteady aerodynamics, wake modeling, Computational Fluid Dynamics (CFD), to flight mechanics and handling qualities. It draws upon extensive wind tunnel and flight test programs conducted to gain physical insight behind the various mechanisms at play as well as development and synthesis of analysis methodologies to model and predict those mechanisms. This work focuses on the modeling, analyses and fundamental understanding of helicopter rotor loads and vibration at high speed level flight.

The rotor loads are the dominant source of helicopter vibration. Helicopter

vibration is a critical aspect of helicopter design and a major reason for extended lead times during the aircraft development phase. Consistent ability to accurately predict helicopter vibration is challenging and beyond the state of the art. This chapter introduces the topic of helicopter vibration - from the physical mechanisms at play, to the analyses methods required to model them, from the state-of-the-art in prediction capabilities to the unsolved problems of fundamental importance. It states the goal of the present research, explains the approach taken and summarizes the contributions.

1.1 Helicopter Vibration

Helicopter vibration is the unsteady acceleration of any given location inside the fuselage, e.g. at the pilot seat, co-pilot seat or at a given crew or passenger station measured along three mutually orthogonal axes (as a fraction of acceleration due to gravity, g).

1.1.1 Measure of Helicopter Vibration

The basic measure of helicopter vibration, as given in the Aeronautical Design Standard (released in 1986 as ADS-27 by the U.S. Army Aviation Systems Command, AVSCOM), is the Intrusion Index (II) [1]. This is computed by normalizing triaxial accelerometer data for the four largest spectral peaks up to 60 Hz. The four largest spectral peaks generally correspond to multiples of the rotor RPM (Revolutions Per Minute) e.g. 1/rev (once per revolution, same as the rotor RPM), 2/rev,

3/rev etc, indicating that they arise from main rotor loads. For conventional helicopter rotors, the RPM corresponds to around 4 to 4.5 Hz. The ADS-27 measure does not include the 1/rev vibration. This is to emphasize the special importance of this harmonic. The 1/rev vibration arises in the fuselage if the blades are out of track - i.e, when all the blades do not follow the same trajectory in space. For tracked and identical rotor blades, the frequencies, in /rev, transmitted to the fuselage via the rotor hub are integral multiples of blade number. For example for a 4-bladed helicopter like the UH-60A, 4/rev, 8/rev, 12/rev and so on are transmitted to the fuselage. The frequency corresponding to the blade number, 4/rev in this case, is called the blade passage frequency. Non-integral multiples are transmitted only in the case of non-identical (damaged or dissimilar) or out of track blades.

The four largest harmonics are measured along each axis and their norm is used to obtain the intrusion index. This produces a single scalar quantity as a measure of vibration which combines 12 harmonics (four each in three axes). The three axes are weighted differently, the vertical vibrations are weighted most heavily, the lateral vibrations have a 0.75 weight relative to the vertical and the longitudinal vibrations have a 0.50 weight relative to the vertical. This is done to allow designers the freedom to trade off between directions and frequency within the confines of a single scalar measure of vibration.

The ADS-27 relaxed the fuselage vibration levels compared to original standards set by the Utility Tactical Transport Aircraft System (UTTAS) and Advanced Attack Helicopter (AAH) developmental programs [2]. None of the helicopter designs even came close to those original specifications. The revised ADS-27 standards

are still too stringent. For example, for the UH-60A Black Hawk helicopter with an articulated 4 bladed main rotor system, the vibration levels can be 100% higher in forward flight compared to the ADS-27 requirements [3].

The intrusion index at the pilot floor for the UH-60A at transition speed of around 40 kts is about 2.1 (ADS-27 level is about 1.1) [3]. 4/rev and 8/rev harmonics account for 91% of this number. At high speed of about 155 kts, 4 and 8/rev contribute to around 67% of the index. 2/rev and 6/rev contribute to 19% and 5% of the index. This shows that frequencies corresponding to non-integer multiples of blade number can contribute significantly to fuselage vibration at certain flight conditions.

Currently, vibration reduction devices, active and passive, are used to meet these requirements. Their cost and weight penalty has been excessive in part because of inadequate vibration prediction capability. Accurate prediction capability at an early design stage may enable the design of low vibration helicopter systems.

1.1.2 Causes of Helicopter Vibration

The dominant source of helicopter vibration is the main rotor. The frequency of vibration caused by the main rotor is at integer multiples of the rotor RPM - 1 per revolution (1/rev) is the rotor RPM, then 2/rev, 3/rev and so on. In addition to the main rotor, other sources of vibration are - the engine/fan system, the main rotor transmission/drive-shaft/gear system, the tail rotor and its transmission system and loose components that are a regular or external part of the aircraft. Examples are

out of balance rotor blades, loose tail fins, loose engine shaft mounts, unsecured canopy, landing gear system or external weapons or cargo systems.

The fuselage vibration at any station depends not only on the external loadings but also on the fuselage dynamic characteristics. The fuselage dynamic characteristics are in general coupled with the dynamics of other component structures. For example, the main rotor loads are transmitted to the fuselage via the rotor hub. The fuselage dynamic response feeds back into the blade motions via the hub and pylon assembly.

In addition to dynamic coupling, a significant amount of aerodynamic interference or coupling exists between the main rotor, airframe and tail rotor structures. The flow around the fuselage affect the aerodynamics of the main rotor and the tail rotor. The downwash from the main rotor changes the aerodynamics of the fuselage, tail rotor and horizontal tail and stabilizers. Under certain low speed conditions, the vortex wake from the main rotor impinges directly on the tail boom that gives rise to fuselage vibration at the blade passage frequency.

For accurate prediction of fuselage vibration, the dynamics and aerodynamics of all components - main rotor, airframe, tail rotor etc and their mutual interactions must be modeled accurately. However, the most significant contribution to fuselage vibration is the loads of the main rotor system. Because only the harmonics of the blade passage frequency are dominantly transferred to the fuselage, main rotor loads which generate those harmonics are termed vibratory loads. In addition to the vibratory loads, oscillatory blade loads arising out of blade dynamics are also critical. They are important for the design of blades, control linkages, hub attachments as

well as rotor performance. The rotor vibratory and oscillatory loads are described in the next subsection.

1.1.3 Rotor Vibratory and Oscillatory Loads

The dominant contributor to fuselage vibration is the main rotor - the oscillatory loads that are transmitted to the airframe via the rotor hub and pylon assembly. The oscillatory and vibratory blade loads originate due to : (1) unsteady aerodynamic environment and (2) dynamic response of the flexible rotor blades. The dynamic response of the blades are determined by non-linear inertial couplings between flap, lag, elastic torsion and axial degrees of motion, moderately large deformations, large pitch angles required for rotor trim, damper properties, material non-linearities and rotor-fuselage dynamic interactions.

The problem of rotor loads and vibration has been the focus of dynamics research since the beginning of the industry. The aerodynamics of a rotor blade differ from that of a fixed wing due to the following phenomenon.

- Rotor inflow, generated by high RPM of the blades (around 250 for conventional main rotors), necessary for vertical flight.
- Cyclic variation of blade pitch angle, necessary for control.
- Time varying, assymetric flow in forward flight with large variations of angle of attack in the advancing and retreating sides.
- Enormous compressibility effects including shocks on the advancing side and

stalled flow on the retreating side.

- The complex, unsteady wake structure of each blade interacting with following blades.

Because of rotation, the outboard span stations of the blades generate more lift and trail strong tip vortices. The tip vortices are the dominant features of the wake and in general contribute to non-uniform inflow variation around the rotor disk. Unlike airplane wings, these vortices remain in the vicinity of the rotor disk and interact with the following blades.

A fixed wing aircraft uses wings for lift, control surfaces for vehicle control and thrusters for propulsion. On the other hand, in a rotary wing aircraft, the main rotor performs all three functions at the same time. The rotor disk angle is controlled by time varying 1/rev pitch inputs to the blades (using swash-plate). The rotor thrust is controlled by steady pitch input to the blades (collective angle). This generates steady and 1/rev air loads at each blade section which collectively determine the magnitude and orientation of the rotor thrust.

In forward flight, the assymetric velocity variation around the rotor disk together with cyclic pitch angles and complex inflow distribution generate higher harmonic air loads, 3/rev and higher. For example, a velocity variation of zero and 1/rev creates a zero, 1 and 2/rev variation in the square of velocity, which when multiplied with 1/rev cyclic angles generates zero, 1, 2 and 3/rev airloads. The steady components are used to trim the vehicle, the 1/rev components are required for control, the higher harmonics give rise to rotor vibration. At certain flight con-

ditions, significant higher harmonic air loads are generated creating severe rotor vibration - e.g., tip vortex induced airloads in transition flight, dynamic stall air loads in high thrust flight, unsteady transonic air loads at high speed flights and a combination of all in maneuvering flight.

The long slender rotor blades are highly flexible. As a result significant elastic bending deformations occur in flap, lag and twist in response to airloads. Because they are equi-spaced from one another in azimuth angle, and identical, their aerodynamic loading and structural dynamic response is expected to differ only in phase. And because they are all joined at the hub, the individual blade loads at the hub add up to cancel the non-integral harmonics of blade passage frequency. For example, as mentioned before, in the case of a 4 bladed rotor system like the UH-60A Black Hawk, only steady, 4/rev, 8/rev, 12/rev, i.e., in general pN_b/rev, where p is an integer, are transmitted from the rotor system to the hub. Dissimilarities or damage of the blades make them non-identical and generate non pN_b/rev loads [4]. This forms a separate field of study and is outside the scope of the present thesis.

For identical blades, only integral harmonics are transmitted. Because of simple trigonometry, the integral blade number harmonics in the fixed hub system are generated by the adjoining harmonics in the rotating blades. Thus, (3/4/5)/rev blade loads in the rotating frame generate 4/rev hub loads in the fixed frame, (7/8/9)/rev blade loads generate 8/rev hub loads and in general $(p+1)N_b$, pN_b, $(p-1)N_b$/rev blade loads in the rotating frame generate pN_b/rev hub loads in the fixed frame. All harmonics of blade loads are important for blade design, but only blade passage harmonics (and multiples) and their adjoining harmonics have the

potential for hub and fuselage vibration. The large deflection response of the rotor blades feeds back to the air loads which generate time varying aerodynamic stiffness and damping matrices. The damping of the rotor system comes primarily from aerodynamics. The structural response of the rotor blades are therefore aeroelastic in nature and governed by the periodic stiffness, damping and forcing functions. In addition, the moderate to large flap, lag and elastic torsion deformations of the blades form a nonlinear coupled system with complex boundary conditions and multiple load paths at the root.

Accurate prediction of rotor loads is key to advanced rotorcraft design. Attractive and radical low noise, high performance (range and endurance) rotor designs may be evaluated quickly and at low cost using reliable analyses methods. For a reliable analysis, it is necessary to understand and model the physics of structural dynamics and aerodynamics accurately. Such a capability does not exist today (discussed later). Designers rely on costly and time consuming wind tunnel and flight tests. Rotor aeromechanics is at the heart of the helicopter system and any modification in existing design cannot be undertaken unless its impact on blade loads, control loads and vibration are clearly ascertained. Prediction of control loads is important for designing more agile and maneuverable rotor systems. While the peak magnitudes are important for sizing and design of the control system components, the phase of the response is important for implementing control algorithms.

Apart from degraded ride quality, high vibration directly increases maintenance and operating costs because of frequent replacement schedules of critical fatigued components. The maintenance, and direct operating cost of a helicopter is

the greatest hindrance toward its becoming a serious candidate for civilian short haul flight. A helicopter with its unique vertical take off and landing capability offers the most promising solution for reducing airport and air traffic congestion. Vibration is one of the major hindrances to fulfilling this potential.

Smart structure actuated on-blade active control mechanisms show enormous potential for reducing and controlling rotor vibration [5, 6, 7]. The actuator requirements and control limits can be reliably designed and tested, without expensive wind tunnel or flight tests, provided the mechanisms of helicopter vibration are well understood and predicted. Passive vibration reduction techniques, using composite tailoring [8] and structural optimization, can be devised and tested with confidence without expensive wind tunnel tests. Detailed discussion of smart structures technology is outside the scope of the present thesis. A comprehensive review of this topic can be found in Chopra [9].

The state of the art in helicopter loads and vibration prediction is well characterized by Johnson in 1985 [10] who said, "*For a good prediction of loads it is necessary to do everything right, all of the time. With current technology it is possible to do some of the things right, some of the time*".

The fundamental difficulty in predicting rotor loads and vibration arises due to its rotary-wings. The kinetic energy of the massive rotating blades are of the order of 1×10^8 Joules. The potential energy change due to blade deformations can at the most be as high as 1×10^6 Joules. To accurately predict the blade loads and vibration it is necessary to pick up fluctuations of potential energy levels that are two orders of magnitude lower than the total energy level of the system. This

enormous imbalance between the magnitudes of kinetic and potential energy makes the rotor loads prediction problem fundamentally difficult and challenging compared to other dynamical systems.

1.2 Analysis of Helicopter Vibration

For accurate prediction of helicopter vibration at any fuselage station, the following physical mechanisms must be modeled.

1. Structural dynamics of the main rotor with non-linear inertial couplings, moderately large deformations, boundary conditions with multiple load paths, pitch link and damper properties at the root, advanced geometry blades with sweep, droop and pre-twist and rotor-airframe coupling terms.

2. Aerodynamics of the main rotor which accounts for time varying unsteady effects, attached flow, stalled flow, dynamic stall, free or prescribed rotor wake, a lifting-line or lifting-surface model for calculating the blade airloads compatible with airfoil property data.

3. Aerodynamic and structural dynamic model of the airframe or fuselage which includes a tail rotor model, properties of the vertical and horizontal tail and fuselage center of gravity location. A detailed structural model of the flexible fuselage would include rotor-body coupling terms and modeling of rotor hub, pylon, tail boom and other difficult components.

4. Rotor-fuselage aerodynamic interaction effects. The downwash from the ro-

tor and the upwash from the fuselage affect the fuselage and rotor airflows respectively as well as coupling their aerodynamic characteristics.

5. A vehicle trim model using a isolated rotor wind tunnel trim, or a free flight propulsive trim under steady level or steady maneuvering conditions.

6. Computation Fluid Dynamic models can be used to replace - from parts of the aerodynamic modeling of the main rotor, to the full rotor system to the entire rotor-fuselage-tail rotor flow field, depending on the level of details sought, scope of analysis and resources available.

7. Active on-blade components like trailing edge flaps, actuators and blade to blade structural and aerodynamic dissimilarities and damage.

The above models can be combined together to synthesize a comprehensive analysis to predict helicopter performance, airloads, blade loads and fuselage vibration. Detailed modeling of all the above mechanisms are prohibitive in terms of computational and modeling costs and cannot be routinely used for design purposes. Nor is it necessary for preliminary design. Depending on the level of accuracy and type of results sought from the analysis, simplifying assumptions can be made which focuses on the key mechanisms. For example, for calculation of basic rotor performance, blade airloads are more important than rotor-fuselage aerodynamic interactions. For calculation of blade airloads at low thrust conditions, dynamic stall models need not be used. For calculation of bending moments, flexible blade modes are more important than fuselage dynamics. At low speed transition flight, a free wake model is more important than transonic effects. At a high speed, transonic

effects are more important than free wake. Thus, if the underlying key mechanisms of a particular flight condition are understood and modeled, reasonably accurate solutions can be obtained from a simplified analysis. In general, for accurate prediction of fuselage vibration at all flight conditions, all the above mechanisms need to be modeled.

A survey of the state-of-the-art in modeling of the above mechanisms is discussed below. A survey of rotor testing is also included. These rotor tests are crucial for the development, validation and refinement of analyses models. For example, the present work uses the UH-60A flight test data extensively for validation purposes. A detailed discussion on the lack of understanding of the key mechanisms at high speed flight condition is treated separately in the next section.

1.2.1 Rotor Structural Model

The linear coupled flap-lag-torsion dynamics of the rotor blades were well established by Houbolt and Brooks in 1958 [11]. Ref [12] used a rigid blade with a spring restrained hinge to show the importance of modeling Coriolis and centrifugal non-linearities even if only flap and lag degrees of freedom were included. Hodges and Dowell [13] presented a rigorous and consistent set of elastic, coupled, nonlinear flap-lag-torsion equations for moderately large deformations. The nature of the elastic torsion variable was later clarified by Hodges, Ormiston and Peters [14] and treated as a quasi-coordinate. A number of researchers like Kvaternik *et al* [15], Friedmann and Rosen [16] and Johnson [17] have extended these formulations to consistently

include the nonlinear structural and inertial terms for moderately large deflections. These formulations laid the foundation of nonlinear structural dynamics of coupled bending, torsion and axial deformation of twisted non-uniform rotor blades with center of gravity offsets. The structural model in all these formulations use the Euler-Bernoulli beam theory for isotropic materials.

The structural model for anisotropic or composite materials is developed in references [18, 19, 20]. These formulations include the effects of cross-sectional warping and transverse shear in the section structural properties. These models also eliminate the assumption that an elastic axis exists. Analysis of advanced geometry blades with tip sweep, drop and pretwist were incorporated in rotor aeroelastic analyses in references [21, 22, 23, 24, 25]. Advanced geometry modeling was incorporated in composite rotor blades in references [26, 27].

The structural equations can be discretized in two ways : (1) using a lumped parameter (or transfer matrix or Myklestad) approach [28, 29], and (2) using a finite element approach [30, 31]. The Myklestad approach becomes involved for blades with load redundancies. Most modern structural analyses solve the governing equations of motion using a finite element method. The finite element method is versatile and can handle complex blade geometries and redundancies. For conventional rotor structural analyses, the first few elastic modes of the rotor blades can be used to reduce the size of the structural dynamic problem. The finite element method is used to construct the normal modes which are then used reduce the degrees of freedom of the problem to improve efficiency and reduce computational cost without a significant loss in solution accuracy. With increase in available computational power,

full finite element solutions can be obtained, without the need for modal reduction.

Conventional formulations of the structural dynamic equations exploit the topology of a helicopter rotor system to simplify the derivation of the governing equations. This leads to a loss of expandability of the analysis. For example, to model a coupled rotor-fuselage system, the blade equations must be rederived. A small increase in the scope of analysis (e.g. modeling the flexible shaft or swash-plate) involves the entire analysis, and the growth becomes progressively harder with each new feature. Moreover with each new formulation, the same model which is now expressed with a new set of equations, must be revalidated again and again. In recent years, multi-body formulations are developed to address this issue [32, 33, 35, 36]. These formulations significantly increase the scope of simulation capability with detailed models of control linkages, complex hub geometries, swash-plate assembly etc., without having to rederive the structural dynamic equations with each additional feature.

1.2.2 Rotor Aerodynamic Model

The rotor aerodynamic model can be conceptualized in two parts - based on a cause and effect relationship.

The first part, the cause, is the excitation which causes the airloads. It consists of the relative motion of the airfoil with respect to air, i.e., the section angle of attack variation. The section angle of attack variation is calculated based on the flexible blade deformations, the air velocities - incident and gust, and the rotor wake induced

velocities. The blade deformations are from structural dynamics, the air velocity depends on flight speed and fuselage trim attitudes, the wake induced velocities depend on wake or inflow modeling.

The second part, the effect, is the pressure response on the surfaces of the airfoil (and the viscous drag) which generate the unsteady airloads. This part depends on the airfoil shape, boundary layer response and the near wake from the airfoil (trailed and shed). Given the blade deformations and air velocities, the aerodynamic model involves two critical calculations : (1) non-uniform inflow or the wake and (2) unsteady pressure or airload response of the airfoils. The state of the art methods of treating these two components are discussed below. CFD methods, to be discussed later, are able to provide more detailed pressure and wake distributions but at a much higher computational cost. On the other hand, Lagrangian wake models (to be discussed later) are ideally suited to handle the first problem, i.e. calculation of induced inflow. This is due to the inherently dissipative nature of the CFD solvers which artificially destroy the vortical wake structures in the flow field.

Rotor Inflow Calculation

It was understood during the 1950s that non-uniform inflow is important to predict rotor aerodynamics. Piziali and DuWaldt [37, 38], showed improved airload prediction using prescribed wake geometry. Landgrebe developed a prescribed wake geometry model based on experimental observations of induced velocities [39, 40] which significantly improved predictions of rotor hover performance. Around the same time Scully [41], showed that the wake geometry can be modeled as a distorted

or free wake without being prescribed a priori. His Euler time-marching wake algorithm, similar to the time-marching approach introduced by Crimi [42], had limited success due to severe numerical instabilities. The convergence problem was subsequently overcome with Scully's relaxation wake model [43]. In the relaxation wake model, the wake is constrained to be periodic in time and the solution is valid for steady-state flight conditions. Crimi, Scully, Piziali and Landgrebe's work form the basis of modern time accurate free wake, relaxation (periodic, steady-state) free wake and prescribed wake geometry models.

Prescribed wake geometry models have been subsequently refined [44] and extended to forward flight, e.g. Egolf and Landgrebe [45] and Beddoes [46]. Free wake geometry models have since developed adopting different numerical methods. Broadly, they can be classified into relaxation methods and time-marching methods. The relaxation methods include - constant vorticity contour method by Quackenbush and Wachspress [47], pseudo-implicit predictor-corrector method by Bagai and Leishman [49], the general free wake geometry method by Johnson [48] and more recently a refinement of the later in the form of the multiple trailer with consolidation method [50]. Scully's relaxation free wake was applicable to a single rotor with identical blades, a single tip vortex and a single peak circulation distribution. Modern free wake analysis incorporate multiple rotors [51], multiple trailers, dual peak circulation distributions [52] and dissimilar blades [48].

The time marching free wake methods underwent subsequent developments by Clark and Leiper [53], Landgrebe [39] and Sadler [54]. Clark and Leiper used a predictor-corrector approach to remove instabilities in hover. This is because wake

periodicity was explicitly enforced. Landgrebe focussed on forward flight. Landgrebe's hover calculations showed similar instabilities as Scully. Sadler developed an explicit Euler time-marching wake methodology for multiple rotors in forward flight. Other time-marching methods are - and explicit Euler vortex lattice rotor wake model by Egolf [55] and a second-order time marching using an Adams-Bashforth type method by Baron and Baffadossi [56].

Time-marching wake studies by Jain *et al.* [57] and Lee *et al.* [58] have focussed on the numerical instabilities in hover and found them consistent with experiments [59]. Near real time simulations have been shown by Quackenbush [60]. Recently, comprehensive time accurate vortex wake methods have been developed by Bhagwat and Leishman [61, 62]. They showed that the instabilities in hover are due to various inherent physical disturbances in the wake but are not related to instabilities in numerical solution. Thus good correlations may often be fortuitous but in general not always possible. The time accurate wake geometry models are necessary for the analyses of unsteady maneuvers.

Over the past three decades these free-vortex methods have emerged as practical tools for modeling the vortical wake geometry generated by helicopter rotors. The models are based on the assumption of irrotational, incompressible (i.e. potential) flow with all of the vorticity concentrated into filaments. The motion of a point in the vortex filament is given by the Lagrangian fluid equation of motion, which simply states that the time derivative of position equals velocity. The free-vortex wake is therefore also called Lagrangian wake. Once the vortex wake geometry is known, the induced inflow can be obtained at any point in the flow field

Another type of inflow calculations are performed by the *Dynamic Inflow* models. They are not used for detailed modeling of the localized unsteady inflow at the blade element level. These models assume a inflow distribution over the rotor disk in terms of a time series and relate the coefficients of the series to the net rotor thrusts and moments. A popular dynamic inflow model is that of Pitt and Peters [63] with subsequent refinements by Peters and He [64] and Morillo and Peters [65]. The dynamic inflow models do not calculate the wake geometry. Dynamic inflow models appear adequate for aeroelastic stability calculations but not for prediction of rotor vibration.

Unsteady Airloads Calculation

In the rotor environment, the blade pitching motions supply both an angle of attack as well as a rate of change of angle of attack, the flapping motion supplies a plunging motion, the inflow supplies a gust type velocity pattern, the unsteady response to all these stimuli are different and complex. An comprehensive treatment of these effects can be found in a recent text by Leishman [66]. In general, most rotor simulations combine these effects to define an instantaneous angle of attack for each airfoil section calculated at the 3/4 chord location. The airloads are then calculated using the 'look-up' tables obtained from wind tunnel tests. These can be termed pseudo-steady airloads. For quasi-steady airloads, the next level of refinement, unsteady non-circulatory airloads are added to the pseudo-steady components using a quasi-steady thin airfoil theory. For a truly unsteady prediction, the pseudo-steady airloads are corrected in phase and magnitude using classical Theodorsen's theory

(frequency domain). These corrections account for the near shed wake effects. The Wagner's problem formulation is more useful for rotor problems. It is formulated in the time domain, and accounts for both non-circulatory and shed wake effects (circulatory). These classical 2D theories ignore compressibility, viscous effects, affect of airfoil shape and most significantly separation and dynamic stall.

Over the last three decades, significant improvements have been made in usteady aerodynamic modeling. Oscillating airfoil wind tunnel data have been used to develop semi-empirical models that attempt to capture the real fluid viscous effects, separation and dynamic stall, compressibility effects and can be obtained for each specific airfoil. For example, semi-empirical indicial models were developed for high sub-sonic (up to Mach number 0.8) 2D unsteady aerodynamics by Leishman and Beddoes [67, 68]. The models were further extended to include nonlinear effects of flow separation [69], dynamic stall [70] and effects of blade sweep on dynamic stall [71]. Other dynamic stall models are the Johnson model [72], Boeing model [73], ONERA EDLIN (Equations Differentielles Linearires) model [74] and the ONERA BH (Bifurcation de Hopf)model [75]. All models are 2-D and semi-empirical in nature. Dynamic stall is characterized by a delay in angle of attack before stall (or separation) and high transient loads induced by a leading edge vortex after stall. All dynamic stall models, model the delay in angle of attack and the aerodynamic coefficient increments after stall. In the Leishman-Beddoes model uses first-order differential equations for the delayed angle of attack and leading-edge vortex lift. The ONERA EDLIN and BH models use second-order differential equations to calculate delayed angle of attack and lift, drag and moment increments. The Johnson

model uses an angle of attack delay proportional to the rate of change of angle of attack. The Boeing model uses an angle of attack delay proportional to the square-root of the rate of change of angle of attack. In general the agreement between different models are good considering the simplicity of the models, but correlation with test data show significant errors, as expected with empirical models [76].

The 3-dimensional flow effects are modeled using lifting-line, nonlinear lifting-line [77] and lifting-surface [47] methodologies. These are adapted to include steady airfoil properties and can be used to add corrections to a 2D strip theory or blade element method based angle of attack calculation to account for 3D effects. 3D effects of advanced geometry swept tip blades have been studied analytically and experimentally by several researchers [78, 79, 80, 81].

1.2.3 Coupled Rotor-Fuselage Analysis

The rotor-fuselage coupled analyses can be classified into four categories - (i) coupled trim analyses, (ii) stability analyses like ground resonance and air-resonance, (iii) fully coupled loads and vibration analyses and (iv) rotor-fuselage aerodynamic interaction studies. The term airframe or fuselage includes the tail rotor, landing gear, engines, tail boom etc, i.e. all non main rotor components of the helicopter.

The trim analysis incorporates the basic fuselage aerodynamic properties, the horizontal and vertical tail aerodynamic properties and center of location, the tail rotor aerodynamics and locations and the vehicle center of gravity offsets. The coupled rotor-fuselage stability analysis is well developed. An excellent review on

the subject is found in Chopra [82]. Rotor-fuselage coupling for vibration analysis and prediction have been performed by Vellaichamy and Chopra [83] and Chiu and Friedmann [84]. The former used a stick fuselage model while the later a full 3D fuselage model. However, both used idealized uniform inflow, quasi-steady aerodynamics. Yeo and Chopra [85] presented a fully coupled rotor-fuselage vibration analysis of the AH-1G helicopter with Leishman-Bagai free wake and detailed difficult component modeling. The AH-1G helicopter has a two bladed teetering rotor system. The calculated 2/rev (blade passage frequency for the AH-1G) at the pilot seat showed good correlation with flight test results. The coupled main rotor pylon roll mode had a significant contribution (26%) in the 2/rev vibration at the pilot seat. The 4/rev vibration prediction was generally poor. The study neglected rotor-fuselage aerodynamic interaction effects.

A recent rotor-body interactional aerodynamics study by Wachspress, Quackenbush and Boschitsch [86] shows the current state of the art. Interactional effects were studied using a full span constant vorticity contour free wake and a panel method to model the fuselage bodies and lifting surfaces. Despite limitations in predicting viscous phenomenon, the potential flow solution captured the fuselage steady and unsteady pressure variations quite well. The test data used were that of a model rotor/fuselage combination obtained by Leishman and Bi [87]. One difficulty in prediction was that of unsteady pressure fluctuations associated with wake/surface interactions on the rear of the fuselage. In recent years, Euler and Navier-Stokes CFD codes have begun to be applied to the problem [88, 89]. In addition to the challenges of computation time and grid generation, one particular

challenge is the numerical dissipation of the main rotor vortex wake. The vortex wake is important is capturing wake/surface interactions.

A full coupled rotor-fuselage model including both dynamic and aerodynamic analyses is however still beyond the current state of the art.

1.2.4 Trim Model

The helicopter model must be trimmed in steady flight to maintain equilibrium. Johnson [90] summarized several trim options. Broadly these can be classified into two categories - free flight trim and wind tunnel trim.

For a free flight trim, the rotor control angles (collective, lateral and longitudinal cyclic angles), the tail rotor collective and the fuselage lateral and longitudinal attitude angles are obtained to maintain three force (vertical, longitudinal, lateral) and three moment equilibrium (pitch, roll and yaw). Vehicle weight, speed and flight path angle are prescribed. In propulsive free flight trim it is assumed that the engine can supply all the power needed to maintain the flight condition. In an auxiliary propulsive trim (or partial power propulsive trim) only a part of the total thrust is provided by the engine. The vehicle equilibrium equations are nonlinear and coupled to rotor response and inflow equations and are solved numerically using an iterative procedure. Frequently, assumptions are made to simplify trim calculations.

- The rotor response is assume flap only, undergoing simple harmonic motion (β_0, β_{1C} and β_{1S}).

- Neglect yawing moment equilibrium and tail rotor collective. The influence

on trim solution is found to be small [94].

- Neglect yawing moment and lateral force equilibrium, dropping both tail rotor collective and shaft lateral tilt (or fuselage tilt) from the solution. This may cause a small change in trim solution at high speed as the lateral tilt does not introduce any vertical flow due to forward speed. However, the lateral tilt affects the rotor wake geometry and can have a larger impact on the trim solution at transition speeds.

- A more simplified procedure assumes that the vehicle center of gravity is at the rotor hub and neglects the the pitch and roll moment equilibriums equations. This results in cyclic flap angles (β_{1C} and β_{1S} with respect to hub plane) equal to zero. The yaw equilibrium and tail rotor collective is ignored. The rotor collective and the longitudinal and lateral shaft tilts are calculated from the three force equilibrium equations.

A wind tunnel trim, or an isolated rotor trim simulates the test conditions in a tunnel. In a wind tunnel trim, the shaft longitudinal and lateral tilt angles and the rotor collective are prescribed. There is no tail rotor. For a given forward speed, the cyclic pitch angles (θ_{1C} and θ_{1S}) are adjusted to trim the flap angles (β_{1C} and β_{1S}) to zero.

1.2.5 Response and Loads Model

The steady blade response involves the calculation of blade deflected positions about the azimuth for one complete revolution. For steady flight, the response

is assumed periodic with a time period of one cycle (i.e. one rotor revolution, 2π). In the first step, the spatial coordinate in the structural dynamic equations is eliminated using finite element, or continuum methods, such as Rayleigh-Ritz or Galerkin. This reduces the flap-lag-torsion-extention partial differential equations to a set of coupled nonlinear ordinary differential equations in time. The number of these equations are often reduced to a few typically 6 to 10, by using the rotating natural vibration modes. These equations are then solved in time using one of the following methods.

- Harmonic balance method [91]. The response is assumed to be a summation of a finite number of sine and cosine harmonics and then using the substitution method or operational method, a set of nonlinear algebraic equations are obtained. These are solved numerically using standard methods like Newton-Raphson.

- Iterative procedure based on Floquet theory [92]. It consists of determining the proper initial conditions for a periodic solution, and then integrating the equations for one period. The method is not very robust for nonlinear problems.

- A finite element in time method using Hamilton's weak principle [93]. This method has been used in the present thesis. This method includes all harmonics and is efficient and robust for nonlinear systems.

- Numerical integration of the nonlinear differential equations until the solution settles to a steady condition. For example Lockheed's REXOR, Bell's C81

and Sikorsky's DYMORE use time integration methods. They are relatively computation heavy because of the settling time required to reach the steady-state solution. Artificial damping is often required in the initial stages to damp out the natural response.

When the blade response is known, the sectional loads (shear forces and bending moments) can be calculated. Two frequently used approaches are the : (1) deflection or curvature method and (2) force summation method. In the curvature method (also called modal method), the loads at a given blade section are determined by the elastic motion induced curvature and structural properties at that section. The accuracy of this calculation depends on the accuracy of the curvature and the number of modes or shape functions used in the solution to represent it. The curvature can be linearized, nonlinear up to second order or exact. If there is a radial step change in structural properties, e.g. bending stiffness, there should be a corresponding step in curvature, so that the physical load remains continuous. With a small number modes or shape functions this discontinuity cannot be captured. The effect of concentrated loading, e.g. a damper force, is similar. Greater number of modes are required to capture its effect on the local blade loads. Also, the curvature method gives zero load on an element without elastic degrees of freedom.

A force summation method rectifies the above deficiencies. It is a force balance method which obtains the section loads from the difference between the applied forces and the inertial forces acting on the blade on one side of the section. The forces used for this purpose must be exactly same as those used for solving the structural

dynamic equations, otherwise inconsistent loads are obtained. For example, the bending moments at a pure hinge would not be identically zero. With lesser number of modes, the force summation method better captures the effects of concentrated loading and radial discontinuities of structural properties. However, with increase in number of modes the curvature method and the force summation method must reach the exact same solution.

1.2.6 Rotor Codes and Comprehensive Analyses

Vibration analyses methodologies have developed which incorporate and combine some or all of the above mentioned analyses capabilities. Most codes focus on the details of one physical mechanism while using simplified or no models for the rest. These codes can be termed in general as rotor analyses codes.

Comprehensive analyses codes are a subset of these general rotor codes. A comprehensive analysis code includes all the basic component models essential for handling the multidisciplinary nature of helicopter problems - i.e., it can calculate performance, loads, vibration, response and stability. It must have a rotor wake model; include airfoil properties and stall, nonlinear dynamics of the flexible rotor blades in flap, lag and torsion, airframe dynamics, fuselage aerodynamics and tail rotor and mode free flight trim to identify the control positions and aircraft orientation required to achieve a specified operating condition. The analyses must perform trim, transient and flutter tasks. Examples of comprehensive analysis are the CAMRAD family, UMARC and RCAS. The value of non-comprehensive rotor

codes is in their capability to model one or more physical phenomenon in greater detail, accuracy and scope than that currently available in a comprehensive code.

A detailed list of the current rotor analyses codes are given below. The specific areas of focus within each code are identified.

- The CAMRAD family - CAMRAD, then CAMRAD JA, updated to CAMRAD II [76]. *Comprehensive Analysis code.*
- 2GCHAS now extensively modified to RCAS [95, 33]. *Comprehensive Analysis code.*
- The UMARC family [96]. *Comprehensive Analysis code.*
- CHARM [47] based on the earlier generations of RotorCRAFT codes. Focus on detailed free wake modeling and includes rotor-fuselage aerodynamic interactions.
- KTRAN-RDYNE-GENHEL (Sikorsky). KTRAN for structural dynamics, RDYNE for structural dynamics and aerodynamics. GENHEL [34] for flight dynamics, trim etc.
- DYMORE and DYMORE II [35]. Focus on generalized multibody dynamics capability. Simplified aerodynamics with dynamic inflow model.
- R150 and Westland/DERA [97] (GKN-Westland Helicopters).
- C81 and COPTER [98] (Bell Helicopter Textron).
- R85/METAR (developed by Eurocopter France) [97].

None of the codes, in general, include all capabilities. For example, CAMRAD II, RCAS and UMARC have recently included full main rotor 3D-CFD coupling option but does not include rotor-body interactional aerodynamics. CHARM has full rotor-body interactional aerodynamics but no CFD coupling. UMARC has fully coupled rotor-flexible fuselage dynamic coupling but no generalized multi-body dynamics capability. DYMORE has detailed multibody dynamics capability but a simplified aerodynamic model.

Validation studies with wind tunnel and flight test data, show significant discrepancies in main rotor loads prediction from all of the above analyses methods. A sample set of references documenting airload and blade load validation studies from some of the above codes can be found in the following references. Bousman [99] and Lim [100] for CAMRAD/JA and 2GCHAS predictions and correlation of airloads and blade loads with UH-60A flight test data, Yeo [101] for CAMRAD II predictions and correlation of airloads for five different wind tunnel and flight tests, reference [102] for UMARC predictions of airloads and blade loads for the full scale UH-60A, Wang [103] showed predictions from UMARC/S (UMARC modified by Sikorsky), RDYNE and KTRAN, Wachspress *et al.* [47] showed predictions from CHARM and Sopher and Duh [104] for predictions from KTRAN, RDYNE coupled with GENHEL (flight dynamics code). In some cases, the peak to peak magnitude of blade loads, air loads and control loads were reasonably predicted, but in all cases large errors in waveform and phase predictions were observed. The details of these prediction discrepancies are discussed later in section 1.4.

1.2.7 CFD methods

The use of CFD for studying fuselage flow and rotor-fuselage interactional effects have already been discussed (section 1.2.3). Of great importance is the application of CFD to calculate main rotor blade airloads - replacing conventional look-up tables and unsteady models. A CFD analysis that can be used to calculate the rotor blade airloads must satisfy the two key requirements - (i) flexible blade deformations using deforming meshes, and (ii) calculate or incorporate the vortex wake. In addition, for comprehensive analysis, it must be consistently coupled to the structural analysis and it should include a trim methodology. The blade deformations can be included by moving the mesh points to conform to the deformed blade surface while preserving the geometric conservation laws of the surfaces and volumes of the control cells [105]. The vortex wake can be included externally using a Field Velocity Approach [106] or simulated directly using a multi-block or over-set mesh to prevent numerical dissipation.

Coupling between CFD and rotorcraft comprehensive codes can be accomplished in two ways : (1) loose or weak coupling, and (2) tight or strong coupling. In loose coupling, airloads and blade deformations are transferred between comprehensive code and CFD once every rotor revolution. It allows for modular communication between the CFD and comprehensive code using an interface without the need for modifying the original codes. The time accuracy in each can be handled independently of the other. Trim solution can be easily achieved within the comprehensive analysis.

Tight coupling is a more rigorous approach in that the fluid dynamic and structural dynamic equations are integrated simultaneously. Time accuracy must be ensured and rotor trim is problematic. On the other hand aeroelastic stability analysis can be performed using transient response. Altmikus [107] compared the two coupling approaches and showed that the tight coupling requires a 2.5 times increase in computational cost while generating same airload predictions at high speed using a loose coupling. References [108, 109] have studied tight coupling with fixed control angles thus avoiding the trim issue.

The first CFD loose coupling procedure to structural codes were developed by Tung, Caradonna and Johnson in 1987 [110]. In this procedure, called the *delta* method, the comprehensive analysis supplies the airload sensitivities to blade deformations which provide aerodynamic damping during convergence. The CFD code was a conservative full potential code for transonic small disturbances (TSD). Only the 3D CFD lift was coupled. Subsequent efforts by Strawn and Desopper [111] and Strawn and Bridgeman [112] led to the refinement of the coupling technique and inclusion of unsteady aerodynamic terms due to the airfoil pitch rate and large lag angle. In 1991, Kim, Desopper and Chopra [113] coupled a TSD code with UMARC. This analysis further refined the coupling technique by consistently updating the vehicle trim and rotor response in the coupling process, and using both the 3D lift and pitching moment results. Direct pitching moment coupling led to divergence. The divergence could be avoided by including an average of 3D pitching moments and 2D pitching moments in the aeroelastic analysis. The reason for divergence was identified as inaccurate 3D pitching moments due to the inherent inability of a TSD

code in modeling the shock boundary layer interaction. Loose coupling with Euler codes have been performed recently by Altmikus [107] and Servera, Beaumier and Costes [114]. Navier-Stokes loose coupling have been performed by Pahlke [115].

Baeder and Sitaraman [116] obtained Navier-Stokes solution to a prescribed set of blade deformations for the UH-60A at high speed forward flight. The TURNS-3D code was used. The blade deformations were obtained using measured airloads as part of the present research work. The control angles were measured. Coupling between TURNS-3D and UMARC comprehensive analysis have been carried out, as part of the present work in reference [117]. The loose coupling scheme used was different from that proposed in Reference [110] in that the airload sensitivities from the comprehensive analyses were not used during convergence. The coupling scheme was unstable and ill-posed and required numerical sub-iterations for calculation of control angles in trim response. Although good vibratory airload predictions were obtained, the blade loads gradually diverged. The study showed that loose coupling between a pure structural dynamic analysis and an aerodynamic analyses is an ill-posed problem.

Subsequently, the TURNS-3D code underwent significant refinements in the way far field boundary conditions were handled. Free stream boundary conditions were changed to characteristics boundary conditions [118]. With the refined boundary conditions, the vibratory normal force predictions deteriorated at the mid-span stations (67.5% R, 77.5% R). However, predictions further inboard were improved, predictions further outboard remain unchanged. It was found that the use of free stream boundary conditions together with Newton sub-iterations to ensure the time

accuracy, caused oscillations in the pressure distribution at the blade surface, which emerge as impulses in the sectional air loads. These impulses were misinterpreted as physically significant effects. Yawed flow and 3D blade flap effects were investigated in order to understand this effect. Both these mechanisms have been subsequently discarded as dominant contributors of vibratory normal force at these radial stations.

The coupling methodology was re-formulated using the original method [110], and the up-dated TURNS-3D code was coupled with UMARC in reference [118]. Stable and converged trim, air loads and blade loads were obtained for the UH-60A helicopter at high speed forward flight. A contemporary research effort at NASA Ames/AFDD was carried out with OVERFLOW-D coupled with CAMRAD-II and RCAS by Potsdam, Yeo and Johnson [119]. The key difference is in the implementation of far wake. OVERFLOW-D includes all four blades in the analysis and directly computes the far field inflow using multi-block or overset meshes. TURNS-3D is a single blade analysis which obtains the far wake inflow from the Bagai-Leishman free wake model in UMARC.

1.2.8 Model and Full Scale Rotor Tests

Accurate prediction of helicopter vibration and rotor vibratory loads is a complex, multi-disciplinary and difficult problem. Development of a reliable prediction capability requires careful comparison of theory and experiment. Over the last fifty years, major wind tunnel and flight tests have been conducted where detailed blade airloads and structural loads were measured. An enormous volume of data is avail-

able from the NACA/Langley 2 bladed, 15 ft dia. teetering model tested by Rabbott and Churchill in the 1950s to the most recent U.S.Army/NASA Ames 4 bladed, 52 ft dia. articulated Black Hawk flight tests in the 1990s.

Test data, model scale and full scale, for various types of rotor systems and blade numbers are necessary for the development and validation of theoretical analysis. A theoretical analyses is successfully validated when - (i) it captures the fundamental loading patterns common to all rotor systems and (ii) captures the differences observed among different rotor configurations.

An survey of all major rotor tests, wind tunnel and full-scale, from the 1950s to the first half of the 1980s can be found in Hooper [120]. It focussed on measured airloads and identified consistent patterns that are common to all rotor systems - regardless of blade number, size and trim conditions. The work showed that the vibratory airloads are remarkably consistent in the transition regime. At high speed, they were similar but in general more variable.

Bousman [121] made a comprehensive survey of full scale rotor tests focusing on the vibratory structural response. Like in the case of vibratory airloads, consistent patterns were identified in vibratory structural response behavior, largely independent of rotor configuration. For example, the dominant vibratory flap response always occurs at 3/rev, the root chord bending moment shows a negative to positive loading at the start of the third quadrant and the pitch-link loads for articulated rotors showed large positive-negative oscillations between the first and second quadrants. On the other hand the vibratory chord bending moments differed significantly between rotor to rotor. The pitch-link load of teetering rotors like the

AH-1G differed significantly from that of articulated rotors like the UH-60A.

A summary of the major rotor tests, which focussed on airloads and blade loads of main rotor systems are given in tables 1.1 and 1.2. Tiltrotor tests have been left out of this summary. Acoustic tests have also been left out, except, the HART and ONERA tests, from which airloads measurements are often used for validation purposes.

Other rotor test programs for loads measurements are those of Lynx fitted with BERP blades [137], NASA model hover test [138], DNW tests of the Boeing 360 rotor [139] and McDonnell Douglas HARP rotor [140]. The BERP data were helpful in identifying regions of blade stall and the NASA model rotor was used to study blade-vortex interactions. UTRC and Sikorksy, under sponcership of U.S.Army (USAAATD) have carried out extensive wind-tunnel testing (at Duits Nederlands Windtunnel, DNW, in Holland) of a 4 bladed 9.4 ft dia scale (1:5.73) model of the UH-60A BlackHawk articulated rotor system [141]. The hover test program included blade pressures, surface flow, performance, wake geometry and flow field velocities (using a laser velocimeter). The tests were extended to forward flight in 1989 and included acoustic, dynamic, performance and airloads measurements of baseline pressure-instrumented rotors and non-instrumented rotors with modified tip geometries. An detailed discussion of the measured airloads can be found in Lorber [142].

In addition, two recent acoustic tests provide reliable airloads data. They are the HART/HART II [143] and HELISHAPE [114]. The HART test was conducted on 40% geometrically and aeroelastically scaled model of a hingeless BO-105 ro-

tor in the DNW tunnel, in 1994. The HART II test was conducted in 2001. The HART II tests were carried out to emphasize on wake measurements. Both were collaborations between German DLR, French ONERA, NASA Langley and U.S.Army. The HELISHAPE program was an initiative between all 3 European manufacturers, Eurocopter, Augusta and Westland, and 13 other Research Institutes and Universities. Airloads measurements are available for the ONERA-Eurocopter swept-back parabolic/anhedral tip 7AD1 blade and rectangular tip 7A blades [114].

Although all the above tests were used to validate numerical models, in general, each test focussed on a specific set of phenomenon. None of them were fully comprehensive, covering steady and maneuvering flight, high thrust dynamic stall conditions, pressure data, strain gauge data, pitch link loads and fuselage vibration measurements. Wind tunnel models, even when full scale, do not include full helicopter components. For example, the model UH-60A rotor did not have a non-linear lag damper or bifilar pendulums at the hub. On the one hand, wind tunnel tests are more controlled thereby limiting uncertainties in atmospheric conditions, variations in speed due to gusts and sideslip angles, pilot error etc. On the other hand, the real objective of measuring fuselage vibration cannot be accomplished by wind tunnel models. Only a full-scale flight test program can provide fuselage vibration data, with associated rotor airloads, blade loads, control loads, performance data and vehicle trim data, which can then be used to validate all aspects of a comprehensive analysis consistently. A truly extensive flight test program would cover steady level flight, steady and unsteady maneuvers, low speed and high speed flight, low thrust and high thrust flight, each conducted multiple times to ensure repeata-

bility and accuracy of the data. The test conditions and the blade and helicopter properties (fuselage properties, c.g. location, fuel content, armament weight and placement etc) must be accurately and carefully documented before and after each flight, minimizing uncertainties as much as possible. The U.S.Army/NASA-Ames UH-60A Black Hawk Airloads Program [144] is such a detailed flight test program. The comprehensive set of repeatable test data from the UH-60A Airloads Program have established benchmarks to validate various aspects of a comprehensive rotor analyses.

The UH-60A flight test program conducted 31 flights. They covered Steady flight (7 flights), Maneuver flight (3), Ground Acoustic Measurements (9), In-flight Acoustic Measurements (6) and Flight dynamics (6). Pressure gauge measurements (airloads obtained by integrating) were taken at 9 stations, flap bending gauges at 9 stations, chord bending gauges at 8 stations and torsion bending gauges at 4 stations. All four pitch links were instrumented to measure control loads. This is perhaps the most extensive instrumentation suites used in a flight test, providing reliable and repeatable test data. The present work uses the UH-60A flight test data. Details of the structural, aerodynamic and trim data sets are discussed in the appropriate chapters.

1.2.9 Prediction Capability of Analysis Methods

The 1973 AGARD (Advisory Group for Aerospace Research and Development) Specialists Meeting on Helicopter Rotor Loads and Prediction Methods [145]

summarized the state-of-the-art in loads prediction up to that time. The status was summarized by Loewy [146] as, "*Instead of running into unexpected high loads almost everywhere the first time the full flight envelop is explored, we now only run into them occasionally, at some extreme flight condition*". In terms of physical understanding, more emphasis was called for on diagnostics, for example instead of comparing only peak magnitudes of blade stresses to compare magnitude and phase. The prediction of phase was poor, indicating fundamental deficiencies in physical understanding of the problem. Piziali in his commentary [147] summarized, "*...the progress has been primarily in the expansion of the scope of predictive capability. Over the last 10-12 years, the improvement in the correlation of the predicted and measured results has not been significant*". He concluded that for improved prediction, the air loads and dynamic response must be resolved into meaningful components to provide information as to the source of the discrepancies.

The state of the art in helicopter loads and vibration prediction up to 1994 was summarized by the AHS organized Lynx helicopter workshop [148]. Vibratory hub load predictions from eight comprehensive codes were compared with Lynx level flight test data. None of the codes achieved prediction accuracy of more than 50%. The greatest deficiency was at high speed (158 kts) where the predictions not only differed greatly from the test data but also equally greatly from one another. The Lynx blades were not pressure instrumented and therefore air loads correlation could not be performed. Extensive air loads correlation was then performed with the Research Puma data [97]. Predictions from four Lifting-line codes and two CFD analyses (FPR and TSP) were compared with test data. Although in general

satisfactory prediction of vibratory lift was obtained from all codes, some suggested wake as the most important phenomenon, others suggested blade elasticity. The role of trim solution was not clear. The pitching moment predictions from lifting-line models were poor. Predicted pitching moments from the CFD method diverged the solution procedure and could not be iteratively coupled.

Bousman in 1999 [3] reviewed the lack of progress in understanding the physics of vibratory rotor loads over the past three decades. As understood, high vibrations take place in two flight regimes in level flight, low speed transition and high speed forward flight. In transition flight, the key source of vibratory loads is identified as the intertwining of rotor tip vortices below the rotor disk. In high speed flight the mechanism is not clear. The negative loading on the advancing blade appear to play a key role. The problems of *negative lift in high speed flight* and *erroneous blade pitching moments* were identified as the two fundamental prediction deficiencies in aeromechanics. The focus of the present work lies in the investigation and understanding of these two prediction deficiencies. The details of the two prediction deficiencies and prior research focussed on understanding them are discussed in greater detail in the section on *High Speed Loads and Vibration Prediction*. Bousman suggested that it is not only important to break up a difficult problem into manageable pieces and solve those pieces but it is equally important to "*...remember the purpose of what we are doing and that is to complete the synthesis, to bring the parts back together and demonstrate that they work. We need to understand that the value of our work exists only in that it will be used and contribute to the whole*".

The present work embodies Piziali and Bousman's ideas of resolving the prob-

lem into meaningful components, investigating them separately and finally bringing the pieces back together as a whole.

1.3 Objective of Present Research

The objective of this research is to refine a state of the art comprehensive analysis for accurate and consistent prediction of rotor vibratory loads in steady level flight. There are two critical vibration regimes in steady level flight - (1) low speed transition (around 40 kts) and (2) high speed forward flight (around 160 kts). Unlike low speed, where inter-twinning of rotor tip vortices are understood to be the dominant source of rotor vibration [3, 99, 149, 150], the mechanism of rotor vibration at high speed flight is not fully understood. Aeroelastic predictions show more than 50% error compared to flight test measurements, specially in the prediction of phase [148]. The focus of this research is therefore on high speed flight. The goal is to gain fundamental understanding of the key vibration mechanisms involved and to develop a consistent and accurate prediction capability.

The approach is to isolate the physics of vibratory air loads from that of vibratory blade loads by systematically comparing UH-60A flight test data with predictions. Vibratory loads, as explained before, are defined as those harmonics of air loads and blade loads which contribute to the shaft transmitted vibration of a helicopter. In the present work, three and higher harmonics (3/rev and higher) are collectively referred to as vibratory harmonics. Zero, one and two harmonics are collectively referred to as non-vibratory harmonics. One and higher harmonics are

collectively referred to as oscillatory harmonics.

1.4 Rotor Loads Prediction at High Speed - State of Art

The state-of-the-art in rotor loads and vibration prediction in high-speed flight is far from satisfactory, even though both vibratory air loads and structural response show consistent patterns for a large number of helicopters [120, 121]. A good indicator is the AHS organized Dynamics Workshop (1994) where predicted vibratory hub loads from eight aeroelastic analyses were compared with Lynx flight test data [148] (figure 1.1). Accuracy of prediction was less than 50% with significant discrepancy between predictions from various codes. The Lynx blades were not pressure instrumented, hence, the discrepancies could not be traced back to blade air loads.

The UH-60A flight test data provide the opportunity for tracing back the sources of prediction deficiencies to discrepancies in air loads and blade loads calculation. Figure 1.2 shows the predicted and measured mid-span flap bending moments for the UH-60A in high speed forward flight. None of the two state-of-the-art comprehensive analyses predictions (Lim [151]) capture the correct waveform. Both analyses include elastic blade model, free wake, test airfoil tables, 2D unsteady aerodynamics and tip sweep. The vibratory component of the flap bending moment (3/rev and higher) is dominated by 3/rev component. This is due to the proximity of the second flap mode frequency (2.82/rev) to 3/rev. Figure 1.3 shows the

predicted magnitude and phase of 3/rev flap bending moment over a range of level flight speeds. At high speed, the bending moment is under-predicted by more than 50%. Accuracy of predicted flap bending depends on predicted blade lift. Figure 1.4 compares flight test lift with predictions from three comprehensive analysis. None of the analyses capture the advancing blade lift correctly, inboard or outboard. The drop in the predicted lift on the advancing side leads the flight test lift by a phase error of around 40 degrees. This discrepancy is linked to inaccurate vibratory lift prediction (to be discussed in chapter 3) 3/rev and higher. At an inboard station, e.g. 77.5% R, the vibratory harmonics show an impulsive behavior in the advancing blade. Towards the tip, e.g., 96.5% R, the vibratory harmonics have a dominant 3/rev character. Both analyses consistently miss the phase of vibratory harmonics.

The lift phase error is the *first* of the *two fundamental prediction deficiencies* of articulated rotor aeromechanics identified by Bousman in 1999 [3]. The *second* fundamental prediction error for articulated rotors is the prediction of pitch-link load (or control load). The two problems are inter-connected, as described below. The two problems, form the focus of the present research effort.

Comprehensive predictions showed relatively good agreement with measured negative lift for the Research Puma helicopter [97]. However, for the UH-60A, both 2GCHAS and CAMRAD/JA showed significant deviation in phase prediction [151]. Lim [151] studied the effects of various modeling options in 2GCHAS on full scale lift prediction. Effects of fuselage trim attitude and detailed blade sweep modeling were investigated. However, no improvement of the prediction of lift phase was noticed.

Model-scale UH-60A data obtained from DNW wind-tunnel tests [142] also

show the same negative lift at high-speed flight as measured in the full-scale helicopter [152], figure 1.5. The model rotor did not have bifilar absorbers unlike the full scale UH-60A, and had a viscous lag damper to prevent ground resonance. Because both the full-scale helicopter and the model-scale rotor have the same measured negative lift phase, it is possible to rule out fuselage up wash, fuselage dynamics, side slip angle, non-linear lead-lag damper or bifilar modeling as possible sources of error in the prediction of negative lift phase. References [153] and [154] investigated model scale lift prediction. In Ref. [153], measured air loads were used to predict structural response. In Ref. [154], measured deflections were used to predict air loads. With measured air loads, blade torsional bending was not accurately predicted, but with measured elastic twist, good correlation of lift phase was obtained. The measured elastic twist in the later case, was not physically measured. It was deduced from blade torsion bending using a modal approach. Recently another articulated rotor system, the French ONERA 7A has shown similar advancing blade lift phase behavior during wind tunnel tests, figure 1.5, [114]. Although the negative lift peak occurs at a slightly different azimuth, the lift drop off occurs at the same azimuth as the UH-60A flight test.

The H-34 articulated rotor system, also exhibits similar high-speed negative lift characteristics as the Black Hawk - both in flight test and wind tunnel test [120]. This similarity is strong near the tip and gradually diminishes inboard. A section at 75% span on the H-34 blades, shows no phase delay [155]. None of the analytical methods reported in Ref. [120] were successful in accurate prediction of lift phase towards the blade tip. Recently in 2004, Yeo and Johnson [101] compared high

speed measured air loads in level flight for five articulated rotor configurations and compared with CAMRAD II calculations. The configurations were - H-34 full scale in wind tunnel ($\mu = 0.39$, $C_T/\sigma = 0.06$), SA 330 or the Research Puma full scale in flight ($\mu = 0.362$, $C_T/\sigma = 0.07$), SA 349/2 full scale in flight ($\mu = 0.361$, $C_T/\sigma = 0.071$) and also the UH-60A full scale in flight as discussed above ($\mu = 0.368$, $C_T/\sigma = 0.0783$). Except the Research Puma, all the rotor systems showed the advancing blade lift phase problem. H-34 has a trapezoidal tip, SA 349/2 has a straight tip, UH-60A has a swept tip - clearly tip shape alone cannot be the source of the problem. The rigid pre-twist for the rotors range from -8.3 degrees (ONERA 7A) to approximately -16 degrees for the UH-60A. Therefore, high rigid twist alone cannot be the problem either. Moreover, the SA 349/2 blades do not show a negative loading near the tip at all, yet, has the same phase error as the UH-60A.

The pitch-link loads are the rotor control loads near the blade root - primarily an integrated effect of the blade torsion bending moments. The pitch-link loads are under-predicted by 50% at all flight speeds, figure 1.7. Figure 1.8 shows the predicted pitch-link load at high speed. Inaccurate pitch-link load arises due to to inaccurate aerodynamic pitching moments. Pitching moment predictions, for all the rotors, including the research Puma was poor. Figure 1.6 shows the predicted pitching moments of the UH-60A at high speed flight (taken from Lim [151]). They are over-predicted inboard and under-predicted at the outboard stations.

The section pitching moments determine elastic torsion which directly affects the blade lift as a contributing component of the angle of attack. It can be shown that elastic torsion is the dominant contributor to advancing blade lift in high speed

flight (chapter 4). Thus the two problems of advancing blade lift and pitching moment prediction are related to each other via the accuracy of structural response calculation. Lim [156], in agreement with Bousman's assessment summarized the state of the art as [3], "*We are still in the stage that we do not understand the basics : is this discrepancy from the structural or aerodynamic (especially wake) modeling or both ?*".

The intent of the present work is to isolate these two effects - decouple aerodynamics from structural dynamics, study them separately, understand the prediction deficiencies in each, improve upon them, and bring them back together.

1.5 Approach of Present Research

The present research differs from previous work in that it tries to separate the physics of aerodynamics and structural dynamics from the complex aeroelastic problem, investigate them separately and then bring them back together again.

Flight test measured air loads are used to validate and refine a structural model - the errors in prediction now originate entirely from structural modeling. Once validated, the obtained deformations are prescribed to calculated air loads - the errors in prediction originate from aerodynamic modeling. Lifting-line and CFD aerodynamic models are investigated and compared. The lifting-line and CFD aerodynamic models are then used to perform comprehensive analysis of the UH-60A Black Hawk helicopter. The lifting-line comprehensive analysis is used to gain fundamental insights into the two key problems of articulated rotor aeromechanics

- advancing blade lift phase and pitch link loads. Consistency of rotor modeling is investigated with step-wise modeling refinements. The CFD aerodynamic model is then consistently coupled with the lifting-line comprehensive analysis to resolve the two problems and significantly improve the prediction of air loads and blade loads. The reasons for improvements are established and understood from the prescribed deformations air loads study.

1.6 Contributions of the Present Research

The key contributions of this research can be divided into two categories - 1. fundamental understanding of rotor vibration in high speed forward flight and 2. improvements in the accuracy and scope of prediction capability to capture them. The specific conclusions can be summarized as follows.

1. Prediction errors in vibratory and oscillatory blade loads and pitch link loads in high-speed forward flight stem from *inaccurate aerodynamic modeling, not structural modeling*. Error in oscillatory pitch link load stems from inaccurate aerodynamic pitching moments. Error in vibratory blade loads stems from inaccurate vibratory lift. Fundamental deficiency in the prediction of vibratory lift manifests as an advancing blade lift phase error.

2. Vibratory lift at high speed is dominated by elastic torsion at outboard stations (85% outboard) and a combination of elastic torsion and wake of preceding blades inboard (60%-85% radial stations). *Both elastic torsion and rotor wake, together, are key to accurate prediction of vibratory lift at the inboard*

stations. Either of the factors alone does not improve vibratory lift or lift phase predictions at these stations.

3. A 3D-CFD analyses (TURNS 3D) consistently coupled to a comprehensive aeroelastic analyses (UMARC) predicts the aerodynamic pitching-moments accurately and therefore the elastic torsion deformations at high speed. The coupling methodology is robust, stable, well-posed and easy to converge in five or six iterations. Improved predictions from CFD coupling stem from improved aerodynamic pitching moment predictions - most significantly near the blade tip, and all across the span in general.

4. An accurate set of blade deformations are obtained by using flight test measured airloads at high speed flight. In absence of measured deformations, this deformation set forms a reasonably accurate alternative to validate airloads calculations.

5. UMARC/TURNS-3D loose coupling methodology significantly resolves the high speed vibratory airloads, blade loads, lift phase and pitch link load prediction problem from first principles.

1.7 Organization of the thesis

Chapter 1 describes the helicopter loads and vibration problem, surveys the evolution and state of the art in analyses capability, focuses on the fundamental high speed flight prediction errors and discusses the main focus and key contributions of

the present work.

Chapter 2 to 5 describes the present research work step by step. Chapter 2 describes the structural modeling and validation. At the end of Chapter 2, a set of prescribed deformations are obtained with which to validate the aerodynamic models. Chapter 3 deals with aerodynamic modeling and validation. Chapter 4 describes lifting-line comprehensive analysis with focus on fundamental understanding issues. Chapter 5 describes 3D CFD-comprehensive code loose coupling methodology for improved prediction of air loads and blade loads predictions from first principles. A set of summary observations are included at the end of each chapter.

Chapter 6 states the key conclusion of the present research along with recommendations for future work.

Table 1.1: Major Rotor Tests

Rotor Test	**Configuration**	**Reference**
NASA Langley model rotor	2 bladed teetering rotor 15 ft dia	1956 [122]
Bell UH-1 flight tests	2 bladed teetering rotor	1961 [123]
Sikorsky H-34 (CH-34) flight test, NASA Langley	4 bladed articulated	1964 [124]
H-34 (CH-34) full scale wind tunnel test, NASA Ames	4 bladed articulated	1966 [125]
Vertol CH-47A flight tests, USAAVLABS	3 bladed tandem rotor	1968 [126]
Lockheed XH-51A flight tests	4 bladed compound helicopter	1968 [127]
Sikorsky NH-3A flight tests	5 bladed, compound version of the S-61	1970 [128]
Sikorsky CH-53A flight tests, U.S.Navy	6 bladed articulated	1970 [129]
Bell AH-1G flight tests, U.S.Army	2 bladed teetering. Test conducted for aero and structural loads	1976 [130]

Table 1.2: Major Rotor Tests Continued

Rotor Test	**Configuration**	**Reference**
Bell AH-1G flight tests, NASA	2 bladed teetering. Test conducted for aero-acoustic measurements	1983 [131]
Sikorksy S-76 full scale wind tunnel tests	4 bladed articulated	1980 [132]
Bell AH-1G flight tests	2 bladed teetering	1988 [133]
Aerospatial SA-330 Research Puma flight tests	4 bladed articulated	1983, 1986.[97]
Aerospatial SA 349/2 Gazelle flight tests	3 bladed articulated	1986 [134]
Westland Lynx flight tests	4 bladed hingeless	1993 [135]
McDonnell Douglas MDART full scale wind tunnel tests	4 bladed advanced bearingless rotor, pre-production version of MD900 rotor	1993 [136]

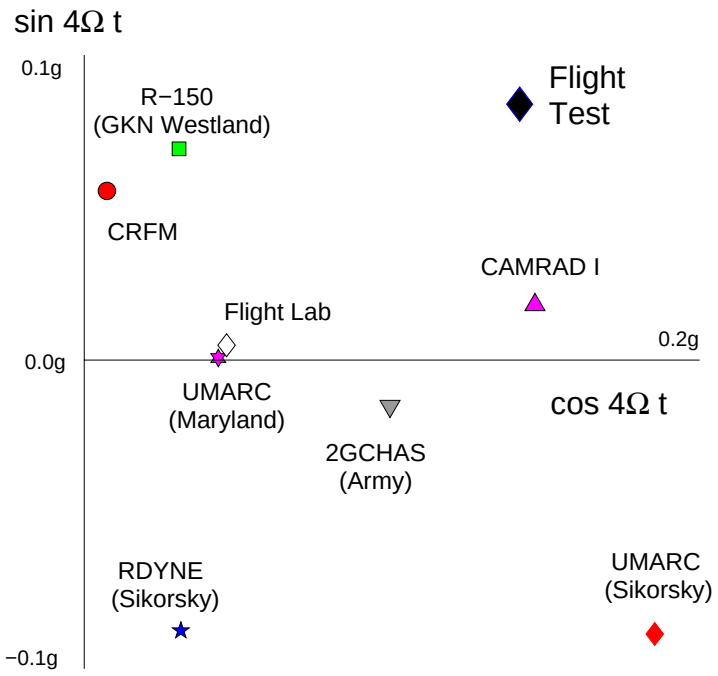

Figure 1.1: **Vibratory hub load predictions from eight aeroelastic codes compared with Lynx data, Cockpit starboard location, high-speed steady level flight at 158 knots, Hansford and Vorwald [148]**

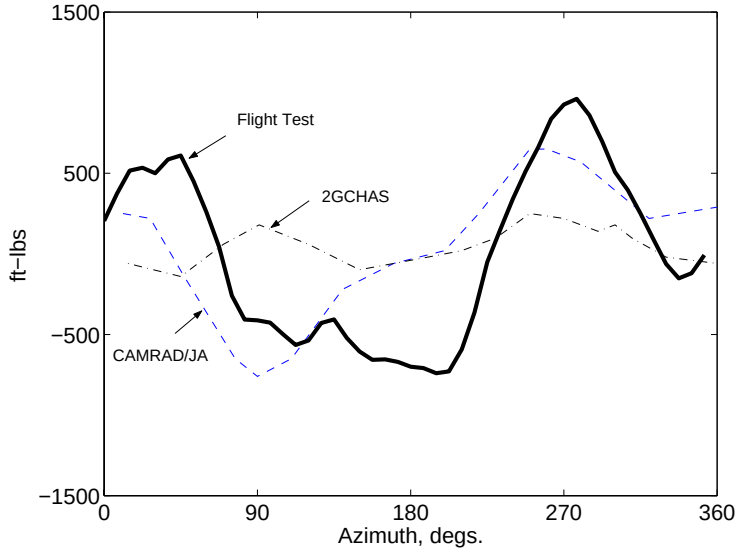

Figure 1.2: **Predicted Flap Bending Moment at 50% R radial station in high-speed steady level flight compared with UH-60A data; $\mu = 0.368$, $C_w/\sigma = 0.0783$, Lim [151]**

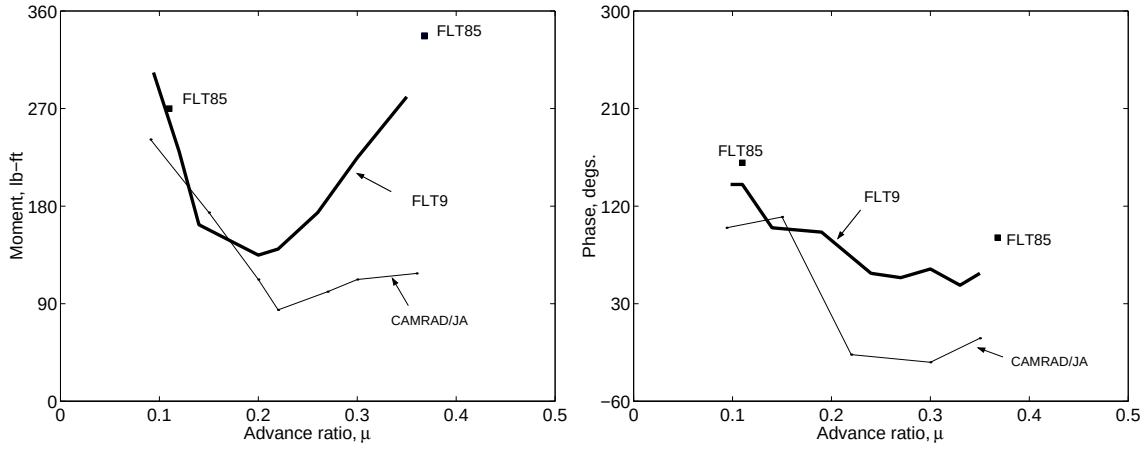

Figure 1.3: **Predicted and measured 3p flap bending moment at 50% R for UH-60A Black Hawk in steady level flight; $C_W/\sigma = 0.0783$, Bousman [99]**

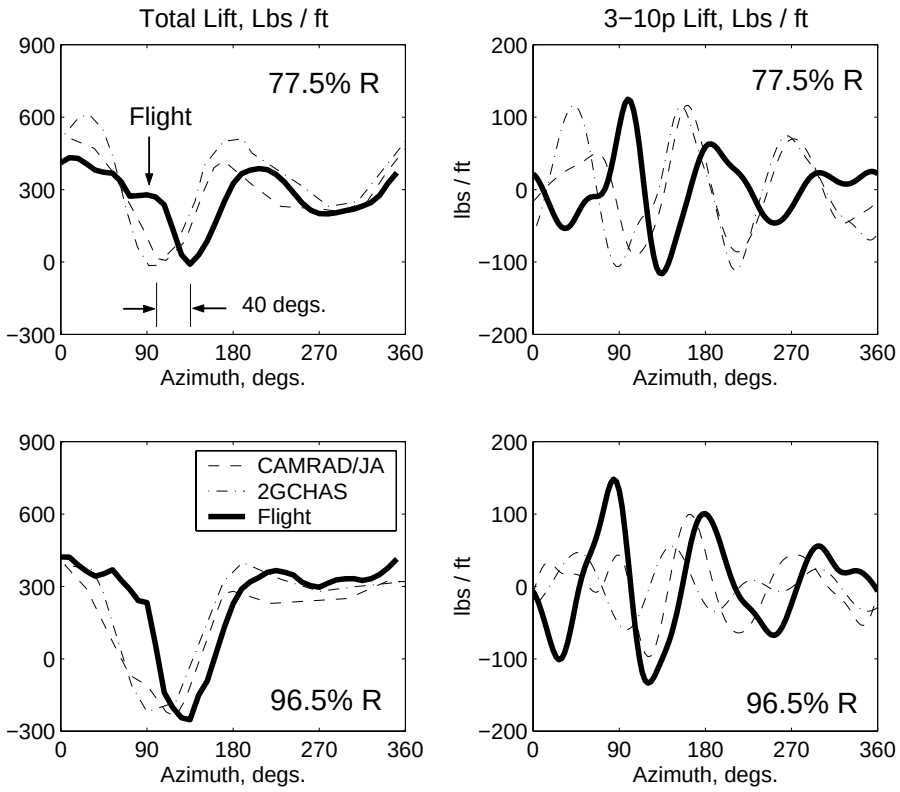

Figure 1.4: **State-of-the-Art normal force prediction in high-speed steady level flight compared with UH-60A data; $\mu = 0.368$, $C_w/\sigma = 0.0783$, Lim [151]**

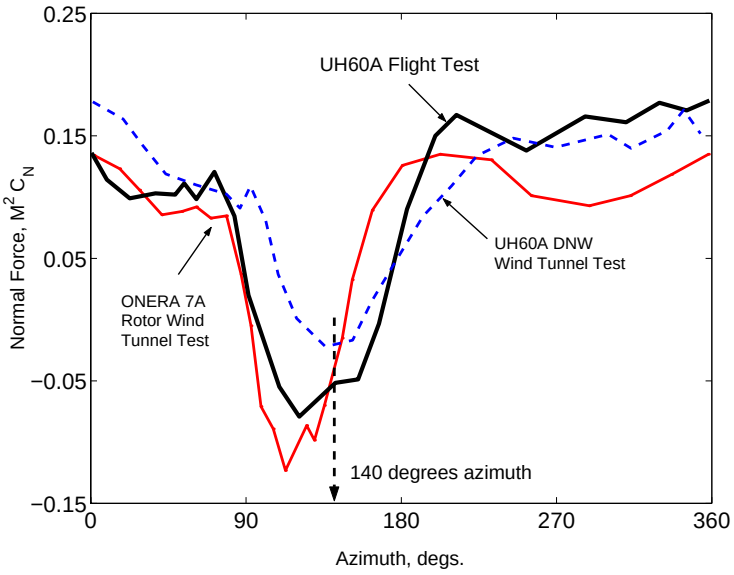

Figure 1.5: **Measured normal force on UH-60A full scale flight test compared with DNW wind tunnel test and ONERA 7A articulated rotor wind tunnel test data, Bousman [152], ONERA [114]**

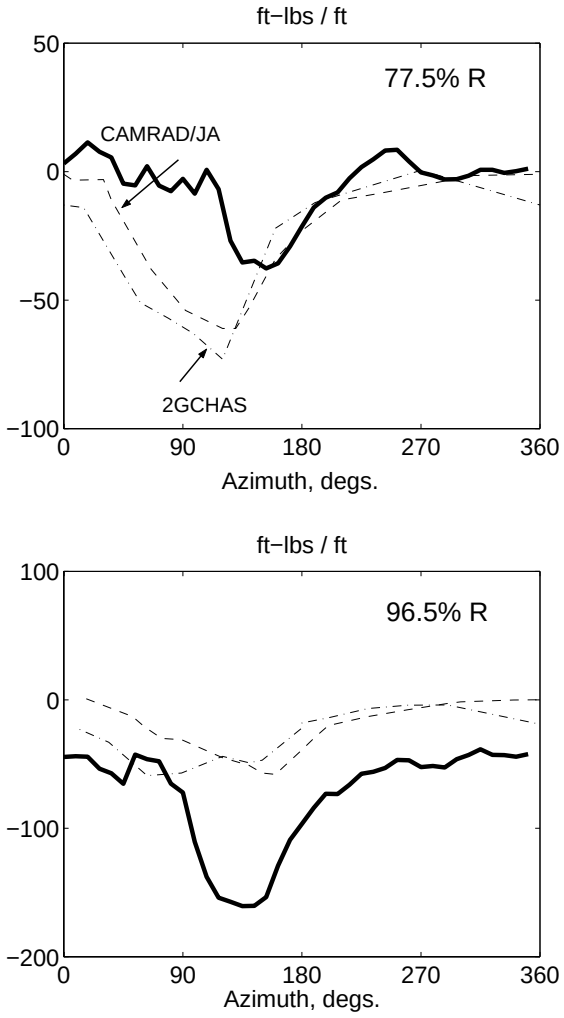

Figure 1.6: **State-of-the-Art pitching moment prediction (about quarter-chord) in high-speed steady level flight compared with UH-60A data; μ = 0.368, C_w/σ = 0.0783, Lim [151]**

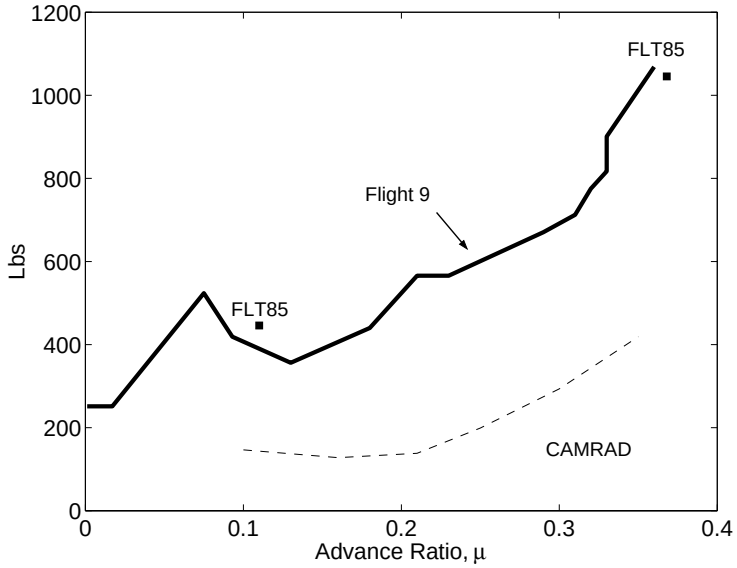

Figure 1.7: **State-of-the-Art in Pitch Link Load prediction in high-speed steady level flight compared with UH-60A data; $\mu = 0.368$, $C_w/\sigma = 0.0783$, Bousman [3]**

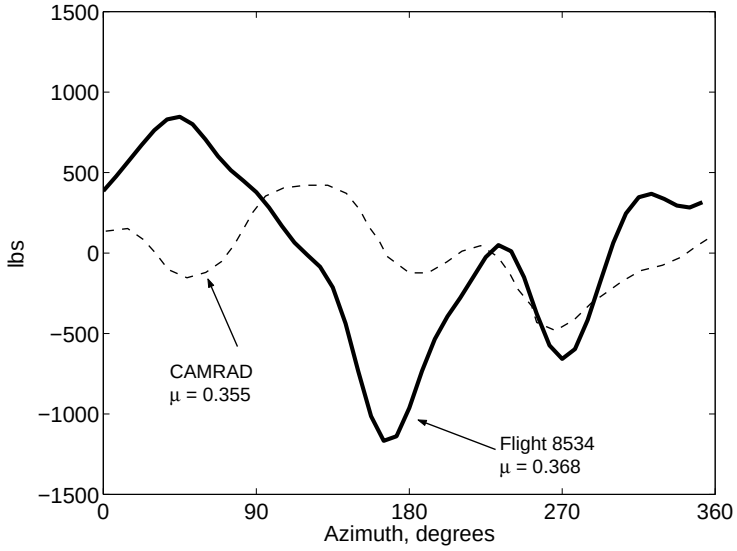

Figure 1.8: **State-of-the-Art in pitch link load prediction in high-speed steady level flight compared with UH-60A data; $\mu = 0.368$, $C_w/\sigma = 0.0783$, Bousman [3]**

Chapter 2

Structural Model of Rotor Blades

This chapter describes and validates the structural dynamic model of UH-60A rotor blades. Flight test measured air loads, control angles and lag damper force are used to calculate the rotor structural response and dynamic blade loads. Prediction errors originate entirely from structural modeling. Thus the physics of structural dynamics is isolated from the aeroelastic response problem. The focus is on fundamental understanding of the structural dynamic mechanisms behind oscillatory and vibratory blade loads.

A similar study was carried out in reference [157] using flight test and wind tunnel air loads of a CH-34 rotor. The equations governing blade response in flap, lag and torsion were linear. Flap and lag degrees of freedom were coupled only by the local pitch angle. Torsion degree of freedom was uncoupled from flap and lag. In

the present study, a fully coupled set of non-linear equations are used, as derived in references [13, 14]. The effect of couplings produced by sectional center of gravity offsets, tip sweep and structural nonlinearities are shown. A similar investigation was carried out in Reference [153] for the UH-60A but the airloads used were that of a model scale rotor.

The outcome of this exersize, once the structural model is satisfactorily validated, is an accurate set of blade deformations data. This set of deformations data is valuable because flight test measurements of blade deformations are not available. In absence of measured deformations, the deformation set obtained using measured air loads, provides an opportunity for isolating the physics of aerodynamics from the aeroelastic response problem. The deformations obtained using measured air loads is termed *prescribed blade deformations*. Using this set of *prescribed blade deformations* constant, different aerodynamic models can be evaluated by comparing air load predictions with flight test air loads. This study forms the subject matter of Chapter 3. The success of isolating aerodynamics therefore depends on the accuracy of the structural model. This forms the subject matter of this chapter.

First, the blade deformation geometry, governing equations of motion, modeling assumptions, response and blade loads solution methods are described. Then the structural model is validated using flight test data. Finally, using the validated structural model, an accurate set of blade deformations at high-speed flight is obtained.

2.1 Governing Equations of Motion

The rotor blades are modeled as long, slender, homogeneous, isotropic beams undergoing axial, flap, lag and torsion deformations. The deformations can be moderate as the model includes geometric non-linearities up-to second order. Radial non-uniformities of mass, stiffness, twist, etc., chordwise offsets of mass centroid (center of gravity) and area centroid (tension axis) from the elastic axis, precone, and warp of the cross section are included. The model follows the Hodges and Dowell formulation [13] while treating elastic torsion and elastic axial deformation as quasi-coordinates [14]. The baseline model assumes a straight blade. Modeling refinements required to incorporate structural sweep and droop are described in details in Ganguli and Chopra [25]. The governing equations and their derivations remain same, the swept and drooped elements require additional coordinate transformations and a modified finite element assembly procedure. The equations of motion are developed using Hamilton's Principle.

The governing partial differential equations are solved using finite element method in time and space. The finite element method provides flexibility in the implementation of boundary conditions for modern helicopter rotors. For example, specialized details not treated in Ref. [13], like blade root pitch flexibility (pitch link stiffness), pitch damping, elastomeric bearing stiffness and damping are incorporated within a finite element model.

2.1.1 Blade Coordinate Systems

There are 4 coordinate systems of interest, the hub-fixed system, (X_H, Y_H, Z_H) with unit vectors $\hat{I_H}, \hat{J_H}, \hat{K_H}$, the hub-rotating system, (X, Y, Z) with unit vectors $\hat{I}, \hat{J}, \hat{K}$, the undeformed blade coordinate system, (x, y, z) with unit vectors $\hat{i}, \hat{j}, \hat{k}$ and the deformed blade coordinate system, (ξ, η, ζ) with the unit vectors $\hat{i_\xi}, \hat{j_\eta}, \hat{k_\zeta}$. These frames of references are denoted as H, R, U and D respectively. The hub-rotating coordinate system is rotating at a constant angular velocity $\Omega\hat{K}$ with respect to the hub-fixed coordinate system. The transformation between the hub-fixed system and the hub-rotating system is defined as

$$\begin{Bmatrix} \hat{I} \\ \hat{J} \\ \hat{K} \end{Bmatrix} = \begin{bmatrix} \cos\psi & \sin\psi & 0 \\ -\sin\psi & \cos\psi & 0 \\ 0 & 0 & 1 \end{bmatrix} \begin{Bmatrix} \hat{I_H} \\ \hat{J_H} \\ \hat{K_H} \end{Bmatrix} = \mathbf{T_{RH}} \begin{Bmatrix} \hat{I_H} \\ \hat{J_H} \\ \hat{K_H} \end{Bmatrix} \tag{2.1}$$

where the azimuth angle, ψ, equals $\Omega\, t$. The undeformed blade coordinate system is at a precone angle of β_p with respect to the hub-fixed system. The transformation between the undeformed blade coordinate system and the hub-fixed system is defined as

$$\begin{Bmatrix} \hat{i} \\ \hat{j} \\ \hat{k} \end{Bmatrix} = \begin{bmatrix} \cos\beta_p & 0 & \sin\beta_p \\ 0 & 1 & 0 \\ -\sin\beta_p & 0 & \cos\beta_p \end{bmatrix} \begin{Bmatrix} \hat{I} \\ \hat{J} \\ \hat{K} \end{Bmatrix} = \mathbf{T_{UR}} \begin{Bmatrix} \hat{I} \\ \hat{J} \\ \hat{K} \end{Bmatrix} \tag{2.2}$$

The transformation between the undeformed blade coordinate system and the deformed blade coordinate system remains to be determined.

2.1.2 Blade Deformation Geometry

Consider a generic point P on the undeformed blade elastic axis. The orientation of a frame consisting of the axes normal to and along principle axes for the cross section at P defines the undeformed coordinate system (x, y, z). When the blade deforms, P reaches P'. The orientation of a frame consisting of the axes normal to and along principle axes for the cross section at P' defines the deformed coordinate system (ξ, η, ζ). Adequate description of the deformed blade requires in general a total to six variables : three translational variables from P to P', u, v, w along x, y, z, and three rotational variables from (x, y, z) system to (ξ, η, ζ) system, and any out of plane deformations of the cross section, e.g., warp. These out of plane deformations are neglected, which results in plane sections remaining plane after deformation i.e., the Euler-Bernoulli beam assumption. The Euler-Bernoulli assumption leads to a further simplification - two of the three angles can be expressed as derivatives of the deflection variables. Thus four deformation variables - three deflections u, v, w and one rotational angle, completely determine the deformed geometry. The definition of this rotation angle - the angle of elastic twist is described below.

The coordinate transformation matrix between the undeformed system and the deformed system is defined by the direction cosines of (ξ, η, ζ) with respect to (x, y, z), where x is tangent to the elastic axis of the undeformed blade and ξ is tangent to the elastic axis of the deformed blade. The transformation matrix can

be written as

$$\begin{Bmatrix} \hat{i_\xi} \\ \hat{j_\eta} \\ \hat{k_\zeta} \end{Bmatrix} = \mathbf{T_{DU}} \begin{Bmatrix} \hat{i} \\ \hat{j} \\ \hat{k} \end{Bmatrix} \tag{2.3}$$

where $\mathbf{T_{DU}}$ can be described as a function of three successive angular rotations in space required to align (x, y, z) along (ξ, η, ζ). The two intermediate orientations can be described as (x_1, y_1, z_1) and (x_2, y_2, z_2). Classical Euler angles use rotation ψ about z, θ about x_1 and ϕ about z_2 to orient (x, y, z) along (ξ, η, ζ). Singularities result when the second angle is zero because the first and third transformations are then about the same axis. Small angle rotations are important for a rotor problem, zero rotations being a special case. Therefore, instead of Euler angles, modified Euler angles are used where the axes do not approach one another for rotations in the neighborhood of zero. We assume that the unit vectors $\hat{i}, \hat{j}, \hat{k}$, initially coincident with (x, y, z), undergo rotations ξ_1, β_1, θ_1 about $\hat{i}, -\hat{j}, \hat{k}$ respectively, but necessarily in that order, to finally align with $\hat{i_\xi}, \hat{j_\eta}, \hat{k_\zeta}$. Depending on the choice of order, six combinations are possible. All lead to identical transformation matrices. Here the following sequence is chosen - ξ_1 about z resulting in the new set (x_1, y_1, z_1), β_1 about $-y_1$ resulting in (x_2, y_2, z_2) and θ_1 about x_2 resulting in (ξ, η, ζ). This produces

$$\mathbf{T_{DU}} = \begin{bmatrix} c_{\beta_1} c_{\xi_1} & c_{\beta_1} s_{\xi_1} & s_{\beta_1} \\ -c_{\xi_1} s_{\beta_1} s_{\theta_1} - c_{\theta_1} s_{\xi_1} & c_{\xi_1} c_{\theta_1} - s_{\xi_1} s_{\beta_1} s_{\theta_1} & c_{\beta_1} s_{\theta_1} \\ -c_{\xi_1} s_{\beta_1} c_{\theta_1} + s_{\theta_1} s_{\xi_1} & -c_{\xi_1} s_{\theta_1} - s_{\xi_1} s_{\beta_1} c_{\theta_1} & c_{\beta_1} c_{\theta_1} \end{bmatrix} \tag{2.4}$$

where $c_{(\,)} = \cos(\,)$, $s_{(\,)} = \sin(\,)$ and $\mathbf{T_{DU}}^{-1} = \mathbf{T_{DU}}^{\mathbf{T}}$. The goal is to express this transformation as a function of blade deflections and one rotation angle.

The position vector of any point on the deformed-blade elastic axis can be written as

$$\bar{\mathbf{r}} = (x+u)\hat{i} + v\hat{j} + w\hat{k} \tag{2.5}$$

and the unit vector tangent to the elastic axis of the deformed blade is

$$\frac{\partial \bar{\mathbf{r}}}{\partial r} = (x+u)^{+}\hat{i} + v^{+}\hat{j} + w^{+}\hat{k} \tag{2.6}$$

where r is the curvilinear distance coordinate along the deformed-beam elastic axis and $()^{+} = \partial/\partial r()$. Assuming pure bending and the cross sections remain normal to the elastic axis during deformation

$$\frac{\partial \bar{\mathbf{r}}}{\partial r} = \hat{i_{\xi}} = T_{11}\hat{i} + T_{12}\hat{j} + T_{13}\hat{k} \tag{2.7}$$

where T_{ij} is the element on the ith row and $j$the column of $\mathbf{T_{DU}}$. Thus

$$\left.\begin{aligned} T_{11} &= (x+u)^{+} \\ T_{12} &= v^{+} \\ T_{13} &= w^{+} \end{aligned}\right\} \tag{2.8}$$

In the case of a pure elastic axial elongation, u_e, in addition to pure bending, it is subtracted from total axial elongation to calculate the unit vector tangent to the elastic axis of the deformed blade.

$$\hat{i_{\xi}} = (x+u-u_e)^{+}\hat{i} + v^{+}\hat{j} + w^{+}\hat{k} \tag{2.9}$$

and then

$$\left.\begin{aligned} T_{11} &= (x+u-u_e)^{+} \\ T_{12} &= v^{+} \\ T_{13} &= w^{+} \end{aligned}\right\} \tag{2.10}$$

Because $\mathbf{T_{DU}}$ is orthonormal

$$ {T_{11}}^2 + {T_{12}}^2 + {T_{13}}^2 = 1 \tag{2.11} $$

and therefore

$$ (x + u - u_e)^+ = \sqrt{1 - v^{+\,2} - w^{+\,2}} \tag{2.12} $$

Using equations (2.4) and (2.10) it can be deduced

$$ \left.\begin{aligned} s_{\beta_1} &= w^+ \\ c_{\beta_1} &= \sqrt{1 - w^{+\,2}} \\ s_{\xi_1} &= \tfrac{v^+}{\sqrt{1-w^{+\,2}}} \\ c_{\xi_1} &= \tfrac{\sqrt{1-v^{+\,2}-w^{+\,2}}}{\sqrt{1-w^{+\,2}}} \end{aligned}\right\} \tag{2.13} $$

c_{θ_1} and s_{θ_1} remain to be expressed in terms of the blade deflections and some appropriate measure of elastic torsion. The angular velocity of the frame (x, y, z) as it moves to (ξ, η, ζ) is

$$ \begin{aligned} \omega = &\ \dot{\xi}_1 \hat{k} - \dot{\beta}_1 \hat{j_1} + \dot{\theta}_1 \hat{i_2} \\ = &\ \omega_\xi \hat{i_\xi} + \omega_\eta \hat{i_\eta} + \omega_\zeta \hat{i_\zeta} \end{aligned} \tag{2.14} $$

where $\hat{j_1}$ and $\hat{i_2}$ are unit vectors of the intermediate frames (x_1, y_1, z_1) and (x_2, y_2, z_2), and $\dot{(\ )} = \partial/\partial t(\ )$. The components of the angular velocity are

$$ \left.\begin{aligned} \omega_\xi &= \dot{\theta}_1 + \dot{\xi}_1\, s_{\beta_1} \\ \omega_\eta &= -\dot{\beta}_1\, c_{\theta_1} + \dot{\xi}_1\, c_{\beta_1} s_{\theta_1} \\ \omega_\zeta &= \dot{\xi}_1\, c_{\beta_1}\, c_{\theta_1} + \dot{\beta}_1\, s_{\theta_1} \end{aligned}\right\} \tag{2.15} $$

The bending curvatures and torsion (or angle of twist per unit length) can be deduced with the use of Kirchhoff's kinetic analog [158] by replacing $\dot{(\ )}$ with $(\ )^+$.

Thus,

$$\left.\begin{aligned} \kappa_\xi &= \theta_1^+ + \xi_1^+ \, s_{\beta_1} \\ \kappa_\eta &= -\beta_1^+ \, c_{\theta_1} + \xi_1^+ \, c_{\beta_1} s_{\theta_1} \\ \kappa_\zeta &= \xi_1^+ \, c_{\beta_1} c_{\theta_1} + \beta_1^+ \, s_{\theta_1} \end{aligned}\right\} \tag{2.16}$$

where κ_ξ, κ_η and κ_ζ are the components of bending curvatures in the deformed blade ξ, η, ζ directions. κ_ξ is the torsion. The angle of elastic twist, ϕ is defined such that

$$(\theta_t + \phi)^+ = \kappa_\xi \tag{2.17}$$

where $\theta_t^+ = \theta_t' \xi^+$. θ_t is the rigid pretwist of the blade. From (2.16a) and (2.17) we have

$$\theta_1^+ = (\theta_t + \phi)^+ - \xi^+ \, w^+ \tag{2.18}$$

ξ can be expressed as a function of blade deflections. Using (2.4), (2.10b) and (2.13b) we have

$$s_\xi = \frac{v^+}{\sqrt{(1 - w^+)}} \tag{2.19}$$

Differentiating equation (2.19) and substituting equation (2.13d) we have

$$\xi_1^+ = \frac{v^{++}}{\sqrt{1 - v^{+2} - w^{+2}}} + \frac{v^+ w^+ w^{++}}{(1 - w^{+2})\sqrt{1 - v^{+2} - w^{+2}}} \tag{2.20}$$

From (2.20) and (2.18) we have

$$\theta_1^+ = (\theta_t + \phi)^+ - \frac{w^+}{\sqrt{1 - v^{+2} - w^{+2}}} \left(v^{++} + \frac{v^+ w^+ w^{++}}{1 - w^{+2}} \right) \tag{2.21}$$

or

$$\theta_1 = \theta_t + \phi - \int_0^r \frac{w^+}{\sqrt{1 - v^{+2} - w^{+2}}} \left(v^{++} + \frac{v^+ w^+ w^{++}}{1 - w^{+2}} \right) dr \tag{2.22}$$

and

$$\theta_1 = \theta_t + \hat{\phi} \tag{2.23}$$

where θ_t is the blade rigid twist arising from pre-twist and control angles. ϕ is the blade elastic twist which is used in [13] as the rotation variable. $\hat{\phi}$ is the blade elastic twist including the kinematic integral component and is used in the present work as the rotation variable. The T_{DU} matrix can now be expressed as a function of the unknown blade deflections and one rotation angle θ_1 related to the unknown blade twist $\hat{\phi}$ via equation (2.23).

$$\mathbf{T_{DU}} = \begin{bmatrix} \sqrt{(1-v^{+2}-w^{+2})} & v^{+} & w^{+} \\ \frac{-v^{+}c_{\theta_1} - w^{+}s_{\theta_1}\sqrt{(1-v^{+2}-w^{+2})}}{\sqrt{(1-w^{+2})}} & \frac{c_{\theta_1}\sqrt{(1-v^{+2}-w^{+2})} - v^{+}w^{+}s_{\theta_1}}{\sqrt{(1-w^{+2})}} & s_{\theta_1}\sqrt{(1-w^{+2})} \\ \frac{v^{+}s_{\theta_1} - w^{+}c_{\theta_1}\sqrt{(1-v^{+2}-w^{+2})}}{\sqrt{(1-w^{+2})}} & \frac{-s_{\theta_1}\sqrt{(1-v^{+2}-w^{+2})} - v^{+}w^{+}c_{\theta_1}}{\sqrt{(1-w^{+2})}} & c_{\theta_1}\sqrt{(1-w^{+2})} \end{bmatrix} \tag{2.24}$$

The above expressions and coordinate transformation T_{DU} are exact. Now they are reduced to second order. To second order $(\ )^{+} = (\ )'$. To second order

$$\begin{aligned} \frac{\sqrt{1-v^{+2}-w^{+2}}}{\sqrt{1-w^{+2}}} &= \frac{1-\frac{1}{2}(v'^2+w'^2)}{1-\frac{1}{2}w'^2} \\ &= \frac{1-\frac{1}{2}w'^2}{1-\frac{1}{2}w'^2} - \frac{\frac{1}{2}v'^2}{1-\frac{1}{2}w'^2} \\ &= 1-\frac{1}{2}v'^2 \end{aligned} \tag{2.25}$$

Finally we have

$$\mathbf{T_{DU}} = \begin{bmatrix} 1-\frac{v'^2}{2}-\frac{w'^2}{2} & v' & w' \\ -v'c_{\theta_1} - w's_{\theta_1} & (1-\frac{v'^2}{2})c_{\theta_1} - v'w's_{\theta_1} & (1-\frac{w'^2}{2})s_{\theta_1} \\ v's_{\theta_1} - w'c_{\theta_1} & -(1-\frac{v'^2}{2})s_{\theta_1} - v'w'c_{\theta_1} & (1-\frac{w'^2}{2})c_{\theta_1} \end{bmatrix} \tag{2.26}$$

where θ is expressed as

$$\begin{aligned} \theta_1 &= \theta_0 + \theta_{1C}\,cos(\psi) + \theta_{1S}\,sin(\psi) + \theta_{tw} + \hat{\phi} \\ &= \theta + \hat{\phi} \end{aligned} \tag{2.27}$$

$\theta_0, \theta_{1C}, \theta_{1S}$ are the collective, lateral and longitudinal cyclic angles respectively, ψ is the blade azimuth location, θ_{tw} is the rigid twist angle and $\hat{\phi}$ is the elastic rotation angle. From equation (2.22), the elastic rotation is related to the blade elastic twist as follows

$$\hat{\phi} = \phi - \int_0^r w'v''dr \tag{2.28}$$

where r denotes a blade radial station. Now the blade equations can be formulated using Hamilton's Principle. The equations are formulated in a non-dimensional form.

2.1.3 Nondimensionalization and Ordering scheme

The entire analysis has been done in a nondimensional form. This avoids scaling problems while computing results and increases the generality of the analysis. Table 2.1 shows the reference parameters used to nondimensionalize the relevant physical quantities.

In deriving a nonlinear system of equations, it is necessary to neglect higher-order terms to avoid over-complicating the equations of motion. A systematic and consistent set of guidelines has been adopted for determining which terms to retain and which to ignore. The ordering scheme is same as in Ref. [13]. It is based on a parameter ε which is of the order of nondimensional flap deflection w or lag deflection v (nondimesionalized with respect to radius, R, as described in table 2.1). u is of the same order as the square of w or v. The elastic twist ϕ is a small angle in the sense that $sin\,\phi \approx \phi$ and $\cos\,\phi \approx 1$. The axial coordinate x is of order R and

Physical Quantity	**Reference Parameter**
Length	R
Time	$1/\Omega$
Mass/Length	m_0
Velocity	ΩR
Acceleration	$\Omega^2 R$
Force	$m_0\Omega^2 R^2$
Moment	$m_0\Omega^2 R^3$
Energy or Work	$m_0\Omega^2 R^3$

Table 2.1: Nondimensionalization of Physical Quantities

the lateral coordinates are of order chord, c, and thickness, t. Chord, c, thickness, t and rigid blade twist θ_t are all of same order as v and w. The warp function λ_T is of the same order of magnitude as u so that the warp displacement, which is λ_T multiplied with twist is one order of magnitude less than u. Thus,

$$\left.\begin{array}{ll} \frac{u}{R} = O(\varepsilon^2) & \frac{\lambda}{R} = O(\varepsilon^2) \\ \frac{v}{R} = O(\varepsilon) & \frac{w}{R} = O(\varepsilon) \\ \frac{\eta}{R} = O(\varepsilon) & \frac{\zeta}{R} = O(\varepsilon) \\ \phi = O(\varepsilon) & \frac{\delta\lambda/\delta\eta}{R} = O(\varepsilon) \\ \frac{x}{R} = O(\varepsilon) & \frac{\delta\lambda/\delta\zeta}{R} = O(\varepsilon) \end{array}\right\} \tag{2.29}$$

The order of magnitude of the other nondimensional physical quantities are

are as follows.

$$\left.\begin{array}{c}
\frac{EA}{m_0\Omega^2R^2} = O(\varepsilon^{-2}) \\
\frac{x}{R}, \frac{h}{R}, \frac{x_{cg}}{R}, \frac{y_{cg}}{R}, \frac{m}{m_0}, \frac{\delta}{\delta\psi}, \frac{\delta}{\delta x} = O(1) \\
\mu, \cos\psi, \sin\psi, \theta, \theta_t, \frac{c_1}{a}, \frac{d_2}{a} = O(1) \\
\frac{EI_y}{m_0\Omega^2R^4}, \frac{EI_z}{m_0\Omega^2R^4}, \frac{GJ}{m_0\Omega^2R^4} = O(1) \\
\beta_p, \frac{k_A}{R}, \frac{k_{m1}}{R}, \frac{k_{m2}}{R} = O(\varepsilon) \\
\alpha_s, \phi_s = 0(\varepsilon) \\
\lambda, \frac{\eta_c}{R}, \frac{c_0}{a}, \frac{d_1}{a}, \frac{f_0}{a} = O(\varepsilon) \\
\frac{EB_2}{m_0\Omega^2R^5}, \frac{EC_2}{m_0\Omega^2R^5} = O(\varepsilon) \\
\frac{e_d}{R}, \frac{e_g}{R}, \frac{e_a}{R} = O(\varepsilon^{\frac{3}{2}}) \\
\dot{\alpha_s}, \dot{\phi_s} = 0(\varepsilon^{\frac{3}{2}}) \\
\frac{EB_1}{m_0\Omega^2R^6}, \frac{EC_1}{m_0\Omega^2R^6} = O(\varepsilon^2) \\
\frac{d_0}{a}, \frac{f_1}{a} = O(\varepsilon^2)
\end{array}\right\} \quad (2.30)$$

R is the rotor radius, Ω is the rotational speed, E is the Young's Modulus, G is the shear modulus, I_y and I_z are cross-section moment of inertia from the y and z axis in the undeformed blade frame, J is the torsional rigidity constant, a is the lift curve slope and m_0 is mass per unit length of the blade. Rest of the symbols are defined in the beginning and later on as they appear. m_0 is defined as the mass per unit length of an uniform beam which has the same flap moment of inertia as the actual beam. Therefore

$$m_0 = \frac{3I_\beta}{R^3} \approx \frac{3\int_0^R mr^2dr}{R^3} \quad (2.31)$$

Azimuth angle is considered as nondimensional time, therefore

$$\left.\begin{aligned} \dot{(\,)} &= \frac{\delta(\,)}{\delta t} = \frac{\delta(\,)}{\delta\psi}\frac{\delta\psi}{\delta t} = \Omega\frac{\delta(\,)}{\delta\psi} \\ \ddot{(\,)} &= \frac{\delta^2(\,)}{\delta^2 t} = \frac{\delta^2(\,)}{\delta^2\psi}\frac{\delta^2\psi}{\delta^2 t} = \Omega^2\frac{\delta^2(\,)}{\delta^2\psi} \end{aligned}\right\} \tag{2.32}$$

The ordering scheme is systematically and consistently adopted within the total energy context as is explained during the calculation of the energy terms. However, while following the scheme, terms are lost, which destroy the symmetric nature of the mass and stiffness matrix of the system, or, the antisymmetric gyroscopic nature of the modal equations, then those terms must be retained in violation to the ordering scheme.

2.1.4 Formulation Using Hamilton's Principle

Hamilton's variational principle is used to derive the blade equations of motion. For a conservative system, Hamilton's principle states that the true motion of a system, between prescribed initial conditions at time t_1 and final conditions at time t_2, is that particular motion for which the time integral of the difference between the potential and kinetic energies is a minimum [159]. For an aeroelastic system, e.g., the rotor, there are nonconservative forces which are not derived from a potential function. The generalized Hamilton's Principle, applicable to nonconservative systems, is expressed as

$$\delta\Pi_b = \int_{t_1}^{t_2} (\delta U - \delta T - \delta W)\, dt = 0 \tag{2.33}$$

where δU is the virtual variation of strain energy and δT is the virtual variation of kinetic energy. The δW is the virtual work done by the external forces. These

virtual variations have contributions from the rotor blades and the fuselage.

The variations can be written as

$$\delta U = \delta U_R + \delta U_F = \left(\sum_{b=1}^{N_b} \delta U_b \right) + \delta U_F \tag{2.34}$$

$$\delta T = \delta T_R + \delta T_F = \left(\sum_{b=1}^{N_b} \delta T_b \right) + \delta T_F \tag{2.35}$$

$$\delta W = \delta W_R + \delta W_F = \left(\sum_{b=1}^{N_b} \delta W_b \right) + \delta W_F \tag{2.36}$$

where the subscript R denotes the contribution from the rotor, which is the sum of individual contributions from the N_b blades, and F denotes the contribution from the fuselage. In the present study, only the rotor contribution is considered. Strain energy variation from the flexible pitch links are included in the blade energy terms. The expression for the virtual work δW has been dealt with in the chapter on Aerodynamic Modeling.

2.1.5 Derivation of Strain Energy

Because each blade is assumed to be a long slender isotropic beam, the uniaxial stress assumption ($\sigma_{yy} = \sigma_{yz} = \sigma_{zz} = 0$) can be used. The relation between stresses and classical engineering strains are

$$\sigma_{xx} = E\epsilon_{xx} \tag{2.37}$$

$$\sigma_{x\eta} = G\epsilon_{x\eta} \tag{2.38}$$

$$\sigma_{x\zeta} = G\epsilon_{x\zeta} \tag{2.39}$$

where ϵ_{xx} is axial strain, and $\epsilon_{x\eta}$ and $\epsilon_{x\zeta}$ are engineering shear strains. The expression for strain energy of the bth blade is

$$U_b = \frac{1}{2}\int_0^R \int\int_A (\sigma_{xx}\epsilon_{xx} + \sigma_{x\eta}\epsilon_{x\eta} + \sigma_{x\eta}\epsilon x\eta) d\eta d\zeta dx \tag{2.40}$$

Using the stress-strain relations the variation of strain energy becomes

$$\delta U_b = \int_0^R \int\int_A (E\epsilon_{xx}\delta\epsilon_{xx} + G\epsilon_{x\eta}\epsilon_{x\eta} + G\epsilon_{x\eta}\epsilon x\eta) d\eta d\zeta dx \tag{2.41}$$

The general non-linear strain displacement equations to second order are (from Ref. [13])

$$\begin{aligned}\epsilon_{xx} = u' + \frac{v'^2}{2} + \frac{w'^2}{2} - \lambda_T\phi'' + (\eta^2+\zeta^2)(\theta'\phi' + \frac{\phi'^2}{2}) \\ - v''\left[\eta cos(\theta+\phi) - \zeta sin(\theta+\phi)\right] \\ - w''\left[\eta sin(\theta+\phi) + \zeta cos(\theta+\phi)\right]\end{aligned} \tag{2.42}$$

$$\epsilon_{x\eta} = -\left(\zeta + \frac{\partial\lambda_T}{\partial\eta}\right)\phi' = -\hat{\zeta}\phi' \tag{2.43}$$

$$\epsilon_{x\zeta} = -\left(\eta - \frac{\partial\lambda_T}{\partial\zeta}\right)\phi' = \hat{\eta}\phi' \tag{2.44}$$

where λ_T is the cross-sectional warping function. From equation (2.28) we have the relations between the deformation variable ϕ and quasi-coordinate $\hat{\phi}$.

$$\left.\begin{aligned}\phi' = \hat{\phi}' + w'v'' \\ \delta\phi' = \delta\hat{\phi}' + w'\delta v'' + v''\delta w'\end{aligned}\right\} \tag{2.45}$$

From equation (2.12) we have the relations between the deformation variable u and

the quasi-coordinate u_e.

$$\left.\begin{aligned} u' &= u'_e - \tfrac{1}{2}(v'^2 + w'^2) \\ u &= u_e - \tfrac{1}{2}\int_0^x (v'^2 + w'^2) \\ \delta u' &= \delta u'_e - v'\delta v' - w'\delta w' \\ \delta u &= \delta u_e - \int_0^x (v'\delta v' + w'\delta w')dx \end{aligned}\right\} \tag{2.46}$$

Using equations (2.45) and (2.46) we obtain the strains as follows.

$$\begin{aligned} \epsilon_{xx} =& u'_e - \lambda_T(\hat{\phi}'' + w'v''' + v''w'') + (\eta^2 + \zeta^2)(\theta'\hat{\phi}' + \theta'w'v'' + \frac{\hat{\phi}'^2}{2} + \frac{w'^2v''^2}{2} + \hat{\phi}'w'v'') \\ & - v''\left[\eta cos(\theta + \hat{\phi}) - \zeta sin(\theta + \hat{\phi})\right] - w''\left[\eta sin(\theta + \hat{\phi}) + \zeta cos(\theta + \hat{\phi})\right] \end{aligned} \tag{2.47}$$

$$\epsilon_{x\eta} = -\hat{\zeta}(\hat{\phi}' + w'v'') \tag{2.48}$$

$$\epsilon_{x\zeta} = \hat{\eta}(\hat{\phi}' + w'v'') \tag{2.49}$$

The variation of the strains are

$$\begin{aligned} \delta\epsilon_{xx} =& \delta u'_e + \lambda_T(\delta\hat{\phi}'' + w'\delta v'' + v''\delta w'' + v'''\delta w' + w''\delta v'') \\ & + (\eta^2 + \zeta^2)[\theta'\delta\hat{\phi}' + \theta'w'\delta v'' + \theta'v''\delta w' + (\hat{\phi}' + w'v'')(\delta\hat{\phi}' + w'\delta v'' + v''\delta w')] \\ & - [\eta cos(\theta + \hat{\phi}) - \zeta sin(\theta + \hat{\phi})]\delta v'' + [\eta sin(\theta + \hat{\phi}) + \zeta cos(\theta + \hat{\phi})]v''\delta\hat{\phi} \\ & - [\eta sin(\theta + \hat{\phi}) + \zeta cos(\theta + \hat{\phi})]\delta w'' - [\eta cos(\theta + \hat{\phi}) - \zeta sin(\theta + \hat{\phi})]w''\delta\hat{\phi} \end{aligned} \tag{2.50}$$

$$\delta\epsilon_{x\eta} = -\hat{\zeta}(\delta\phi' + w'\delta v'' + v''\delta w') \tag{2.51}$$

$$\delta\epsilon_{x\zeta} = \hat{\eta}(\delta\phi' + w'\delta v'' + v''\delta w') \tag{2.52}$$

Substituting equations (2.50), (2.51) and (2.52) in equation (2.41) gives the variation of strain energy as function of the deformation variables. It can be expressed in nondimensional form as follows.

$$\delta U = \frac{\delta U_b}{m_0 \Omega^2 R^3} = \int_0^1 (U_{u'_e}\delta u'_e + U_{v'}\delta v' + U_{w'}\delta w' + U_{v''}\delta v'' + U_{w''}\delta w'' + U_{\hat{\phi}}\delta\hat{\phi} + U_{\hat{\phi}'}\delta\hat{\phi}' + U_{\hat{\phi}''}\delta\hat{\phi}'')dx \tag{2.53}$$

In deriving the expressions the following section properties are used.

$$\left.\begin{aligned}
\int\int_A d\eta d\zeta &= A \\
\int\int_A \eta d\eta d\zeta &= Ae_A \\
\int\int_A \zeta d\eta d\zeta &= 0 \\
\int\int_A \lambda_T d\eta d\zeta &= 0 \\
\int\int_A (\eta^2+\zeta^2) d\eta d\zeta &= AK_A^2 \\
\int\int_A (\eta^2+\zeta^2)^2 d\eta d\zeta &= B_1 \\
\int\int_A \eta(\eta^2+\zeta^2)^2 d\eta d\zeta &= B_2 \\
\int\int_A \eta^2 d\eta d\zeta &= I_Z \\
\int\int_A \zeta^2 d\eta d\zeta &= I_Y \\
\int\int_A \lambda_T^2 d\eta d\zeta &= EC_1 \\
\int\int_A \zeta\lambda_T d\eta d\zeta &= EC_2
\end{aligned}\right\} \tag{2.54}$$

The coefficients, up to second order of non-linearities are given below.

$$\begin{aligned}
U_{u'_e} =& EA\left[u'_e + K_A^2(\theta'\hat{\phi}' + \theta' w' v'' + \frac{\hat{\phi}'^2}{2})\right] \\
&- EAe_A\left[v''(cos\theta - \hat{\phi}sin\theta) + w''(sin\theta + \hat{\phi}cos\theta)\right]
\end{aligned} \tag{2.55}$$

$$U_{v'} = 0 \tag{2.56}$$

$$U_{w'} = (GJ + EB_1\theta'^2)\hat{\phi}' v'' + EAK_A^2\theta' v'' u'_e \tag{2.57}$$

$$
\begin{aligned}
U_{v''} =& v''[EI_Z cos^2(\theta+\hat{\phi}) + EI_Y sin^2(\theta+\hat{\phi})] \\
&+ w''(EI_Z - EI_Y)cos(\theta+\hat{\phi})sin(\theta+\hat{\phi}) \\
&- EB_2\theta'\hat{\phi}'cos\theta - EAe_A u'_e(cos\theta - \hat{\phi}sin\theta) + EAK_A^2 u'_e w'\theta' \\
&+ (GJ + EB_1\theta'^2)\hat{\phi}'w' - EC_2\hat{\phi}''sin\theta
\end{aligned}
\tag{2.58}
$$

$$
\begin{aligned}
U_{w''} =& w''[EI_Z sin^2(\theta+\hat{\phi}) + EI_Y cos^2(\theta+\hat{\phi})] \\
&+ v''[EI_Z - EI_Y]cos(\theta+\hat{\phi})sin(\theta+\hat{\phi}) \\
&- EAe_A u'_e(sin\theta + \hat{\phi}cos\theta) - EB_2\hat{\phi}'\theta'sin\theta + EC_2\hat{\phi}''cos\theta
\end{aligned}
\tag{2.59}
$$

$$
\begin{aligned}
U_{\hat{\phi}} =& w''^2(EI_Z - EI_Y)cos(\theta+\hat{\phi})sin(\theta+\hat{\phi}) - v''^2(EI_Z - EI_Y)cos(\theta+\hat{\phi})sin(\theta+\hat{\phi}) \\
& v''w''(EI_Z - EI_Y)cos2(\theta+\hat{\phi})
\end{aligned}
\tag{2.60}
$$

$$
\begin{aligned}
U_{\hat{\phi}'} =& GJ(\hat{\phi}' + w'v'') + EAK_A^2(\theta' + \phi')u'_e \\
& EB_1\theta'^2\hat{\phi}' - EB_2\theta'(v''cos\theta + w''sin\theta)
\end{aligned}
\tag{2.61}
$$

$$
U_{\hat{\phi}''} = EC_1\hat{\phi}'' + EC_2(w''cos\theta - v''sin\theta) \tag{2.62}
$$

Note that in the above expressions, the $cos(\theta+\hat{\phi})$ and $sin(\theta+\hat{\phi})$ terms associated with bending curvature, i.e., with EI_Z and EI_Y, have been retained. These terms are expanded to second order as

$$
\left.
\begin{aligned}
sin(\theta+\hat{\phi}) &= (1 - \tfrac{\hat{\phi}^2}{2})sin\theta + \hat{\phi}cos\theta \\
cos(\theta+\hat{\phi}) &= (1 - \tfrac{\hat{\phi}^2}{2})cos\theta - \hat{\phi}sin\theta
\end{aligned}
\right\}
\tag{2.63}
$$

This expansion introduces third order terms in $U_{v''}$, $U_{w''}$ and $U_{\hat{\phi}}$ which are retained in violation of the ordering scheme. This is to maintain consistency between the

force-summation and modal methods of blade loads calculation. Thus we have the following

$$\begin{aligned} U_{v''} =& v''(EI_Z cos^2\theta + EI_Y sin^2\theta) + w''(EI_Z - EI_Y)cos\theta sin\theta \\ & - v''\hat{\phi}sin2\theta(EI_Z - EI_Y) + w''\hat{\phi}cos2\theta(EI_Z - EI_Y) \\ & - v''\hat{\phi}^2 cos2\theta(EI_Z - EI_Y) - w''\hat{\phi}^2 sin2\theta(EI_Z - EI_Y) \end{aligned} \tag{2.64}$$

$$\begin{aligned} U_{w''} =& v''(EI_Z sin^2\theta + EI_Y cos^2\theta) + v''(EI_Z - EI_Y)cos\theta sin\theta \\ & + w''\hat{\phi}sin2\theta(EI_Z - EI_Y) + v''\hat{\phi}cos2\theta(EI_Z - EI_Y) \\ & + w''\hat{\phi}^2 cos2\theta(EI_Z - EI_Y) - v''\hat{\phi}^2 sin2\theta(EI_Z - EI_Y) \end{aligned} \tag{2.65}$$

$$\begin{aligned} U_{\hat{\phi}} =& (w''^2 - v''^2)cos\theta sin\theta(EI_Z - EI_Y) + v''w''cos2\theta \\ & \hat{\phi}(w''^2 - v''^2)cos2\theta(EI_Z - EI_Y) - 2\hat{\phi}v''w''sin2\theta \end{aligned} \tag{2.66}$$

2.1.6 Derivation of Kinetic Energy

The kinetic energy of the bth blade, δT_b depends on the blade velocity relative to the hub and the velocity of the hub itself. The velocity of the hub originates from fuselage dynamics and is neglected in the present analysis.

Let the position of an arbitrary point after the beam has deformed is given by (x_1, y_1, z_1) where

$$\bar{\mathbf{r}} = \begin{bmatrix} x_1 & y_1 & z_1 \end{bmatrix} \begin{Bmatrix} \hat{i} \\ \hat{j} \\ \hat{k} \end{Bmatrix} = \begin{bmatrix} x+u & v & w \end{bmatrix} \begin{Bmatrix} \hat{i} \\ \hat{j} \\ \hat{k} \end{Bmatrix} + \begin{bmatrix} -\lambda\phi' & \eta & \zeta \end{bmatrix} \begin{Bmatrix} \hat{i_\xi} \\ \hat{j_\eta} \\ \hat{k_\zeta} \end{Bmatrix}$$

$$= \left\{ \begin{bmatrix} x+u & v & w \end{bmatrix} + \begin{bmatrix} -\lambda\phi' & \eta & \zeta \end{bmatrix} \mathbf{T_{DU}} \right\} \begin{Bmatrix} \hat{i} \\ \hat{j} \\ \hat{k} \end{Bmatrix} \tag{2.67}$$

Using equation (2.26) we obtain

$$\left.\begin{aligned} x_1 &= x + u - \lambda\phi' - v'(y_1 - v) - w'(z_1 - w) \\ y_1 &= v + (y_1 - v) \\ z_1 &= w + (z_1 - w) \end{aligned}\right\} \tag{2.68}$$

where

$$\left.\begin{aligned} y_1 - v &= \eta cos(\theta + \hat{\phi}) - \zeta sin(\theta + \hat{\phi}) \\ z_1 - w &= \eta sin(\theta + \hat{\phi}) + \zeta cos(\theta + \hat{\phi}) \end{aligned}\right\} \tag{2.69}$$

Now,

$$\bar{V}_b = \frac{\partial \bar{\mathbf{r}}}{\partial t} + \bar{\Omega} \times \bar{\mathbf{r}} \tag{2.70}$$

where using equation (2.2) we have

$$\bar{\Omega} = \Omega \hat{K} = \Omega sin\beta_p \hat{i} + \Omega cos\beta_p \hat{k} \tag{2.71}$$

and

$$\frac{\partial \bar{\mathbf{r}}}{\partial t} = \dot{x}_1 \hat{i} + \dot{y}_1 \hat{j} + \dot{z}_1 \hat{k} \tag{2.72}$$

Using equations (2.72) and (2.2) in equation (2.70) we have

$$\bar{V}_b = V_{bx}\hat{i} + V_{by}\hat{j} + V_{bz}\hat{k} \tag{2.73}$$

where all velocities are non-dimensionalized with respect to ΩR and $\dot{(\ )} = \partial(\ )/\partial\psi$.

$$V_{bx} = \dot{x}_1 - y_1 \cos\beta_p \tag{2.74}$$

$$V_{by} = \dot{y}_1 + x_1 \cos\beta_p - z_1 \sin\beta_p \tag{2.75}$$

$$V_{bz} = \dot{z}_1 + y_1 \sin\beta_p \tag{2.76}$$

Taking variations of the velocities we have

$$\begin{aligned}\bar{V}.d\bar{V} = {} & \dot{x}_1\delta\dot{x}_1 - y_1\cos\beta_p\delta\dot{x}_1 - \dot{x}_1\cos\beta_p\delta y_1 + y_1\cos^2\beta_p\delta y_1 \\ & \dot{y}_1\delta\dot{y}_1 + x_1\cos\beta_p\delta\dot{y}_1 - z_1\sin\beta_p\delta\dot{y}_1 + \dot{y}_1\cos\beta_p\delta x_1 \\ & x_1\cos^2\beta_p\delta x_1 - z_1\sin\beta_p\cos\beta_p\delta x_1 - \dot{y}_1\sin\beta_p\delta z_1 - x_1\cos\beta_p\sin\beta_p\delta z_1 \\ & + \dot{z}_1\sin^2\beta_p\delta z_1 + \dot{z}_1\delta\dot{z}_1 + y_1\sin\beta_p\delta\dot{z}_1 + \dot{z}_1\sin\beta_p\delta y_1 + y_1\sin^2\beta_p\delta y_1\end{aligned} \tag{2.77}$$

According to variational method, this equation must be integrated in time between two arbitrary points in time, t_1 and t_2 [13]. The initial and final values (e.g.,$\dot{x}_1\delta x_1|_{t1}^{t2}$) are taken as zero. Anticipating integration by parts the various terms can be combined in equation (2.77) to obtain

$$\begin{aligned}\bar{V}.d\bar{V} = {} & -\ddot{x}_1\delta x_1 + 2\dot{y}_1\cos\beta_p\delta x_1 + y_1\cos^2\beta_p\delta y_1 - \ddot{y}_1\delta y_1 \\ & - 2\dot{x}_1\cos\beta_p\delta y_1 + 2\dot{z}_1\sin\beta_p\delta y_1 + x_1\cos^2\beta_p\delta x_1 \\ & - z_1\sin\beta_p\cos\beta_p\delta x_1 - 2\dot{y}_1\sin\beta_p\delta z_1 - x_1\cos\beta_p\sin\beta_p\delta z_1 + z_1\sin^2\beta_p\delta z_1 \\ & - \ddot{z}_1\delta z_1 + y_1\sin^2\beta_p\delta y_1\end{aligned} \tag{2.78}$$

For the bth, the resultant kinetic energy expression in non-dimensional form is given by

$$\frac{\delta T_b}{m_0 \Omega^2 R^3} = \int_0^1 \iint_A \rho \bar{V}.\delta\bar{V}\, d\eta\, d\zeta\ \ dx \tag{2.79}$$

where ρ is the structural mass density. Substituting the velocity expressions as given before we have

$$\frac{\delta T_b}{m_0 \Omega^2 R^3} = \int_0^1 \left[\iint_A \rho \left(T_{x1}\delta x_1 + T_{y1}\delta y_1 + T_{z1}\delta z_1 \right)\, d\eta\, d\zeta \right] dx \tag{2.80}$$

where

$$T_{x1} = -\ddot{x}_1 + 2\dot{y}_1 \cos\beta_p + x_1 \cos^2\beta_p - z_1 \sin\beta_p \cos\beta_p \tag{2.81}$$

$$T_{y1} = y_1 \cos^2\beta_p - \ddot{y}_1 - 2\dot{x}_1 \cos\beta_p + y_1 \sin^2\beta_p + 2\dot{z}_1 \sin\beta_p \tag{2.82}$$

$$T_{z1} = -2\dot{y}_1 \sin\beta_p - \ddot{z}_1 + z_1 \sin^2\beta_p - x_1 \cos\beta_p \sin\beta_p \tag{2.83}$$

Now, using equations (2.68) and (2.69) we have

$$\left.\begin{aligned} \dot{y_1} &= \dot{v} - (z_1 - w)\dot{\theta}_1 \\ \dot{z_1} &= \dot{w} + (y_1 - v)\dot{\theta}_1 \\ \dot{x_1} &= \dot{u} - \lambda_T \dot{\phi}' - (\dot{v}' + w'\dot{\theta}_1)(y - 1 - v) - (\dot{w}' - v'\dot{\theta}_1)(z_1 - w) \end{aligned}\right\} \tag{2.84}$$

and

$$\left.\begin{aligned} \ddot{y}_1 &= \ddot{v} - (z_1 - w)\ddot{\theta}_1 - (y_1 - v)\dot{\theta}^2 \\ \ddot{z}_1 &= \ddot{w} + (y_1 - v)\ddot{\theta}_1 - (z_1 - w)\dot{\theta}^2 \\ \ddot{x}_1 &= \ddot{u} - \lambda_T \ddot{\theta}_1' - (y_1 - v)(\ddot{v}' + w'\ddot{\theta}' - v'\dot{\theta}^2 + 2\dot{w}'\dot{\theta}_1) \\ &\quad -(z_1 - w)(\ddot{w}' - v'\ddot{\theta}_1 - w'\dot{\theta}_1^2 - 2\dot{v}'\dot{\theta}_1) \end{aligned}\right\} \tag{2.85}$$

The variations are as follows

$$\left.\begin{aligned} \delta y_1 &= \delta v - \delta\hat{\phi}(z_1 - w) \\ \delta z_1 &= \delta w + \delta\hat{\phi}(y_1 - v) \\ \delta x_1 &= \delta u - \lambda_T \delta\hat{\phi}' - (y_1 - v)(\delta v' + w'\delta\hat{\phi}) \\ &\quad -(z_1 - w)(\delta w' - v'\delta\hat{\phi}) \end{aligned}\right\} \tag{2.86}$$

Using equations (2.86), (2.85), (2.84), (2.68) in (2.79) we obtain

$$\delta T = \frac{\delta T_b}{m_0 \Omega^2 R^3} = \int_0^1 m(T_{u_e}\delta u_e + T_v \delta v + T_w \delta w + T_{w'}\delta w' + T_{v'}\delta v' + T_\phi \delta phi + T_F)dx \tag{2.87}$$

In deriving the expressions the following section properties are used.

$$\left.\begin{aligned} \int\int_A \rho d\eta d\zeta &= m \\ \int\int_A \rho\eta d\eta d\zeta &= me_g \\ \int\int_A \rho\zeta^2 d\eta d\zeta &= mk_{m_1}^2 \\ \int\int_A \rho\eta^2 d\eta d\zeta &= mk_{m_2}^2 \\ k_{m_1}^2 + k_{m_1}^2 &= k_m^2 \\ \int\int_A \rho\zeta d\eta d\zeta &= 0 \\ \int\int_A \rho\eta\zeta d\eta d\zeta &= 0 \\ \int\int_A \rho\lambda_T d\eta d\zeta &= 0 \end{aligned}\right\} \tag{2.88}$$

assuming cross-section symmetry about the η axis and an antisymmetric warp function λ_T. The terms involving $(y_1 - v)$ and $(z_1 - w)$ are given by

$$\left.\begin{aligned} \int\int_A \rho(y_1 - v)d\eta d\zeta &= me_g cos(\theta + \hat{\phi}) \\ \int\int_A \rho(z_1 - w)d\eta d\zeta &= me_g sin(\theta + \hat{\phi}) \\ \int\int_A \rho(z_1 - w)(y_1 - v)d\eta d\zeta &= m(k_{m_2}^2 - k_{m_1}^2)sin(\theta + \hat{\phi})cos(\theta + \hat{\phi}) \\ \int\int_A \rho[(y_1 - v)^2 - (z_1 - w)^2]d\eta d\zeta &= mk_m^2 \end{aligned}\right\} \tag{2.89}$$

The coefficients in equation (2.87) are written up to second order, $O(\epsilon^2)$, as follows

$$T_{U_e} = -\ddot{u} + u + x + 2\dot{v} \tag{2.90}$$

where

$$\left.\begin{aligned} u &= u_e - \tfrac{1}{2}\int_0^x (v'^2 + w'^2)dx \\ \ddot{u} &= \ddot{u}_e - \int_0^x (\dot{v}'^2 + v'\ddot{v}' + \dot{w}'^2 + w'\ddot{w}')dx \end{aligned}\right\} \tag{2.91}$$

$$\begin{aligned} T_v = &- \ddot{v} + e_g\ddot{\theta}sin\theta + e_g cos\theta + v - \hat{\phi}sin\theta + 2\dot{w}\beta_p + 2e_g\dot{v}'cos\theta \\ &+ 2e_g\dot{w}'sin\theta + \ddot{\hat{\phi}}e_g sin\theta - 2\dot{u}_e + 2\int_0^x (v'\dot{v}' + w'\dot{w}')dx \end{aligned} \tag{2.92}$$

$$T_{v'} = -e_g(xcos\theta - \hat{\phi}xsin\theta + 2\dot{v}cos\theta) \tag{2.93}$$

$$\begin{aligned} T_w = &- \ddot{w} - e_g\ddot{\theta}cos\theta - e_g\ddot{\hat{\phi}}cos\theta \\ &- 2\dot{v}\beta_p - x\beta_p \end{aligned} \tag{2.94}$$

$$T_{w'} = -e_g(xsin\theta + \hat{x}cos\theta + 2\dot{v}sin\theta) \tag{2.95}$$

$$\begin{aligned} T_{\hat{\phi}} = &- k_m^2\ddot{\hat{\phi}} - \hat{\phi}(k_{m_2}^2 - k_{m_1}^2)cos2\theta - (k_{m_2}^2 - k_{m_1}^2)cos\theta sin\theta - x\beta_p e_g cos\theta \\ &- ve_g sin\theta + xv'e_g sin\theta - xw'e_g cos\theta + \ddot{v}e_g sin\theta - \ddot{e}_g cos\theta - k_m^2\ddot{\theta} \end{aligned} \tag{2.96}$$

The non-variation term T_F is given by

$$\begin{aligned} T_F &= -(-\ddot{u} + u + x + 2\dot{v})\int_0^x (v'\delta v' + w'\delta w') \\ &= -T_{U_e}\int_0^x (v'\delta v' + w'\delta w') \end{aligned} \tag{2.97}$$

Note that the ordering scheme is violated in equation (2.97). It is important to keep the entire T_{U_e} in the non-variation form for articulated rotors where the bending moments at the hinge must go to zero. For hingeless rotors with large bending moments at the blade root the error is negligible.

2.1.7 Virtual Work

For each degree of freedom, there is a corresponding external force (or moment) which contribute to virtual work on the system. The general expression is given by

$$\frac{\delta W_b}{m_0 \Omega^2 R^3} = \int_0^1 (L_u^A \delta u + L_v^A \delta v + L_w^A \delta w + M_{\hat{\phi}}^A \delta \hat{\phi}) dx \tag{2.98}$$

where L_u^A, L_v^A, L_w^A, $M_{\hat{\phi}}^A$ are the distributed air loads in the x, y and z directions and $M_{\hat{\phi}}^A$ is the aerodynamic pitching moment about the undeformed elastic axis. Calculated air loads are motion dependent. Measured air loads are not motion dependent.

In addition to distributed air loads, there can be concentrated forces and moments acting on locations over the blade span, e.g. a prescribed damper force. They can be included as follows.

$$\begin{aligned}\frac{\delta W_b}{m_0 \Omega^2 R^3} = & \int_0^1 (L_u^A \delta u + L_v^A \delta v + L_w^A \delta w + M_{\hat{\phi}}^A \delta \hat{\phi}) dx \\ & + \int_0^1 (F_x \delta u + F_y \delta v + F_z \delta w + M_x \delta \hat{\phi} - M_y \delta w' + M_z \delta v') \delta(x - x_f) dx\end{aligned} \tag{2.99}$$

where F_x, F_y, F_z, M_x, M_y, M_z are the concentrated forces and moments acting at $x = x_f$ along the blade span. The calculated forces and moments are described in Chapter 3.

2.1.8 Equations of Motion

Integrating the strain energy, kinetic energy and virtual work expressions (2.53), (2.87) and (2.98) by parts we obtain

$$\left.\begin{aligned} \delta U &= \int_0^1 (Y_{u_e}\delta u_e + Y_v\delta v + Y_w\delta w + Y_{\hat{\phi}}\delta_{\hat{\phi}})dx + b(U) \\ \delta T &= \int_0^1 (Z_{u_e}\delta u_e + Z_v\delta v + Z_w\delta w + Z_{\hat{\phi}}\delta_{\hat{\phi}})dx + b(T) \\ \delta W &= \int_0^1 (W_{u_e}\delta u_e + W_v\delta v + W_w\delta w + W_{\hat{\phi}}\delta_{\hat{\phi}})dx + b(W) \end{aligned}\right\} \tag{2.100}$$

where $b(U)$, $b(T)$ and $b(W)$ are the force and displacement boundary conditions. Using equation (2.33) and collecting terms associated with δu, δv, δw and $\delta\hat{\phi}$ we obtain the blade equations as follows.

u_e equation :

$$\begin{aligned} & EA\left[u_e' + K_A^2(\theta'\hat{\phi}' + \theta' w' v'' + \frac{\hat{\phi}'^2}{2})\right]' \\ & - EAe_A\left[v''(cos\theta - \hat{\phi}sin\theta) + w''(sin\theta + \hat{\phi}cos\theta)\right]' \\ & + m(\ddot{u}_e - u_e - x - 2\dot{v}) = L_u \end{aligned} \tag{2.101}$$

v **equation :**

$$
\begin{aligned}
&[v''[EI_Z cos^2(\theta+\hat{\phi}) + EI_Y sin^2(\theta+\hat{\phi})] \\
&+ w''(EI_Z - EI_Y)cos(\theta+\hat{\phi})sin(\theta+\hat{\phi}) - EB_2\theta'\hat{\phi}'cos\theta \\
&- EAe_A u_e'(cos\theta - \hat{\phi}sin\theta) + EAK_A^2 u_e' w'\theta']' \\
&- m[-\ddot{v} + e_g\ddot{\theta}sin\theta + e_g cos\theta + v - \hat{\phi}sin\theta + 2\dot{w}\beta_p + 2e_g\dot{v}'cos\theta \\
&+ 2e_g\dot{w}'sin\theta + \ddot{\hat{\phi}}e_g sin\theta - 2\dot{u}_e + 2\int_0^x (v'\dot{v}' + w'\dot{w}')dx] \\
&- me_g(xcos\theta - \hat{\phi}xsin\theta + 2\dot{v}cos\theta)' + \left\{ mv' \int_x^1 (-\ddot{u}_e + u_e + x + 2\dot{v}) \right\}' = L_v
\end{aligned}
\tag{2.102}
$$

w **equation :**

$$
\begin{aligned}
&[w''[EI_Z sin^2(\theta+\hat{\phi}) + EI_Y cos^2(\theta+\hat{\phi})] \\
&+ v''[EI_Z - EI_Y]cos(\theta+\hat{\phi})sin(\theta+\hat{\phi}) \\
&- EAe_A u_e'(sin\theta + \hat{\phi}cos\theta) - EB_2\hat{\phi}'\theta' sin\theta + EC_2\hat{\phi}''cos\theta]' \\
&- m(-\ddot{w} - e_g\ddot{\theta}cos\theta - e_g\ddot{\hat{\phi}}cos\theta - 2\dot{v}\beta_p - x\beta_p) \\
&- me_g(xsin\theta + \hat{x}cos\theta + 2\dot{v}sin\theta)' + \left\{ mw' \int_x^1 (-\ddot{u}_e + u_e + x + 2\dot{v}) \right\}' = L_v
\end{aligned}
\tag{2.103}
$$

$\hat{\phi}$ **equation :**

$$
\begin{aligned}
&w''^2(EI_Z - EI_Y)cos(\theta+\hat{\phi})sin(\theta+\hat{\phi}) - v''^2(EI_Z - EI_Y)cos(\theta+\hat{\phi})sin(\theta+\hat{\phi}) \\
&v''w''(EI_Z - EI_Y)cos2(\theta+\hat{\phi}) \\
&- [GJ(\hat{\phi}' + w'v'') + EAK_A^2(\theta' + \phi')u_e' + EB_1\theta'^2\hat{\phi}' - EB_2\theta'(v''cos\theta + w''sin\theta)]' \\
&[EC_1\hat{\phi}'' + EC_2(w''cos\theta - v''sin\theta)]'' \\
&- (-k_m^2\ddot{\hat{\phi}} - \hat{\phi}(k_{m_2}^2 - k_{m_1}^2)cos2\theta - (k_{m_2}^2 - k_{m_1}^2)cos\theta sin\theta - x\beta_p e_g cos\theta \\
&- ve_g sin\theta + xv'e_g sin\theta - xw'e_g cos\theta + \ddot{v}e_g sin\theta - \ddot{e}_g cos\theta - k_m^2\ddot{\theta}) = L_{\hat{\phi}}
\end{aligned}
\tag{2.104}
$$

2.2 Finite Element Method of Solution

A finite element method of solution, both in space and time, is formulated directly from the energy and virtual work expressions. For the bth blade, the virtual energy expression in equation (2.33) can be written in space and time discretized form as

$$
\delta\Pi_b = \int_{\psi_I}^{\psi_F} \left[\sum_{i=1}^{N}(\delta U_i - \delta T_i - \delta W_i)\right]_b d\psi = \int_{\psi_I}^{\psi_F} \left[\sum_{i=1}^{N}\Delta_i\right]_b d\psi = 0 \tag{2.105}
$$

where i is the ith spatial beam element out of a total of N. Applying the finite element method in space domain for this virtual energy expression yields the discretized equations of motion for the bth blade.

2.2.1 Finite Element in Space

Each beam element consists of fifteen degrees of freedom [31] distributed over five element nodes - two boundary nodes and three interior nodes. There are six degrees of freedom at each element boundary node. These six degrees of freedom are u_e, v, v', w, w' and $\hat{\phi}$. There are two internal nodes for u_e and one for elastic twist $\hat{\phi}$. Between elements there is continuity of displacement and slope for flap and lag bending deflections, and continuity of displacement for elastic twist and axial deflections. This element insures physically consistent linear variations of bending moments and torsional moment, and quadratic variation of axial force within each element. Using the interpolating polynomials, the distribution of deflections over a beam element is expressed in terms of the elemental nodal displacements $\mathbf{q_i}$. For the ith element the blade deflection, $u(s)$, where $s = x_i/l_i$, l_i is the length of the $i$the beam element, is as follows.

$$\mathbf{u(s)} = \left\{ \begin{array}{c} u(s) \\ v(s) \\ w(s) \\ \hat{\phi}(s) \end{array} \right\} = \left\{ \begin{array}{cccc} \mathbf{H_u} & 0 & 0 & 0 \\ 0 & \mathbf{H} & 0 & 0 \\ 0 & 0 & \mathbf{H} & 0 \\ 0 & 0 & 0 & \mathbf{H}_{\hat{\phi}} \end{array} \right\} \mathbf{q_i} \tag{2.106}$$

where the elemental nodal displacement vector is defined as

$$\mathbf{q_i}^{\mathbf{T}} = [\mathbf{u_1 u_2 u_3 u_4 v_1 v_1' v_2 v_2' w_1 w_1' w_2 w_2' \hat{\phi}_1 \hat{\phi}_2 \hat{\phi}_3}] \tag{2.107}$$

and the interpolating polynomial shape functions are

$$\mathbf{H_u}^{\mathbf{T}} = \begin{Bmatrix} H_{u1} \\ H_{u2} \\ H_{u3} \\ H_{u4} \end{Bmatrix} = \begin{Bmatrix} -4.5s^3 + 9s^2 - 5.5s + 1 \\ 13.5s^3 - 22.5s^2 + 9s \\ -13.5s^3 + 18s^2 - 4.5s \\ 4.5s^3 - 4.5s^2 + s \end{Bmatrix} \tag{2.108}$$

$$\mathbf{H^T} = \begin{Bmatrix} H_1 \\ H_2 \\ H_3 \\ H_4 \end{Bmatrix} = \begin{Bmatrix} 2s^3 - 3s^2 + 1 \\ l_i(s^3 - 2s^2 + s) \\ -2s^3 + 3s^2 \\ l_i(s^3 - s^2) \end{Bmatrix} \tag{2.109}$$

$$\mathbf{H}_{\hat{\phi}}{}^{\mathbf{T}} = \begin{Bmatrix} H_{\hat{\phi}_1} \\ H_{\hat{\phi}_2} \\ H_{\hat{\phi}_3} \end{Bmatrix} = \begin{Bmatrix} 2s^2 - 3s + 1 \\ -4s^2 + 4s \\ 2s^2 - s \end{Bmatrix} \tag{2.110}$$

For flap and lag deflections the shape functions allow continuity of displacement and slope (Hermite Polynomials), for elastic twist and axial deflection the shape functions allow continuity of displacement (Lagrange Polynomials). Using the appropriate shape functions, the elemental variation in energy, Δ_i can be written in the following matrix form.

$$\Delta_i = \delta \mathbf{q_i}^{\mathbf{T}} (\mathbf{M_b}\ddot{\mathbf{q}} + \mathbf{C_b}\dot{\mathbf{q}} + \mathbf{K_b}\mathbf{q} - \mathbf{F_b})_\mathbf{i} \tag{2.111}$$

where $(M_b)_i, (C_b)_i, (K_b)_i$ are elemental mass, damping, stiffness and forcing matrices respectively. The matrices $(M_b)_i, (C_b)_i, (K_b)_i$ are obtained from linear terms only. The non-linear terms are linearized using a first order Taylor series approximation

and included in the forcing matrix $(F_b)_i$.

$$\begin{aligned}(F_b)_i &= (F_0)_i + (F_{NL})_i \\ &= (F_0)_i + (F_{NL})|_{q_{0_i}} + \frac{\partial (F_{NL})_i}{\partial \mathbf{q_i}}|_{q_{0_i}}(\mathbf{q_i} - \mathbf{q_0})\end{aligned} \tag{2.112}$$

The linearized part of the nonlinear force is derived analytically by differentiating the nonlinear force vector terms with respect to the blade deformations. Each of the mass, damping, stiffness and forcing matrices are dependent on space and azimuth. Summation over the beam elements is achieved by assembling (adding) the elemental matrices.

The elemental matrices are assembled ensuring compatibility between degrees of freedom at adjoining nodes. By assembling elemental matrices over N spatial beam elements, the following expression for the variation of total energy is obtained.

$$\delta\Pi = \int_{\psi_I}^{\psi_F} \delta\mathbf{q}^{\mathbf{T}}(\mathbf{M_b}\ddot{\mathbf{q}} + \mathbf{C_b}\dot{\mathbf{q}} + \mathbf{K_b}\mathbf{q} - \mathbf{F_b}) = \mathbf{0} \tag{2.113}$$

Because the virtual displacements, $\delta\mathbf{q}$, are arbitrary, the integrand in equation (2.113) must vanish. This gives the finite element equations of motion for the blade as follows.

$$M_b\ddot{\mathbf{q}} + C_b\dot{\mathbf{q}} + K_b\mathbf{q} = \mathbf{F_b} \tag{2.114}$$

The geometric and force boundary conditions at the root end are enforced during assembly of the element matrices. For an articulated rotor, as in the present study, u, v and w are set to zero at the flap-lag hinge. Spring and damper properties of the elastomeric bearing at the hinge are incorporated at the hinge for the v' and w' nodes. The pitch link stiffness and damping values are incorporated for

the root $\hat{\phi}$ node. In general, kinematic boundary conditions for articulated, hingeless and bearingless rotors can be incorporated depending on the particular rotor configuration.

The number of global degrees of freedom, N_G (typically 150-200, here 182 for 20 elements) is reduced to m degrees of freedom (typically 5 to 10) using the blade natural vibration modes. The natural vibration modes about the mean deflected position are obtained by neglecting the damping and force matrices. The nonlinear terms are not used for natural mode calculation. Thus the linearized contributions of the nonlinear terms to mass, stiffness and damping matrices are neglected. Once calculated, however, the normal modes are used to reduce the entire nonlinear equation.

The final normal mode equations for the blade are as follows.

$$\bar{M}\ddot{\mathbf{p}}_\mathbf{b} + \bar{C}\dot{\mathbf{p}}_\mathbf{b} + \bar{K}\mathbf{p}_\mathbf{b} = \bar{\mathbf{F}} \tag{2.115}$$

where the matrices are functions of ψ. The new reduced mass, stiffness, damping and force matrices are as follows

$$\left.\begin{aligned} \bar{M} &= \Phi^T M_b \Phi \\ \bar{C} &= \Phi^T C_b \Phi \\ \bar{K} &= \Phi^T K_b \Phi \\ \bar{F} &= \Phi^T F_b \end{aligned}\right\} \tag{2.116}$$

where Φ is an $N_G \times m$ matrix of m normal modes, used to transform the global displacement vector $\mathbf{q_b}$ in terms of m modes. Thus

$$\mathbf{q_b} = \mathbf{\Phi p_b} \tag{2.117}$$

The eigen vectors are orthogonal to each other. Each eigen vector has a real and positive eigenvalue associated with it. The square root of each eigen value gives the blade natural frequency corresponding to a particular natural mode. The nonlinear force matrix, after modal reduction, is of the following form.

$$\begin{aligned}\bar{F}(\psi, \mathbf{p_b}) &= \bar{F}_0(\psi) + \bar{F_{NL}}(\psi, \mathbf{p_b}) \\ &= \bar{F}_0 + \bar{F_{NL}}(\psi, p_{b0}) + \frac{\partial \bar{F_{NL}}}{\partial \mathbf{p_b}}|_{p_{b0}}(\mathbf{p_b} - p_{b0})\end{aligned} \tag{2.118}$$

The normal mode equations given in (2.115) are nonlinear, periodic, ordinary differential equations. They are solved in time using either a first order time marching or a finite element in time method. A finite element in time is suitable for steady flight conditions. It is, by comparison, an order of magnitude faster because it directly provides the steady state response. In the present study the finite element in time method is used. The finite element in time method is described in the next section.

2.2.2 Finite Element in Time

A temporal finite element method based on the Hamilton's principle in weak form is used to discretize the temporal dependence of the blade equations. The normal mode coordinate $\mathbf{p_b}$ around the azimuth is approximated by using Lagrange polynomials as shape functions. In particular, if an nth order polynomial is used in the approximation, then $n+1$ nodes per degree of freedom are required to describe the variation of $\mathbf{p_b}$ within the element. The temporal nodal coordinates are denoted by ξ. Continuity of the generalized displacements is assumed between the

time elements. The final result is a set of nonlinear algebraic equations which are then solved using a modified Newton Method. Using Hamilton's principle, equation (2.115) is rewritten as

$$\int_0^{2\pi} \delta \mathbf{p_b}^{\mathbf{T}} (\bar{\mathbf{M}}\ddot{\mathbf{p_b}} + \bar{\mathbf{C}}\dot{\mathbf{p_b}} + \bar{\mathbf{K}}\mathbf{p_b} - \bar{\mathbf{F}}) \mathbf{d}\psi = \mathbf{0} \tag{2.119}$$

where 2π is the period of response and $\bar{C}(\psi)$ and $\bar{K}(\psi)$ contain periodic coefficients. At this stage, all nonlinear terms are contained in $\bar{F}$, $\bar{M}, \bar{C}, \bar{K}$ are not displacement dependent. Assume $\bar{M}$ is not a function of ψ. Integration by parts of equation (2.119) gives

$$\int_0^{2\pi} \begin{Bmatrix} \delta \mathbf{p_b} \\ \delta \dot{\mathbf{p_b}} \end{Bmatrix}^T \begin{Bmatrix} \bar{F} - \bar{C}\dot{\mathbf{p_b}} - \bar{K}\mathbf{p_b} \\ \bar{M}\dot{\mathbf{p_b}} \end{Bmatrix} d\psi = \begin{Bmatrix} \delta \mathbf{p_b} \\ \delta p_b \end{Bmatrix}^T \begin{Bmatrix} \bar{M}\dot{\mathbf{p_b}} \\ 0 \end{Bmatrix}_0^{2\pi} \tag{2.120}$$

The right hand side of equation (2.120) is zero because of periodicity i.e., $\dot{\mathbf{p_b}}(2\pi) = \dot{\mathbf{p_b}}(0)$. Equation (2.120) can be written as the following.

$$\int_0^{2\pi} \delta y^T Q d\psi = 0 \tag{2.121}$$

where

$$y = \begin{Bmatrix} \mathbf{p_b} \\ \dot{\mathbf{p_b}} \end{Bmatrix} \tag{2.122}$$

and

$$Q = \begin{Bmatrix} \bar{F} - \bar{C}\dot{\mathbf{p_b}} - \bar{K}\mathbf{p_b} \\ \bar{M}\dot{\mathbf{p_b}} \end{Bmatrix} \tag{2.123}$$

In discretized for equation (2.121) takes the form

$$\sum_{i=1}^{N_t} \int_{\psi_i}^{\psi_{i+1}} \delta y_i^T Q_i d\psi = 0 \tag{2.124}$$

where $\psi_1 = 0, \psi_{N_t+1} = 2\pi$ and N_t is the number of time elements used to discretize one rotor revolution. Linearizing the vector Q about a steady state value of $y_0 = [\mathbf{p_{b0}}^{\mathbf{T}} \quad \mathbf{\dot{p}_{b0}}^{\mathbf{T}}]^{\mathbf{T}}$ we have

$$\sum_{i=1}^{N_t} \int_{\psi_i}^{\psi_{i+1}} \delta y_i^T Q_i(y_0 + \Delta y) d\psi = \sum_{i=1}^{N_t} \int_{\psi_i}^{\psi_{i+1}} \delta y_i^T [Q_i(y_0) + K_{t_i}(y_0)\Delta y] d\psi = 0 \tag{2.125}$$

where

$$K_{t_i} = \begin{bmatrix} \frac{\partial \bar{F}}{\partial \mathbf{p_b}} - \bar{K} & \frac{\partial \bar{F}}{\partial \dot{\mathbf{p}}_\mathbf{b}} - \bar{C} \\ 0 & \bar{M} \end{bmatrix}_i \tag{2.126}$$

where i denotes the ith time element. For the $i$the time element, the time variation of the modal displacement vector can be expressed in terms of temporal shape functions, H_t, and temporal nodal displacement vector, ξ_i, as

$$\left.\begin{aligned} \mathbf{p_{b_i}}(\psi) &= \mathbf{H_t}(\mathbf{s})\xi_\mathbf{i} \\ \dot{\mathbf{p}}_{\mathbf{b_i}} &= \dot{H_t}(s)\xi_i \\ \delta\mathbf{p_{b_i}}(\psi) &= \mathbf{H_t}(\mathbf{s})\delta\xi_\mathbf{i} \\ \delta\dot{\mathbf{p}}_{\mathbf{b_i}} &= \dot{H_t}(s)\delta\xi_i \end{aligned}\right\} \tag{2.127}$$

where the local temporal coordinate s for the ith time element is

$$s = \frac{\psi - \psi_i}{\psi_{i+1} - \psi_i} \tag{2.128}$$

and $0 <= s <= 1$. $\psi_{i+1} - \psi_i$ is the time-span of the ith time element. $H_t(s)$ is the temporal shape function matrix which has the form

$$H_t = [H_{t_1}\mathbf{I_m}, ..., \mathbf{H_{t_{n_t+1}}}\mathbf{I_m}] \tag{2.129}$$

$\mathbf{I_m}$ is an $m \times m$ identity matrix. m is the dimension of the modal displacement vector. In the above expression, the subscript n_t refers to the order of the polynomial used

in approximating the temporal variation of the modal displacement vector. For example, if an *nth* order polynomial is used in the approximation, then $n+1$ nodes for each blade mode are required to completely describe the variation of $\mathbf{p_b}$ within the time element. Therefore, H_t is an $mxm(n_t+1)$ matrix, and ξ_i is an $m(n_t+1)$ vector. In the present study, fifth order shape functions (Lagrange Polynomials) are used. Now, using equations (2.127) in equation (2.125) we have the following,

$$\sum_{i=1}^{N_t} \int_{\psi_i}^{\psi_{i+1}} \delta\xi_i^T N^T [Q_i + K_{t_i} N \Delta\xi_i] d\psi = 0 \tag{2.130}$$

where

$$N = \left\{ \begin{array}{c} H_t(\psi) \\ \\ \dot{H}_t(\psi) \end{array} \right\} \tag{2.131}$$

For a periodic solution, the boundary condition for the temporal finite element equations are $\mathbf{p_b}(\mathbf{0}) = \mathbf{p_b}(\mathbf{2}\pi)$. Finally, because the $\delta\xi_i$ are arbitrary for $i = 1, ..., N_t$, equation (2.130) takes the form

$$Q^G + K_t^G \Delta\xi^G = 0 \tag{2.132}$$

where G signifies *global* matrices after assembly as follows

$$\left. \begin{array}{c} Q^G = \sum_{i=1}^{N_t} \int_{\psi_i}^{\psi_{i+1}} N^T Q_i d\psi \\ K_t^G = \sum_{i=1}^{N_t} \int_{\psi_i}^{\psi_{i+1}} N^T K_{t_i} N d\psi \\ \Delta\xi^G = \sum_{i=1}^{N_t} \Delta\xi_i \end{array} \right\} \tag{2.133}$$

Matrix K_{t_i} given by equation (2.126) and the time element vector, Q_i given by equation (2.123) are calculated for each time element about a steady value of y_0. The element matrix K_{t_i} and the element vector Q_i are assembled into the global matrix K_t^G and global vector Q^G using equations (2.133). Equations (2.132) are a set

of time discretized nonlinear algebraic equations and are solved using the Newton's method. The updated response at the ith iteration is

$$\xi^G_{i+1} = \xi^G_i + \Delta\xi^G_i \tag{2.134}$$

Converged steady response implies $\Delta\xi^G_i = 0$.

2.3 Blade loads

The blade sectional loads, i.e. the flap, lag and torsion bending moments, are calculated using two methods - (1) Modal Curvature and (2) Force Summation Method. For converged blade response, i.e. when the response does not change with increase in the number of blade normal modes, both methods should produce identical loads. In the immediate vicinity of a concentrated loading, e.g., lag damper force, the force summation method captures the blade loads with lesser number of modes.

To obtain the same loads using force summation and modal curvature methods, the response equations must be consistent with loads calculations. Consistency is specially important for articulated rotors where the bending loads must reduce to zero at the hinge.

2.3.1 Modal Curvature Method

The flap and lag bending moments, M_η and M_ζ are obtained as follows.

$$\begin{aligned} M_\eta &= \int\int_A \zeta\sigma d\eta d\zeta = \int\int_A E\zeta\epsilon_{xx} d\eta d\zeta \\ &= EI_\eta[v''sin(\theta+\hat{\phi}) - w''cos(\theta+\hat{\phi})] - EC_1\hat{\phi}'' \end{aligned} \tag{2.135}$$

$$\begin{aligned} M_\zeta &= -\int\int_A \eta\sigma d\eta d\zeta = -\int\int_A E\eta\epsilon_{xx} d\eta d\zeta \\ &= EI_\zeta[v''cos(\theta+\hat{\phi}) + w''sin(\theta+\hat{\phi})] - EAe_A u_e' - EB_2\theta'\hat{\phi}' \end{aligned} \tag{2.136}$$

The expression for torsion bending moment from Ref. [13] is given by

$$\begin{aligned} M_\xi = &\int\int_A \left[\eta\sigma_{x\zeta} - \zeta\sigma_{x\eta} + \lambda_T(\frac{\partial\sigma_{x\eta}}{\partial\eta} + \frac{\partial\sigma_{x\zeta}}{\partial\zeta})\right] d\eta d\zeta \\ &+ \frac{\partial}{\partial x}\int\int_A \lambda_T\sigma_{xx} d\eta d\zeta \\ &+ (\theta+\hat{\phi})'\int\int_A (\eta^2+\zeta^2)\sigma_{xx} d\eta d\zeta \\ &= EAk_A^2(\theta+\hat{\phi})'u_e' + EB_1\theta'^2\hat{\phi}' - EB_2\theta'(v''cos\theta + w''sin\theta) \\ &+ GJ(\hat{\phi}' + w'v'') \\ &- [EC_1\hat{\phi}'' + EC_2(w''cos\theta - v''sin\theta)]' \end{aligned} \tag{2.137}$$

2.3.2 Force Summation Method

The loads occurring at a blade section are the reaction forces (and moments) to those occurring outboard. It is equal (and opposite) to the integrated air loads and inertial loads from blade tip to the desired section. The inertial forces and moments at each blade section are given by the following.

$$\left.\begin{aligned} F^I &= -\int\int_A \rho\bar{a}d\eta d\zeta \\ M^I &= -\int\int_A \bar{s} \times \rho d\eta d\zeta \end{aligned}\right\} \tag{2.138}$$

The acceleration of the section, $\bar{a}$ is given by

$$\bar{a} = \ddot{\bar{r}} + \Omega \times (\Omega \times \bar{r}) + 2(\Omega \times \dot{\bar{r}}) \tag{2.139}$$

The moment arm of a point on the blade section measured from the deformed shear center, $\bar{s}$ is obtained from equation(2.68) as

$$\bar{s} = -[v'(y_1 - v) + w'(z_1 - w)]\hat{i} + (y_1 - v)\hat{j} + (z_1 - w)\hat{k} \tag{2.140}$$

Using equations (2.68), (2.71), (2.84), and (2.85) we obtain

$$\bar{a} = a_x\hat{i} + a_y\hat{j} + a_z\hat{k} \tag{2.141}$$

where

$$\begin{aligned} a_x =& \ddot{u} - \lambda_T\ddot{\theta}_1' - (y_1 - v)(\ddot{v}' + w'\ddot{\theta}_1 + 2\dot{w}'\dot{\theta}_1 - v'\dot{\theta}_1^2) \\ & - (z_1 - w)(\ddot{w}' - 2\dot{v}'\dot{\theta}_1 - v'\ddot{\theta}_1 - w'\dot{\theta}_1^2) - 2[\dot{v} - \dot{\theta}_1(z_1 - w)] \\ & + \beta_p[w + (z_1 - w)] - [x + u - v'(y_1 - v) - w'(z_1 - w)] \end{aligned} \tag{2.142}$$

$$\begin{aligned} a_y =& \ddot{v} - \ddot{\theta}_1(z_1 - w) - \dot{\theta}_1^2(y_1 - v) - 2\beta_p[\dot{w} + \dot{\theta}_1(y_1 - v)] \\ & 2[\dot{u} - \lambda_T\dot{\theta}_1' - (y_1 - v)(\dot{v}' + w'\dot{\theta}_1) - (z_1 - w)(\dot{w}' - v'\dot{\theta}_1)] - \\ & \beta_p[v + (y_1 - v)] - [v + (y_1 - v)] \end{aligned} \tag{2.143}$$

$$\begin{aligned} a_z =& \ddot{w} + (y_1 - v)\ddot{\theta}_1 - (z_1 - w)\dot{\theta}_1^2 + 2\beta_p[\dot{v} - \dot{\theta}_1(z_1 - w)] \\ & + \beta_p[x + u - v'(y_1 - v) - w'(z_1 - w)] \end{aligned} \tag{2.144}$$

Let L_u^I, L_v^I, L_w^I and M_u^I, M_v^I, M_w^I be the inertial forces and moments in the undeformed frame x, y, z directions. Then, to second order, we have the following.

$$L_u^I = -\int\int_A \rho a_x d\eta d\zeta = T_{U_e} \tag{2.145}$$

$$L_v^I = -\int\int_A \rho a_y d\eta d\zeta = T_v \tag{2.146}$$

$$L_w^I = -\int\int_A \rho a_z d\eta d\zeta = T_w \tag{2.147}$$

$$\begin{aligned} M_v^I &= -\int\int_A [v'(y_1 - v) + w'(z_1 - w)a_z + (z_1 - w)a_x] d\eta d\zeta \\ &\approx -\int\int_A (z_1 - w)a_x d\eta d\zeta \\ &= -T_w' \end{aligned} \tag{2.148}$$

$$\begin{aligned} M_w^I &= \int\int_A [v'(y_1 - v) + w'(z_1 - w)a_y + (z_1 - w)a_x] d\eta d\zeta \\ &\approx \int\int_A (y_1 - v)a_x d\eta d\zeta \\ &= T_v' \end{aligned} \tag{2.149}$$

$$\begin{aligned} M_u^I &= \int\int_A [(z_1 - w)a_y - (y_1 - v)a_z] d\eta d\zeta \\ &= T_{\hat{\phi}} - v' M_v^I - w' M_w^I \\ &= T_{\hat{\phi}} + v' T_w' - w' T_v' \end{aligned} \tag{2.150}$$

where $T_{U_e}, T_v, T_w, T_v', T_w', T_{\hat{\phi}}$ are identical to those given in equations (2.90) to (2.96). Thus the kinetic energy terms derived before are identical to the inertial terms obtained here. This shows the equivalence of Hamilton's Principle and Newton's Laws.

Let the external loads (air loads and other concentrated loadings if any e.g., a prescribed lag damper force) be denoted by the superscript A. Then the total loads

distribution at a section is given by the sum of inertial and external loads

$$\left.\begin{aligned} L_u &= L_u^A + L_u^I \\ L_v &= L_v^A + L_v^I \\ L_w &= L_w^A + L_w^I \\ M_u &= M_{\hat{\phi}}^A + M_u^I \\ M_v &= v' M_{\hat{\phi}}^A + M_v^I \\ M_u &= w' M_{\hat{\phi}}^A + M_w^I \end{aligned}\right\} \tag{2.151}$$

$M_{\hat{\phi}}^A$ is the external pitching moment (e.g. aerodynamic pitching moment) acting in the blade deformed frame. Its components in the x, y, z directions, $M_{\hat{\phi}}^A, v' M_{\hat{\phi}}^A, w' M_{\hat{\phi}}^A$ are obtained using T_{DU} from equation (2.26).

The resultant shear forces and bending moments at any blade section x_0 is given by the following.

$$\left\{\begin{array}{c} f_x \\ f_y \\ f_z \end{array}\right\} = \int_{x_0}^{1} \left\{\begin{array}{c} L_u \\ L_v \\ L_w \end{array}\right\} dx \tag{2.152}$$

$$\left\{\begin{array}{c} m_x \\ m_y \\ m_z \end{array}\right\} = \int_{x_0}^{1} \left\{\begin{array}{c} -L_v(w - w_0) + L_w(v - v_0) + M_u \\ L_u(w - w_0) - L_w(x + u - x_0 - u_0) + M_v \\ -L_u(v - v_0) + L_v(x + u - x_0 - u_0) + M_w \end{array}\right\} dx \tag{2.153}$$

To compute the contribution of the blade loads to the hub loads in the rotating frame, the spanwise integration is carried out from the hub center to the blade tip, and $u_0, v_0, w_0, x_0 = 0$ The hub loads in the fixed frame is calculated using

transformation (2.1).

$$\left.\begin{aligned} F_X(\psi) &= \textstyle\sum_{m=1}^{N_b}(f_x^m cos\psi_m - f_y^m sin\psi_m - f_z^m cos\psi_m \beta_p) \\ F_Y(\psi) &= \textstyle\sum_{m=1}^{N_b}(f_x^m sin\psi_m + f_y^m cos\psi_m - f_z^m sin\psi_m \beta_p) \\ F_Z(\psi) &= \textstyle\sum_{m=1}^{N_b}(f_z^m + f_x^m \beta_p) \\ M_X(\psi) &= \textstyle\sum_{m=1}^{N_b}(m_x^m cos\psi_m - m_y^m sin\psi_m - m_z^m cos\psi_m \beta_p) \\ M_Y(\psi) &= \textstyle\sum_{m=1}^{N_b}(m_x^m sin\psi_m + m_y^m cos\psi_m - m_z^m sin\psi_m \beta_p) \\ M_Z(\psi) &= \textstyle\sum_{m=1}^{N_b}(m_z^m + m_x^m \beta_p) \end{aligned}\right\} \tag{2.154}$$

where $f_x, f_y, f_z, m_x, m_y, m_z$ are the rotating frame hub loads, i.e., blade loads integrated up to the hub. The steady values of the fixed frame hub loads (2.154) are used for trimming the helicopter. The higher harmonics cause helicopter vibration. For a tracked rotor, with identical structural and aerodynamic behavior, the higher harmonics contain only those frequencies which are integral multiples of rotor frequency. These harmonics are generated by harmonics of rotating frame blade loads which are one higher and one lower than the rotor frequency.

For example, for an N_b bladed rotor, the higher harmonics in the fixed frame hub loads are pN_b/rev, where p is an integer. These harmonics are generated by $pN_b \pm 1$/rev in-plane shear forces (f_x, f_y), pN_b/rev vertical shear force (f_z), $pN_b \pm 1$/rev flap and torsion bending moments (m_x, m_y) and pN_b/rev chord bending moment (m_z). To predict helicopter vibration these rotating frame blade loads must be predicted correctly.

2.4 Validation of Structural Model

The structural model is validated using flight test measured air loads, damper load and rotor control angles. Thus, errors in response and blade loads prediction originate entirely from structural modeling.

2.4.1 Flight Test Data

The test data used in the present study are from Flight 85 of the UH-60A Black Hawk Air Loads Program [144]. Flight 85 is a steady level flight and corresponds to a nominal vehicle weight coefficient, C_W/σ, of 0.08. Within Flight 85, Counter numbers indicate air speed. For example, counter 34 data corresponds to high speed forward flight - 155 kts : advance ratio, μ, of 0.368, $C_W/\sigma = 0.0783$. Counter 15 data corresponds to low speed transition flight - 45 kts : advance ratio, μ, of 0.110, $C_W/\sigma = 0.0782$. The focus is on high speed flight, i.e. Flight 8534.

The loads data from this test condition are repeatable and considered highly accurate. Most of the uncertainties are in the steady values not in the oscillatory components. Figure 2.1(a) shows the measured pitch-link or push-rod loads on all four blades of the Black Hawk in high-speed forward flight. The push rod loads are generated by integrated blade torsion loads and therefore show the effect of integrated span-wise errors. In addition, they are from four different blades with different sets of instrumentation. In spite of these differences the push rod loads from all four blades are remarkably similar.

For purposes of validation, measurements corresponding to Blade 1 are used.

In general the first ten harmonics of all blade loads are extracted and compared with analysis results. For example, figure 2.1(b) compares the first ten harmonics of the push rod loads with the total oscillatory waveform.

2.4.2 Solution Procedure

The problem of determining rotor response with a prescribed set of air loads which remain fixed and do not change with the response itself, can be termed as a *mechanical air loads problem*. In the present case the measured airloads are used as the prescribed set.

The mechanical air loads problem is fundamentally an ill-posed problem because the air loads are fixed and do not change in response to blade deformations. This leads to zero aerodynamic damping. It cannot be solved for all rotor systems. Consider a teetering, gimbaled or articulated rotor with fundamental flap frequency of 1/rev (1p) with zero structural damping. If the measured aero hinge moment is infinitesimally accurate, the 1p component will be identically zero in which case the rotor response is undefined. The 1p component is identically zero because, at resonance the damping force is equal and opposite to the forcing and they are both are parts of the measured air loads. In practice measured air loads will have errors. These errors will produce a 1p aerodynamic hinge moment which will drive the rotor response to infinity. In presence of structural damping, which are small compared to aerodynamic damping e.g. in flap 2% compared to 50%, the response will not be infinite but the accuracy of the measured air loads required for a reasonably accurate

response solution will be impossible to meet. The mechanical air loads problem is therefore fundamentally inaccurate for low damped systems with natural frequencies close to excitation harmonics. The Black Hawk blade frequencies are reasonably well separated from excitation harmonics except the first natural frequency which is 1.036/rev.

The rotor blade is modeled as a fully articulated beam with flap and lag hinges coincident at 4.66% span. All blades are identical. Each blade is defined by 20 finite elements undergoing flap, lag, torsion and axial degrees of motion. The blade property data, including nonlinear aerodynamic and structural twist distributions are obtained from the NASA Ames master database. The tip sweep in the outer 6.9% of the blade span (reaching a maximum of 20 degrees at 94.5% span) is modeled in two ways. The baseline model incorporates the tip sweep as a center of gravity offset from a straight undeformed elastic axis. Thus, in the swept part of the blade, the total center of gravity offset is the sum of the local offset with respect to swept elastic axis and the offset due to blade sweep. The elastic axis of the UH-60A blade is at the local quarter chord line. A refined model incorporates a structurally swept elastic axis [23, 25]. The refined sweep model is seen to affect only the predicted torsion dynamics. The measured air loads are applied at the local quarter chord locations at all radial stations.

The non-linear lag damper force is imposed on the structure as a set of concentrated forces and moments acting at 7% of the blade span. These damper imposed forces and moments vary with azimuth based on the nominal damper geometry. The damper geometry is obtained from the master database. The pitch link is modeled

as a linear spring-damper system. The elastomeric bearing stiffness and damping are modeled as linear springs and dampers in flap, lag and torsion.

The rotor blade frequency plot and the first ten natural frequencies at the operating RPM are shown in figure 2.2(a). These correspond to a collective angle of 13.21 degrees and a baseline root torsion spring stiffness of 363 ft-lb/degree [160]. The root spring stiffness is an equivalent measure of the pitch link stiffness obtained by multiplying the pitch link stiffness with the square of the pitch link arm perpendicular to the blade elastic axis. A more realistic value of the root torsion spring is 1090 ft-lbs/degree as measured in Ref. [161]. It corresponds to the fixed system control stiffness for reactionless loading. The increased stiffness increases the first torsion frequency from 3.8/rev to 4.2/rev as shown in figure 2.2(b). Flap and lag frequencies remaining nominally constant. Figure 2.3 shows the variation of calculated first torsion frequency with root spring stiffness. The present calculation shows the same trend as that reported in Ref. [161] with a slightly increased value. The swept elastic axis model, has a higher propeller moment in the tip region and generates a marginally increased torsion frequency. The first eight structural modes are used for the present study.

The measured air loads are in the deformed blade frame, and contain the loading caused by the undeformed blade as well as by the aeroelastic response. They are reduced to the undeformed frame iteratively using calculated deformations and the flight test control angles at each step. These iterations have no effect on the pitching moments and are insignificant for the normal force. They are important only for obtaining the chord forces in the undeformed frame.

The periodic blade response is calculated directly using finite element in time. A time-marching algorithm, in comparison, requires more than an order of magnitude longer in computation time to settle down to the final steady state response. This is due to the absence of aerodynamic damping and the proximity of modal frequencies to forcing harmonics (eg., 1st flap is 1.04/rev, 2nd flap is 2.82/rev, 1st torsion is 3.8/rev). In addition, artificial damping is required initially during convergence cycles and needs to be subsequently removed. Artificial damping accelerates the decay of the initial natural mode response in the absence of aerodynamic damping.

2.4.3 Calculated Structural Response

The calculated structural response of the rotor blades are now compared with high speed flight test data (Flight 8534). Root flap and lag angles, flap, lag and torsion bending moments and pitch link loads are investigated. The bending moments and pitch link loads corresponding to Flight 8515 are also shown.

Root Flap, Lag and Pitch Angles

The calculated oscillatory flap angle at the blade root is shown in figure 2.4(a). The waveform is sensitive to structural damping in the first flap mode. A damping value of 4% critical is used to obtain a good peak to peak match. The phase of the resulting waveform shows satisfactory agreement.

The upper shaft bending moment, shown in figure 2.4(b), is consistent with

the root flap angle in that it shows the same trend. Without the 4% damping, the waveforms shows large error in magnitude and phase. The upper shaft bending moment is the bending load at the rotor shaft. There are two sets of values which are mutually orthogonal to each other, one set created by the root flap moments from blades 1 and 3, and another set by the root flap moments from blades 2 and 4. The test data was available for the gauge reading which was generated by blades 1 and 3 and is used for the present comparison. The predicted shaft moments from blades 1 and 3 and blades 2 and 4 are offcourse identical with only a phase shaft as the blades are assumed identical.

A 4% structural damping value is an unrealistically high damping value to be produced by a mechanical flap hinge damper. It appears that the phase error in calculated root flap angle and upper shaft bending moment stems from small errors in airload measurements as explained below. A structural damping value of 4% happens to be the amount required to offset this error. Figures 2.5 shows the harmonics of the root flap angle. The largest contributer is 1/rev followed by 2, 3, 4 in decreasing order of magnitude. The largest magnitude error is in 1/rev with an error in phase of around 50 degrees. The 4% damping rectifies the 1/rev error, both in magnitude and phase, while keeping the higher harmonics unchanged. The structural damping value is effective only at 1/rev because the rotor flap frequency is very near 1/rev, 1.036/rev.

Figure 2.6(a) shows the 1/rev normal force harmonics at all radial stations. The aerodynamic hinge moment shown in figures 2.6(b) and 2.6(c) has, on the contrary, a very small 1/rev component. This is because, out of all the harmonics

of the aerodynamic hinge moment, the 1/rev component is generated as a residual of counter acting inboard and outboard normal forces - which are mutually 180 degree out of phase as shown in figure 2.6(a). This is required to generate a low steady hub moment in trimmed level flight. This radial balance between the inboard and outboard normal forces determine the phase of the 1/rev aerodynamic hinge moment, figure 2.6(d). The radial balance is easily destroyed by a small error at any one radial station. Small errors in air loads measurements at any one station can therefore produce a large error in 1/rev aerodynamic hinge moment phase. It appears that the phase error in calculated root flap angle stems from such an error in the measured air loads. This error is then further magnified in the 1/rev root flap angle prediction due to the proximity of the 1st flap frequency to 1/rev and the lack of any aerodynamic damping in the system. Thus the error in root flap angle prediction is an artifact of the 1/rev trim airload balance in forward flight and the *mechanical air loads problem* which is fundamentally ill-posed rather than an error in structural modeling. In fact the accuracy of lift measurements required to produce an accurate root flap angle prediction may not be possible to meet.

Flap bending moments however are not significantly affected by the critical damping value. This is because the 1/rev component of the hinge moment drives mainly the rigid response of the rotor. The bending moment calculations shown in the following sections therefore do not include this artificial damping value of 4%.

The root lag angle predictions are shown in figure 2.7(a). The root flap response couples with the lag response via the rigid twist angle (which is 9.31 degrees at the root) and hence the prediction is affected by the 4% structural damping value.

The general waveform from Blade 2 and 3 is captured. Blade 1 shows measurement discrepancies. The root pitch angle is shown in figure 2.7(b).

The predicted root pitch angle is the sum of flight test control angles (13.21 degrees of collective, 6.56 degrees of lateral cyclic and -9.07 degrees of longitudinal collective), the rigid pre-twist at the root and an elastic twist component. The elastic twist is very small at the root, but non-zero due to a finite stiffness of the pitch bearing. Blades 2 and 3 shows a higher collective than Blade 1. The difference in collective is around 3 degrees. Later, in comprehensive predictions, predicted collective angles would be around 16.5 degrees compared to the flight test value of 13.21 degree. The flight test value is taken from Blade 1, which appears to be in error. A value of 16.5 degree is more accurate in terms of Blade 2 and Blade 3. In general there is an uncertainty in the flight test control angles both for the collective and lateral cyclic.

Flap Bending Moment

The predicted flapwise bending moment distributions are compared with test data in figure 2.8. The predicted steady values are within 10% of flight test values, except at the 70% radial station, and are not included for comparison. The total (1-10/rev) and vibratory components (3-10/rev) of the predicted bending moment show similar trends as the test data. The vibratory components are dominated by 3/rev loads at all radial stations. The predicted values however, show an over-prediction of 5/rev response near the tip compared to the test data. Figure 2.9 compares the predicted and measured flight test bending moment values at eight radial stations.

The waveform at 10% radial station is affected by the lag damper force in the retreating blade. The damper force affects both the chord-wise and flap-wise (normal to chord) moments via a 9.3 degree blade pre-twist at this station. Figure 2.10 shows the radial distribution of the bending moment harmonics, both magnitude and phase. All the first five harmonics show the correct trends in magnitude and phase. The 3/rev component is under-predicted by about 20% along the blade span. The 5/rev component is over-predicted near the blade tip. The phase prediction is good for all harmonics. Figures 2.9 and 2.10 establish that the flap bending moment prediction problem shown in the introduction (figure 1.2) stem from inaccurate aerodynamic modeling. A similar *mechanical air loads* solution for the low speed transition regime (Flight 8515) also show satisfactory prediction of flap bending moments, figure 2.11.

Torsion Bending Moment

The torsion bending moments at three radial stations and the pitch link load at high speed are shown in figure 2.12. Predictions correspond to a soft pitch link stiffness value, which was the value used by all participants of the UH-60A Black Hawk Air loads Workshop. In general, the torsion loads are not as satisfactory as the flap bending moments. Predicted torsion moments show satisfactory trends in the advancing blade but are somewhat less satisfactory in the retreating blade. Higher harmonics (4/rev and higher) are not captured satisfactorily in magnitude and phase. The lower harmonics (1-3/rev) which determine the peak to peak magnitude are captured. Prediction at 90% R show a significant under-prediction although

the integrated effect on the pitch-link load shows the right magnitude. However, there is an uncertainty in the measurements of torsion bending moment at 90% R. The phase and magnitude of the pitch link load are well predicted. This shows that the under-prediction of pitch link load as discussed in the introduction (figures 1.7 and 1.8) stem from inaccurate aerodynamics. Although the structural model has deficiencies in capturing the accurate torsion loads, it is accurate enough to predict the right peak to peak and lower harmonics given the correct air loads.

The harmonic content of the torsion moments are shown in in figure 2.13. Accurate elastic torsion is crucial for accurate blade lift. Out of all the harmonics of elastic torsion, 1-3/rev are most important for blade lift. 1/rev produces 2/rev lift through the azimuthal velocity variation. 2/rev and 3/rev are the most significant contributors to vibratory lift of which 2/rev is the largest. Prediction of 1-3/rev elastic torsion shows satisfactory trends in magnitude and phase. Prediction of 4/rev phase is improved by the stiffer pitch-link. The stiffer pitch-link shifts the 4/rev phase by around 180 degrees because it increases the first torsion frequency from below 4/rev (3.8/rev) to above 4/rev (4.2/rev). The shift is not exactly 180 degrees due to the pitch bearing damper. 5/rev prediction is poor and is a source of the retreating blade error.

The effect of structural couplings on predicted torsion bending moments and pitch-link load are now investigated. The couplings arise out of three mechanisms: (i) second order non-linear couplings between flap, lag and torsion arising out of geometric curvature, for example, the chord force at a section of an elastically flapped blade and the normal force at a section of an elastically lagged blade create torsion

moment in-board, (ii) flap torsion coupling via sectional center of gravity offsets and (iii) flap torsion coupling due to tip sweep.

Figures 2.14(a) and 2.14(b) show the effect of non-linear structural couplings on torsion moment at 30% R and pitch-link load. The effect is primarily in the second quadrant and not significant. The center of gravity offsets on the other hand, appears to significantly affect the waveform in the advancing blade as shown in figures 2.14(c) and 2.14(d). Not modeling the center of gravity offsets, while keeping the sectional moment of inertias about c.g. constant, decreases the mass moment of inertia about the elastic axis and increases the first torsion frequency from 3.8/rev closer to 4/rev. This increases the 4/rev response. The sensitivity of the c.g. location is in part an artifact of the mechanical air loads problem with zero damping. For comprehensive analysis the effect would be less pronounced due to torsion damping from unsteady aerodynamics.

Figures 2.14(e) and 2.14(f) show the effect of tip sweep. Baseline results with tip sweep are compared with those of a non-swept blade. The non-swept blade ignores the sweep back of the local elastic axis at the tip. The effect of blade sweep appears primarily to be in the retreating blade. Predictions from the baseline sweep model are compared with the refined model in figure 2.15. Figure 2.15(a) shows that even the simplified sweep model captures the correct peak to peak and basic waveform of the pitch link load. The predicted harmonics from both models are compared with test data in figure 2.15(b). The refined model appears to over-predict all harmonics over 1/rev and does not in general provide improved predictions. Predictions show the right trends apart from 5/rev phase and 2/rev magnitude.

The error in 5/rev phase is the integrated effect of the 5/rev phase error in torsion bending moments (figure 2.13).

In addition to air loads and structural properties of the blade, two specific structural characteristics of the UH-60A affect the pitch link loads - pitch bearing damper and non-linear lag damper force. The effect of pitch bearing damper on the torsion loads is shown in figure 2.16. The bearing damper contributes a 1/rev component to the pitch link load. This is because the pitch link forces against the pitch bearing to implement the 1/rev rotor control angles. The feedback effect on the blade loads, as shown in figure 2.16(a) is not significant. The measured pitch bearing damper value is uncertain. In the present model this value is fixed at 30 ft-lbs/rad/sec based on this validation study.

The effect of the lag damper is shown in figure 2.17. The lag damper attaches to the blade at 7% R. The pitch horn attaches to the blade at 4.66% R. The line of action of the damper force changes with respect to the pitch horn as a function of blade azimuth based on the measured damper attachment geometry and kinematics. The lag damper force affects mostly the retreating blade (figure 2.17). The advancing blade waveform and peak to peak variation is not affected by the lag damper.

In summary the lower harmonics of torsion are well predicted (1-3/rev) with measured air loads. These govern the peak to peak torsion moments and pitch link load as well as the advancing blade waveform. Higher harmonic predictions (4/rev and higher) are less satisfactory.

Predicted torsion loads for Flight 8515 (low speed transition flight, $\mu = 0.110$) is shown in figure 2.18. The torsion loads are dominated by higher harmonics at

this flight condition. As a result predictions are not as satisfactory as in high speed. The peak to peak pitch link load and the general waveform is however satisfactorily captured.

Chord Bending Moment

The predicted chord bending moment at high speed is shown in figure 2.19. The root chord moment (11.3% R) is dominated by the non-linear lag damper force. The sharp gradient at the junction of the third and fourth quadrant is a direct effect of the lag damper. The force summation method better predicts the effect of this concentrated loading near the root with eight modes. To capture this effect with the modal curvature method more modes are necessary. In general, the predicted chord moments capture the peak to peak loads satisfactorily.

Figure 2.20 shows the harmonics of predicted chord bending moment. The damper acts at 7.6% R and has a significant effect on the moments up to 50% R. The effect is dominant on the low frequency harmonics, 1-3/rev. The predicted phase of all harmonics show satisfactory correlation with test data. Discrepancies exist in the magnitude prediction. Out of the three vibratory harmonics, 3/rev prediction is good, 4/rev is under-predicted and 5/rev is over-predicted. 1 and 2/rev harmonics show the right trends but are under-predicted at the mid-span stations. The measured chord force, obtained from pressure data, contains only the induced drag component. The effect of viscous drag can play a role in the prediction of chord bending moments. Figure 2.21 shows the predicted lag bending moment for low speed Flight 8515. The errors once again are mainly in 4/rev and 5/rev

predictions. The peak to peak variations are well captured. The root lag bending moment at 11.3% R is again dominated by the damper force and is picked up more easily by a force summation method using only eight modes.

In conclusion, measured air loads, damper force and control angles are used to satisfactorily validate the structural model. The structural model can therefore be used to obtain a set of blade deformations which are close to the actual values in high speed flight. In absence of measured deformations, this set can be used to calculate air loads and validate the aerodynamic models.

2.5 Deformation set for air loads calculation

In addition to blade deformations, the rotor control angles are important for air load calculations. The measured control angles show some uncertainty. Instead of the measured control angles, a set of calculated control angles are used for air load calculations. The control angles are calculated in the following manner. A comprehensive coupled trim of the UH-60A is performed (to be discussed in detail in Chapter 4) to obtain the control angles. During this trim procedure, measured pitching moments from the flight test data are used instead of the calculated values. The measured pitching moments produce accurate elastic torsion (the structural model is validated) which produce a consistent set of control angles - collective, lateral and longitudinal of (17.2, 3.4, -9.9). The flight test values are (13.21, 6.56 and -9.07). Note that the flight test collective is about 4 degrees lower than the calculated collective. The flight test collective along with an elastic torsion peak

value of -8 degrees near the tip in the advancing side stalls the blade in the prescribed deformation air loads calculations (Chapter 3). The purpose of refining the control angles using the coupled trim solution was to avoid this blade stall in lift calculation. Without stall, in general, the vibratory harmonics of the blade lift are not affected significantly by the control angles. The calculated collective is closer to that corresponding to Blade 2 and 3 root pitch angle, figure 2.7(b).

The torsion deformations, crucial for air loads calculation, is obtained using the stiff pitch link value. This is because the stiffer pitch link corresponds to the experimentally measured value [161] and will be used in the comprehensive analyses later (Chapter 4 and 5). While obtaining this set of torsion deformations, the lag damper forcing is not used. This is because the measured damper forces will not be used in the full aeroelastic computations performed in Chapter 4 (lifting-line aerodynamics) and Chapter 5 (CFD aerodynamics). The damper force does not effect the flap and lag deformations which therefore remain same as before - except at 11.3% which however is within the root cut out of 20% R and therefore does not play any role in air loads calculations. The flap and lag bending moments are therefore nominally same as those shown in figures 2.9 and 2.19. The new torsion loads, without lag damper and with stiff pitch link are shown in figure 2.22.

Figure 2.22 shows that the torsion bending moments, and therefore the elastic torsion deformations, are accurate in the advancing blade. Thus the deformations are satisfactory for accurate prediction of advancing blade air loads. The retreating blade predictions are however unsatisfactory. This error is structural dynamic in origin and cannot be resolved by accurate air loads prediction. The flap and elastic

torsion deformations are shown in figure 2.23.

2.6 Concluding Remarks

A nonlinear structural dynamic model of helicopter rotor blades is described. The governing equations of motion are solved using finite element in space and time. Measured air loads, damper loads and control loads from the UH-60A level flight tests (both high speed 158 kts and low speed 40 kts) are used to validate the structural dynamic model. Based on this study the following conclusions are drawn.

1. Modern finite element structural dynamic models are capable of satisfactorily predicting the blade loads given the correct air loads.

2. Predicted flap bending moments are accurate. They capture lower and higher harmonics of blade loads (upto 5/rev shown in the present study) both in magnitude and phase at all radial stations.

3. Predicted lag bending moments show the correct trends in magnitude and phase, but correlation in general is not as satisfactory as the flap bending moments. Although phase prediction is good, significant discrepancies (up to 50%) in magnitude exists in 2/rev, 4/rev and 5/rev loads. The measured chord forces contain only the induced component and this can explain a part of the error.

4. The damper force has a significant effect on the lag bending moments. It

affects primarily the lower harmonics, 1-3/rev, from the root to 50% of the span.

5. The torsion bending moment predictions show the correct magnitudes for 1-5/rev harmonics over the blade span, but a significant discrepancy exists in phase prediction of the higher harmonics, 4 and 5/rev. This discrepancy appears as an error in the retreating blade waveform. The advancing blade waveform and peak to peak magnitudes are accurately captured.

6. The pitch link load is well captured using measured air loads. However, like the torsion bending moments, the higher harmonics are not well captured.

7. Because flap lag and elastic torsion are well predicted (all harmonics of flap, lower harmonics for lag and at least 1-3/rev harmonics of elastic torsion) using measured air loads, the deformation set obtained can be used with confidence to validate aerodynamic models. In absence of measured deformations, this set forms a basis for comparing the prediction capabilities of different aerodynamic models.

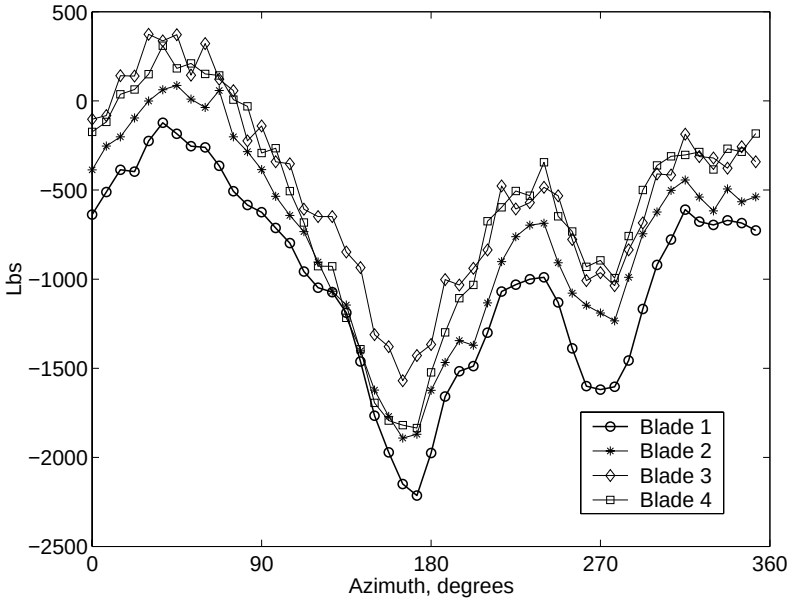

(a) Total Pitch-Link Loads for four blades

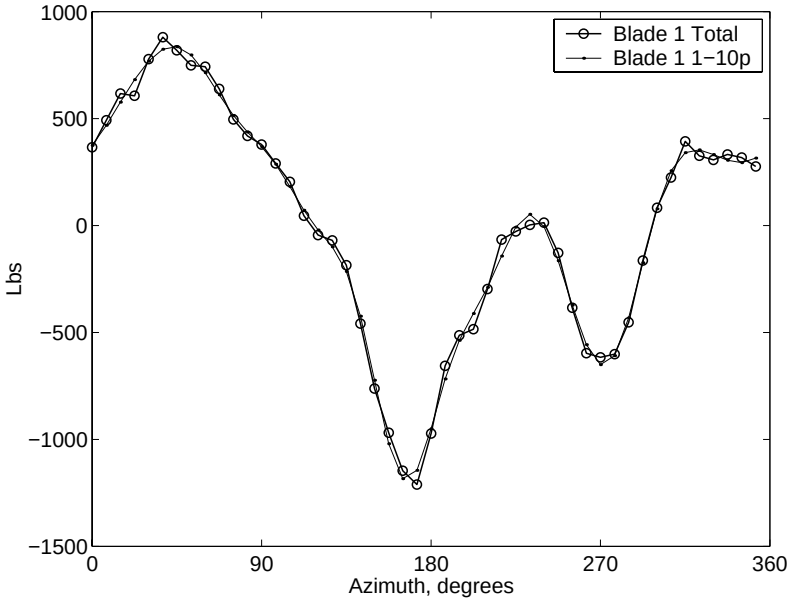

(b) 1-10 Harmonics of Blade 1 Pitch-Link Load

Figure 2.1: **Repeatability of Loads Data for the UH-60A Black Hawk in High-Speed forward Flight; $\mu = 0.368$, $C_W/\sigma = 0.0783$**

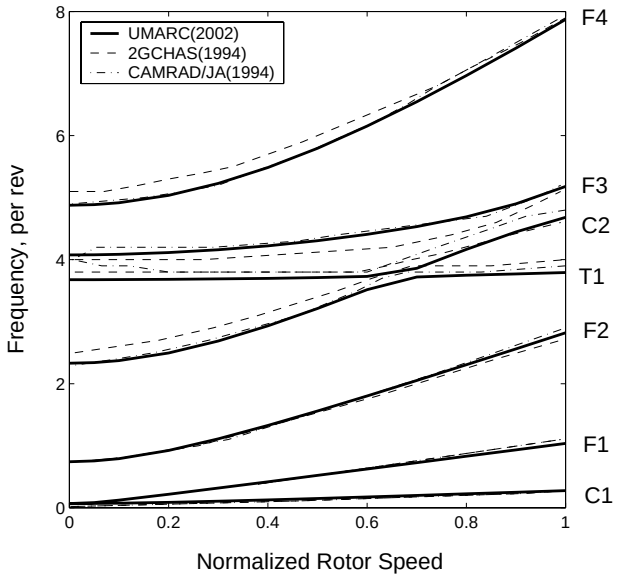

(a) Frequencies compared with other comprehensive analysis; soft pitch link 363 ft-lbs/deg

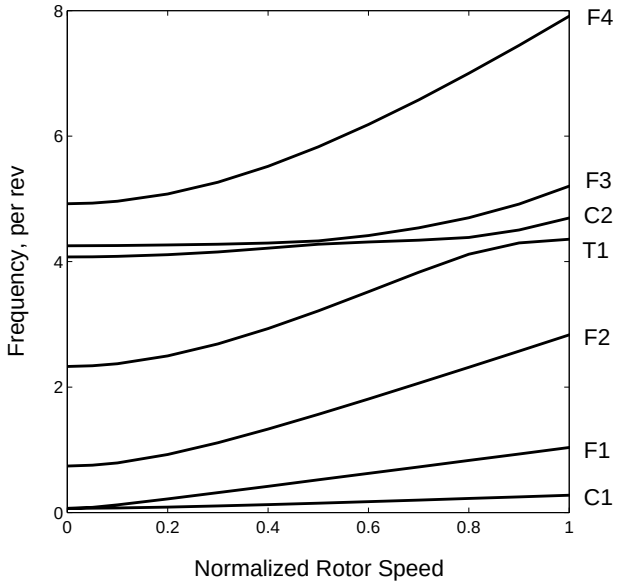

(b) Frequencies with stiff pitch link 1090 ft-lbs/deg

Figure 2.2: **Calculated UH-60A rotor blade frequencies *in vacuo*; F:Flap, C:Lag, T:Torsion**

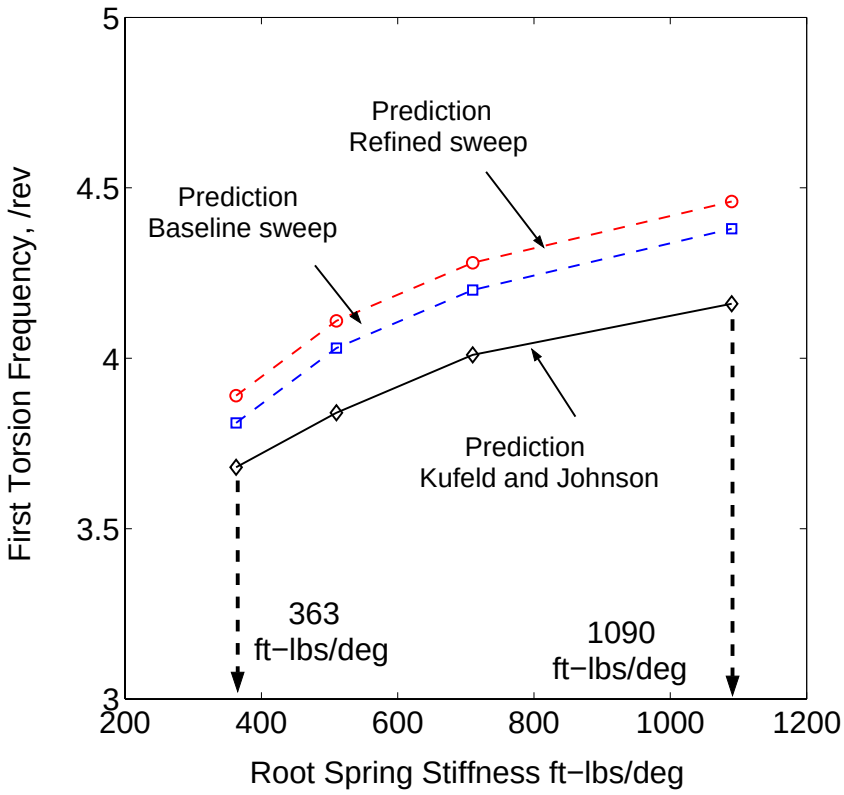

Figure 2.3: **Variation of calculated first torsion frequency with root spring stiffness**

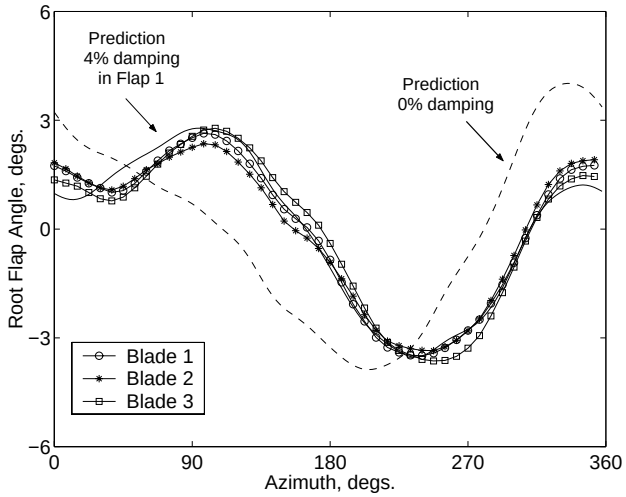

(a) Root flap angle

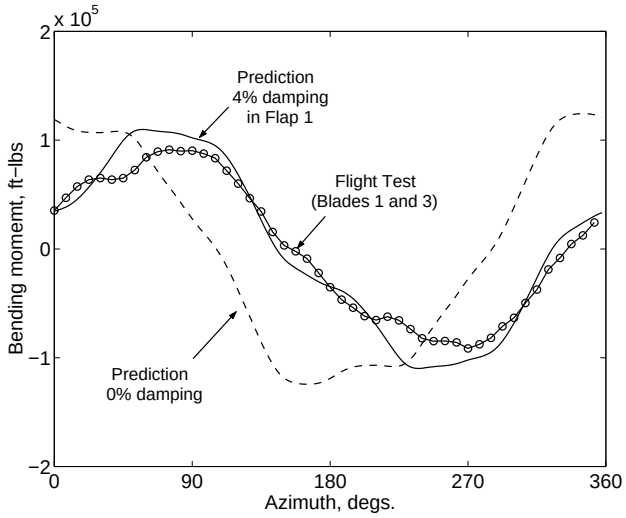

(b) Upper shaft bending moment

Figure 2.4: **Predicted and measured root flap angle and upper shaft bending moment for UH-60A Black Hawk using airloads measured in flight test; C_W/σ = 0.0783, high-speed μ = 0.368**

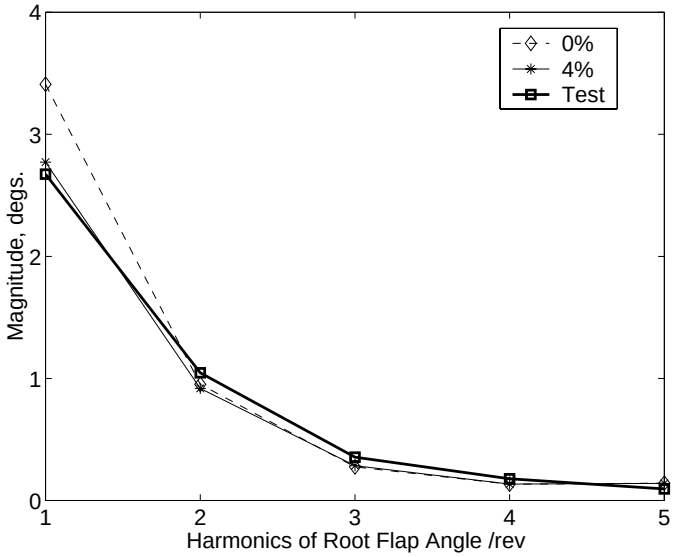

(a)

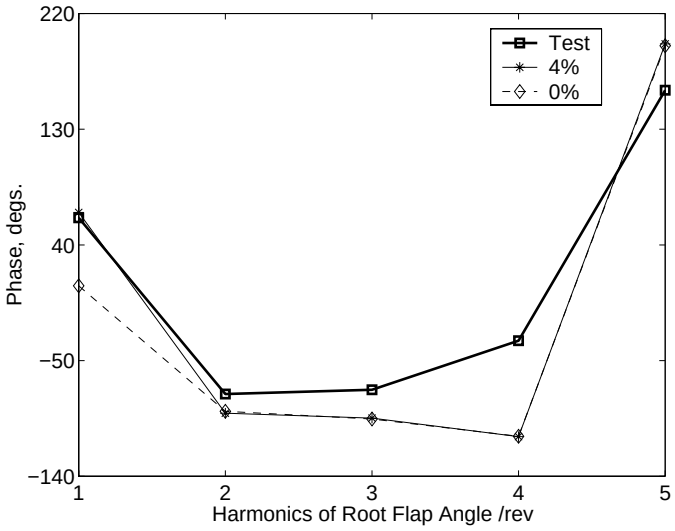

(b)

Figure 2.5: **Harmonics of predicted and measured root flap angle UH-60A Black Hawk using airloads measured in flight test; $C_W/\sigma = 0.0783$, high-speed $\mu = 0.368$**

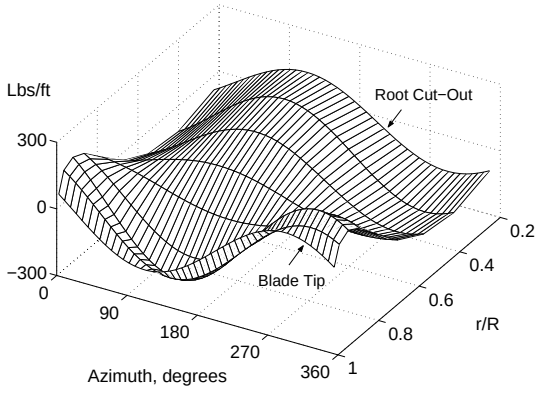

(a) Measured 1/rev Normal Force

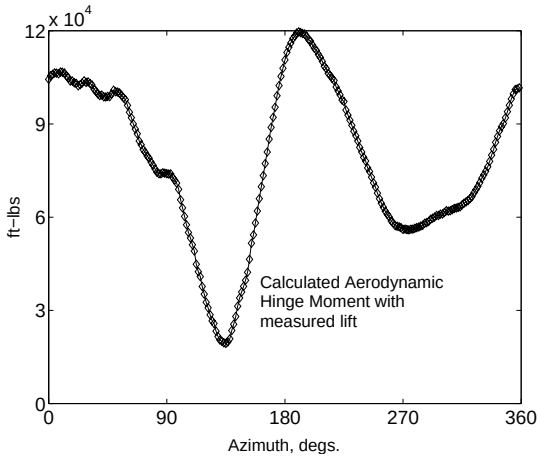

(b) Aerodynamic flap hinge moment

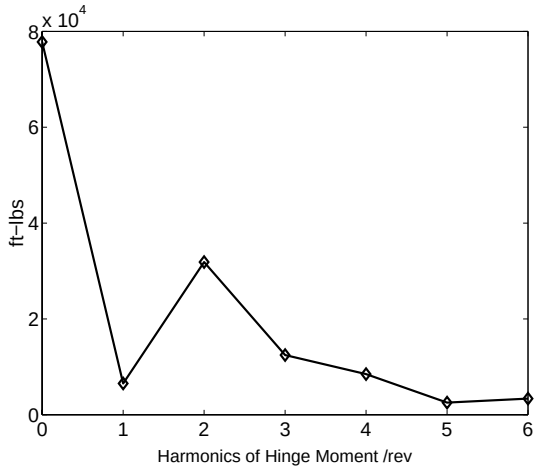

(c) Magnitude of root flap moment harmonics

(d) Phase of root flap moment harmonics

Figure 2.6: **Aerodynamic flap-moment at hinge for the UH-60A Black Hawk using airloads measured in flight test; $C_W/\sigma = 0.0783$, high-speed $\mu = 0.368$**

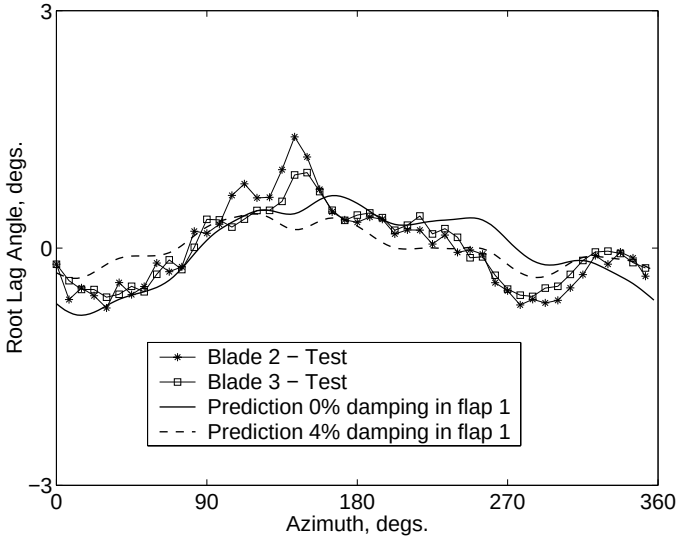

(a) Root lag angle

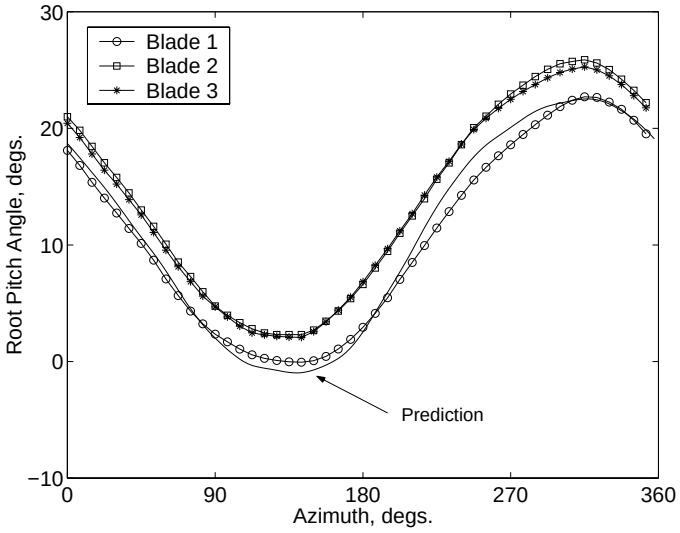

(b) Root pitch angle

Figure 2.7: **Predicted and measured root lag and pitch bearing angle for UH-60A Black Hawk using airloads measured in flight test; C_W/σ = 0.0783, high-speed μ = 0.368**

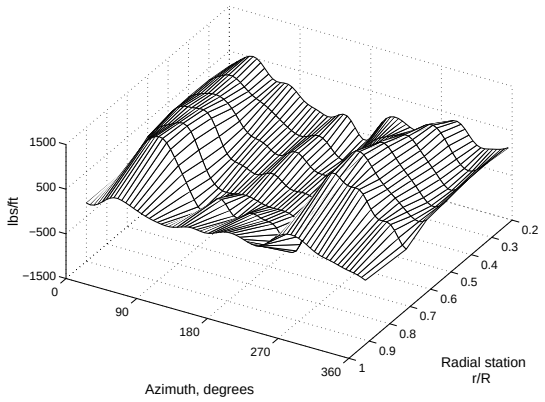

(a) Measured flap bending moment (1-10/rev)

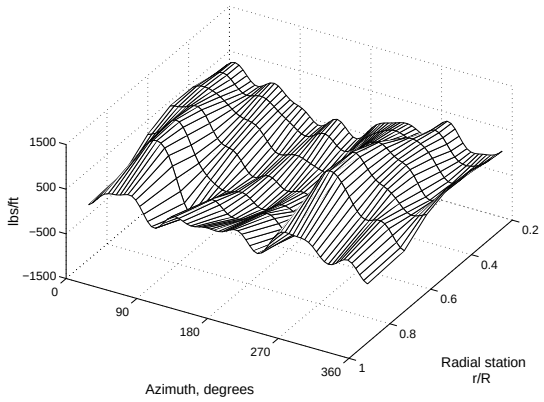

(b) Predicted flap bending moment (1-10/rev)

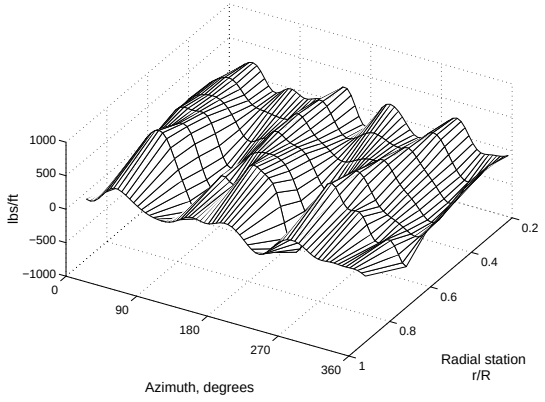

(c) Measured vibratory flap bending moment (3-10/rev)

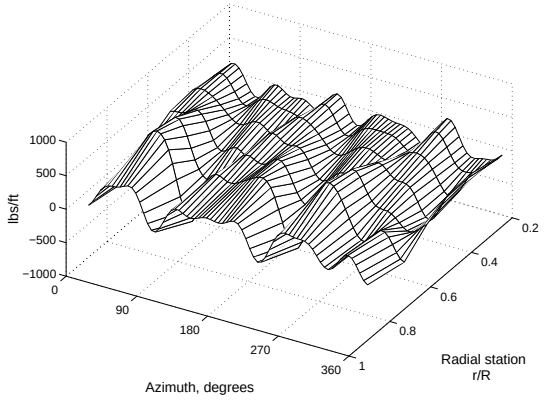

(d) Predicted vibratory flap bending moment (3-10/rev)

Figure 2.8: **Predicted and measured span-wise flap bending moment distribution for UH-60A Black Hawk using airloads measured in flight test; C_W/σ = 0.0783, high-speed μ = 0.368**

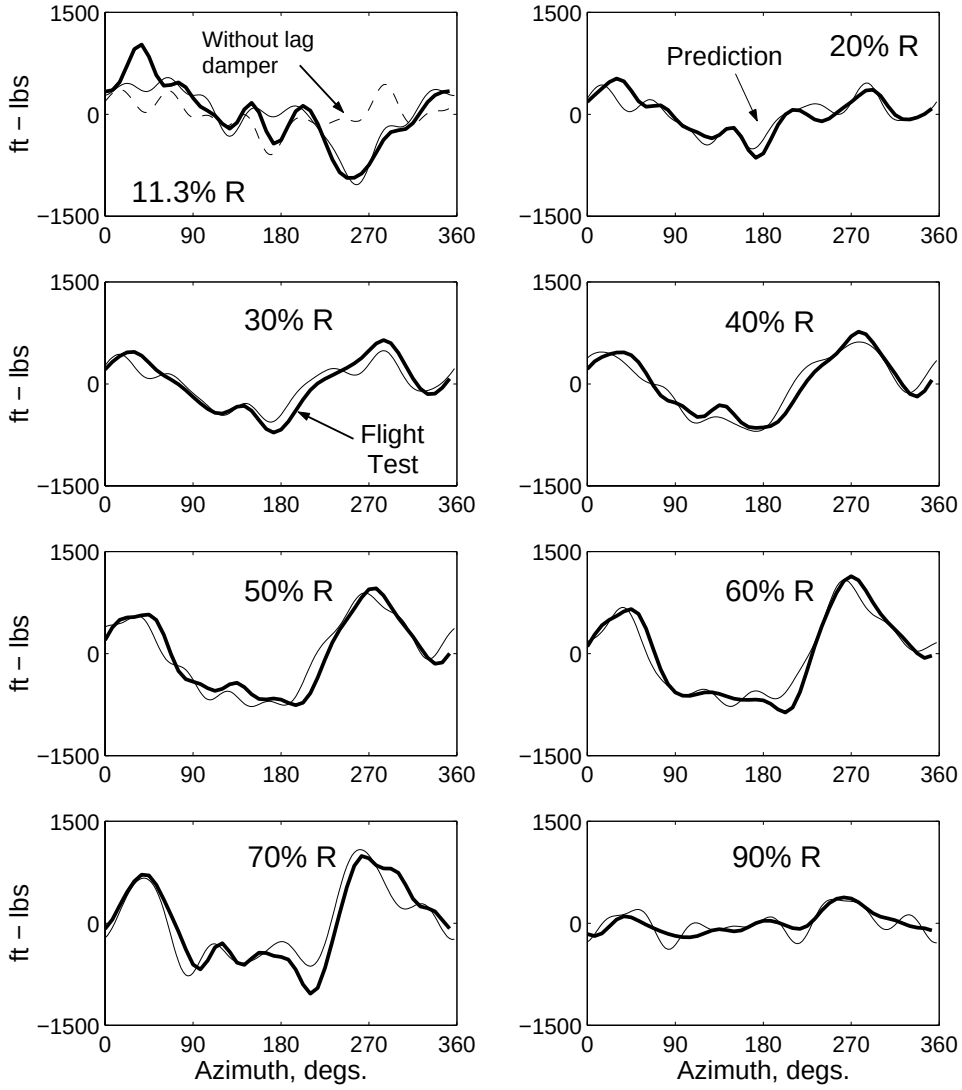

Figure 2.9: **Predicted and measured flap bending moments compared at eight radial stations using airloads measured in flight test; UH-60A Black Hawk $C_W/\sigma = 0.0783$, high-speed $\mu = 0.368$**

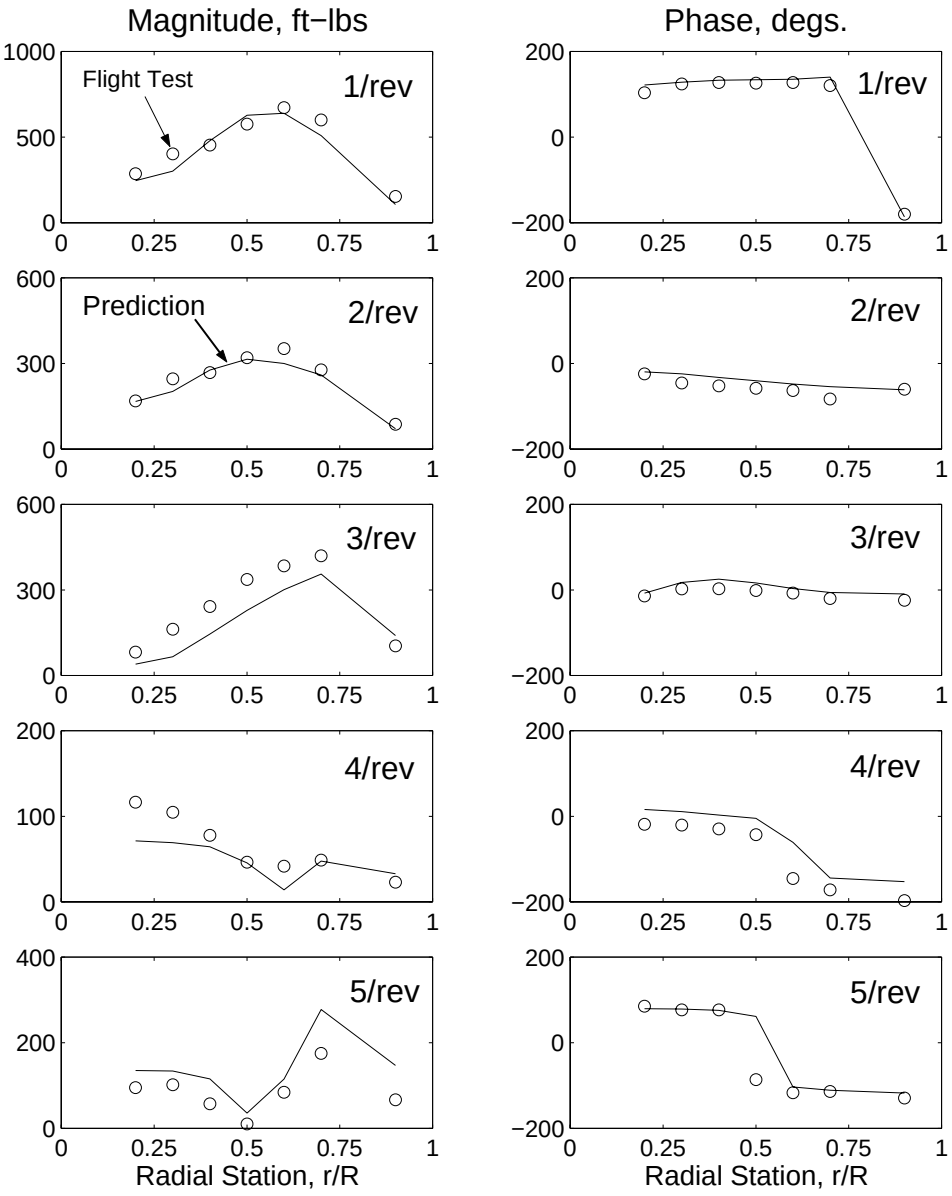

Figure 2.10: **Predicted and measured harmonics of flap bending moment for UH-60A Black Hawk using airloads measured in flight test; $C_W/\sigma = 0.0783$, high-speed $\mu = 0.368$**

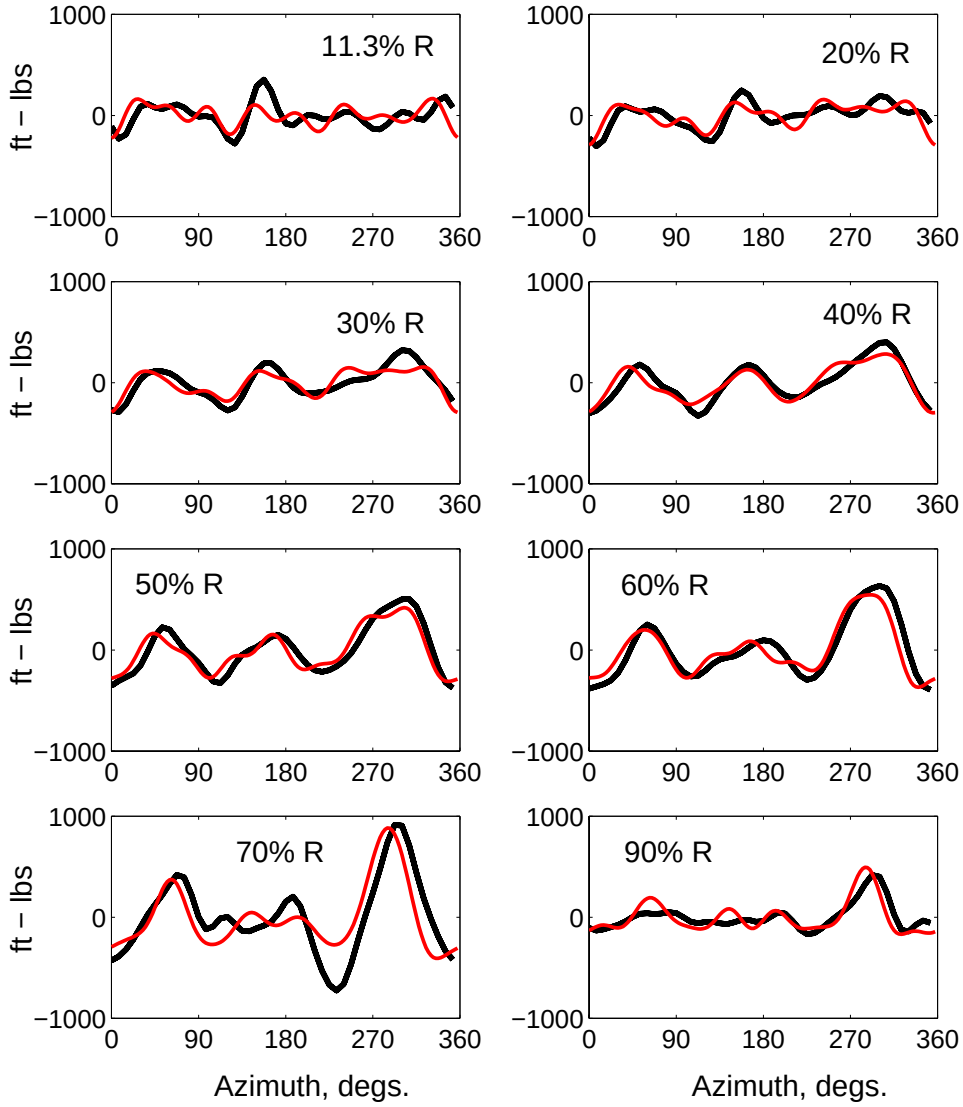

Figure 2.11: **Predicted and measured flap bending moments compared at eight radial stations using airloads measured in flight test; UH-60A Black Hawk $C_W/\sigma = 0.0782$, transition speed $\mu = 0.110$**

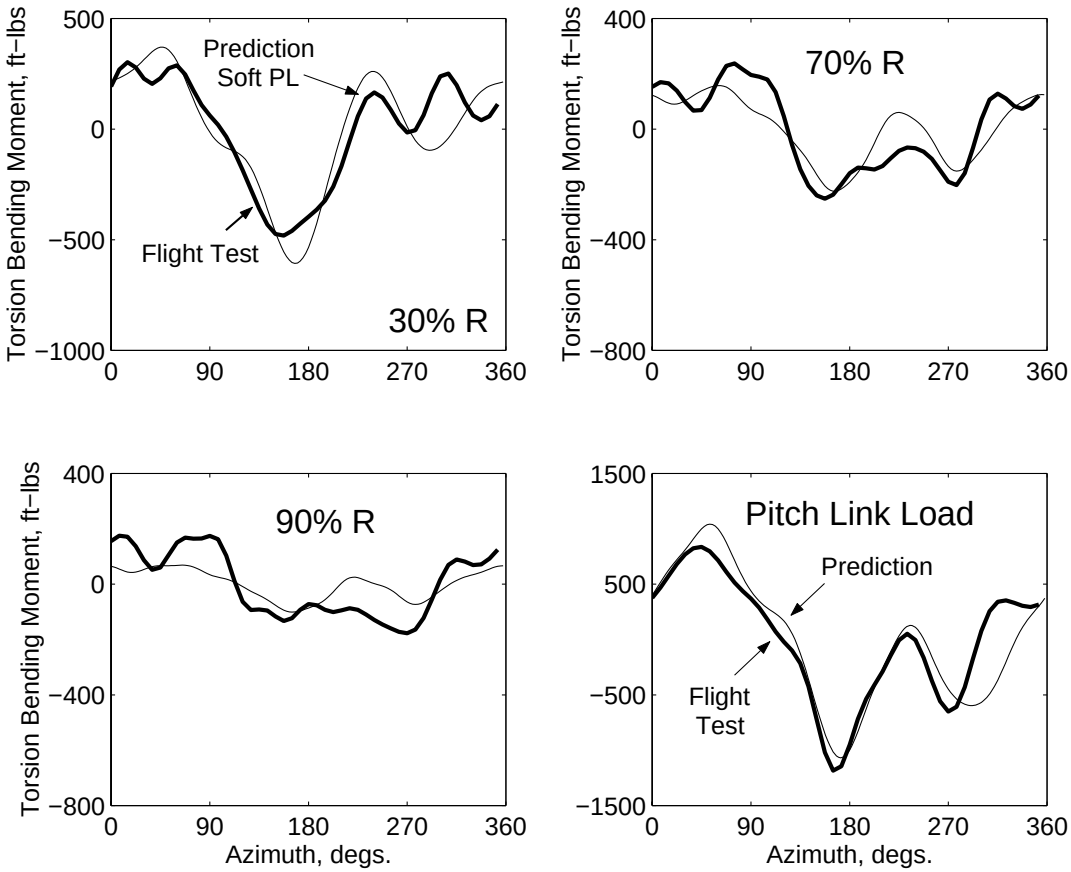

Figure 2.12: **Predicted and measured torsion bending moments and pitch link load for UH-60A Black Hawk using airloads measured in flight test; $C_W/\sigma = 0.0783$, high-speed $\mu = 0.368$**

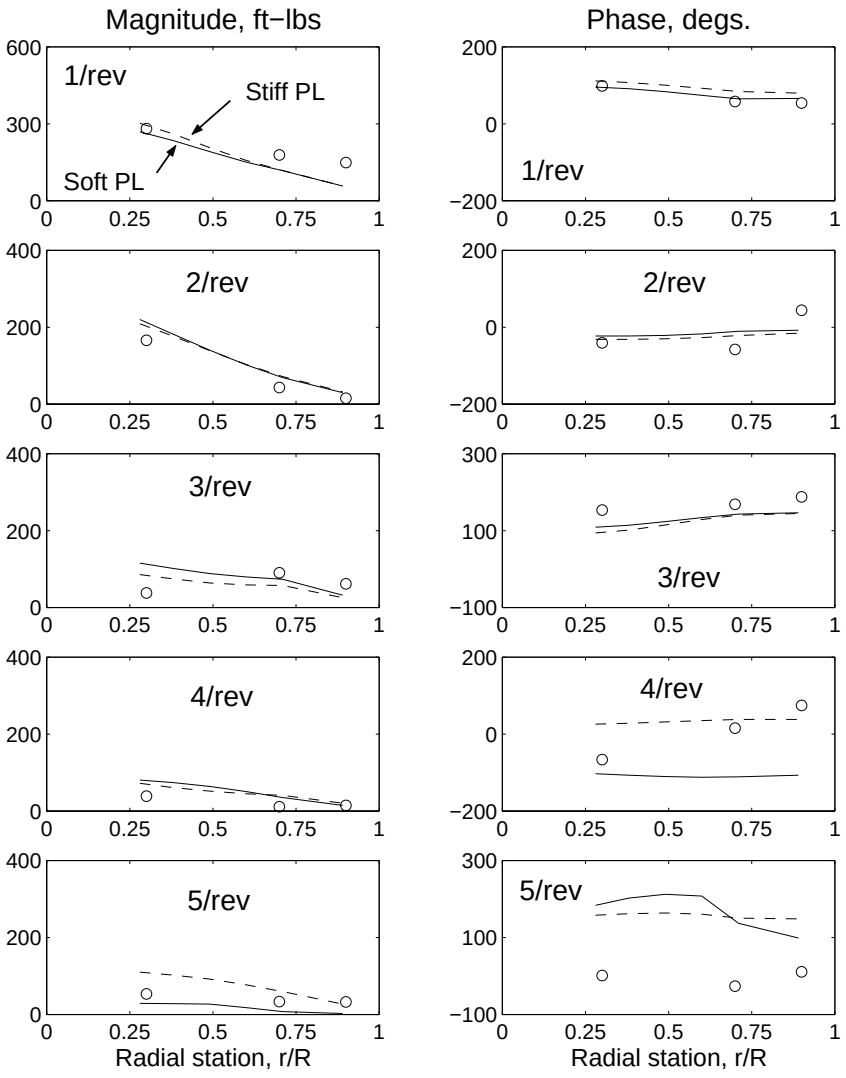

Figure 2.13: **Predicted and measured torsion bending moment harmonics for UH-60A Black Hawk using airloads measured in flight test; $C_W/\sigma = 0.0783$, high-speed $\mu = 0.368$**

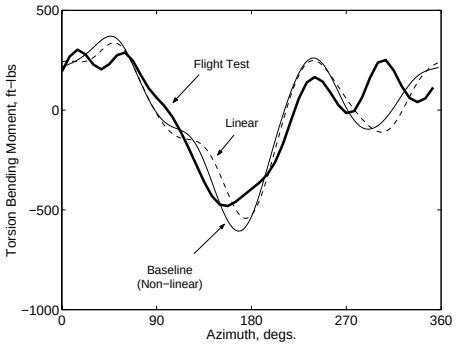

(a) Effect of nonlinear coupling

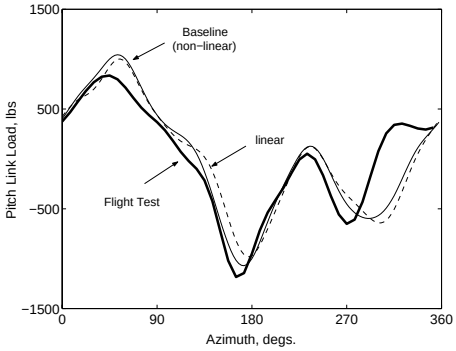

(b) Effect of nonlinear coupling

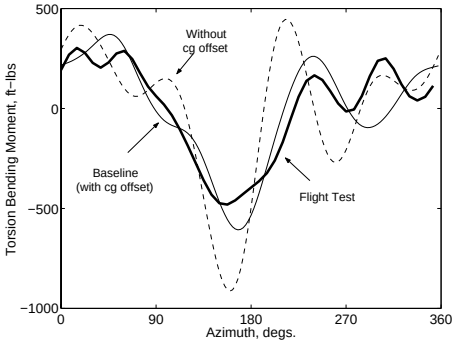

(c) Effect of section cg offset

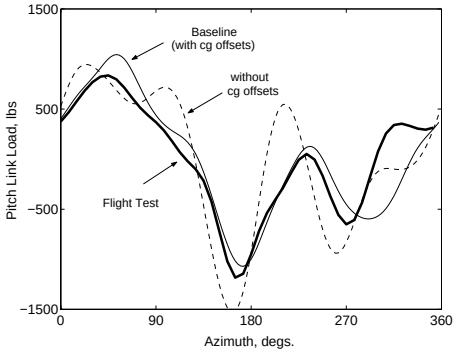

(d) Effect of section cg offset

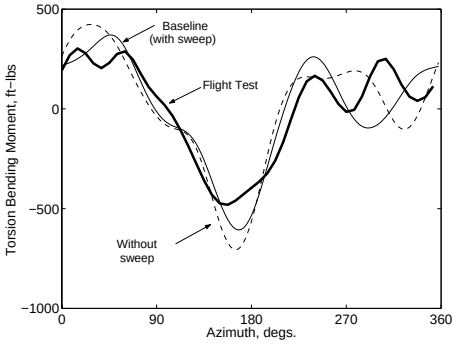

(e) Effect of blade sweep

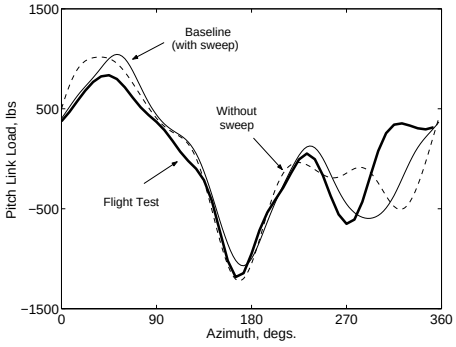

(f) Effect of blade sweep

Figure 2.14: **Effect of structual couplings on predicted torsion bending using measured air loads and damper loads; $\mu = 0.368$, $C_W/\sigma = 0.0783$**

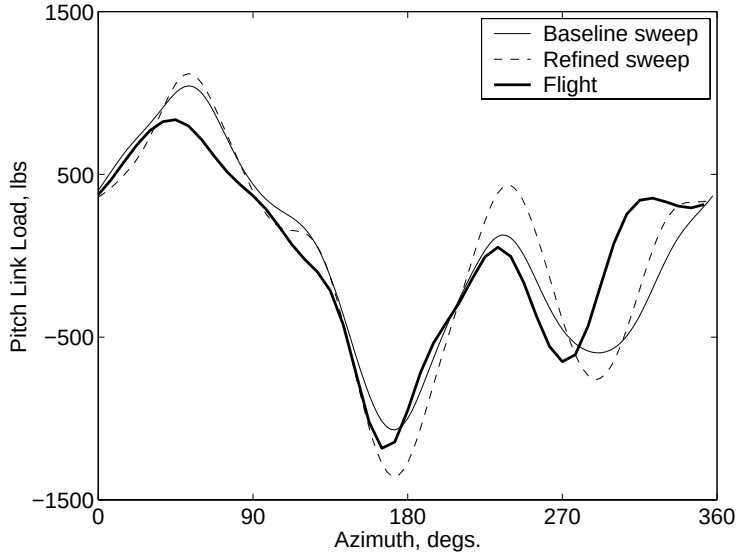

(a) Effect of refined structural sweep on pitch link load

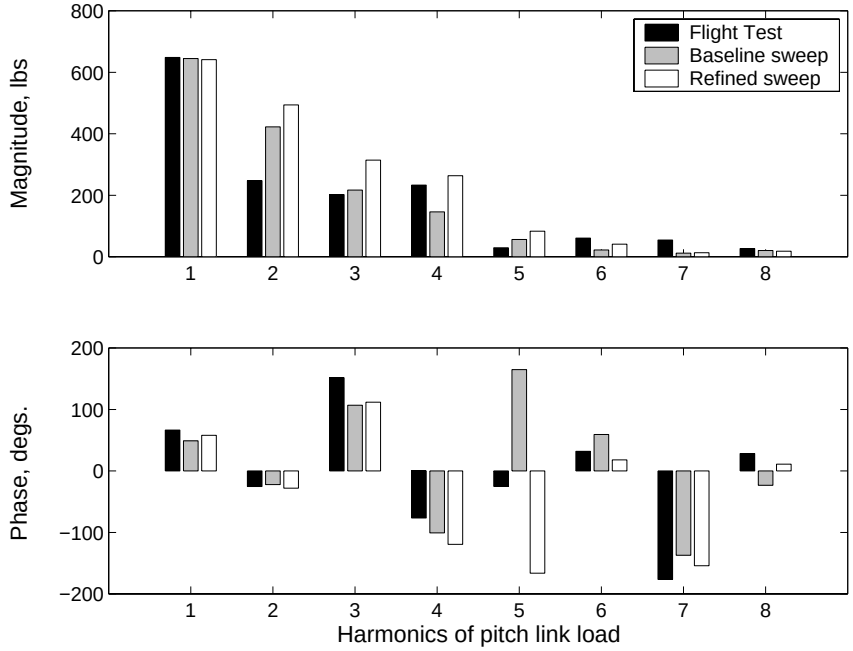

(b) Effect of refined structural sweep on pitch link load harmonics

Figure 2.15: **Effect of refined structural sweep model on pitch link load using measured air loads and damper loads; $\mu = 0.368$, $C_W/\sigma = 0.0783$**

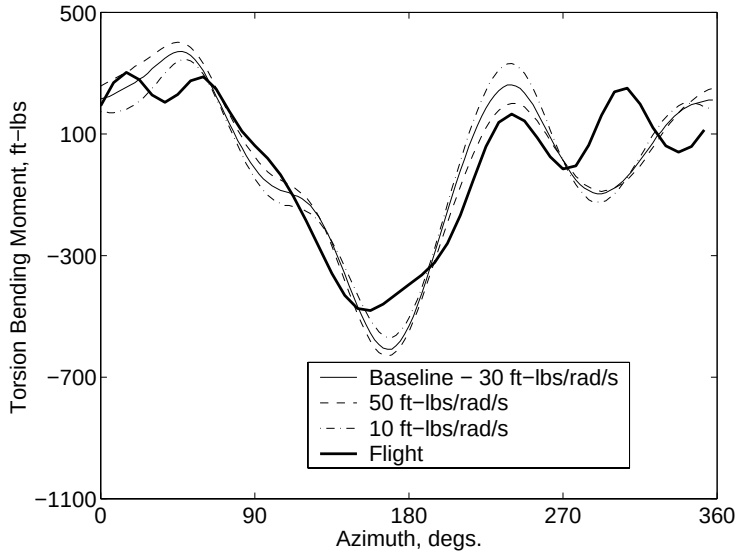

(a) Torsion bending moment at 30% R

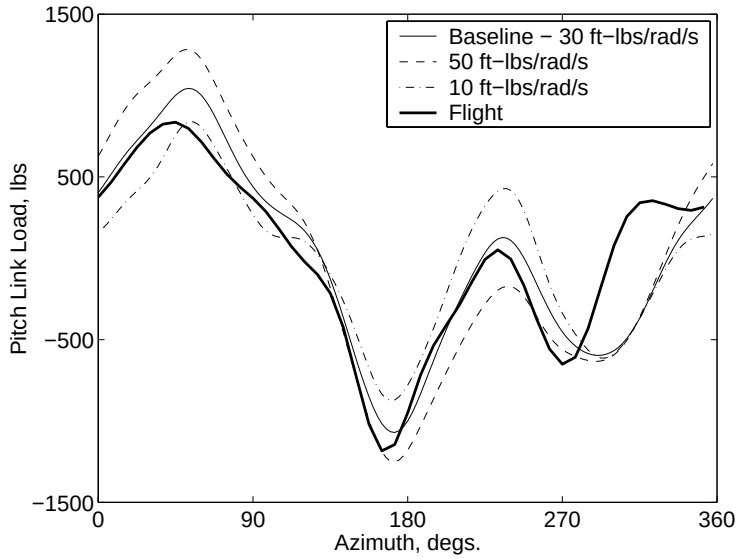

(b) Pitch Link load

Figure 2.16: **Effect of pitch bearing damping on torsion bending moment and pitch link load; $\mu = 0.368$, $C_W/\sigma = 0.0783$**

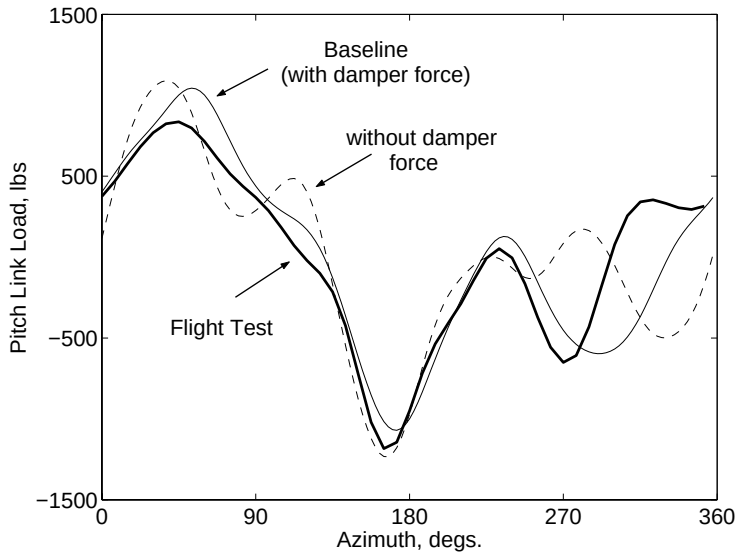

Figure 2.17: **Effect of lag damper force on pitch link load; μ = 0.368, C_W/σ = 0.0783; soft pitch link**

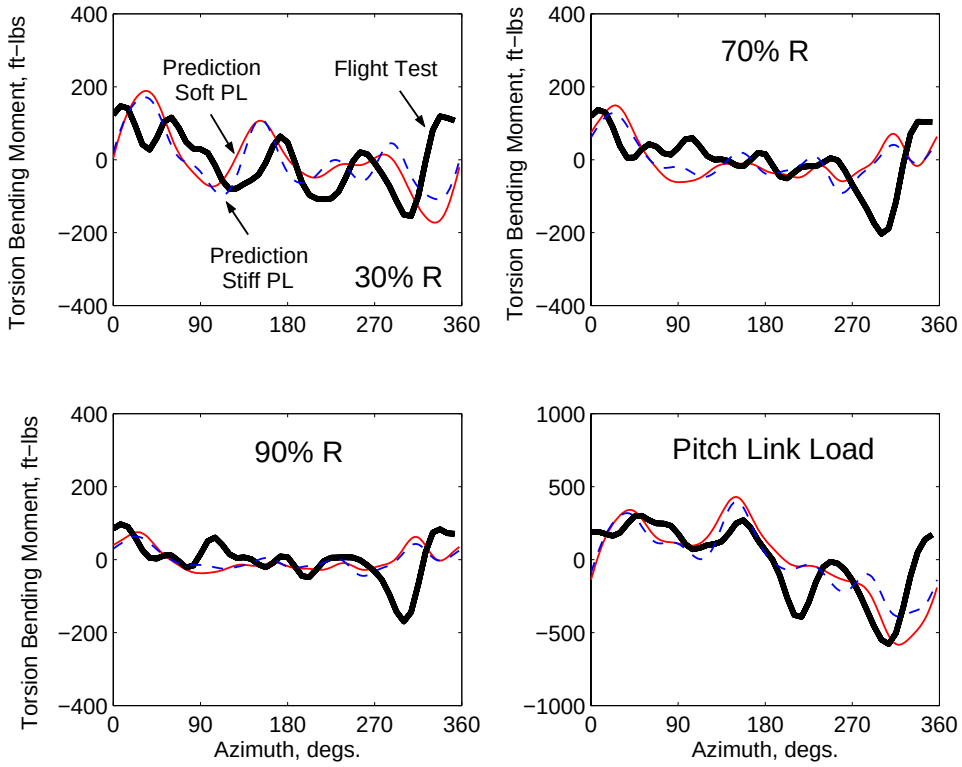

Figure 2.18: **Predicted and measured torsion bending moments and pitch-link load using airloads measured in flight test; UH-60A Black Hawk $C_W/\sigma = 0.0782$, transition speed $\mu = 0.110$**

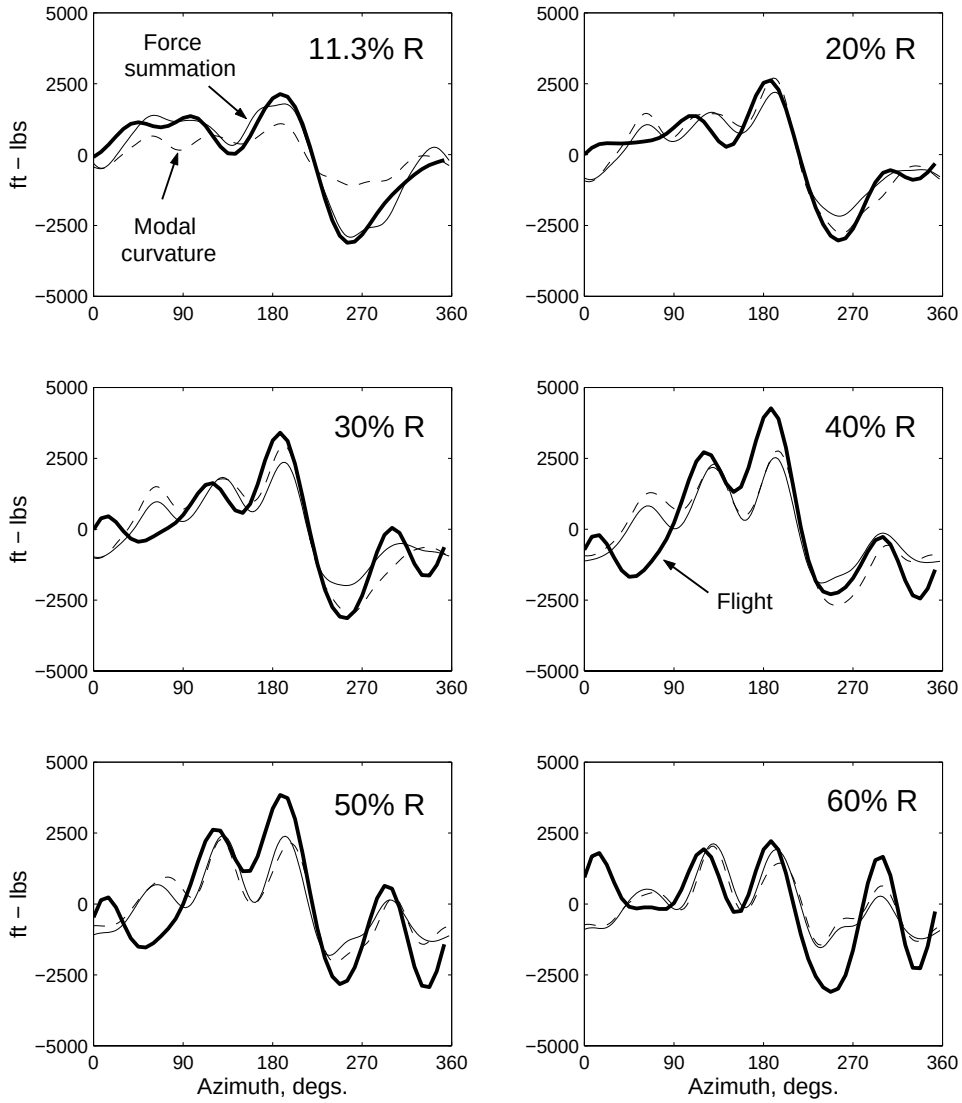

Figure 2.19: **Predicted and measured chord bending moments for UH-60A Black Hawk using measured air loads and damper load; $C_W/\sigma = 0.0783$, high-speed $\mu = 0.368$**

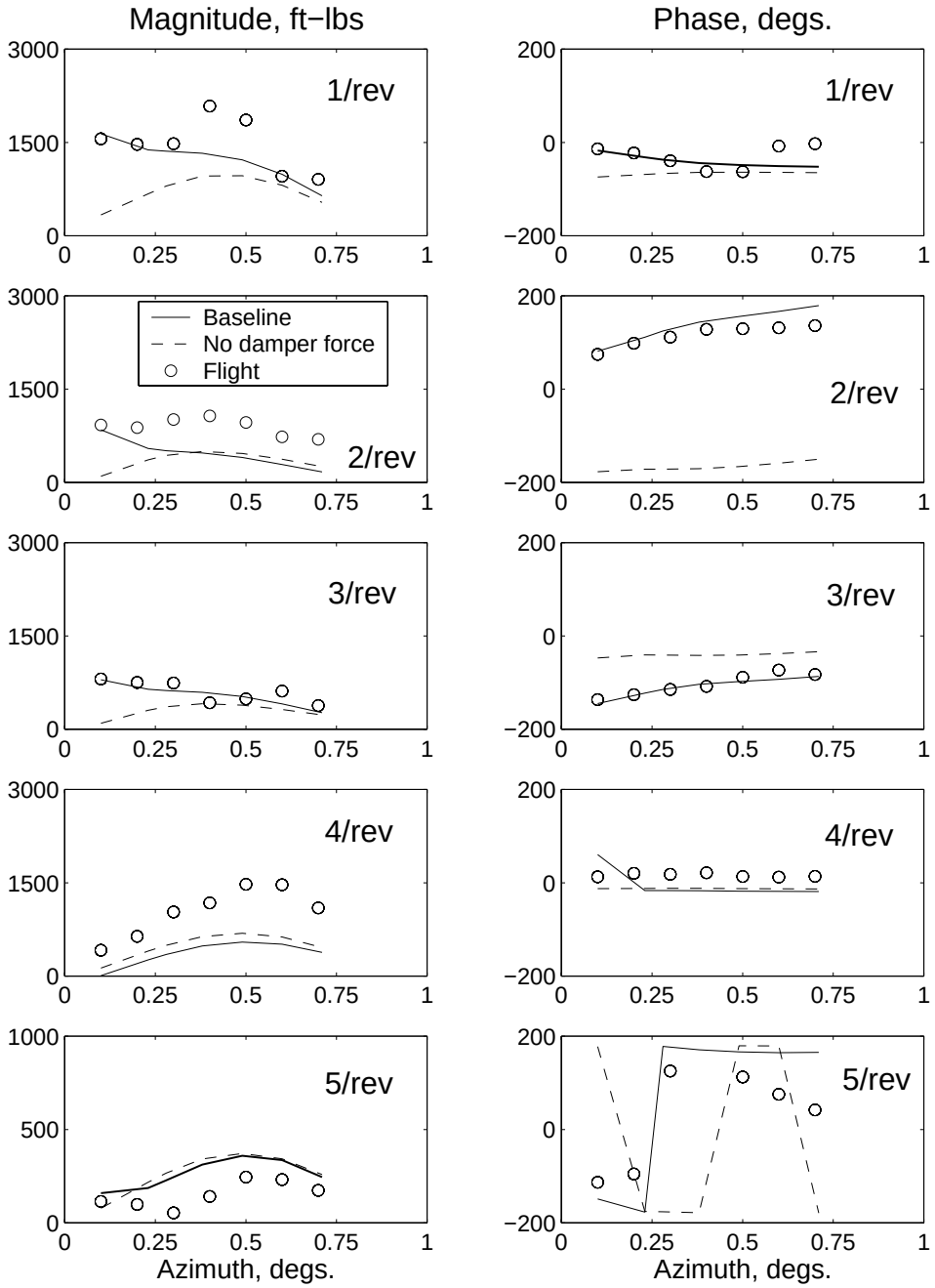

Figure 2.20: **Predicted and measured chord bending moment harmonics for UH-60A Black Hawk using measured air loads and damper load; C_W/σ = 0.0783, high-speed μ = 0.368**

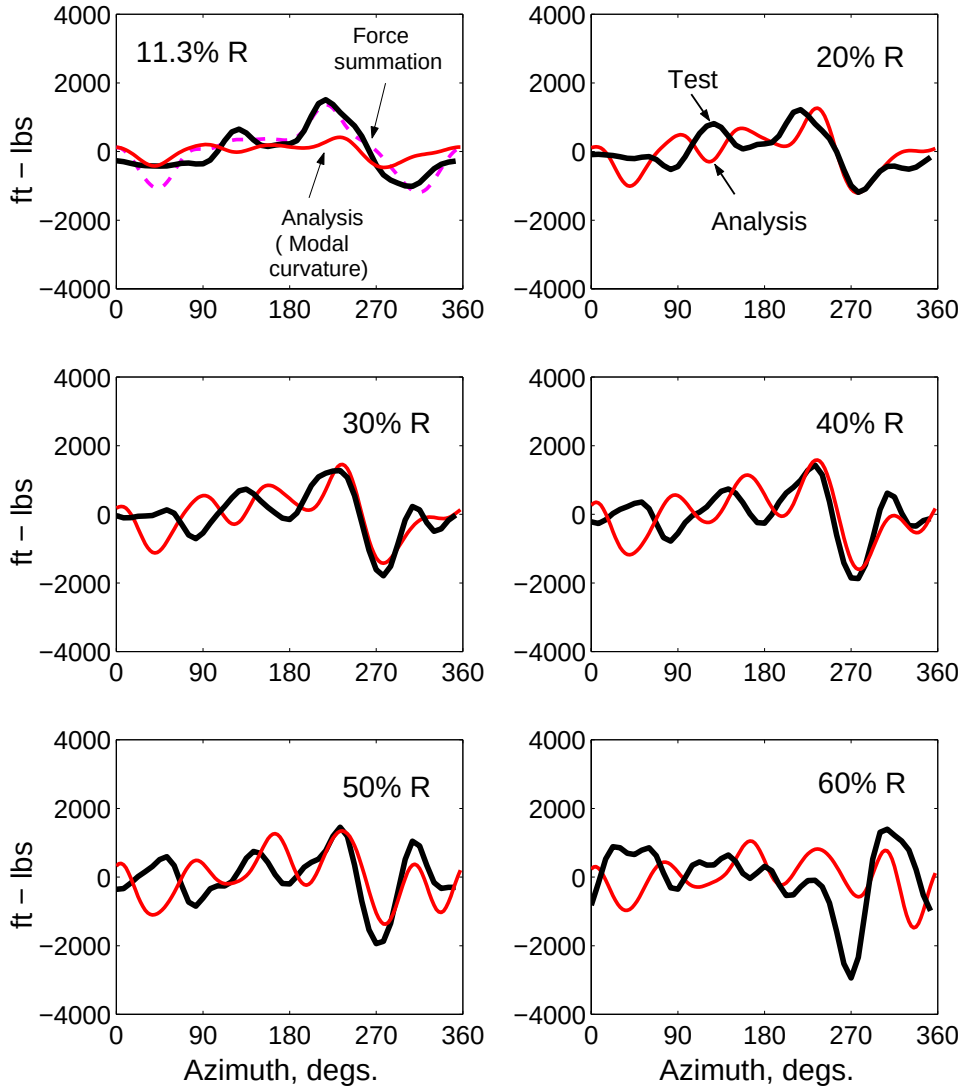

Figure 2.21: **Predicted and measured chord bending moments using airloads measured in flight test; UH-60A Black Hawk $C_W/\sigma = 0.0782$, transition speed $\mu = 0.110$**

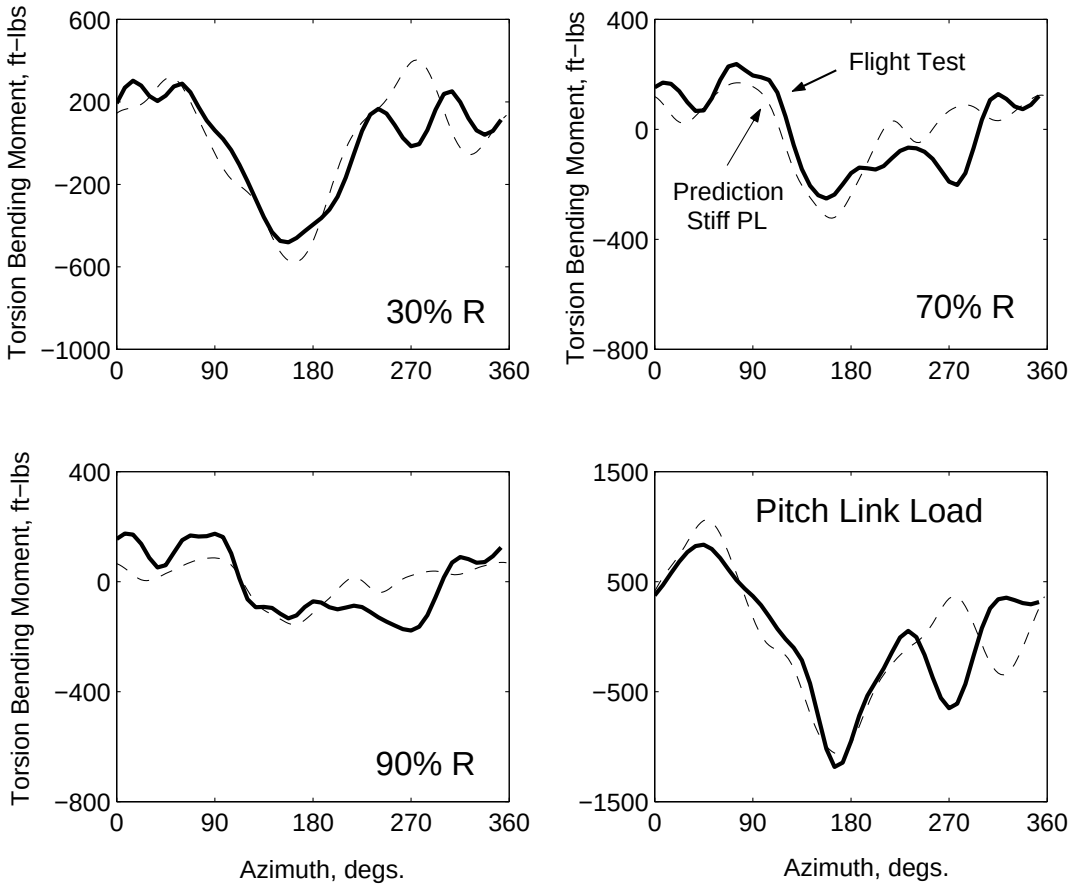

Figure 2.22: **Predicted and measured torsion bending moments and pitch link load for UH-60A Black Hawk using airloads measured in flight test; $C_W/\sigma = 0.0783$, high-speed $\mu = 0.368$, stiff pitch link, no damper force**

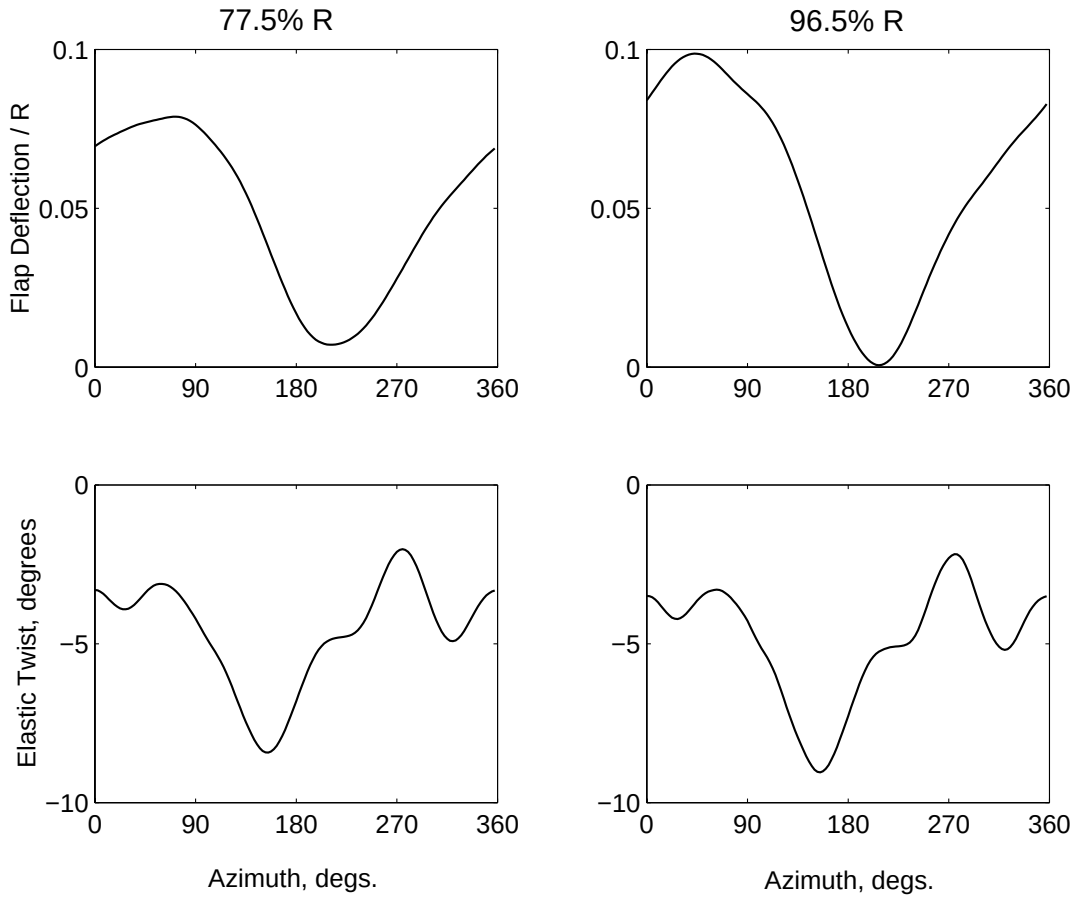

Figure 2.23: **Predicted flap and elastic torsion deformations using measured airloads; $C_W/\sigma = 0.0783$, high-speed $\mu = 0.368$, stiff pitch link, no damper force**

Chapter 3

Aerodynamic Model of Rotor Blades

This chapter describes and validates the aerodynamic model of UH-60A rotor blades. Two types of models are evaluated - 1. A lifting-line model and 2. A 3-D CFD Navier Stokes model. For both models, the same set of *prescribed blade deformations* are used. The *prescribed blade deformations* were obtained in Chapter 2 and represent a reasonably accurate set of blade deformations corresponding to the high-speed flight condition.

The CFD analyses used in the present study, TURNS-3D, is described in References [116, 117]. It is used here as part of the collaborative effort with the CFD group. In the present thesis, the focus is on a lifting-line model, its successive refinements, and comparison with calculations from CFD. The goal is to gain fundamental

understanding of the aerodynamic mechanisms behind the generation of vibratory lift. For all comparisons between the CFD and lifting-line models two sets of inputs are common: (1) the *prescribed blade deformations* and which are held fixed for all aerodynamic models and (2) the far wake strength and geometry. The CFD calculations use a single blade simulation and therefore does not capture the far wake. The far wake strength and geometry are obtained from the lifting-line model. any refinements in the far wake included in the lifting-line model, corresponding calculations using CFD are performed.

This study establishes, along with Chapter 2, that the technical barriers described in Chapter 1, namely, the advancing blade lift phase, vibratory lift, aerodynamic pitching moments and torsion loads, stem from inaccurate aerodynamics, not structural dynamics. In addition to this conclusion, the significant outcomes of this exercise are - to understand the limitations of the lifting-line model in a comprehensive rotor analysis (Chapter 4); to understand the benefits of a CFD model and anticipate the improved prediction capabilities of a CFD coupled comprehensive rotor analysis (Chapter 5); and to devise CFD based generic corrections to improve lifting-line aerodynamics (Chapter 5).

The structure of this Chapter is slightly different from Chapter 2. The theory and the results are in general discussed together and are not separated into distinct groups. This is because the focus is on modeling refinements and fundamental understanding. The lifting-surface model is first described, along with successive refinements and their impact on air loads predictions. Next, the CFD model is briefly described. Calculations from CFD are then compared with the lifting-surface

model.

3.1 Lifting-Line Model

The lifting-surface model described in this section combines the following - 1. sectional angle of attack calculation using blade deformations, 2. a Weissinger-L (W-L) type lifting-line near wake model, 3. a refined Bagai-Leishman pseudo-implicit far wake model [49, 162], 4. 2D airfoil property tables and 5. a Leishman-Beddoes 2D unsteady model for attached flow [67, 68]. The attached flow formulation is used because there is no evidence of dynamic stall at high speed level flight condition [163].

For a prescribed set of blade deformations (and control angles), the airloads are calculated using the following three steps. In the first step, the deformations and a uniform inflow based on the measured thrust are used to calculate the sectional angle of attack. The sectional angle of attack and the incident normal Mach number are used to calculate sectional lift and pitching moment coefficients using the 2D airfoil tables. From the lift, the bound circulation strengths are calculated using 2D Kutta-Joukowski theorem.

In the second step, the bound circulation strengths are used to calculate the rotor far wake (free or prescribed). The baseline wake model is a single fully rolled-up free tip vortex model. The far wake generates a refined non-uniform inflow distribution. Using the non-uniform inflow, the sectional angles of attack are re-calculated.

In the third step, the new angles of attack are used as input to the W-L near

wake model to re-calculate the bound circulation strengths. An iterative procedure is now performed between the near wake and far wake models. Iterations are required because the bound circulation strengths calculated by the near wake model changes the far wake inflow which changes the input angle of attack distribution of the near wake model. The end result of the iterative procedure is to have a converged set of bound circulation strengths that are consistent with near wake and far wake. In addition, the bound circulation strengths are also consistent with air-foil tables and a modified Kutta-Joukowski theorem that accounts for three dimensional effects. The procedure is described in detail in the section on Weissinger-L model.

3.1.1 Section Angle of Attack

The angle of attack of a blade section consists of two components; the wind velocity and the blade velocity. The general expression for the resultant velocity at a radial station x in the rotating undeformed frame is

$$\bar{V} = -\bar{V}_w + \bar{V}_b \tag{3.1}$$

where $\bar{V}_w$ is the wind velocity with contributions from the vehicle forward speed and the rotor inflow and $\bar{V}_b$ is the blade velocity relative to the hub fixed frame resulting from blade rotation and blade motion. The expression for the wind velocity is given

by

$$\bar{V}_w = \begin{bmatrix} \mu\Omega R & 0 & -\lambda\Omega R \end{bmatrix} \begin{Bmatrix} \hat{I_H} \\ \hat{J_H} \\ \hat{K_H} \end{Bmatrix}$$

$$= \begin{bmatrix} \mu\Omega R & 0 & -\lambda\Omega R \end{bmatrix} \mathbf{T_{RH}}^{\mathbf{T}} \mathbf{T_{UR}}^{\mathbf{T}} \begin{Bmatrix} \hat{i} \\ \hat{j} \\ \hat{k} \end{Bmatrix} \tag{3.2}$$

$$= \begin{bmatrix} V_{wx} & V_{wy} & V_{wz} \end{bmatrix} \begin{Bmatrix} \hat{i} \\ \hat{j} \\ \hat{k} \end{Bmatrix}$$

where

$$\frac{V_{wx}}{\Omega R} = \mu \cos\psi \cos\beta_p - \lambda \sin\beta_p \tag{3.3}$$

$$\frac{V_{wy}}{\Omega R} = -\mu \sin\psi \tag{3.4}$$

$$\frac{V_{wz}}{\Omega R} = -\mu \cos\psi \sin\beta_p - \lambda \cos\beta_p \tag{3.5}$$

$\mu = V\cos\alpha_s/\Omega R$ is the rotor advance ratio; V is the vehicle forward speed; α_s is the rotor shaft tilt, positive forward; λ is the rotor non-dimensional inflow; and ΩR is the rotor tip speed. The blade velocities V_{bx}, V_{by} and V_{bz} are given in equations (2.74),(2.75) and (2.76). The angle of attack is calculated at the three-quarter chord location ($\eta = \eta_r$ and $\zeta = 0$). Using equations (2.84) and (2.69) in V_{bx}, V_{by} and V_{bz}

we have the following.

$$\left.\begin{aligned} V_{bx} &= \dot{u} - \lambda_T \dot{\hat{\phi}}' - (\dot{v}' + w'\dot{\theta}_1)\eta_r cos\theta_1 - (\dot{w}' - v'\dot{\theta}_1)\eta_r sin\theta_1 - (v + \eta_r cos\theta_1) \\ V_{by} &= \dot{v} - th\dot{e}ta_1\eta_r sin\theta_1 + x + u - v'\eta_r cos\theta_1 - w'\eta_r sin\theta_1 - \beta_p(w + \eta_r sin\theta_1) \\ V_{bz} &= \dot{w} + th\dot{e}ta_1\eta_r cos\theta_1 + \beta_p(v + \eta_r cos\theta_1) \end{aligned}\right\} \tag{3.6}$$

The resultant blade velocity at a radial station x can be written in rotating undeformed coordinate system as

$$\begin{aligned} \bar{V} &= U_x\hat{i} + U_y\hat{j} + U_z\hat{k} \\ &= (V_{bx} - V_{wx})\hat{i} + (V_{by} - V_{wy})\hat{j} + (V_{bz} - V_{wz})\hat{k} \end{aligned} \tag{3.7}$$

The blade section loads are calculated using the resultant velocity and aerodynamic angle of attack in the deformed blade.

$$\left\{\begin{array}{c} U_R \\ U_T \\ U_P \end{array}\right\} = \mathbf{T_{DU}} \left\{\begin{array}{c} U_x \\ U_y \\ U_z \end{array}\right\} \tag{3.8}$$

Finally, we have

$$\bar{V} = U_R\hat{i_\xi} + U_T\hat{j_\eta} + U_P\hat{k_\zeta} \tag{3.9}$$

where

$$\begin{aligned} \frac{U_R}{\Omega R} = \dot{-}v &+ v'(x + \mu sin\psi) - \mu cos\psi(1 - \beta_p w') + \lambda(\beta_p + w') \\ &- \eta_r cos\theta_0(1 + \dot{v}') + \eta_r sin\theta_0(\dot{\hat{\phi}} - \dot{w}') \\ &+ v'\dot{v} + w'\dot{w} + \frac{1}{2}\mu cos\psi(v'^2 + w'^2) \end{aligned} \tag{3.10}$$

$$
\begin{aligned}
\frac{U_T}{\Omega R} &= [\dot{v} + u - w\beta_p + \hat{\phi}(\lambda + \dot{w}) + v'v + (x + \mu sin\psi)(1 - \frac{v'^2}{2}) \\
&\quad + \mu cos\psi v' + \hat{\phi}(\beta_p + w')]cos\theta_0 + \\
&\quad [\dot{w} + \lambda + v(\beta_p + w') - \hat{\phi}\dot{v} - (x + \mu sin\psi)(v'w' + \hat{\phi}) \\
&\quad \mu cos\psi(w' + \beta_p - \hat{\phi}v')]sin\theta_0 \\
\frac{U_P}{\Omega R} &= [\dot{w} + \lambda + \beta_p v + vw' + \mu cos\psi(\beta_p + w' - \hat{\phi}v') \\
&\quad - (x + \mu sin\psi)(v'w' + \hat{\phi})]cos\theta_0 \\
&\quad [-\dot{-}u - vv' + w\beta_p - \hat{\phi}(\dot{w} + \lambda) - \mu cos\psi(v' + \hat{\phi}(\beta_p + w')) \\
&\quad - (x + \mu sin\psi)(1 - \frac{v'^2}{2})]sin\theta_0 \\
&\quad \eta_r(\dot{\theta_0} + \dot{\hat{\phi}} + w' + \beta_p)
\end{aligned}
\tag{3.11, 3.12}
$$

The angle of attack α, yaw angle Γ and incident Mach number M are given by

$$
\left.
\begin{aligned}
\alpha &\approx -\tfrac{U_P}{U_T} \\
\Gamma &\approx \tfrac{U_R}{U_T} \\
M &= M_{tip}\sqrt{U_P^2 + U_T^2}
\end{aligned}
\right\}
\tag{3.13}
$$

For a given angle of attack and Mach number, the airfoil properties are read from the tables. The normal force, chord force and quarter chord pitching moment (which are in the same frame as the flight test data) and the axial force in the non-dimensional form are given by

$$
\left.
\begin{aligned}
\bar{L}_w &= \tfrac{\gamma \bar{V}^2}{6a}(C_l cos\alpha + C_d sin\alpha) \\
\bar{L}_v &= \tfrac{\gamma \bar{V}^2}{6a}(C_l sin\alpha - C_d cos\alpha) \\
\bar{M}_{\hat{\phi}} &= \tfrac{\gamma \bar{V}^2}{6a}\tfrac{c}{R}C_m \\
\bar{L}_u &= -\tfrac{\gamma \bar{V}^2}{6a}C_d sin\Gamma
\end{aligned}
\right\}
\tag{3.14}
$$

where L_w, L_v, L_u are non-dimensionalized with respect to $m_0\Omega^2 R$ and $M_{\hat{\phi}}$ with respect to $m_0\Omega^2 R^2$. $\bar{V}$ is the resultant velocity $\sqrt{U_P^2 + U_T^2}$ nondimensionalized with respect to ΩR. γ is the Lock Number, $\gamma = \frac{\rho a c R^4}{I_b}$, and flap inertia, $I_b = \frac{m_0 R^3}{3}$.

For comprehensive analysis (Chapter 4) the air load expressions are further manipulated for convenience as follows. First the aerodynamic coefficients are expressed in the following form.

$$C_l = c_0 + c_1\alpha \tag{3.15}$$

$$C_d = d_0 + d_1\alpha + d_2\alpha^2 \tag{3.16}$$

$$C_m = f_0 + f_1\alpha = c_{mac} + f_1\alpha \tag{3.17}$$

Then using equations (3.13) and (3.14) the following expressions are obtained.

$$\bar{L}_w = \frac{\gamma}{6a}(c_0 {U_T}^2 - (c_1 + d_0)U_T U_P + d_1|U_P|U_P) \tag{3.18}$$

$$\bar{L}_v = \frac{\gamma}{6a}(-d_0 {U_T}^2 - (c_0 U_P - d_1|U_P|)U_T + (c_1 - d_2 {U_P}^2) \tag{3.19}$$

$$\bar{L}_u = \frac{\gamma}{6a}(-d_0 U_R U_T) \tag{3.20}$$

$$\bar{M}_{\hat{\phi}} = \frac{\gamma}{6a}(\frac{c}{R}(c_{mac}({U_T}^2 + {U_P}^2) - f_1 U_T U_P)) \tag{3.21}$$

The aerodynamic forces in the undeformed frame are obtained by

$$\begin{Bmatrix} L_U^A \\ L_V^A \\ L_W^A \end{Bmatrix} = \mathbf{T_{DU}}^{\mathbf{T}} \begin{Bmatrix} \bar{L}_U \\ \bar{L}_V \\ \bar{L}_W \end{Bmatrix} \tag{3.22}$$

$$M_{\hat{\phi}}^A \approx \bar{M}\phi \tag{3.23}$$

The above expressions show the circulatory air loads. The non-circulatory loads are incorporated using impulsive terms of the unsteady model discussed later.

3.1.2 Weissinger-L model

The Weissinger-L (W-L) near wake model [164] is used at each azimuth location. For a given radial distribution of angle of attack (*input angle of attack*) it calculates the radial distribution of bound circulation strengths.

The W-L model is essentially a lifting-surface model with only one chord-wise element. It has been shown to give equally good predictions compared to panel methods with several chord-wise elements [44, 165]. The W-L model represents blade lift using a series of spanwise horseshoe vortex elements. The bound circulation is located at the 1/4-chord point. The flow tangency condition is imposed at the 3/4-chord point. This is consistent with the unsteady thin airfoil model [66]. The W-L model predicts improved loading for fixed wings with arbitrary planforms [166]. It is equivalent to a non-linear lifting-line theory as discussed in Ref [167].

The blade surface is divided into N aerodynamic segments. In the present calculations N of 26 is used. For the $i-th$ segment the flow tangency can be written as

$$\begin{aligned} V_{b_i} &= V_{\infty_i}\alpha_{e_i} \\ &= V_{\infty_i}(\alpha_i - \phi_{NW_i}) \\ &= V_{\infty_i}\alpha_i - V_{NW_i} \end{aligned} \tag{3.24}$$

where V_{b_i} is the bound vortex induced velocity at the $i-th$ control point and V_{∞_i} is the incident free stream velocity at the control point. α_{e_i} is the *effective angle of attack* at the section. The *effective angle of attack* is obtained by subtracting the near wake *induced angle of attack* from the *input angle of attack*. The later includes

the effect of blade deformation and far wake inflow. V_{NW_i} is the velocity induced by the nearwake at the $i-th$ control point.

The velocities V_{b_i} and V_{NW_i} are related to the strength of the bound vortices, Γ_i through influence coefficient matrices. These matrices depend both on the blade deformations and on the blade geometry e.g., rigid twist, control angles, planform, sweep etc.

$$V_{b_i} = \sum_{j=1}^{N} I_{b_{i,j}} \Gamma_j \tag{3.25}$$

$$V_{NW_i} = \sum_{j=1}^{N} I_{NW_{i,j}} \Gamma_j \tag{3.26}$$

The linear algebraic governing equations for bound circulation (N equations, N unknowns) are thus obtained as

$$\sum_{j=1}^{N} \left\{ I_{b_{i,j}} + I_{NW_{i,j}} \right\} \Gamma_j = V_{\infty_i} \alpha_i \tag{3.27}$$

Once the bound circulation strengths, Γ_j are known they are used to calculate α_{e_i} using equations (3.26) and (3.24). Assuming thin airfoil theory, i.e., with a lift curve slope of 2π, the local lift coefficient simply becomes

$$\begin{aligned} C_l &= 2\pi \alpha_{e_i} \\ &= \frac{2\pi}{V_{\infty_i}} \sum_{j=1}^{N} I_{b_{i,j}} \end{aligned} \tag{3.28}$$

using equations (3.24) and (3.25). This is the effective angle of attack approach and is consistent with K-J theorem for 3D wings which gives [165]

$$C_l = \frac{2\pi}{V_{\infty_i}} \sum_{j=1}^{N} I_{b_{i,j}} \tag{3.29}$$

In the present analysis, the effective angle of attack approach is used.

The radial distribution of *input angle of attack* is influenced by the far wake (rotor inflow) which in turn is governed by the bound circulation strengths. Therefore, iterations are performed between far wake and near wake until bound circulation strengths are converged. The iterations are started with a uniform inflow far wake (based on helicopter gross weight) which is subsequently replaced with non-uniform inflow.

Within the W-L near wake model, the airfoil property tables are included using the following method. The *input angle of attack* is scaled to an equivalent *flat plate angle of attack* using the lift coefficients obtained from the airfoil tables. This scaled angle of attack is used by the W-L model to calculate bound circulation strengths at 1/4-chord locations. The bound circulation strengths are then used to calculate the circulation strengths of near wake trailers. The near wake trailers are used to estimate the *induced angle of attack* at 3/4-chord locations. This induced angle of attack is subtracted from the *input angle of attack* and the resulting *effective angle of attack* is used to obtain lift (also pitching moment and drag) from the airfoil tables.

3.1.3 2D unsteady model

The 2D unsteady model is the Leishman-Beddoes [67, 68] attached flow formulation. The attached flow formulation is used because test data at the present flight condition show no evidence of dynamic stall [163]. In this formulation, the angle of attack variation over time is discretized as a series of step inputs. The air-

load response to each step input is calculated using semi-empirical indicial response functions. The response depends on the pitch and pitch rate of each step input. The angle of attack contributions from inflow and flap velocities are included in the form of equivalent pitch angles. The resultant unsteady airload at a particular azimuth is calculated using superposition of individual contributions from all step inputs prior to that particular azimuth. The indicial response functions used in the Leishman-Beddoes model have been validated for 2D subsonic flows using experimental data from symmetric airfoils - NACA 0012, Boeing-Vertol V23010-1.58 and NACA 64A010 [67]. In the present study, these indicial models are refined specifically for the two UH-60A cambered airfoils - SC1095 and SC1095 R8.

In-house compressible CFD calculations [116] are used to validate and refine the indicial functions. The refined model is same as the Leishman-Beddoes model, in that the airload response to each step input is assumed to consist of an exponentially decaying impulsive part and an asymptotically increasing circulatory part. For example, the indicial lift response for a step change in angle of attack α and a step change in pitch rate q are described as

$$C_{N_\alpha}(S) = \left[\frac{4}{M}\phi_\alpha^I(S) + C_{N\alpha}\,\phi_\alpha^C(S)\right]\alpha \tag{3.30}$$

$$C_{N_q}(S) = \left[\frac{1}{M}\phi_q^I(S) + \frac{1}{2}C_{N\alpha}\phi_q^C(S)\right]q \tag{3.31}$$

where, M is the section Mach number, S is the distance traveled by the airfoil in semi-chords following the step input, $C_{N\alpha}$ is the local lift curve slope (from airfoil table) and, ϕ_α^I, ϕ_α^C, ϕ_q^I and ϕ_q^C are the indicial functions. The superscripts C and I refer to circulatory and non-circulatory components of the airloads. The circulatory

part is defined as

$$\phi_\alpha^C(S) = 1 - A_1 exp(-b_1\beta^2 S) - A_2 exp(-b_2\beta^2 S) \tag{3.32}$$

with $\phi_q^C = \phi_\alpha^C$. A_1, A_2, b_1, b_2 are constants independent of Mach number and β is the compressibility factor ($\beta = \sqrt{1-M^2}$). The impulsive part is a exponentially decaying part governed by a time constant. Depending on the coefficients chosen to represent the circulatory component, the time constant can be adjusted to match the gradient of the total lift at $S = 0$ with Lomax theory [168]. In the Leishman-Beddoes model, the coefficients of circulatory lift were chosen from low frequency unsteady transonic calculations for the 64A006 airfoil [169]. The time constants were subsequently revised and the indicial functions validated with test data for symmetric airfoils [67].

Figure 3.1(a) shows the indicial lift (normal force) response of SC1095 airfoil to a step change in angle of attack. The original coefficients (Leishman-Beddoes) of circulatory lift, when applied to SC1095 response, predicts a faster growth compared to CFD calculations. In general both sets of coefficients (Leishman-Beddoes and refined) show the same trends as CFD with no significant phenomenological difference. The refined coefficients however, better capture the growth rate.

The indicial functions for lift response are converted to frequency domain using Laplace transforms. This produces explicit frequency response solutions for harmonic pitch oscillations. Both circulatory and impulsive contributions from pitch and pitch rate oscillations are used to calculate the frequency response. The results are shown for two Mach numbers, 0.4 and 0.7 in figure 3.2(a). The refined model

shows improved correlation with CFD results below a reduced frequency of 0.4. Reduced frequencies of interest for airloads calculation lies mostly within this range. For example, the reduced frequency corresponding to a 4/rev torsion oscillation at the blade tip in hover is 0.13. The lift and pitching moment responses of an airfoil undergoing pitch oscillations at such a reduced frequency are shown in figure 3.3. CFD results and the present indicial model are in good agreement up to Mach number 0.6. Mild flow separation predicted by CFD degrades correlation at Mach number 0.7. The separation disappears at a higher Mach number. For a blade section at 77.5% R the high-frequency variation of angle of attack is much lower than the magnitude of pitch oscillations considered here and the flow is expected to remain attached. Flow separation is therefore not a cause of concern and the agreement between 2D CFD and the present indicial model is satisfactory.

3.1.4 Far wake model

The far wake induced inflow is calculated using a refined Bagai-Leishman pseudo-implicit free wake model [162]. Four different far wake models are investigated - (i) Single peak free tip vortex, (ii) Single peak free moving vortex, (iii) Dual peak free wake and (iv) full span free and prescribed wakes. All wakes use 15 degrees discretization angle and 2 turns. Increasing the number of turns or refining the wake discretization angle does not produce any significant change in air loads at the high-speed flight condition.

A single peak free tip vortex model is used as the baseline model. The tip

vortex is assumed to be fully rolled up. The strength of the tip vortex is equal to the maximum bound circulation occurring outboard of 50% span. The tip vortex is considered to originate at the tip of the swept elastic axis.

In the single peak free moving vortex model, the vortex is not trailed from the tip at all azimuths. The vortex is assumed to move inboard in the regions of negative lift. The span location from which it is trailed in the azimuths of negative lift, is the zero bound circulation cross-over point. This is the spanwise location where the circulation changes from a positive value to a negative value. The vortex is trailed from inboard because the largest radial gradient of circulation occurs near this point. The strength of the vortex remains same as that of the previous tip vortex model.

In the dual peak free wake model, a vortex of negative strength is trailed from the tip when the lift at the blade tip is negative [52]. The possibility of a negative vortex in the tip region was suggested by Ref. [120] and the intention here is to study its influence on predicted airloads in presence of accurate deformations. In the dual peak model, the strength of the negative vortex is equal to the maximum negative circulation attained near the blade tip. The positive vortex continues trailing from an inboard radial station. Like the moving vortex model, this station is taken at the zero bound circulation cross-over point. The strength of the positive vortex is equal to the sum of the maximum bound circulation occurring outboard of 50% blade radius and the maximum negative circulation occurring near the blade tip. The later is non-zero only in the azimuths of negative lift.

The full span wake (free and prescribed) models consist of a set of 26 trailers

uniformly trailed across the blade span. The strength of the trailers are compatible with the bound circulation strengths. The contribution of the far wake is considered from behind the near wake region.

3.2 3D CFD model

The 3D CFD model is a viscous, compressible, unsteady Navier-Stokes model. The CFD computations are performed using an in-house modified version of the TURNS research code developed by *Sitaraman and Baeder* [170, 171]. TURNS uses a finite difference numerical algorithm that evaluates the inviscid fluxes using an upwind-biased flux-difference scheme [172, 173]. The van Leer monotone upstream-centered scheme for conservation laws (MUSCL) approach is used to obtain second and third order accuracy with flux limiters to be Total Variation Diminishing (TVD). The Lower-Upper-Symmetric Gauss-Seidel (LU-SGS) scheme [174] is used as the implicit operator. Though the LU-SGS implicit operator increases the stability and robustness of the scheme, the use of a spectral radius approximation renders the method only first order accurate in time. Therefore, a second order backwards differencing in time is used, along with Newton-type sub-iterations to restore formal second order time accuracy.

A single block mesh approach is used to make the calculations computationally viable. Complete wake capturing from CFD techniques requires a multi-block or over-set mesh based approach. In this study, only one blade of the rotor is modeled and the effects of other blades are included using an induced inflow distribution. The

effects of the near shed wake, near tip vortex and bound vortices are captured fairly well in the CFD computations. Hence, only the induced inflow caused by the far-wake tip vortex need to be included to model the returning wake effects. The induced inflow is computed at each grid point using the Bagai-Leishman free wake model. The induced inflow is incorporated into the flow solution using the *Field Velocity Approach*, which is a way of modeling unsteady flows via grid movement [106, 175]. The induced inflow model used is the baseline single free tip vortex model discussed in the previous section.

The present numerical scheme employs a modified finite volume method for calculating the grid and time metrics. The modified finite volume formulation has the advantage that both the space and time metrics can be formed accurately and free stream is captured accurately [105]. The aeroelastic deformations are included into the flow solutions by moving the mesh points to conform to the surface geometry of the deformed blade in a consistent manner. The use of such dynamically deforming mesh geometry mandates the recomputation of space and time metrics at each time step. These quantities are computed in a manner which satisfies the *Geometric Conservation Law* (GCL) [175]. The GCL is used to satisfy the conservative relations of the surfaces and volumes of the control cells in moving meshes.

Body conforming curvilinear meshes which follow both C-H and C-O grid topologies are constructed around the UH-60A rotor blade. The C-H grid topology approximates the tip of the blade to a bevel tip, whereas the C-O mesh could provides a better tip definition. The computations were performed for the same deflections sets using different grid topologies to understand the impact of tip mod-

eling present in the air load prediction. Also, coarse and refined meshes are used to quantify grid dependence of the flow simulation. The refined meshes used 217 points in the wrap around direction of which 145 are on the airfoil surface, 71 points in the normal direction and 61 points in the span-wise direction. The coarse meshes in contrast used 133 points in the wrap around direction of which 99 are on the airfoil surface, 43 points in the normal direction and 43 points in the span-wise direction. Representative C-H and C-O meshes are shown in Fig 3.4. The spacing a the blade surface in the normal direction is $5X10^{-5}$ chords for viscous computations and the outer boundaries are 10 chords away from the blade surface. The details of grid and time independence studies are described in reference [116]. The results were found to show good grid and time step independence. Hence, to facilitate faster turn around time for the CFD coupling process, a coarse mesh with azimuthal step of 0.5 degree is used for all the computations presented in this paper.

The structural dynamic analysis provides deformations as functions of radius and azimuth of form $[u(r,\psi), v(r,\psi), w(r,\psi), v'(r,\psi), w'(r,\psi), \phi(r,\psi)]^T$, where u, v, w are the linear deformations in axial, lag and flap directions, v', w' are the radial derivatives of flap and lag degrees and ϕ is the elastic torsional deformation. The given rotor geometry is dynamically deformed in accordance with these blade motions. At any section, one could define a rotation matrix T_{DU} which is a function of the rotation angles v', w' and ϕ. Then the deformed mesh coordinates in the blade fixed frame are given by the following equation

$$\begin{bmatrix} x' \\ y' \\ z' \end{bmatrix} = (T_{DU})^T \begin{bmatrix} x \\ y \\ z \end{bmatrix} + \vec{x_{lin}} \tag{3.33}$$

The vector $\vec{x_{lin}}$ represents the linear deflections given by $\{u, v, w\}^T$. Once the deformed mesh is obtained in the blade fixed frame, it is rotated about the z-axis to the appropriate azimuthal location. A cosine decay is applied to both the rotations and linear deflections such that the outer boundary of the mesh remains stationary.

Characteristic boundary condition are used at the outer boundaries to improve the accuracy of the CFD algorithm. Riemann invariants from the theory of characteristics are satisfied to determine the flow variables and speed of sound at the boundaries. The boundary condition adjusts itself depending on the direction of the flow (into or out of the boundary).

3.3 Validation of aerodynamic models

The deformation set and trim angles obtained in Section 2.5, Chapter 2 are now used to calculate air loads. Figure 3.5 shows the calculated blade lift (1-10/rev) at six radial stations using the baseline lifting-line model. The baseline lifting-line model incorporates - 2D test airfoil tables, Leishman-Beddoes 2D unsteady aerodynamics and a Single free tip vortex model. In the following section, the aerodynamic model is refined in a step-wise fashion to assess the impact of CFD airfoils, a refined unsteady model and various wake models. All calculations incorporate the W-L

model. The blade deformations and control angles are held fixed. Thus, the errors and differences in prediction originate entirely from aerodynamic modeling.

For the various modeling refinements, the rotor is not re-trimmed for control angles. Therefore, the 1/rev component of lift is henceforth removed for comparison with flight test data. For example figure 3.6 shows the same plots as in figure 3.5 except that the 1/rev component has been removed. The qualitative nature of the lift curves remain the same.

3.3.1 Prediction of Lift

The prescribed deformation set obtained in Section 2.5 includes a 4% structural damping in the first flap mode. This is required to prevent errors in 1/rev flapping response, as shown before in figures 2.4(a) and 2.5. Figure 3.7 shows lift prediction with and without the 4% critical damping in first flap mode. The 1/rev flap response affects the 2/rev lift via the azimuthal velocity variation. The deformation set without the damping (i.e., with 0% damping) shows a better lift phase correlation in the advancing blade (67.5% R to 96.5% R) as shown in figure 3.7. However this corresponds to an incorrect deformation set. The deformation set obtained with the 4% damping is the correct deformation set. The correct deformation set produces a worse correlation of advancing blade lift phase.

Effect of 2D CFD tables

The 2D test airfoil properties are replaced with 2D CFD calculated airfoil

tables. Figure 3.8 shows that the predicted lift from the two sets of airfoil tables are almost identical. There is a marginal improvement in the prediction of vibratory lift (3-10/rev) magnitude near the tip at 96.5% R. This stems from differences in lift coefficients at Mach number 0.8 and above.

Compared to the comprehensive analysis predictions, shown in figure 1.4, figure 3.8 shows accurate advancing blade lift phase and vibratory lift near the tip. This is due to accurate 1/rev and 2/rev elastic torsion affecting 2/rev and 3/rev blade lift via the azimuthal velocity variation. The dominant 3/rev character of the vibratory lift is captured both in magnitude and phase.

Prediction of vibratory lift and lift phase inboard, at 77.5%R, remains unsatisfactory. Unlike the outboard stations where it it dominantly 3/rev, the vibratory lift inboard shows an impulsive behavior in the advancing blade. This phenomenon is not captured even with accurate elastic torsion.

Effect of unsteady aerodynamic models

The effect of 2D high subsonic unsteady models are studied in figure 3.9 Compared to a quasi-steady model, the 2D unsteady models show a marginal improvement in advancing blade lift phase and a slight attenuation of peak magnitude as expected. None of the models, original Leishman-Beddoes or the refined, show any significant improvement in the prediction of vibratory lift at the inboard stations. The refined model shows no improvement over the original model. Hence for all subsequent lifting-line calculations, the original Leishman-Beddoes model is retained.

The effect of 3D compressible unsteady flow is studied by comparing the lifting-

line predictions of figure 3.9 with 3D CFD predictions in figure 3.10. The far wake inflow and blade deformations (and control angles) are common to both sets of calculations. Three sets of results are presented, 2-10/rev, 3-10/rev and 4-10/rev lift. In general, the 3D CFD calculations show the same trends as lifting-line results, particularly in phase. The phasing of the advancing blade lift at the inboard stations (67.5% R and 77.5% R) remain unchanged, although the vibratory harmonics (3-10/rev and 4-10/rev) are marginally improved. Toward the tip (92% R and 96.5% R) the CFD calculations show greater 4/rev harmonics. The lifting-line results show improved predictions for reasons not clearly understood.

Effect of far wake models

The baseline far wake uses a single peak free tip vortex model. It is now progressively replaced with refined wake models. The wake geometry (top view and side view) of the baseline single peak tip vortex model is shown in figure 3.11. The wake geometry of the single peak moving vortex model is shown in figure 3.12. In general, the wake from all four blades are moved downstream quickly within two rotor revolutions. Although, the two wake geometries appear similar there are significant differences in the advancing side. The wake geometries (top view) of the baseline tip vortex model and the moving vortex model are compared in figure 3.13. Figures 3.13(a) and 3.13(b) show the advancing blade interactions of the wake trailed from the two preceding blades 3 and 4 (B3 and B4). Both remain below and close to the rotor plane, as can be seen from the side view figures 3.11(b) and 3.12(b). The trailers from blade 1 and 2 do not interact on the advancing side. The

radial location of the vortex interactions from Blade 3 and 4 on the advancing side depends on the wake model and appears to play a key role in the advancing blade lift waveform.

Figure 3.14 shows the effect of the moving vortex model on lift prediction. Significant improvement is obtained in the advancing blade at the inboard stations. The basic characteristic of the vibratory lift appears to be in place at 77.5% R. Predictions are in general improved both inboard and outboard. Out of the two possible wake interactions, one from Blade 3 and one from Blade 4, the interaction with the wake from Blade 3 appears to play a key role. This is because, from figure 3.13(b), the radial location of wake interaction from Blade 4 onto Blade 1 is not significantly altered by the moving vortex model. Only the wake from Blade 3 appears to interact with Blade 1 at a significantly altered radial location.

The dual peak wake geometry is shown in figure 3.15. Figure 3.15(a) shows the wake geometry from Blade 3. Figure 3.15(b) shows the wake geometry from Blade 4. Lift prediction using the dual peak model, figure 3.16 show only a marginal improvement compared to the moving vortex model. Therefore, it appears that the key phenomenon behind the generation of vibratory lift at the inboard stations is the positive trailed vortex moving inboard, not the negative vortex trailed from the tip. Out of the two possible wake interactions, one from Blade 3 and second from Blade 4, the interaction with the wake from Blade 3 appears to play a key role. This is because, from figure 3.13(b), the radial location of wake interaction from blade 4 on blade 1 in the advancing side not significantly altered by the moving vortex model. Only the wake from Blade 3 appears to interact with Blade 1 at a

significantly altered radial location.

The full span free wake model (figure 3.4) shows a similar inboard lift prediction as the dual peak model (figure 3.18). This suggests that the details of the roll up process is not important at high-speed flight. Moreover, the free wake trailers do not show significant distortion in the first turn where the key interactions occur. Therefore a full span prescribed wake model (figure 3.4) shows same lift prediction as the free wake model (figure 3.19).

Figure 3.20 shows predictions using a 3D CFD Navier-Stokes analyses. Predictions using the baseline tip vortex are compared with the refined moving vortex model. The trends are similar to that observed using the lifting-line model. The inboard vibratory impulse at 67.5% R and 77.5% R is well captured using the moving vortex model. As a result, the phase of the 3-10/rev and 4-10/rev components are accurately picked up. Although the impulse is predicted more accurately by the CFD analysis, the 2-10/rev waveform in the first quadrant is better predicted by the lifting-line model (figure 3.16). Predictions near the tip, as in the case of lifting-line model show marginal improvements. The inboard impulse is captured equally well by both Navier-stokes and Euler analyses as shown in figure 3.21.

To summarize, the advancing blade lift phase and vibratory lift predictions are accurate in figure 3.16 (lifting-line) and figure 3.20 (CFD) because of - accurate elastic torsion and accurate rotor wake. Accurate torsion has been obtained by the use of measured pitching moments. In comprehensive analysis the pitching moments must be predicted. The following section investigates pitching moment predictions by 3D CFD and lifting-line models. Again, the same set of prescribed deformations

and far wake inflow are used.

3.3.2 Prediction of Pitching Moments

Figure 3.22 shows predicted quarter-chord pitching moments from the baseline lifting-line model using test airfoil tables and a refined model using 2D CFD tables. Except for the peak magnitude at 77.5% R, both show similar predictions with no change in waveform. A possible source of error at 77.5% R is the unknown trim tab setting angle used during flight 85. Apart from 77.5% R, the largest discrepancy is at the outboard stations (92% R and 96.5% R).

Unlike lift prediction, the effect of unsteady model has a significant effect on pitching moment predictions. Compared to a quasi-steady model the Leishman-Beddoes unsteady model, figure 3.23, provide improved predictions inboard (67.5% R). However, the improvement is marginal towards the tip and the waveforms remain poor. The refined unsteady model shows no improvement over the original Leishman-Beddoes model.

The 3D CFD predictions offer significant improvement compared to the lifting-line models. Figure 3.24 compares lifting-line and 3D CFD predictions. Inboard, up to 67.5% R, predictions are similar to lifting-line model and both are accurate. Lifting-line predictions on the advancing blade gradually deteriorate towards the outboard stations. Although not accurate, the CFD model shows improved predictions of the unsteady waveform on the advancing blade at the outboard stations. Lifting-line and CFD predictions using the refined moving vortex free wake model

is compared in figure 3.25. Again, predictions are similar up to 67.5% R. For the CFD predictions, the moving vortex wake model shows significantly improved correlation in the second quadrant compared to the baseline wake model (figure 3.24). Like in lift, the impulsive airloads at the junction of the first and second quadrants are well captured by the refined wake model. The peak to peak remain slightly over-predicted at 77.5% R although the waveform is improved.

The accuracy of the CFD predictions does not depend on the near wall viscous effects. Figure 3.26 shows that predictions from an Euler analysis show the same trends as Navier-Stokes. There are marginal differences in higher harmonics at the inboard stations, but near the tip, predictions are same.

The largest discrepancy of the lifting-line predictions are seen at the outboard stations, in the first and second quadrants. The lifting-line predictions show a sharp drop in the first quadrant and an under-prediction of the peak in the second. The sharp drop in the first quadrant are associated with steady transonic effects. The coefficients obtained from 2D airfoil tables show the effect of aerodynamic center movement in transonic flow. In the regions of positive angle of attack (around 45 degree azimuth location) high incident Mach number shifts the aerodynamic center behind quarter chord. This generates a high nose down pitching moment. As the angle of attack drops from positive to negative, the normal force, now negative, generates a nose up pitching moment. Unlike a 2D airfoil, a section near the tip of a 3D wing does not undergo the same aerodynamic center movement. The compressibility effects are delayed to a higher Mach number due to a shock relief effect. The tip effect is discussed in more detail in Chapter 5.

3.4 Concluding Remarks

Using a prescribed set of blade deformations a progressively refined set of aerodynamic models are evaluated for high speed forward flight. The prescribed deformation set was obtained in Chapter 2 using measured air loads on a validated structural model. In absence of measured deformations it forms the closest approximation to flight test data. The lifting-line model incorporates 2D airfoil properties, a W-L type near wake model, Leishman-Beddoes unsteady model and Bagai-Leishman free wake. The unsteady model, originally formulated and validated for symmetric air foils, is refined specifically for the two UH-60A airfoils, SC1095 and SC1094 R8. The 2D test airfoil properties are replaced with 2D CFD generated airfoil tables. Finally, a 3D compressible unsteady CFD calculation is performed using the TURNS-3D code, which accounts for flexible blade deformations and incorporates Bagai-Leishman free wake. Both Navier-Stokes and Euler solutions are studied. Based on this study, the following conclusions are drawn.

1. Error in the advancing blade lift phase can be resolved with - 1. accurate elastic torsion deformation and 2. accurate wake model.

2. Vibratory lift (3/rev and higher) at the outboard stations, 86.5% R to 99% R are well predicted in magnitude and phase with accurate elastic torsion. Vibratory lift at these stations are dominantly 3/rev and arise from 2/rev elastic torsion.

3. Vibratory lift at the relatively inboard stations, 67.5% R and 77.5% R, are

impulsive in nature. The vibratory lift impulses at these stations are not captured by accurate elastic torsion alone. An accurate rotor wake model is necessary along with the correct elastic torsion.

4. A dual peak free wake model captures the vibratory lift impulses inboard when accurate torsion is prescribed. The dominant phenomenon is not the negative vortex near the tip, but the stronger positive vortex moving inboard. Predictions with a single moving vortex model, without the negative vortex at the tip, shows similar results as the dual peak free wake model.

5. The impulse appears to be generated by advancing blade interactions of the wake trailed by the blade immediately ahead. The radial location of this interaction depends on the wake model. A moving vortex model, dual peak model and full span set of trailers (26 prescribed or free) all appear to capture the advancing blade lift phase and vibratory impulse accurately at the inboard stations. Predictions are, in general, improved at all radial stations.

6. The Leishman-Beddoes unsteady aerodynamic model is accurate enough for the UH-60A air foils. Refinements performed on the indicial model specifically for the UH-60A airfoils, SC1095, SC1095 R8 do not show any improvement on lift prediction. In general the effect of unsteady aerodynamics (shed wake) does not have a dominant effect on lift prediction at this flight condition.

7. Lifting-line predictions of lift show same trends as 3D CFD predictions with same deformations and free wake model.

8. Leishman-Beddoes unsteady model has a more significant effect on the lifting-line pitching moments. Using the unsteady model the inboard pitching moments, up to 67.5% R are reasonably well captured. Significant discrepancy in magnitude and waveform exist near the tip. The 3D CFD predictions, with same blade deformations and far wake inflow, show significantly improved prediction at the outboard stations. Predictions are similar, but improved, at the inboard stations.

9. For a given set of prescribed blade deformations and far wake inflow, both Navier-Stokes and Euler analyses show similar predictions of lift and pitching moments.

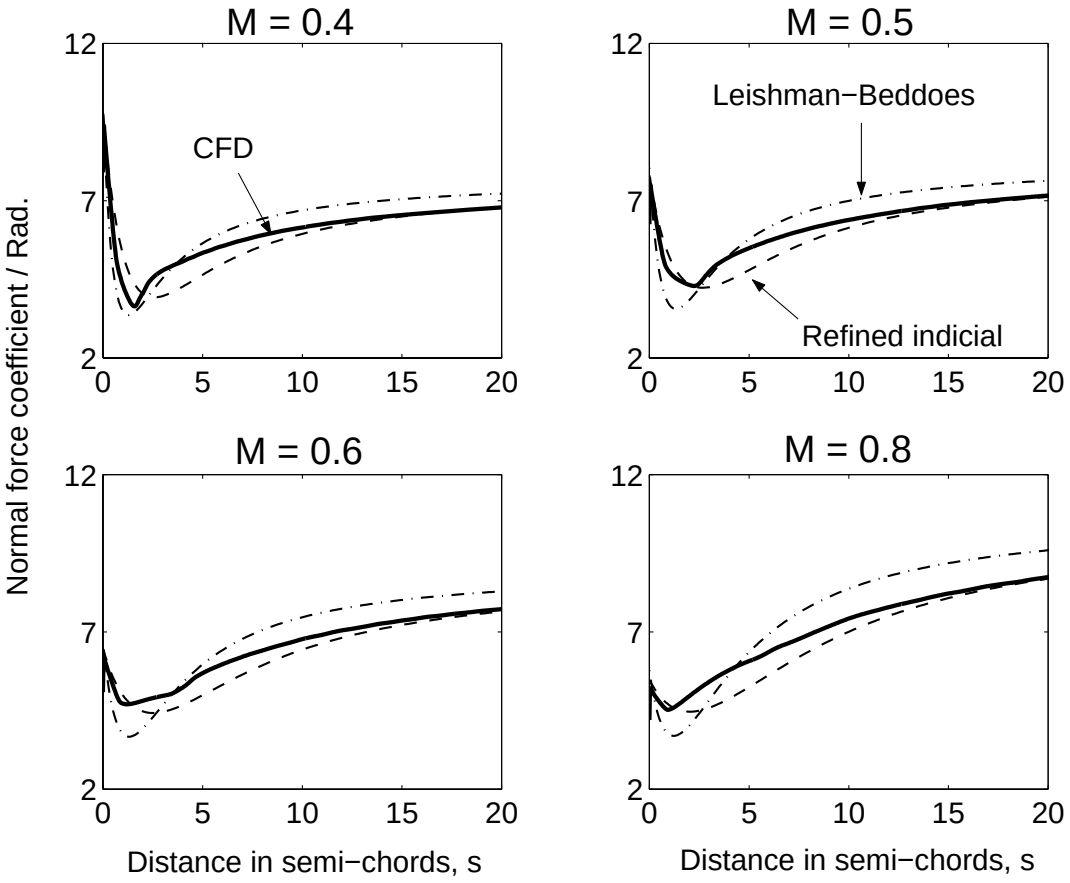

Figure 3.1: **Indicial lift response of SC1095 airfoil to a step change in angle of attack ; Comparison of Leishman-Beddoes and the refined model with CFD prediction**

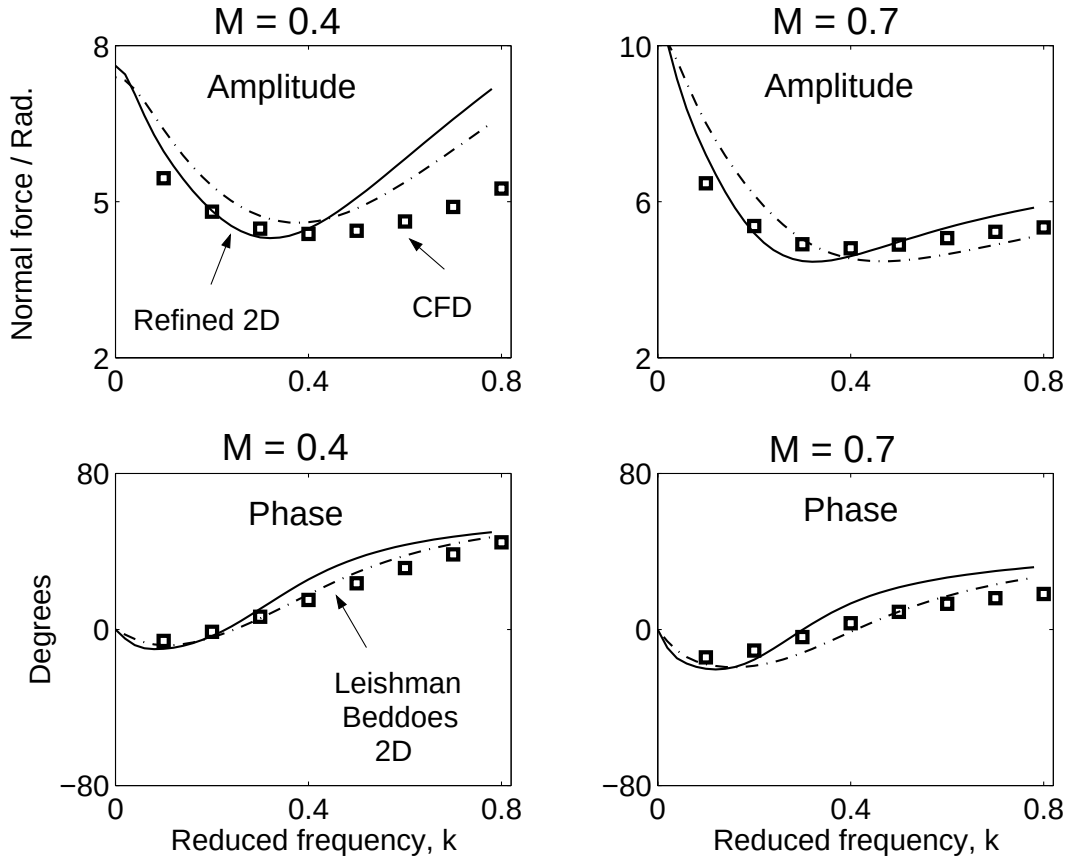

Figure 3.2: **Magnitude and phase of SC1095 lift in response to harmonic pitch oscillations; comparison of indicial models with CFD prediction**

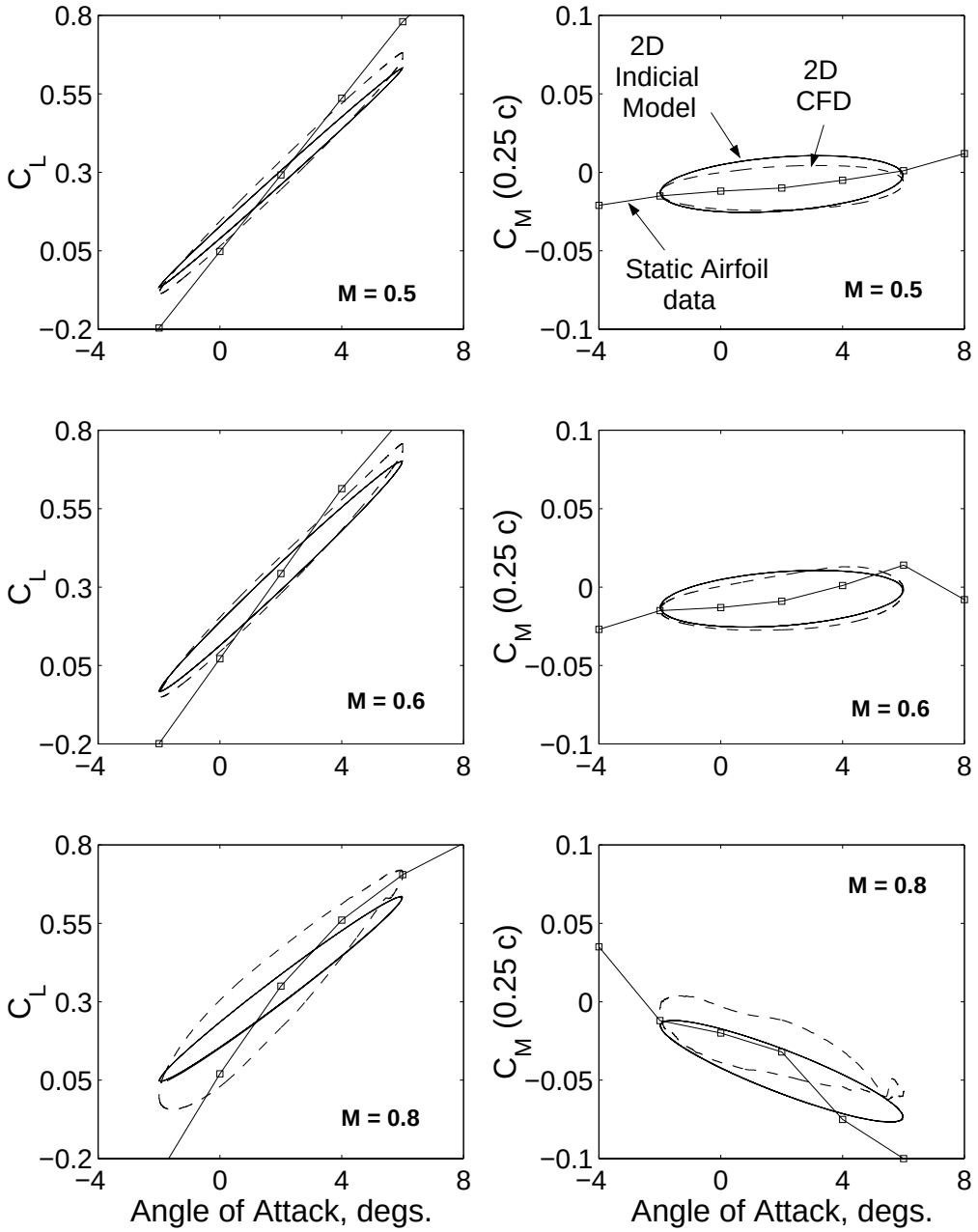

Figure 3.3: **Lift and pitching moment variation of SC1095 airfoil in response to harmonic pitch oscillations at reduced frequency k = 0.125 ;** $\alpha = 2 + 4\,sin\omega t$ **degs.,** $k = \omega C/2U$**,** C **= airfoil chord,** U **= incident velocity; Comparison of refined indicial model with CFD data**

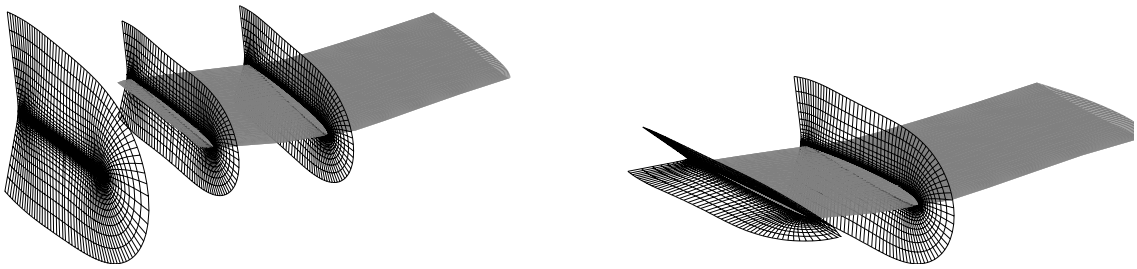

(a) C-H mesh (b) C-O mesh

Figure 3.4: **Near body C-H and C-O meshes at the blade tip used for UH-60A air loads calculations**

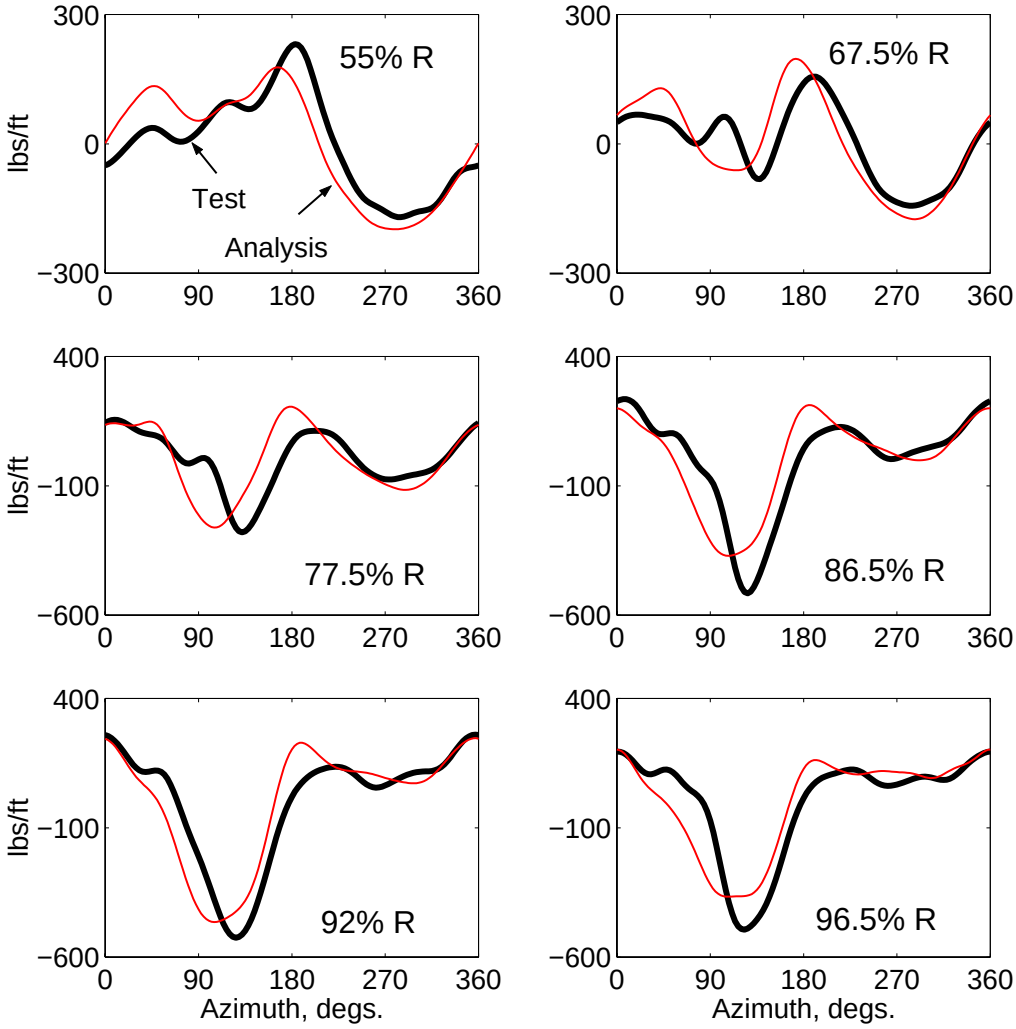

Figure 3.5: **Predicted 1-10p lift by W-L type lifting line model using prescribed blade deformations, test airfoil tables, single tip vortex free wake and Leishman-Beddoes unsteady aerodynamics; $C_W/\sigma = 0.0783$, high-speed $\mu = 0.368$**

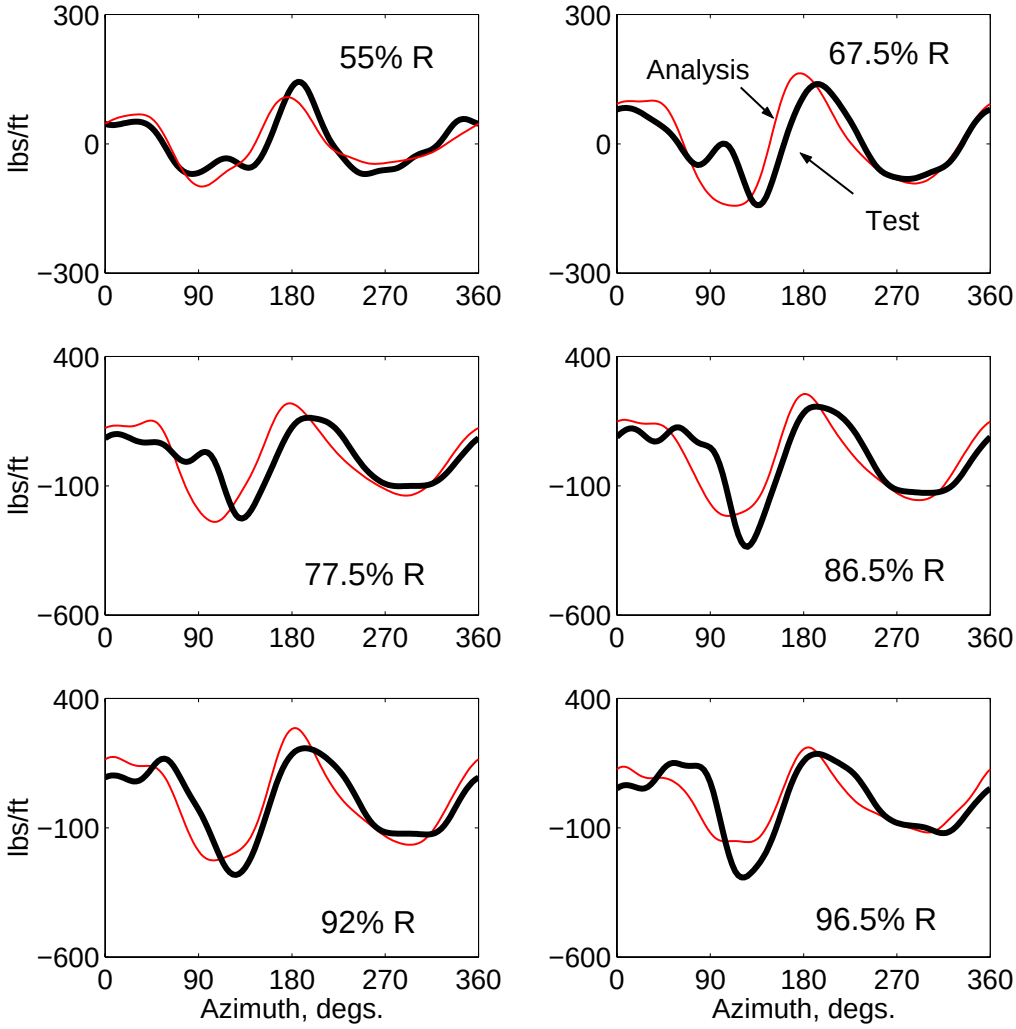

Figure 3.6: **Predicted 2-10p lift by W-L type lifting line model using prescribed blade deformations, test airfoil tables, single tip vortex free wake and Leishman-Beddoes unsteady aerodynamics; $C_W/\sigma = 0.0783$, high-speed $\mu = 0.368$**

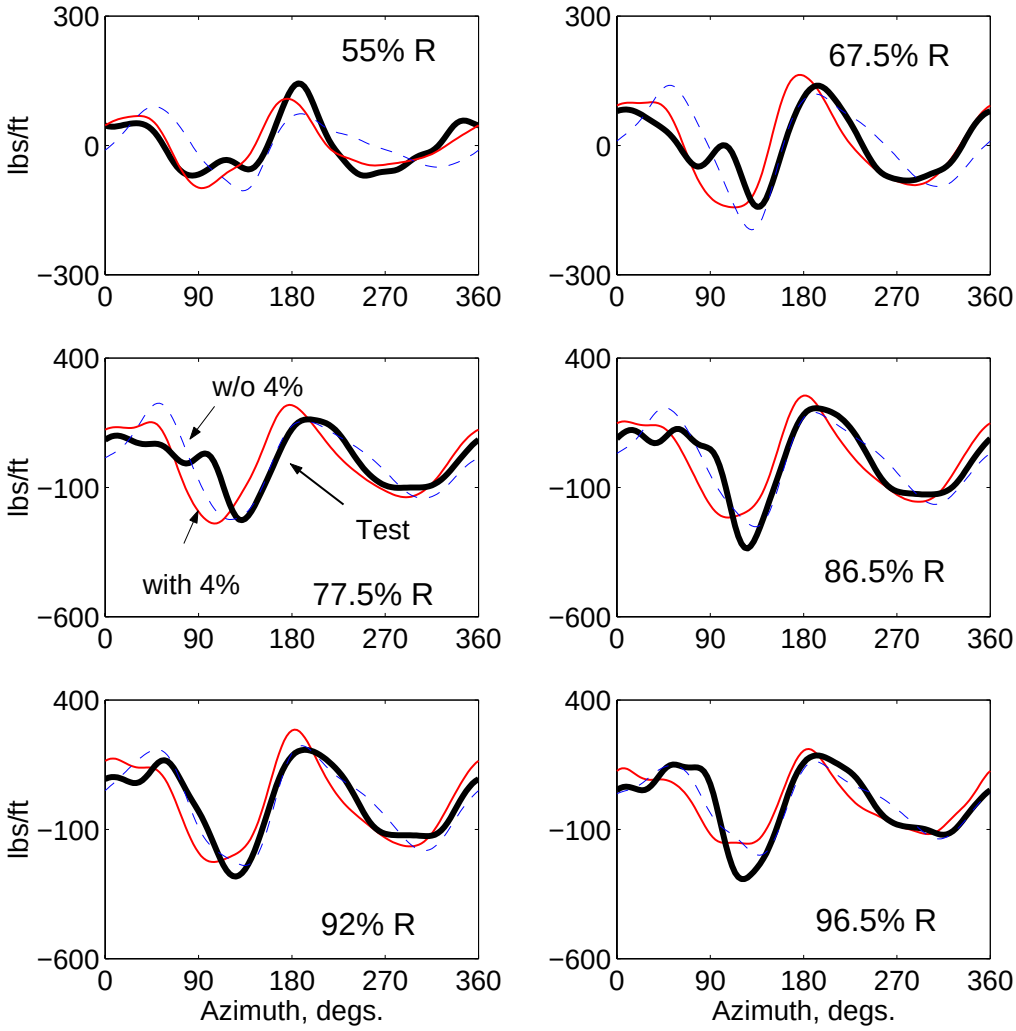

Figure 3.7: **Effect of 4% critical damping in obtaining the prescribed deformations; lift using W-L lifting-line model; ; $C_W/\sigma = 0.0783$, high-speed $\mu = 0.368$**

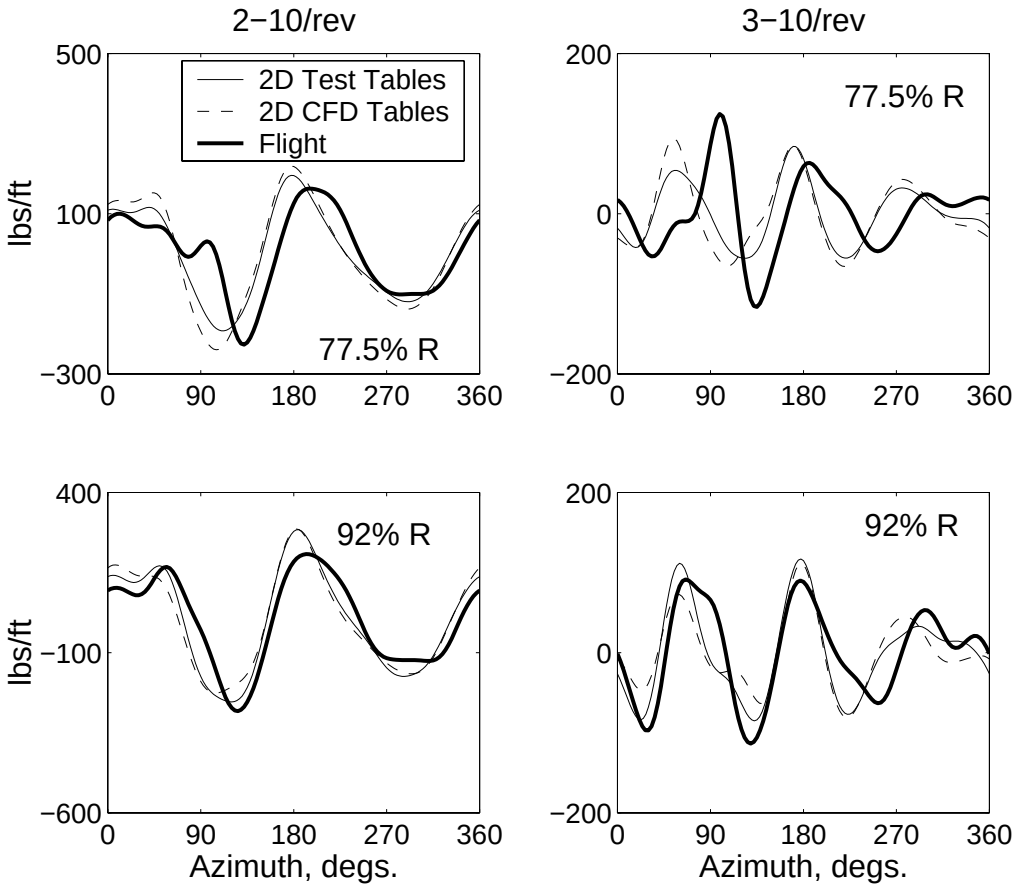

Figure 3.8: **Effect of 2D CFD generated airfoil tables on the prediction of lift by W-L type lifting line model; $C_W/\sigma = 0.0783$, high-speed $\mu = 0.368$**

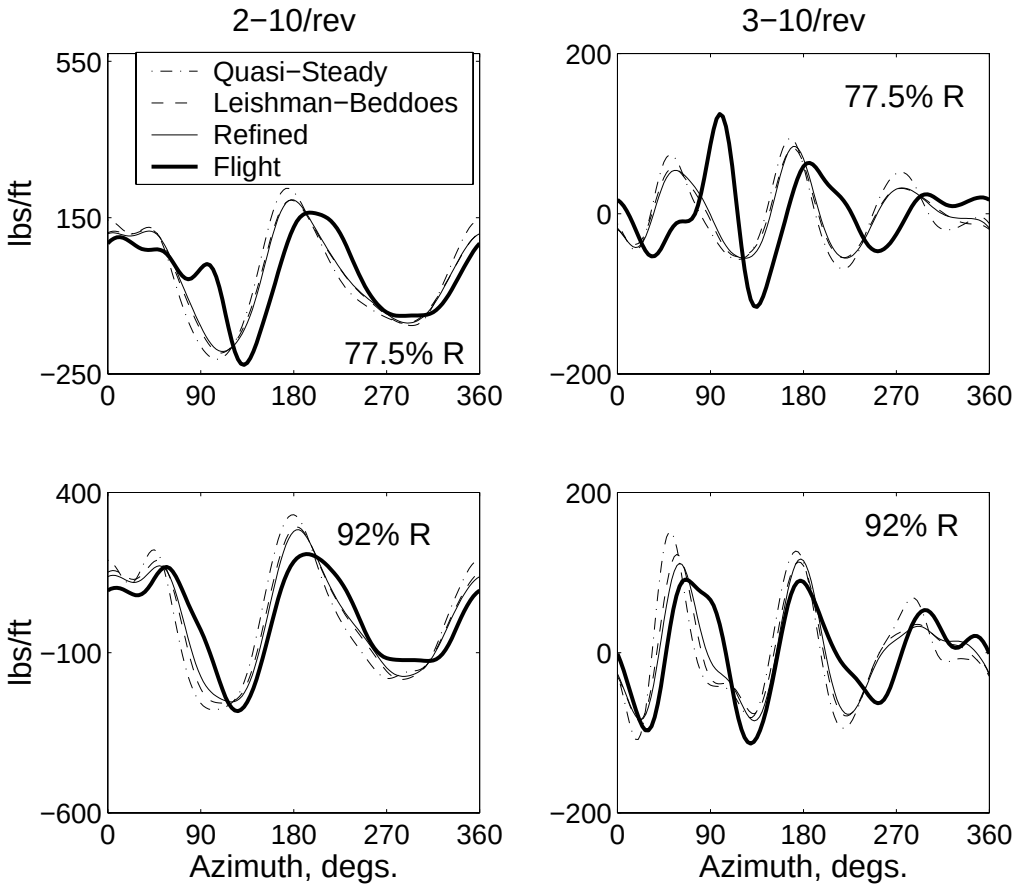

Figure 3.9: **Effect of 2D unsteady aerodynamics on the prediction of lift by W-L lifting line model; $C_W/\sigma = 0.0783$, high-speed $\mu = 0.368$**

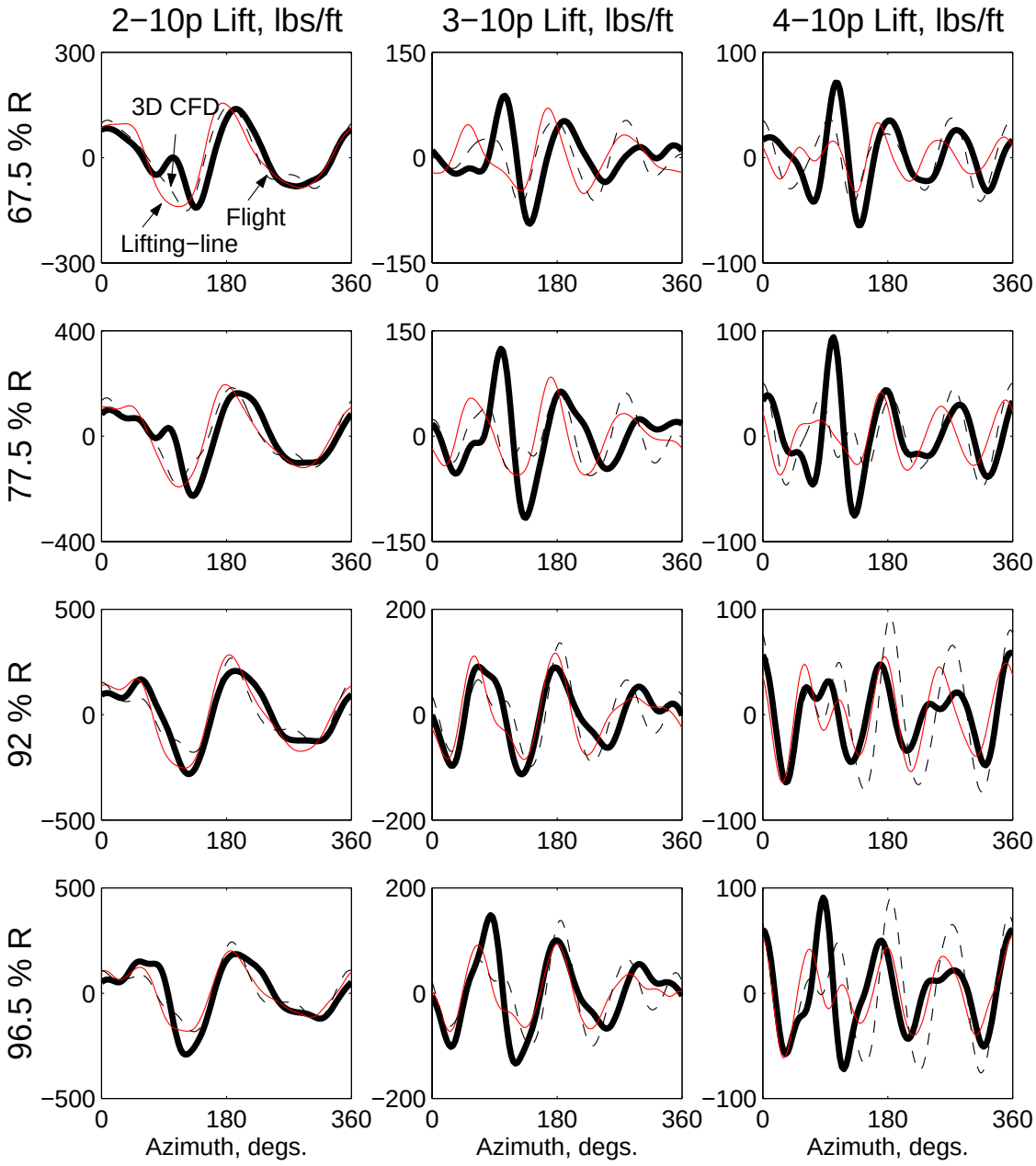

Figure 3.10: **Lifting line predictions compared with 3D CFD predictions ; same prescribed deformations and single peak tip vortex free wake;** C_W/σ **= 0.0783, high-speed** μ **= 0.368**

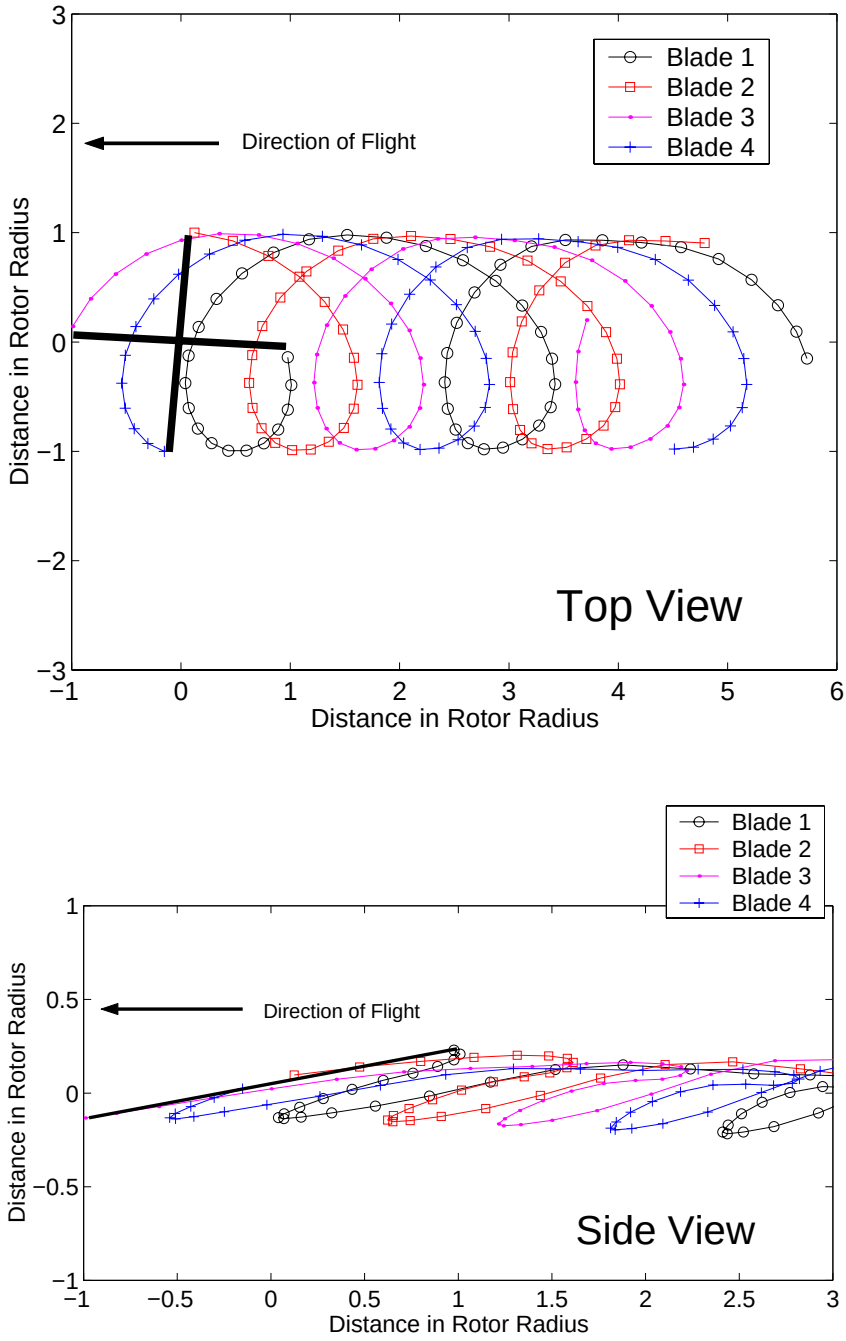

Figure 3.11: **Fully rolled up Single peak tip vortex free wake geometry; $C_W/\sigma = 0.0783$, high-speed $\mu = 0.368$; prescribed deformations**

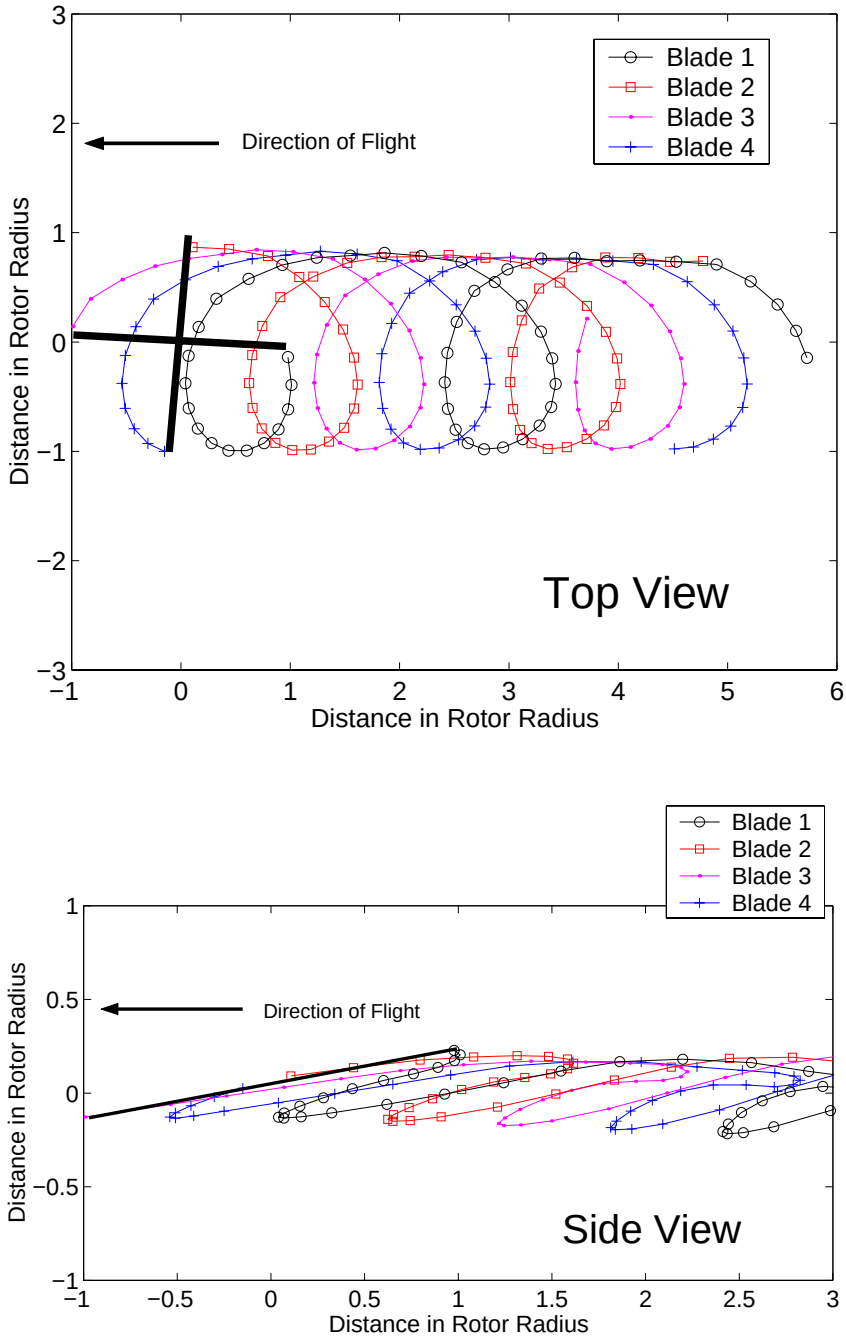

Figure 3.12: **Fully rolled up Single peak moving vortex free wake geometry; $C_W/\sigma = 0.0783$, high-speed $\mu = 0.368$; prescribed deformations**

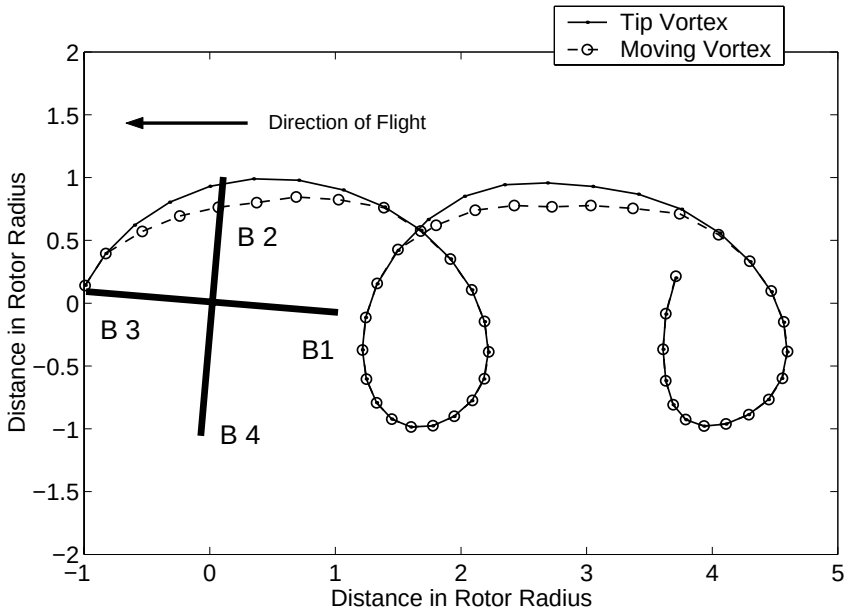

(a) Trailed vortex from Blade 3

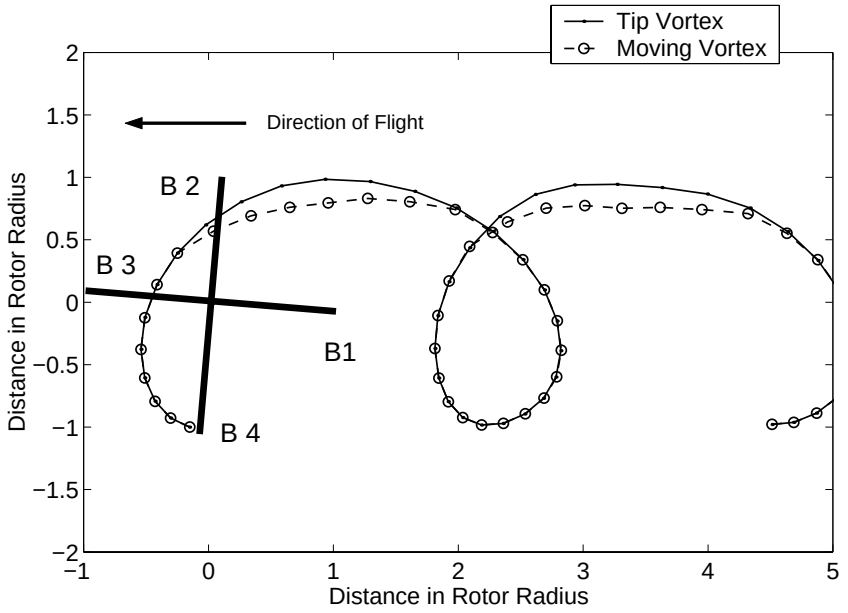

(b) Trailed vortex from Blade 4

Figure 3.13: **Top View of tip and moving trailed vortex free wake geometries; $C_W/\sigma = 0.0783$, high-speed $\mu = 0.368$; prescribed deformations**

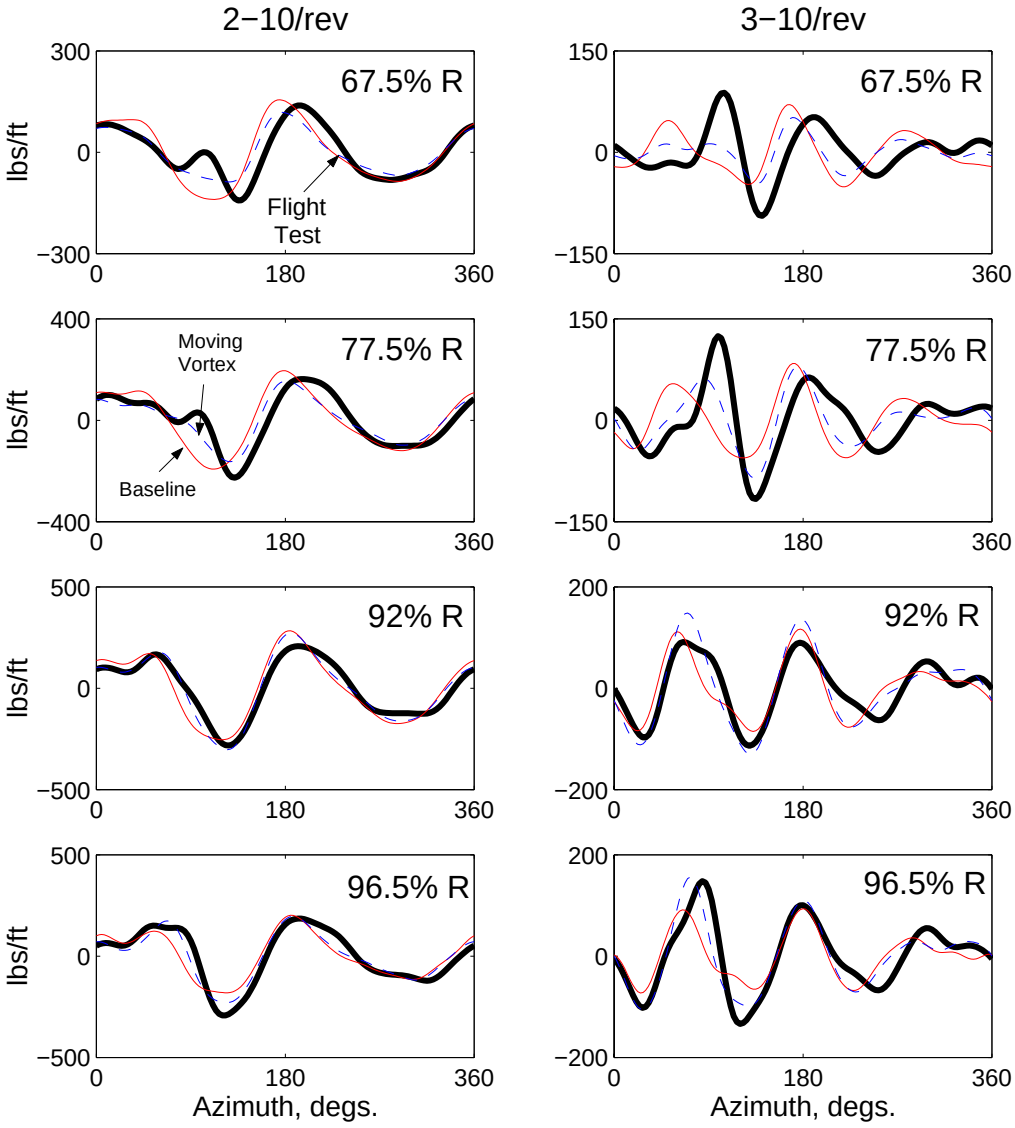

Figure 3.14: **Effect of moving vortex free wake model on W-L Lifting line predictions of lift; prescribed deformations ; $C_W/\sigma = 0.0783$, high-speed $\mu = 0.368$**

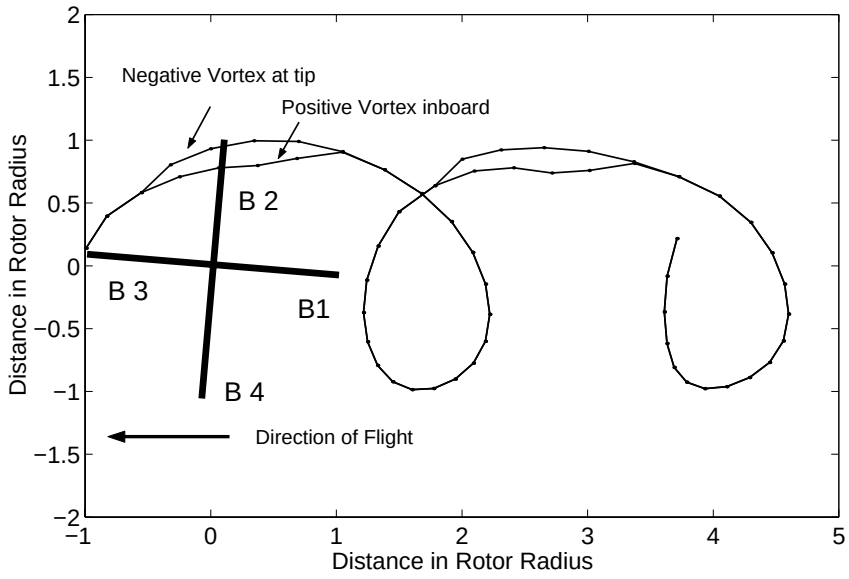

(a) Dual peak vortices from Blade 3

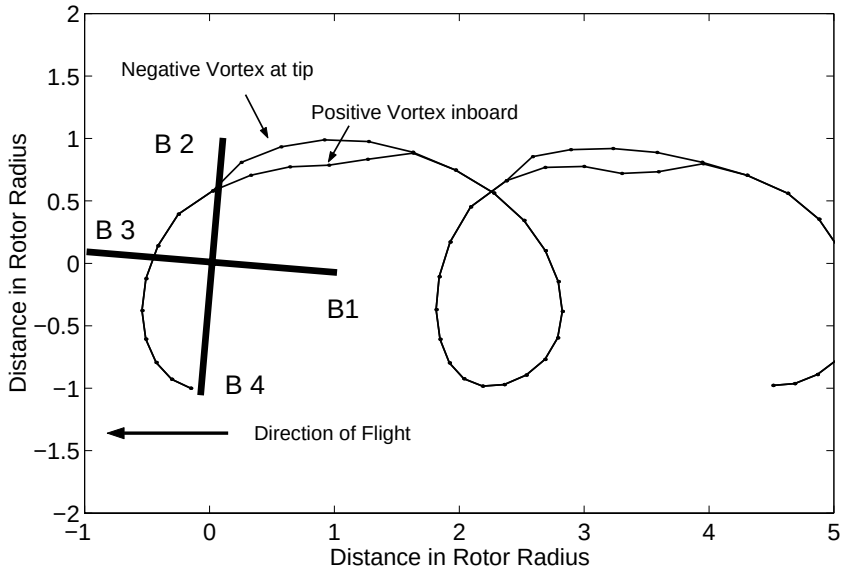

(b) Dual peak vortices from Blade 4

Figure 3.15: **Top View of Dual peak free wake trailed vortex geometries; C_W/σ = 0.0783, high-speed μ = 0.368; prescribed deformations**

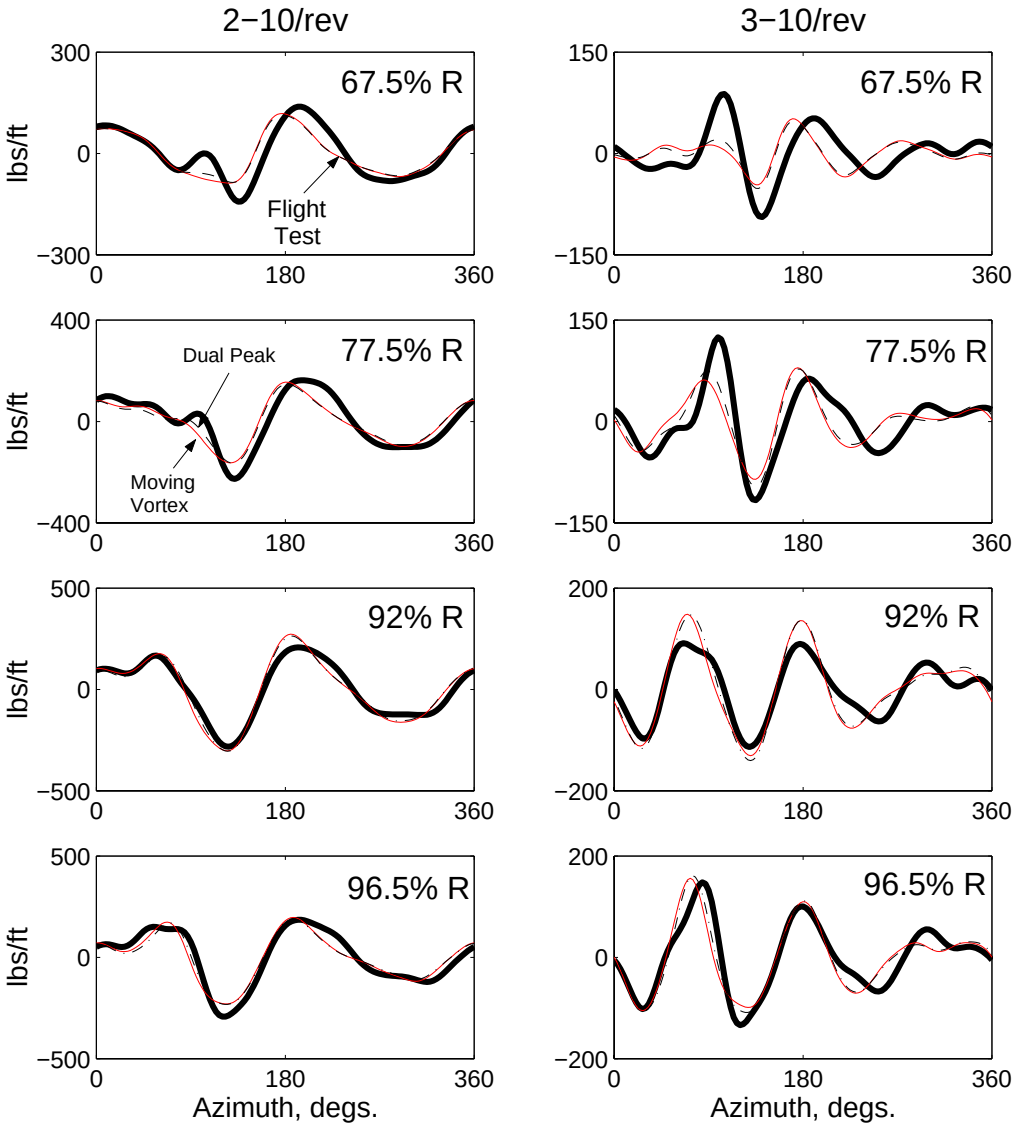

Figure 3.16: **Effect of dual peak free wake model on W-L Lifting line predictions of lift; prescribed deformations; $C_W/\sigma = 0.0783$, high-speed $\mu = 0.368$**

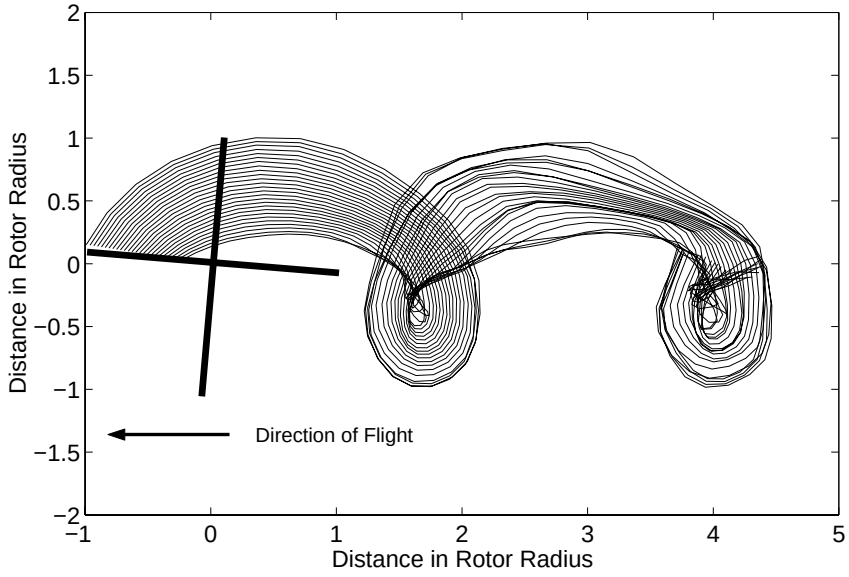

(a) Full span free wake from Blade 3

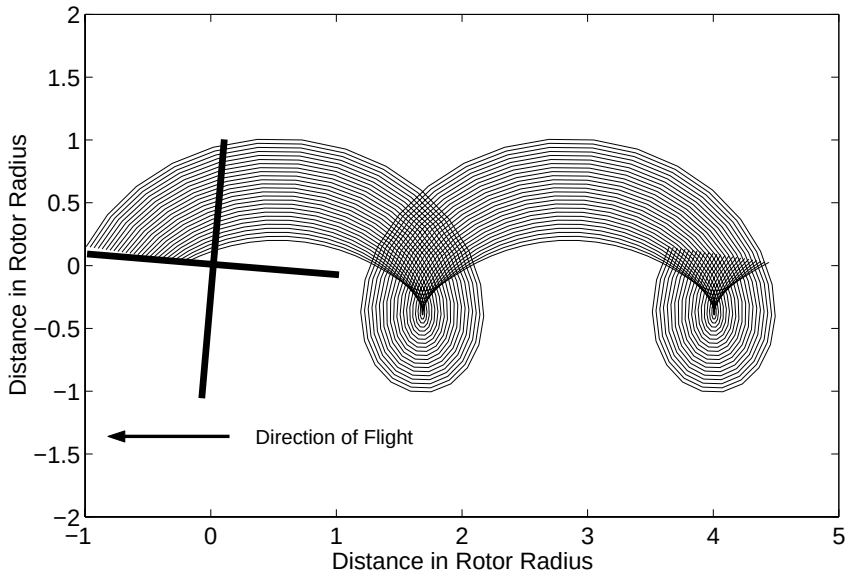

(b) Full span prescribed wake from Blade 3

Figure 3.17: **Comparison of full span free and prescribed trailed vortex geometries; $C_W/\sigma = 0.0783$, high-speed $\mu = 0.368$; prescribed deformations**

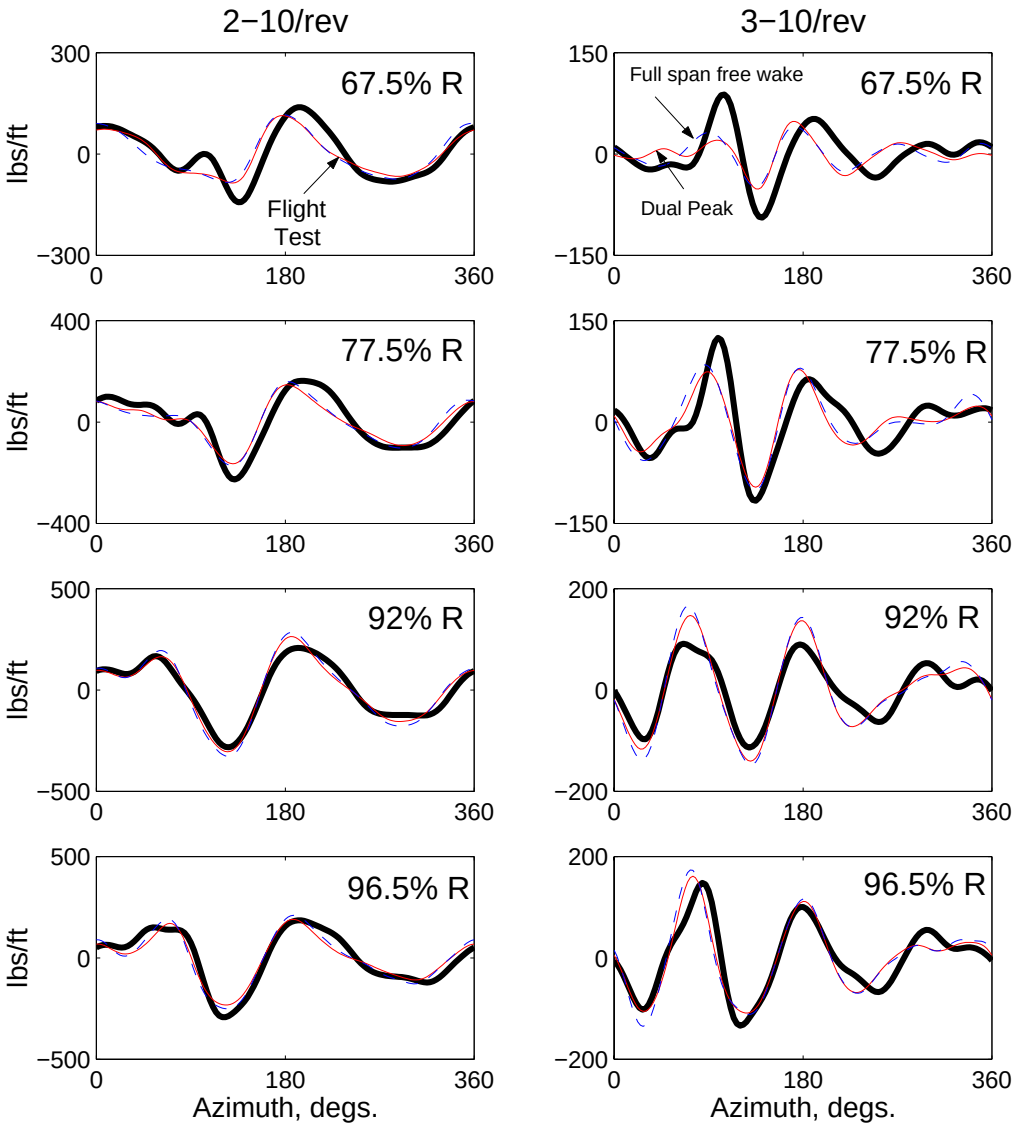

Figure 3.18: **Effect of full span free wake on W-L Lifting line predictions of lift; prescribed deformations; $C_W/\sigma = 0.0783$, high-speed $\mu = 0.368$**

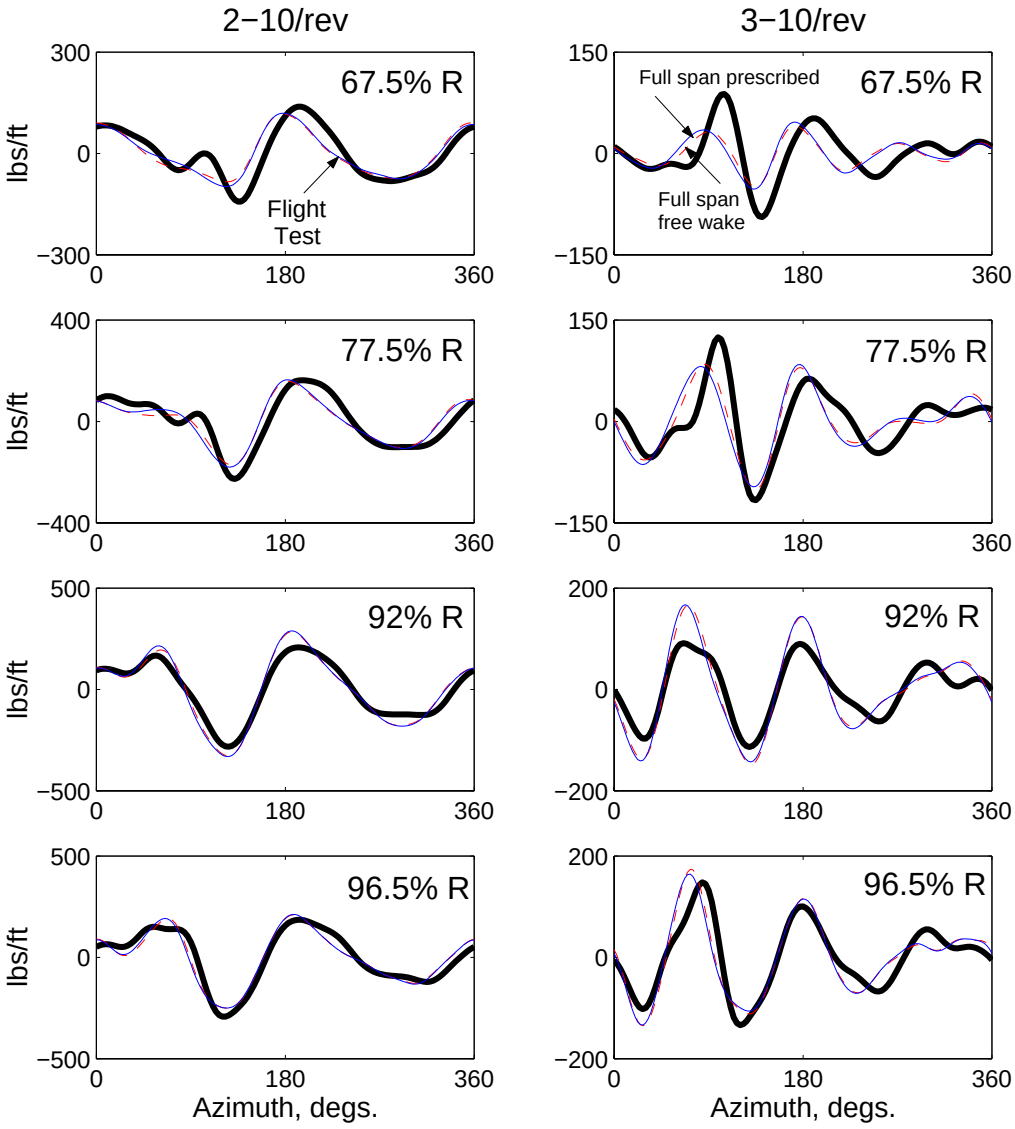

Figure 3.19: **Effect of full span prescribed wake on W-L Lifting line predictions of lift; prescribed deformations; $C_W/\sigma = 0.0783$, high-speed $\mu = 0.368$**

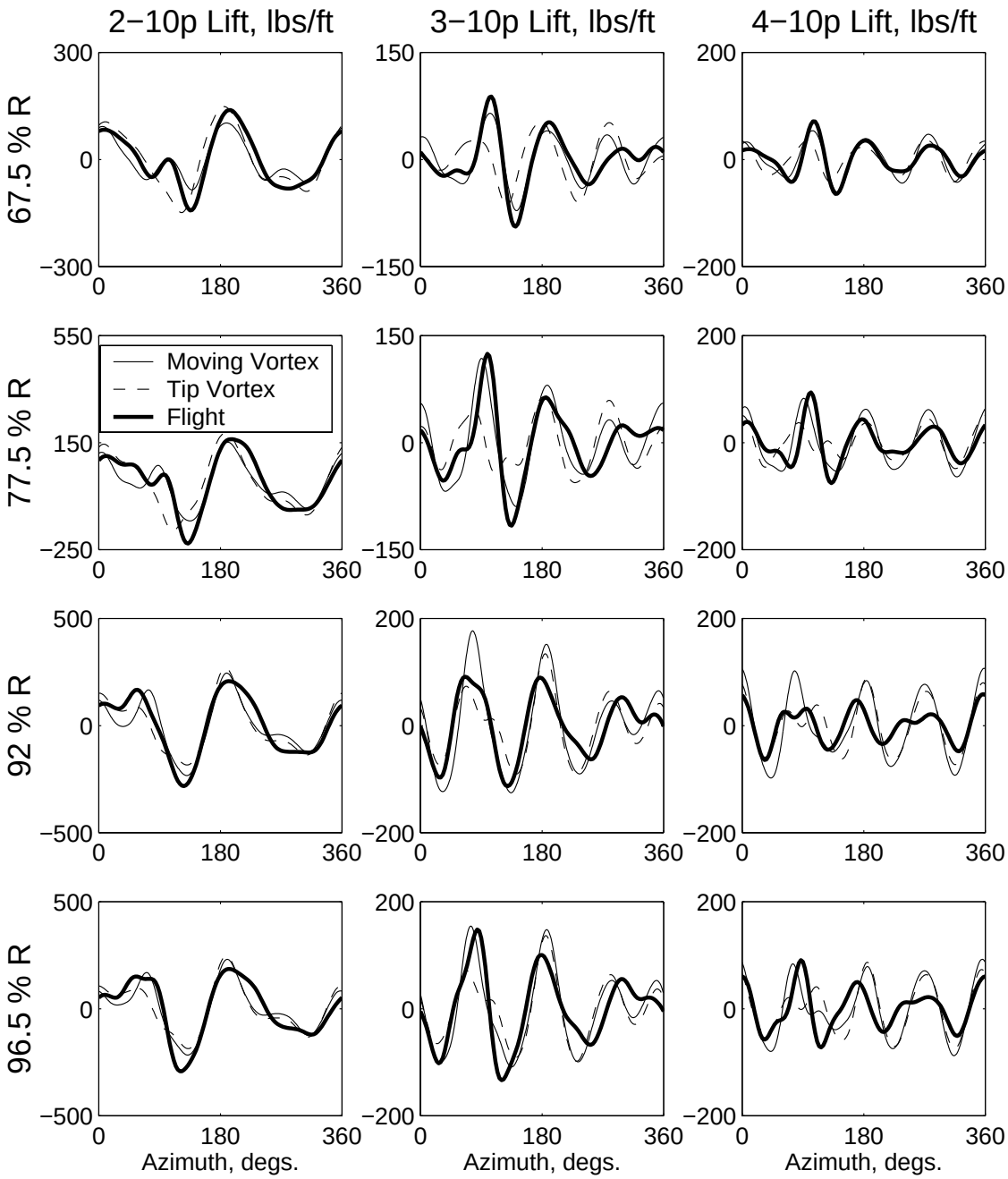

Figure 3.20: **3D CFD predictions with single peak tip vortex and moving vortex free wake models; same prescribed deformations; $C_W/\sigma = 0.0783$, high-speed $\mu = 0.368$**

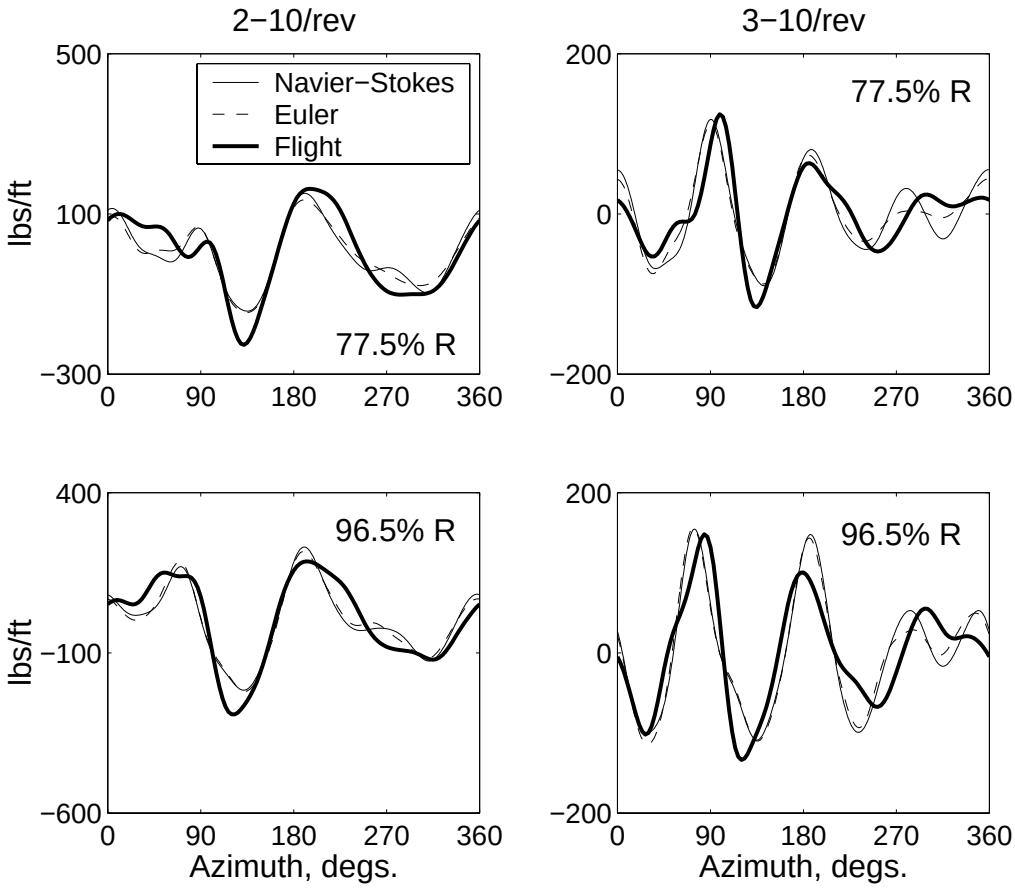

Figure 3.21: **3D CFD predictions with Navier-Stokes and Euler Analyses; same prescribed deformations and free wake; $C_W/\sigma = 0.0783$, high-speed $\mu = 0.368$**

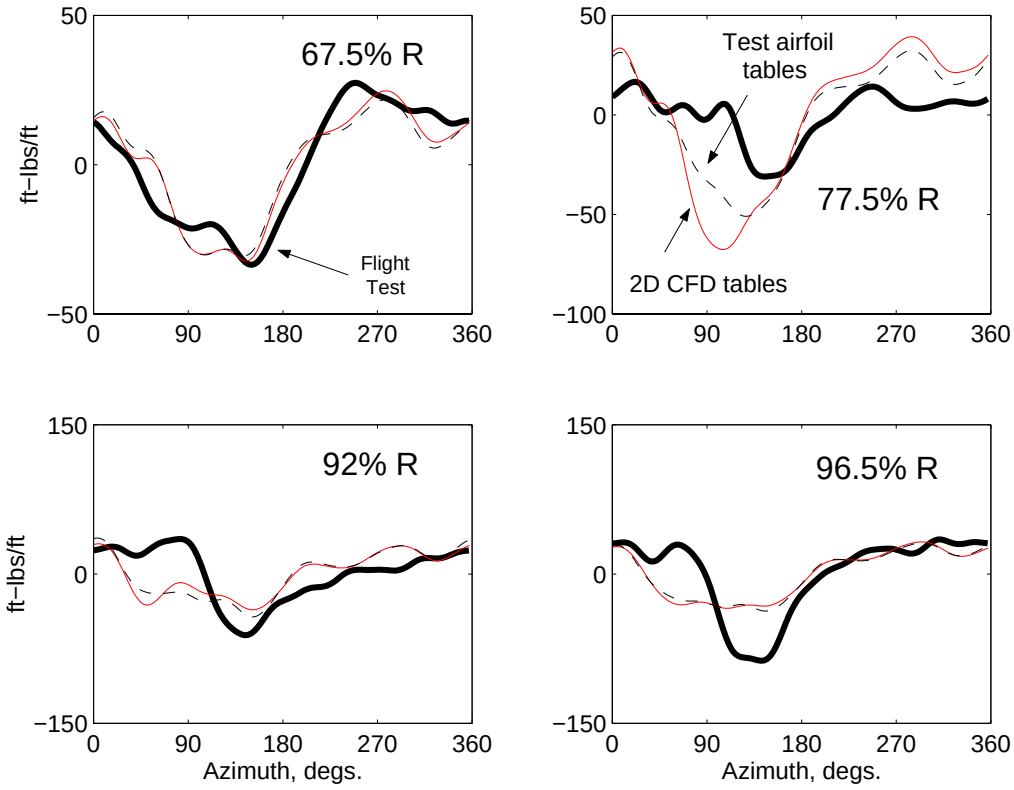

Figure 3.22: **Lifting line predictions of quarter-chord pitching moment using prescribed deformations, 2D unsteady aerodynamics and free wake; $C_W/\sigma = 0.0783$, high-speed $\mu = 0.368$**

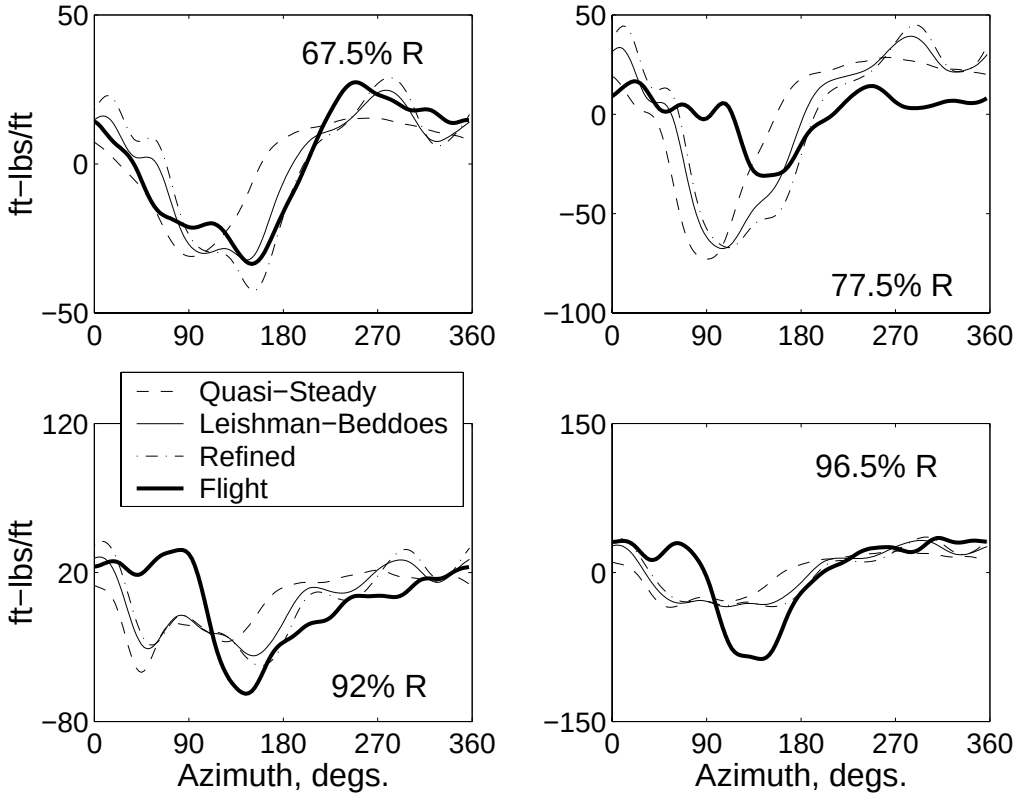

Figure 3.23: **Quasi-steady predictions compared with Leishman-Beddoes 2D unsteady model using prescribed deformations, 2D unsteady aerodynamics and free wake; $C_W/\sigma = 0.0783$, high-speed $\mu = 0.368$**

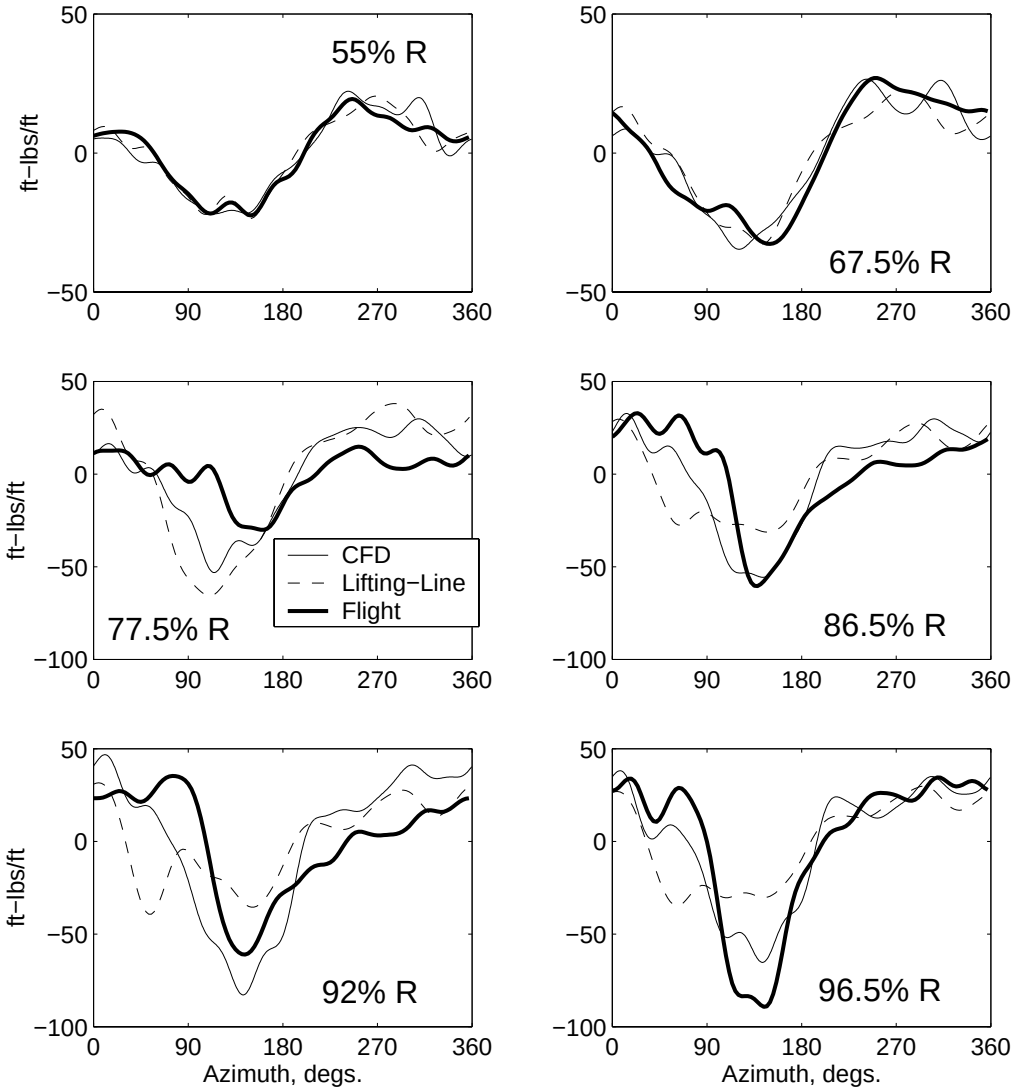

Figure 3.24: **Lifting line predictions of quarter-chord pitching moment compared with 3D CFD predictions using same prescribed deformations and single peak tip vortex free wake; $C_W/\sigma = 0.0783$, high-speed $\mu = 0.368$**

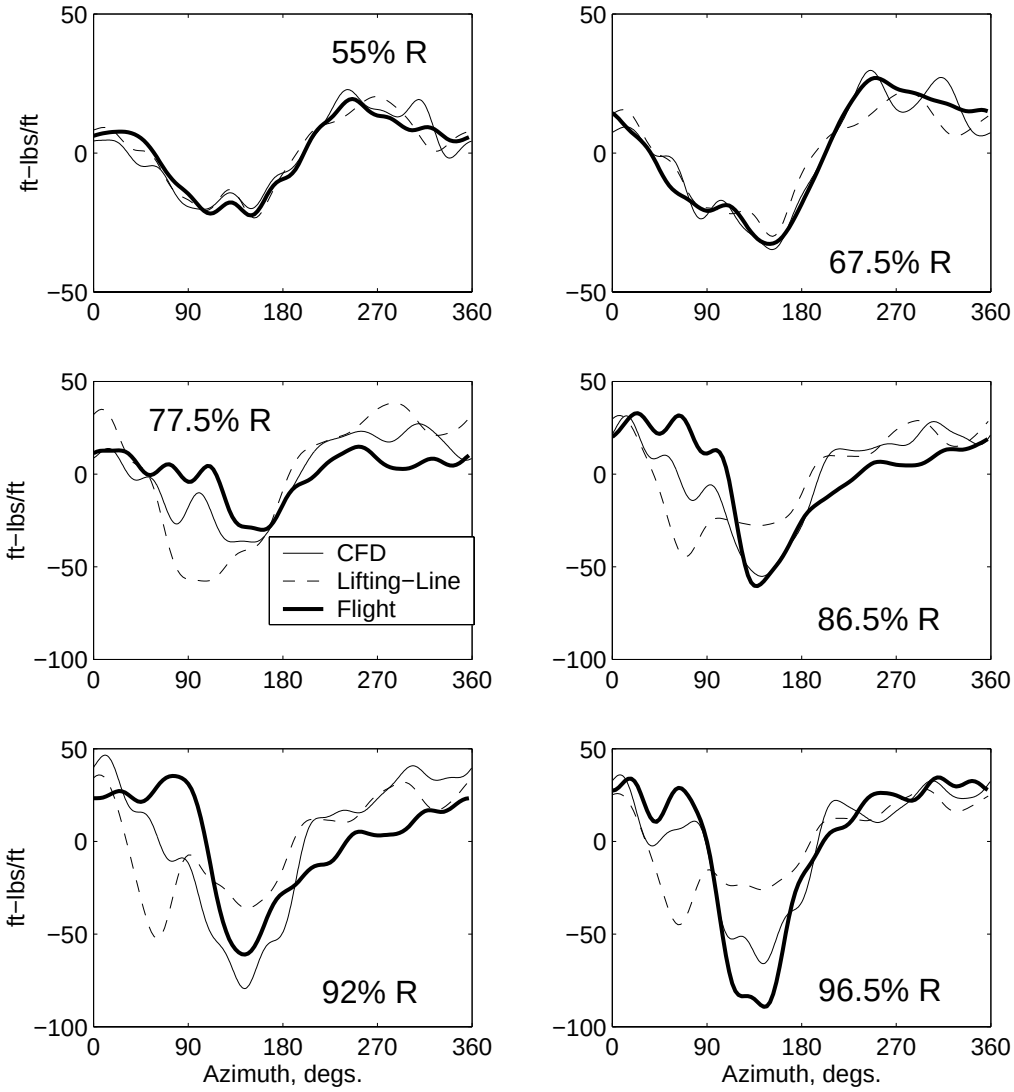

Figure 3.25: **Lifting line predictions of quarter-chord pitching moment compared with 3D CFD predictions using same prescribed deformations and single peak moving vortex free wake; C_W/σ = 0.0783, high-speed μ = 0.368**

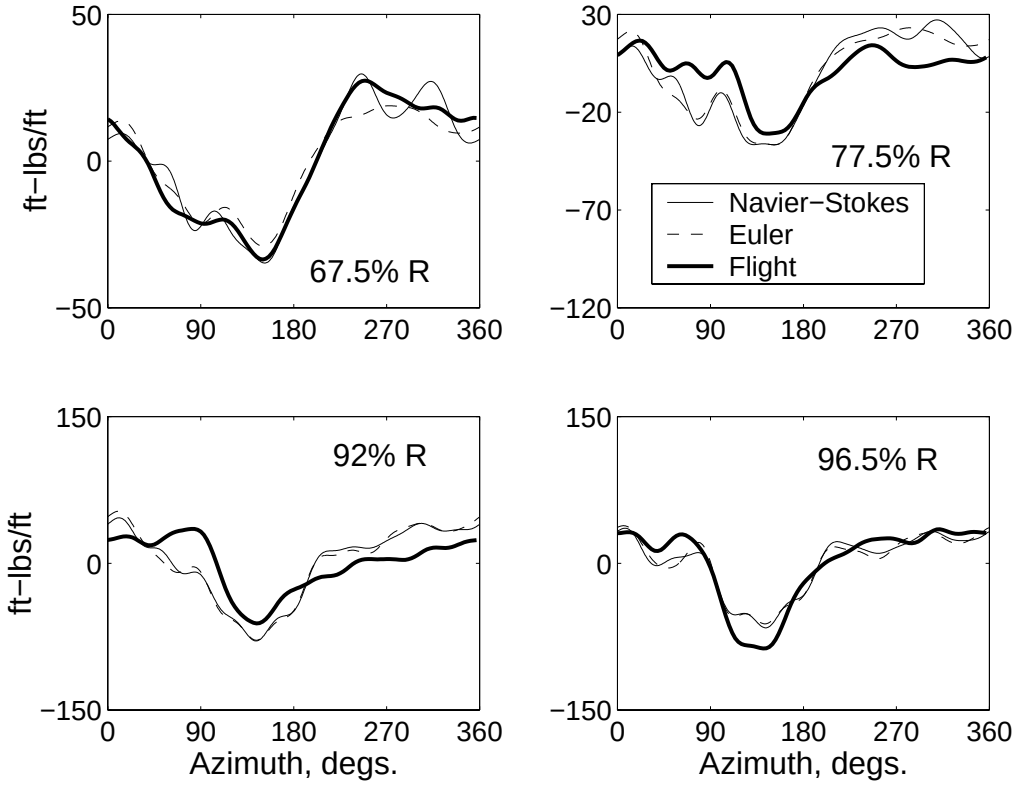

Figure 3.26: **Lifting line predictions of quarter-chord pitching moment compared with 3D CFD predictions using same prescribed deformations and single peak moving vortex free wake; C_W/σ = 0.0783, high-speed μ = 0.368**

Chapter 4

Lifting-Line Comprehensive Analysis

This chapter presents prediction and validation of basic performance, air loads and blade loads of a the UH-60A Black Hawk helicopter in steady level flight. The focus is on high-speed flight. Blade air loads and deformations are not measured or prescribed as in chapter 2 and 3 - they are calculated, along with rotor trim angles and aircraft trim attitudes, using a comprehensive rotor aeroelastic analysis. The comprehensive analysis described in this chapter uses a W-L type lifting-line aerodynamic model. Basic performance, trim, airloads and blade loads calculations in steady level flight are systematically validated with flight test data to gain insights into the fundamental mechanisms of rotor vibration and understand the limitations of prediction capabilities.

The goal is to study the consistency of air load prediction in high-speed flight

by step-wise modeling refinements. None of the modeling refinements, as will be shown, accurately predicts the phase of advancing blade lift. Harmonic analyses of flight test lift and comparison with prediction reveal that the phase prediction problem is a manifestation of inaccurate vibratory lift prediction. Between 60%-90% span location, the phase of the advancing blade lift is dominated by vibratory lift. Near the tip, the phase of the negative lift is dominated by non-vibratory components. None of the modeling refinements of blade flexibility, unsteady aerodynamics and free wake models can fully capture the basic physics of vibratory lift at high speed. At high speed, the advancing blade lift is shown to be dominated by elastic twist. Section pitching moments show significant prediction errors inboard and close to the tip.

The physics of vibratory loading is also examined from the perspective of rotor structural response. Predicted flap and lag bending moments and pitch link loads are compared with flight test data. Oscillatory and vibratory load patterns that are common to rotors of all configurations are used to assess the validity of the present analysis.

This study, along with the conclusions of chapter 2 and 3, demonstrates that both rotor wake and aerodynamic pitching moments are essential for advancing blade lift phase prediction. Accurate aerodynamic pitching moments produce accurate elastic torsion. Accurate torsion, in presence of wake effects (e.g., moving vortex free wake as shown in chapter 3) predict accurate lift phase. Without the correct elastic torsion, wake effects alone, do not improve lift phase prediction. Without wake effects, elastic torsion alone, does not completely resolve the lift phase problem

at the inboard stations (e.g., 67.5%, 77.5% R).

4.1 Comprehensive Analysis Methodology

Comprehensive Analysis involves calculation of the rotor control angles, vehicle orientation, tail rotor collective and blade response such that the vehicle trim equations and the blade periodic response equations are simultaneously satisfied. Satisfaction of the vehicle trim equations implies that the resultant forces and moments on the vehicle, averaged over one rotor revolution, become zero. There are many forms of trim equations. Broadly they can be classified into two categories; free flight and wind tunnel trim. The experimental data of interest in the present study is from flight tests, therefore a free flight trim procedure is used. In this trim procedure, it is assumed that the engine can supply all the power needed to maintain the flight condition - hence referred to as *propulsive trim*.

4.1.1 Free Flight Propulsive Trim

A free flight propulsive trim solution in steady level flight is obtained by solving the three force (vertical, longitudinal and lateral) and three moment (pitch, roll and yaw) vehicle equilibrium equations, for a specified gross weight, flight speed, flight path angle and structural and aerodynamic properties of the rotor, fuselage and tail rotor. The expressions for the vehicle equilibrium condition can be expressed as

$$\bar{\mathbf{F}} = 0 \tag{4.1}$$

where the exact form of $\bar{\mathbf{F}}^T = [F_1, ..., F_n]$ depends on the trim condition considered. In steady level flight they are

$$F_1 = D_f cos\theta_{fp} + H cos\alpha_s - T sin\alpha_s \tag{4.2}$$

$$F_2 = Y_f + Y cos\phi_s + T sin\phi_s + T_{tr} \tag{4.3}$$

$$F_3 = T cos\alpha_s cos\phi_s - D_f sin\theta_{fp} + H sin\alpha_s - Y sin\phi_s - W \tag{4.4}$$

$$\begin{aligned} F_4 =& M_{xr} + M_{xf} + Y_f(\bar{h} cos\phi_s + y_{cg} sin\phi_s) \\ & W(\bar{h} sin\phi_s - y_{cg} cos\phi_s) + T_{tr}(\bar{h} - z_{tr}) \end{aligned} \tag{4.5}$$

$$\begin{aligned} F_5 =& M_{yr} + M_{yf} + W(\bar{h} sin\alpha_s - x_{cg} cos\alpha_s) \\ & - D_f \bar{h} cos(\theta_{fp} + \alpha_s) + x_{cg} sin(\theta_{fp} + alpha_s) \end{aligned} \tag{4.6}$$

$$F_6 = M_{zr} + M_{zf} + T_{tr}(x_{tr} - x_{cg}) - D_f y_{cg} cos\alpha_s - Y x_{cg} cos\phi_s \tag{4.7}$$

where F_1, F_2, F_3 and F_4, F_5, F_6 are the vehicle force and moment (about vehicle center of gravity) residuals in the fuselage X (from hub towards tail), Y (from hub towards starboard) and Z (from hub away from fuselage, i.e. upward for level flight) directions. The fuselage fixed coordinate system X_F, Y_F, Z_F are same as the hub fixed coordinate system, X_H, Y_H, Z_H, described in section 2.1.1 (Chapter 2) except that they are fixed to the fuselage center of gravity instead of at the hub. H, Y, T are rotor drag, side force and thrust; D_f, Y_f, W are fuselage drag, side force and gross weight; similarly $M_{xr}...$, $M_{xf}...$ denote the rotor and fuselage moments; T_{tr}, x_{tr}, z_{tr} are tail rotor thrust, distance of tail rotor hub behind vehicle c.g., and distance of the tail rotor hub above the vehicle c.g.; $x_{cg}, y_{cg}, \bar{h}$ are the relative location of the rotor hub center with respect to the vehicle c.g. in the X_F, Y_F, Z_F directions. α_s

(positive nose down) and ϕ_s (positive advancing side down) are the longitudinal and lateral shaft tilts, respectively, and θ_{fp} is the flight path angle relative to an axis perpendicular to the gravity vector.

The fuselage forces and moments can be obtained using tables (in the present case from 1/4 scale wind tunnel data, as discussed later) as functions of fuselage attitude angles. The rotor forces and moments are obtained from equations (2.154). The rotor forces and moments depend on the rotor structural response to air loads.

4.1.2 Blade Response to Air Loads

Structural response is calculated by solving equations (2.101) to (2.104) using finite element method, as described in section 2.2. The treatment of the aerodynamic forcing terms occurring in the right hand side of these equations is as follows. The aerodynamic forcing terms are obtained from equations (3.22) and (3.23). Defining the following vector notations

$$\mathbf{L^A} = [\mathbf{L^A_u L^A_v L^A_w L^A_{\hat{\phi}}}]^{\mathbf{T}} \tag{4.8}$$

$$\mathbf{u} = [\mathbf{uvw}\hat{\phi}]^{\mathbf{T}} \tag{4.9}$$

the aerodynamic forces can be expressed as

$$\mathbf{L^A} = (\mathbf{L^A})_{\mathbf{0}} + (\mathbf{L^A})_{\mathbf{q}} + (\mathbf{L^A})_{\mathbf{q^2}} \tag{4.10}$$

where the subscripts $0, q, q^2$ refer to constant, linear and non-linear terms with respect to blade deformations. The linear terms are written as

$$(\mathbf{L^A})_{\mathbf{q}} = \mathbf{A_u u} + \mathbf{A_{u'} u'} + \mathbf{A_{\dot{u}} \dot{u}} + \mathbf{A_{\ddot{u}} \ddot{u}} \tag{4.11}$$

The displacement vector, $\mathbf{u}$ is discretized in terms of spatial shape functions, $\mathbf{H_s}$ and nodal degrees of freedom, $\mathbf{q}$. This discretization yields

$$\left.\begin{aligned} \mathbf{u} &= \mathbf{H_s q} \\ \mathbf{u}' &= \mathbf{H_s' q} \\ \dot{\mathbf{u}} &= \mathbf{H_s} \dot{\mathbf{q}} \\ \ddot{\mathbf{u}} &= \mathbf{H_s} \ddot{\mathbf{q}} \end{aligned}\right\} \tag{4.12}$$

where $\mathbf{H_s}$ is defined in equation (2.106) and $\mathbf{q}$ is defined in equation (2.123). The nonlinear terms, $(\mathbf{L^A})_{\mathbf{q^2}}$, are linearized as given in equation (2.112). The total aerodynamic forces are the summation of the constant, linear and nonlinear (with respect to blade deformations) forces.

$$\begin{aligned} \mathbf{L^A} =& (\mathbf{L^A})_{\mathbf{0}} + (\mathbf{L^A})_{\mathbf{q}} + (\mathbf{L^A})_{\mathbf{q^2}} \\ &= (\mathbf{L^A})_{\mathbf{0}} + (\mathbf{L^A})_{\mathbf{q}}|_{\mathbf{0}} \\ &= \mathbf{A_u H_s} + \mathbf{A_{u'} H_s'} + (\mathbf{A_u})_{\mathbf{NL}} \mathbf{H_s} + (\mathbf{A_{u'}})_{\mathbf{NL}} \mathbf{H_s' q} \\ &= \mathbf{A_{\dot{u}} H_s} + (\mathbf{A_{\dot{u}}})_{\mathbf{NL}} \mathbf{H_s} \dot{\mathbf{q}} \\ &= \mathbf{A_{\ddot{u}} H_s} \ddot{\mathbf{q}} \end{aligned} \tag{4.13}$$

Using equation (4.13) in the virtual work expression given in equation (2.98), the aerodynamic mass, stiffness and damping matrices, $(M_b^A)_i, (K_b^A)_i, (C_b^A)_i$ are obtained. These aerodynamic matrices are then added to the structural matrices in equation (2.111). Note that, for subsequent natural mode calculation, the aerodynamic mass and stiffness matrices are not used. The aerodynamic mass matrices arise out of unsteady, noncirculatory forces. In the present formulation, they are incorporated through impulsive terms in the unsteady aerodynamic model. Therefore

the aerodynamic mass matrix is zero.

4.1.3 Solution Procedure

A comprehensive analysis solution is obtained when the trim angles and vehicle attitudes, blade response and rotor wake converge. The blade response requires trim angles and wake (inflow) as input. The wake model require prior knowledge of the circulation and blade motion and, therefore, cannot be used in the first iteration. The trim angles require rotor forces and moments as input which depend on blade response. Clearly, an iterative procedure is necessary.

The comprehensive analysis solution involves three steps - 1. Initial control angle estimate, 2. Vehicle Jacobian calculation and 3. Coupled trim. The third step involves blade response, air loads and vehicle trim iterations. The solution procedure involving the three steps are described below. Step 1 and 2 describe the initial control estimate and Jacobian calculation. Step 3 describes the coupled trim iterations.

1. Because of the non-linear nature of the trim analysis, it is important to have a reasonably accurate first guess for the trim angles. An analysis based on flap dynamics of a rigid blade, uniform (or linear) inflow and linearized (with small angle assumption) vehicle trim equations provides this initial guess. The fuselage air loads are obtained using the vehicle attitude angle and fuselage property tables. The tail rotor thrust is related to the tail rotor collective using a simple momentum theory.

2. The vehicle Jacobian matrix is calculated about the control angles obtained in Step 1. In general, it can be calculated about any set of user input control angles. For a given set of control angles, the blade air loads, full structural response (flap, lag and torsion) and hub loads are calculated. The steady component of the hub loads (that is 0p harmonics) are the rotor forces and moments. Using these rotor forces and moments, the vehicle residuals are calculated using equations (4.2) to (4.7). These non-linear vehicle equilibrium equations are linearized about the initial controls using a Taylor's series expansion,

$$F(\theta_i + \Delta\theta_i) = F(\theta_i) + \frac{\partial F}{\partial \theta}|_{\theta=\theta_i}\Delta\theta_i = 0 \tag{4.14}$$

Equation (4.14) can be re-arranged to give

$$\left[\frac{\partial F}{\partial \theta}\right]_{\theta=\theta_i} \Delta\theta_i = F(\theta_i) \tag{4.15}$$

Equation (4.15) is used in Step 3 to take the control angles from the initial estimate to a final converged solution. For a converged solution, $\Delta\theta$ and $F(\theta_i)$ are zero. In this step, the goal is to find the trim Jacobian, $\partial F/\partial\theta$. The trim Jacobian is calculated using a forward difference approximation at $\theta = \theta_0$, where θ_0 are the initial control estimates, and it is generally held constant throughout the analysis to computation time. To compute the Jacobian, the controls are perturbed individually and structural response and hub loads are calculated. The loads are then input to the vehicle trim equations (4.2) to (4.7) and the change in residuals, F, are computed using

$$\frac{\partial F}{\partial \theta} \approx= \frac{F(\theta + \Delta\theta) - F(\theta)}{\Delta\theta} \tag{4.16}$$

where $\Delta\theta$ are small control perturbations. These are taken as 5% of the initial control estimates.

3. Step 3 involves the iterative convergence of blade response, vehicle trim and rotor wake solution using the vehicle Jacobian computed in Step 2. Starting from the initial controls estimate, the control angles are updated using

$$\theta_{i+1} = \theta_i + \Delta\theta_i \tag{4.17}$$

where $\Delta\theta_i$ is obtained from equation (4.15). The blade response is considered converged, when the current response is within one percent of the previous response. The vehicle trim is considered converged when the trim convergence function reaches a value of 0.001. The trim convergence function is defined as

$$\epsilon = \sqrt{\sum_{i=1}^{6} F_i^2} \tag{4.18}$$

For example, if only the thrust equation is considered

$$\epsilon \approx \frac{T - W}{m_0 \Omega^2 R^2} \tag{4.19}$$

The value 0.001 was found satisfactory in that the control angles and steady hub loads converged to within 1 to 2% of their previous values. The first 20 iterations use a linear inflow model, then the inflow is calculated using a free or prescribed wake model. This is to let the blade response converge to a reasonable extent before a refined inflow model is used. The wake model and the unsteady model are both activated at the same time for consistency. The wake model accounts for the trailed wake, the unsteady model accounts for the shed wake.

In high-speed flight, $30 - 35$ coupled trim iterations are necessary for convergence. In transition flight, about $18 - 22$ iterations are required. The non-uniform wake models and the unsteady model are activated after 12 iterations in this case. Note that the first 7 iterations involve the vehicle Jacobian calculation. The non-uniform inflow (and air foil tables) are not used during the Jacobian calculation.

4.2 UH-60A Baseline Model

The UH-60A helicopter is modeled in UMARC (University of Maryland Advanced Rotorcraft Code) as an aircraft with a single main rotor and a tail rotor. The structural model of the rotor blades is same as that discussed in Chapter 2. The aerodynamic model of the rotor blades is same as that discussed in Chapter 3.

The main rotor has a 3 degrees of forward shaft tilt angle. Fuselage aerodynamic properties, obtained from 1/4-scale wind tunnel experimental data are shown in Fig. 4.1. Fuselage 'tail on' aerodynamics are used in the present analysis. 'Tail on' aerodynamics include the effect of the horizontal tail. For example, from Fig. 4.1, fuselage lift at a positive angle of attack (nose down) is more negative with 'tail on', while the pitching moment is positive (nose up). The zero-angle fuselage flat plate area of a UH-60A ranges from 25.69 to 26.2 ft^2. The UH-60A of the Airloads Program contained additional components that increased the flat plate area to 36.34 ft^2 at zero angle of attack [176]. This drag curve is plotted in bold in Fig. 4.1. It is

obtained by fitting a parabola to the 'tail on' drag curve between -10 to 10 degrees and then shifting it up. Fuselage side slip angle is assumed to be zero. All airfoil and fuselage aerodynamic properties are obtained from the master database. Fuselage dynamics are neglected in this study.

The tail rotor has a -18 degrees of twist and a cant angle of 20 degrees to the port side (i.e. towards the retreating blade). The tail rotor thrust is calculated using uniform inflow and a 2D strip theory.

The main rotor radius is 26.83 ft with an aerodynamic root cut out of 20%. The nominal chord is 1.73 ft. The rotor RPM is 258. All blades are identical. For the baseline comprehensive analysis, a fully rolled-up single tip vortex free wake model is used. As in Chapter 3, unsteady aerodynamics is modeled using Leishman-Beddoes attached flow formulation [67, 68]. In this formulation the angle of attack variation over time is discretized as a consecutive series of step inputs. The airload response to each step input is calculated using semi-empirical indicial response functions depending on contributions of plunge, pitch and inflow to each step input. The lift response to each step input assymptotes to the airfoil table supplied steady state lift value. The total response is then calculated using Duhamel's integral based superposition principle. The attached flow formulation is used because flight test data show no evidence of dynamic stall at high-speed flight below a vehicle weight coefficient of $C_W/\sigma = 0.12$ [163]. The W-L type lifting-line model is used to calculate air loads.

Aerodynamic blade sweep is accounted for by a swept bound vortex line in the free wake and W-L models. The airfoil table look up in the swept region is

based on effective normal Mach number correction. In the swept region, the SC1095 airfoil is oriented normal to the local leading edge. The pressure taps for air load measurements are however normal to the unswept blade leading edge. The airfoil property tables are read on the basis of local angle of attack and effective normal Mach number. The properties are then reduced to the pressure tap axis by dividing them by the square of the cosine of the sweep angle.

Aerodynamic interactions between main rotor, fuselage and tail rotor is neglected in this study.

4.3 Trim Solution

In order to validate overall aerodynamics, basic performance calculations at steady level flight are compared with flight test data. Main rotor power predictions are plotted in Fig. 4.2 for two different vehicle weight coefficients. Satisfactory predictions are obtained at all flight speeds. Next, main rotor control angles, fuselage attitudes and tail rotor collective angle are compared with flight test data. Figure 4.3 shows these angles corresponding to $C_W/\sigma = 0.08$, for a range of forward speeds. In general, prediction of longitudinal trim angles are good at high speed. Prediction of lateral trim angles does not show the correct trends compared to flight test data. A fuselage lateral center of gravity offset of 4% rotor radius to the starboard side affects the lateral cyclic, but does not produce the right trends.

4.4 Lift Prediction

Lift variation near the blade tip is calculated over a range of forward speeds and is shown in Fig. 4.4. At the low speed transition regime ($\mu = 0.110$), high lift gradients occur in the first and fourth quadrants. At high speed ($\mu = 0.368$), a large region of negative lift occurs in the first and second quadrants. These are the two vibration critical regimes in steady level flight. In the following section, the airloads at these two speeds are studied in details.

Calculated lift at transition speed is compared with flight test data at six radial stations in Fig. 4.5. The strong lift gradients occurring in the first and fourth quadrants are the primary source of rotor vibration at this speed. This can be demonstrated by extracting the lift harmonics and then adding three to ten harmonics at all radial stations to generate a surface plot, Fig. 4.6(a). The surface plot shows that the addition of three to ten harmonics cancel out at all radii and azimuths and only result in two impulsive loadings outboard of 60% radius. Thus, these two impulsive loadings are the source of all vibratory harmonics.

The predicted vibratory lift, Fig. 4.6(b), shows similar impulsive airloads near the blade tip. In the computation, they arise from the free wake model, due to the intertwining of tip vortices whose effect is felt near the outer edges of the rotor disk [3]. In the case of prescribed wake, the trajectories of the tip vortices from the four blades form a prescribed sequence of epicycloids. These epicycloids overlap in radial direction in the first and fourth quadrants as they convect sequentially below the rotor plane. In the case of free wake, they do not convect sequentially

below the rotor plane. The older tip vortices from the blades ahead convect above the rotor plane. As they gradually descend towards the rotor plane they start wrapping around the newer tip vortices because of their mutual interactions. This intertwining happens only in the transition speed and occurs twice in the two regions of radial overlap, once in the first and then in the fourth quadrant. This effect is experimentally observed in Refs. [149, 150]. The effect of this phenomenon on blade loads calculations have also been shown in Ref. [99].

The impulsive airloads remain strong as far inboard as 55% radius. Although, the analysis captures the basic physics of vibratory lift at the transition speed, it under-predicts the radial extent of the first impulse. This error leads to significant under-prediction of vibratory blade bending moments at this speed. A possible source of this discrepancy is discussed later in the study of section angle of attack.

The measured vibratory lift (3-10/rev) at high speed is plotted in Fig. 4.7(a). The reverse flow regions in the retreating blade have no contribution to vibratory lift. The vibratory lift starts appearing in the advancing blade outboard of 40% radius increasing towards the blade tip. It appears in the form of a strong up-down impulse at the junction between first and second quadrant, followed by a second impulse in the second quadrant. The first impulse occurs earlier in azimuth from the tip inboard. It then occurs progressively later in azimuth with decreasing radius. The second impulse occurs at a relatively constant azimuth irrespective of the radial station. Both the impulsive ridges remain strong from tip to 50% radius. Very similar high-speed vibratory lift was reported in Ref. [120] for the H-34 rotor (wind tunnel and flight test), which is also an articulated rotor. However, for the H-34

rotor these extended from the tip to only 80% radius inboard. Unlike at transition speed, the analysis at high speed, Fig. 4.7(b), does not appear to pick up all the basic physics of vibratory loading. The strong impulse in the advancing blade is not correctly predicted. This deficiency in prediction appears as a phase error in section lift. The section lift at different stations is compared with flight test data in Fig. 4.8. The error in lift phase is conspicuous inboard (67.5%, 77.5% radius), where the effect of the up-down impulse is clearly visible. It occurs in the flight test lift near the 90 degree azimuth causing an up-down bump at 67.5% R and a plateau at 77.5% R. The impulse delays the drop in lift by 35 degrees.

One of the possible reasons of the first up-down impulse was indicated in Ref. [120] to be the presence of a negative tip vortex, shed from the blade tip in the regions of negative lift. Such a model will be investigated in the next two sections to study its effect on lift prediction.

4.5 Effects of Modeling Refinements on High-Speed Lift

One of the goals of the present work is to examine the sensitivity of lift prediction to various modeling assumptions. Starting from a simplified model, progressive modeling refinements are incorporated one at a time. The simplified model assumes that the rotor is represented by one flap and one lag mode and aerodynamics is represented by linear wake and quasi-steady flow. The model is then refined in a

step-wise manner to study the effects of (i) blade flexibility, (ii) prescribed wake models, (iii) free wake models and (iv) linear unsteady aerodynamics. The 77.5% radial station is chosen for this study.

Figure 4.9(a) shows that even with the simplified model, the basic 2/rev nature of the lift appears to be in place. This implies that proper vehicle trim is the first step for accurate lift prediction. Addition of flexible flap and lag modes improve lift prediction in the first and second quadrant. The most significant improvement is noticed with the addition of a torsion mode. It improves lift prediction both in magnitude and phase at all rotor azimuths. Therefore the torsion mode is important for lift prediction. Considerable lift fluctuations occur in the first quadrant and in the beginning of the second quadrant. The most conspicuous of them occur as a sharp up-down impulse near 75 degree azimuth. None of these fluctuations are captured by changes in blade flexibility.

Prescribed and free wake models are investigated next. All wake models use 4 turns of the wake and a wake discretization angle of 15 degrees. Figure 4.9(b) shows the result of replacing the linear inflow model with two prescribed wake models. The first prescribed wake model is a single peak model. Here, the wake consists of a single rolled up tip vortex trailed from the blade tip. The strength of the tip vortex trailed from each azimuth location is equal to the value of maximum bound circulation occurring outboard of 50% blade radius. The second model consists of nine prescribed trailers trailing from nine equally-spaced span locations, with strengths compatible with blade bound circulation. This model predicts highly distorted lift on the advancing blade. The single peak model is qualitatively closer

to flight test data. This suggests that the trailed vortices quickly roll up into a strong tip vortex very near the blade. The single peak prescribed wake model is then replaced with a single peak free wake model , Fig. 4.9(c). There is no significant difference between a single peak free wake and a single peak prescribed wake model.

Next, several refinements are performed on the free wake model. Figure 4.9(d) shows the effect of three free wake models on lift prediction at 77.5% radius : a single peak model, a dual peak model and a dual peak with prescribed inboard trailers. In the dual peak free wake model, a vortex of negative strength is trailed from the tip when the lift at the blade tip is negative [52]. The possibility of a negative vortex in the tip region was suggested by Ref. [120] and the intention here is to study its influence on predicted airloads. In the dual peak model, the strength of the negative vortex is equal to the maximum negative circulation attained near the blade tip. The positive vortex continues trailing from an inboard radial station. This station is taken where the circulation changes from a positive value to a negative value. The strength of the positive vortex is equal to the sum of the maximum bound circulation occurring outboard of 50% blade radius and the maximum negative circulation occurring near the blade tip. The later is non-zero only in the azimuths of negative lift. The dual peak model deteriorates lift prediction in the advancing blade at this radius station. A set of five prescribed trailers are then added to the dual peak model. These trailers trail the inboard 50% of the blade bound circulation from equally spaced span locations and include a root vortex. The presence of these trailers deteriorates lift prediction further.

The next modeling complexity incorporated is unsteady aerodynamics in form

of Leishman Beddoes attached flow formulation [67, 68]. Figures 4.9(e) and 4.9(f) show the effect of this refinement. The effect of unsteady aerodynamics is a slight attenuation in lift magnitude and a small lag in phase. Although the change is favorable, there is no significant improvement in lift prediction at 77.5% radial station with unsteady aerodynamics. The single tip vortex model with unsteady aerodynamics , Fig. 4.9(e), in general shows improved prediction than the dual peak model, Fig. 4.9(f) at this radial station.

Next, lift prediction near the blade tip is investigated using two free wake models : a single peak free wake model and a dual peak free wake model. The single peak free wake model is used both with quasi-steady and unsteady aerodynamic models. Figure 4.10 shows lift prediction near the blade tip at 92% and 96.5% radius. The unsteady aerodynamic model improves lift prediction at the tip by improving the lift phase. The dual peak model appears to further refine the lift prediction in the advancing blade.

In conclusion, none of the modeling refinements captures the lift phase delay in the advancing blade lift. The dual peak free wake model marginally improves lift prediction near the blade tip. However, it deteriorates prediction inboard. In order to better understand the problem of this phase delay, the high-speed lift at four radial stations are broken up into their harmonic contents. This diagnostic approach is presented in the following section.

4.6 Diagnosis of High-Speed Lift

An approach similar to Hooper [120] is adopted to understand the source of lift phase error at high speed. The flight test lift is separated into 0-24 harmonics. The first 10 harmonics form the subject of study. They are divided into two groups: (i) non-vibratory group involving 0 (steady), 1 and 2/rev harmonics and (ii) vibratory group involving 3-10/rev harmonics. The non-vibratory and vibratory lift groups are studied at four radial stations.

The first station is at 67.5% radius. Figure 4.11 describes the lift diagnosis at this station. In Fig. 4.11(a), the total flight test lift is broken into its non-vibratory and vibratory components. The vibratory component is plotted with the steady lift for ease of illustration. The vibratory lift appears to dominate the phase of the total lift in the advancing blade. This is further verified in Figs. 4.11(b) and 4.11(c). In Fig. 4.11(b), the flight test data is compared with two plots. The first plot is predicted lift (all harmonics). Next, from this predicted lift the non-vibratory part (0,1,2/rev) is removed and replaced with the non-vibratory part of flight test lift. This is the second plot. The phase prediction does not improve. In Fig. 4.11(c), the vibratory part (3-10/rev) of the predicted lift is removed and replaced with the vibratory part of flight test lift. In this case, the phase problem appears resolved. Therefore, in order to predict the correct lift phase, it is necessary to predict the correct vibratory lift. Figure 4.11(d) compares predictions with measurements for the vibratory lift harmonics with two free wake models : single peak and dual peak. Large phase and magnitude deviations occur in the advancing blade. The impulsive

loading at the junction of the first and second quadrant is not captured at all. The dual peak model deteriorates the predicted phase at this station.

The same diagnosis is performed at the 77.5% radial station, Fig. 4.12. From Fig. 4.12(a), it is seen that the phase delay and the sharp up-down impulse near 75 degree azimuth is clearly the effect of vibratory lift. As a result, replacing the non-vibratory part of the predicted lift with flight test data does not bring the lift phase any closer in the advancing blade, Fig. 4.12(b). But replacing the vibratory part does, Fig. 4.12(c). Comparison between calculated and measured vibratory lift harmonics is performed in Fig. 4.12(d). The effect of the dual peak model at this station is similar to 67.5% Radius. It produces a deterioration in the phase of vibratory lift. Vibratory lift predictions show very large phase errors with both the free wake models. This error dominates the overall lift prediction and produces the error in phase of the advancing blade.

Next, the diagnosis is performed at two outboard stations. Figure 4.13 shows the analysis at 92% radial station. At this radial station, the lift phase is dominated by the non-vibratory lift harmonics, Fig. 4.13(a). As a result, improvements are noticed in the first quadrant by replacing the 0,1,2/rev of analysis with flight test data, Fig. 4.13(b). The vibratory components still continue to play a part in the gentle undulations of lift before its final plunge into the peak negative value, Fig. 4.13(c). Figure 4.13(d) shows the comparison of predicted and measured vibratory lift harmonics. The vibratory lift harmonics show improved prediction at this station. The dual peak model provides further refinement in the advancing blade capturing the peak loading in the first quadrant. However, predictions in the second quadrant are

deteriorated.

Diagnosis of lift at 96.5% radial station (Fig. 4.14) reveals a similar trend as at the 92% station. Once again the negative lift phase is dominated by the non-vibratory lift, Figs. 4.14(a), 4.14(b) and 4.14(c). But the vibratory lift continues to contribute to the undulations before the final lift drop (Fig. 4.14(d)) in the advancing side. Figure 4.14(d) compares vibratory lift of flight test data with analysis. As in the case of 92% radius station, the vibratory lift harmonics show improved prediction at this station. Again, the dual peak model provides significant improvement in capturing the peak loading in the first quadrant. Predictions in the second quadrant are deteriorated. The effect of improved vibratory lift prediction in the first quadrant near the blade tip is seen later on the prediction of flap bending moments.

4.7 Study of Section Angle of Attack

To gain insight into the mechanism of lift generation, the azimuthal variation of angle of attack is calculated. The net angle of attack at a section consists of a combination of four factors : (i) collective and cyclic controls added to the rigid pretwist, (ii) inflow distribution, (iii) blade flap and lag motion, and (iv) elastic torsion. The study is performed first at transition flight and then at high-speed flight.

Figure 4.15(a) shows the detailed angle of attack distribution at transition speed for a station at 77.5% radius. The angle of attack distribution multiplied by the square of section Mach number shows the qualitative nature of lift contributed by these effects, as shown in Fig. 4.15(b). (The lift coefficient depends both on angle of attack and incident Mach number but the variation with respect to incident Mach number is being neglected here as a first order approximation). In the transition speed, the shape of both the angle of attack and the lift are dominated by the inflow component. The inflow contribution to the section lift clearly generates the impulsive lifts in the first and second quadrant. But the accuracy of the first impulse is affected by torsion response which shows a noticeable impact only on the advancing blade, Fig. 4.15(b). An error in torsion response can significantly contribute to the error in the prediction of the first impulse, Fig. 4.5.

Figure 4.16(a) shows the detailed angle of attack distribution at high speed for a station at 77.5% radius. Figure 4.16(b) shows the qualitative lift contribution from each component. The sinusoidal increase of the retreating blade angle of attack

above the advancing blade angle of attack, Fig. 4.16(a) shows the dominating effect of cyclic pitch variation. Effects of wake (inflow) and blade flap and lag motions are secondary. The drop in angle of attack in the advancing side is due to cyclic pitch effect. The section lift, however, depends on both the angle of attack variation and the relative velocity variation. This effect is significant in high speed. When relative velocity variation is taken into account, Fig. 4.16(b), elastic torsion is seen to dominate the lift curve shape in the advancing side. In the retreating side, cyclic pitch, wake and blade motions have an equally significant influence. In conclusion, although the angle of attack on the advancing blade is dominated by cyclic pitch, the drop in lift is most strongly influenced by the elastic torsion. This is due to the relative phasing of velocity variation, elastic torsion deformation and the cyclic pitch angles.

Figure 4.3 showed that there is a significant discrepancy in the prediction of lateral cyclic angle. An increased lateral cyclic like the test data would shift the phase of the cyclic pitch input. It is now investigated whether this effect can be carried to the advancing blade lift phase. Sensitivity of section angle of attack to an increase in lateral cyclic pitch is shown in Figs. 4.17(a) and 4.17(b) (values corresponding to increased cyclic are plotted in bold). A higher lateral cyclic of 8 degrees is obtained by shifting the vehicle center of gravity by 4% of rotor radius to the starboard side. Increase in lateral cyclic shifts the phase of the cyclic pitch favorably by around 35 degrees, Fig. 4.17(a). But this phase shift is not transmitted to the final angle of attack distribution. The increased lateral cyclic produces a flapping motion which reduces the retreating side angle of attack distribution and

generates a roll moment to the left. The angle of attack distribution on the advancing side is not influenced. The lift in the advancing blade therefore remains dominated by the torsion response, Fig. 4.17(b), which is affected marginally by the increase in lateral cyclic.

4.8 Pitching Moment Prediction

In the preceding sections, it is observed that the lift on the advancing blade in high-speed flight is dominated by elastic torsion. Elastic torsion also appears to affect the accuracy of advancing blade lift in transition flight. Prediction of elastic torsion depends on the prediction of section pitching moments.

Figure 4.18 compares the predicted pitching moments with flight test data at low speed ($\mu = 0.110$). The qualitative trends in predicted values compare well with flight test data from 77.5% to 96.5% radius. However, except 86.5% and 92% radius location, all other stations show a significant deviation in the steady value. The inboard sections at 55% and 67.5% radius show significant error both in steady value and in the 1/rev waveform.

Figure 4.19 shows comparison of calculated pitching moments with flight test data at high speed ($\mu = 0.368$). Pitching moment predictions in the advancing blade are in general less satisfactory in the high-speed case compared to the low speed case. Like the low speed case, predictions at the inboard stations and near the tip show a significant deviation in the steady value. At 77.5% radius, the predicted pitching moment drops about 45 degrees earlier in phase than flight test data. The prediction

is poor at all rotor azimuths at this station although the oscillatory amplitude is satisfactorily predicted. The premature drop in predicted pitching moment at this station at high-speed can be a possible cause of the premature drop in predicted lift. The pitching moment determines elastic torsion which is the dominant contributer to the advancing blade lift at high-speed lift. However, at 96.5% span there is a lag in predicted pitching moment drop, which does not appear to get translated into a phase lag as needed in lift prediction. Although the peak to peak variations are well captured at 86.5% and 92% radius stations, significant errors occur in the prediction of phase and higher harmonics. In general, except near the blade tip at 96.5% radius station, the magnitude of oscillatory pitching moments are similar to flight test values at all radial stations. Significant deviations occur in waveform. This is reflected in the pitch-link loads.

4.9 Blade Structural Loads

The problem of vibratory loading is now examined from the perspective of rotor structural response. Bousman [121], examined and compared structural response of eight full-scale rotors at high-speed level flight conditions in absence of dynamic stall. Consistent oscillatory and vibratory load patterns were observed which were largely independent of rotor configurations. These behavioral similarities in vibratory loading were identified as appropriate tests for evaluation of a comprehensive analysis. In this section, predicted vibratory loads are compared with UH-60A flight test data. Prediction of load patterns common to all rotor configurations are

investigated.

First, the predicted flap bending moment variations at high speed are compared with flight test data, Fig. 4.20(a). The predicted values show the right trends in the first and fourth quadrants but show large deviations at the junction between the second and third quadrants. The predicted lag bending moments, Fig. 4.20(b), show similar 4/rev and 5/rev qualitative behavior as flight test.

The dominant flap vibratory response of helicopter rotors occur at 3/rev, independent of rotor type or blade number [121]. This is due to the proximity, in general, of the second flap frequency to 3/rev. Also, the phase of the 3/rev response is seen to remain largely constant with increase in forward speed. These trends are correctly predicted by the present analysis. Figure 4.21(a) shows the radial distribution of predicted vibratory flap bending moment at high speed. The primary response is clearly at 3/rev with the second flap bending mode playing a dominant role. The vibratory moment at 50% radius is then plotted for a range of advance ratios (0.110 - 0.368). The predicted values, as shown in Fig. 4.21(b), capture the qualitative behavior of magnitude and phase variation as seen in flight tests [121]. An initial peak in the transition regime is followed by gradual reduction. Above advance ratio 0.25, the bending moment starts increasing again. The phase of the dominant 3/rev component, on the other hand, does not alter with increase in forward speed.

The 3/rev and 4/rev components of the vibratory flap bending moment are now extracted and compared with flight test data in Figs. 4.22 and 4.23 respectively. Predictions are compared with both Flight 85 and Flight 9 data. The Flight 85 data are available only at two flight speeds. Flight 9 data, produced from Ref. [99] are

the closest data available in the published literature for validating bending moment predictions at progressively increasing forward speeds. They are used here to obtain a general understanding of the characteristic values of magnitude and phase. The 3/rev moment is at 50% span. The 4/rev moment is at 70% span. Predictions are performed with the following wake models - (i) linear wake, (ii) prescribed wake with a single tip vortex, (iii) free wake with a single tip vortex (baseline analysis) and (iv) dual peak free wake.

Figure 4.22 shows the 3/rev flap bending moments. A large part of the 3/rev moment at high speed arises directly from azimuthal velocity variation. Hence predictions from linear inflow model are close in magnitude to predictions from prescribed and free wake models, Fig. 4.22(a). However the prescribed and free wake models improve the phase prediction, Fig. 4.22(b). The free wake model significantly under-predicts the 3/rev flap bending moment at transition speed. This is because of the significant under-prediction of the impulsive lift in the first quadrant at the inboard stations (Fig. 4.5). The analysis captures the rapid increase from moderate to high speeds. The dual peak model has an influence on the calculations only above advance ratio 0.2 because the negative tip vortex starts forming above that speed. The dual peak free wake model improves 3/rev flap bending moment prediction at high speed, both in magnitude and in phase.

For 4/rev flap bending moment calculation, nine flap modes are used in the analysis. The accuracy of the bending moment predictions are assessed by comparing predictions by two methods: (i) force summation (integration of spanwise aerodynamic and inertial force distributions) and (ii) modal method (direct calcu-

lation from beam curvature). When both the methods converge exactly to the same solution, it is considered accurate. For this purpose, nine flap modes are necessary for 4/rev moment. However, with five flap modes, force summation method generates a closer approximation to the nine mode converged solution.

Figure 4.23 shows the 4/rev flap bending moments. Predictions show a substantial contribution of wake modeling at high-speed. Unlike the prediction of 3/rev moment, the prescribed and free wakes differ in the prediction of 4/rev magnitude. The baseline analysis (single peak free wake model) shows a significant over-prediction for 4/rev at high speed. Prediction of 4/rev phase is not as satisfactory as the 3/rev phase. The test data for 4/rev flap bending moment show a sudden drop in magnitude above advance ratio 0.2 (Fig. 4.23(a)). This behavior is not predicted by the baseline analysis. However, as the negative vortex starts forming above advance ratio 0.2, the dual peak model appears to move towards the correct trend.

The predicted torsion bending moments at three radial stations and the pitch link load at high speed is shown in figure 4.24. There is a measurement uncertainty at 90% R. The peak magnitudes are under-predicted at 30% R and 70% R. The waveforms are unsatisfactory. The integrated effect of the errors in torsion bending moments is seen in the pitch link load. Although the peak to peak magnitude is reasonably predicted, the predicted waveform is erroneous. This is because of inaccurate pitching moment predictions.

4.10 Concluding Remarks

Based on the lifting-line comprehensive analysis described in this chapter, the following conclusions can be drawn :

1. The lift phase error in high-speed flight is not limited to negative lift at the outer portions of the rotor blade. The problem extends as far inboard as 67.5% span. The lift phase error is a manifestation of inaccurate prediction of vibratory lift. Between 60%-90% span location, the phase of the advancing blade lift is dominated by vibratory lift. Therefore, for accurate prediction of blade lift at these locations, it is necessary to predict the vibratory component accurately. Near the tip, outboard of 90% radius, the phase of the negative lift is dominated by non-vibratory components involving 0, 1 and 2/rev. A satisfactory prediction of 1 and 2/rev phase, therefore, can provide a good phase prediction of negative lift. The undulating delay in the decay of lift is still a contribution of vibratory lift.

2. High-speed vibratory lift in Black Hawk is very similar to the 'up-down impulse and ridge' phenomenon noted by Hooper for H-34 test data. However, in the case of H-34 rotor, this phenomenon appears only near the outer 20% of the blade. For the Black Hawk, this phenomenon is observed to take place as inboard as 40% span. As a result, modeling a negative tip vortex (dual peak free wake) shows no improvement in lift prediction at the inboard stations. Near the tip, the dual peak model improves prediction of vibratory lift in the first quadrant but deteriorates in the second.

3. Error in lateral cyclic prediction does not appear to be the cause of the lift phase error. Elastic torsion is the most significant contributer to the advancing blade lift in high-speed forward flight.

4. At transition speed, the far wake generated rotor inflow is the most significant contributer to blade lift. While a free wake model captures the basic phenomenon of vibratory airloads at this speed, the accuracy of prediction is also affected by elastic torsion.

5. Section pitching moment predictions are unsatisfactory at high-speed. However, errors in predicted pitching moments at high-speed are not consistent with errors in predicted lift phase at all radial stations.

6. The predicted 3/rev flap bending moments show the correct trends as in flight test. The magnitude is under-predicted by 50% at all flight speeds. At transition speed, the under-prediction is due to the under-prediction of the impulsive airload in the first quadrant. At high-speed, improved prediction of 3/rev flap bending moment is obtained with the dual peak free wake model. 4/rev flap bending moment predictions are less satisfactory with the dual peak free wake model producing marginal improvements.

7. Errors in predicted pitching moments are reflected in torsion bending moment and pitch link load. Although the peak to peak magnitude of the pitch link loads shows reasonable agreement with test data at high speed, the predicted waveform is unsatisfactory.

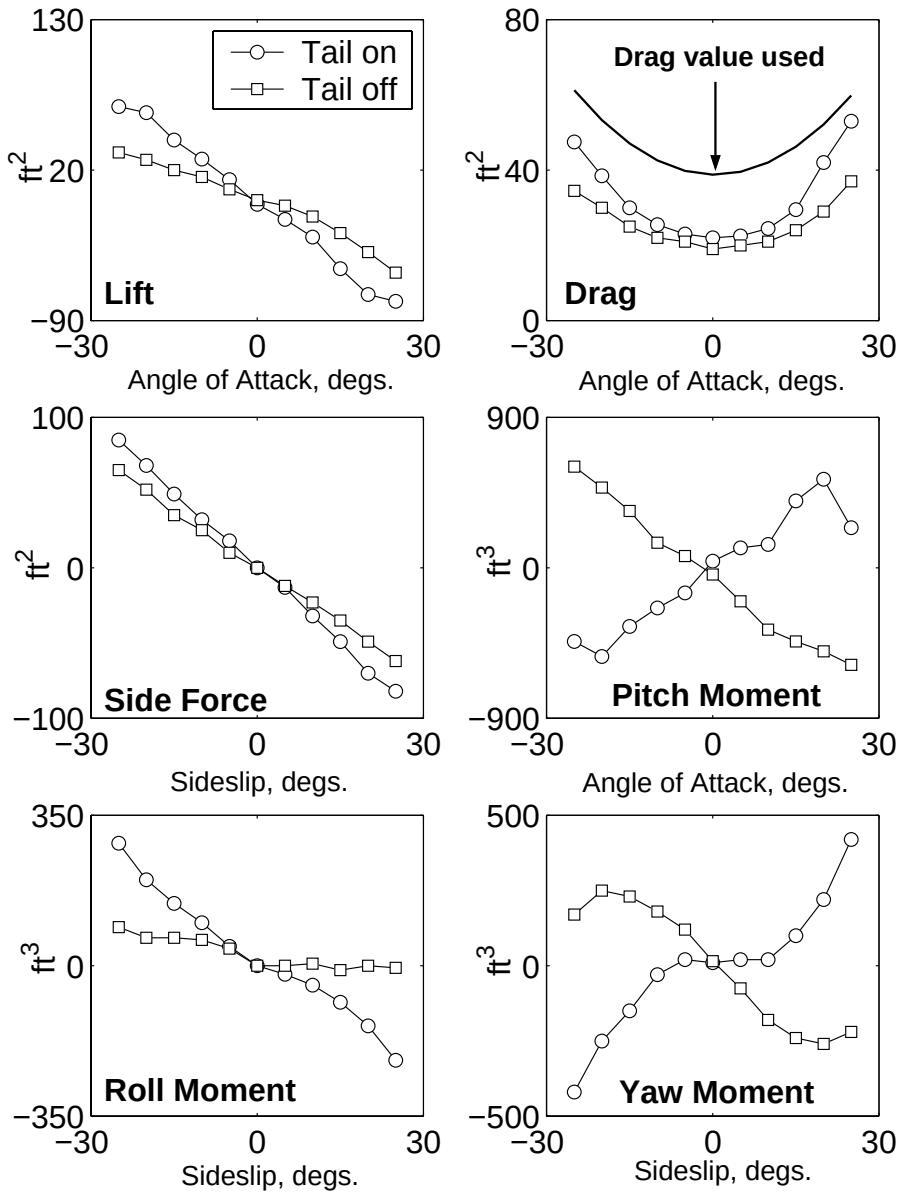

Figure 4.1: **UH-60A fuselage properties with (tail on) and without (tail off) horizontal tail (1/4-scale wind tunnel data)**

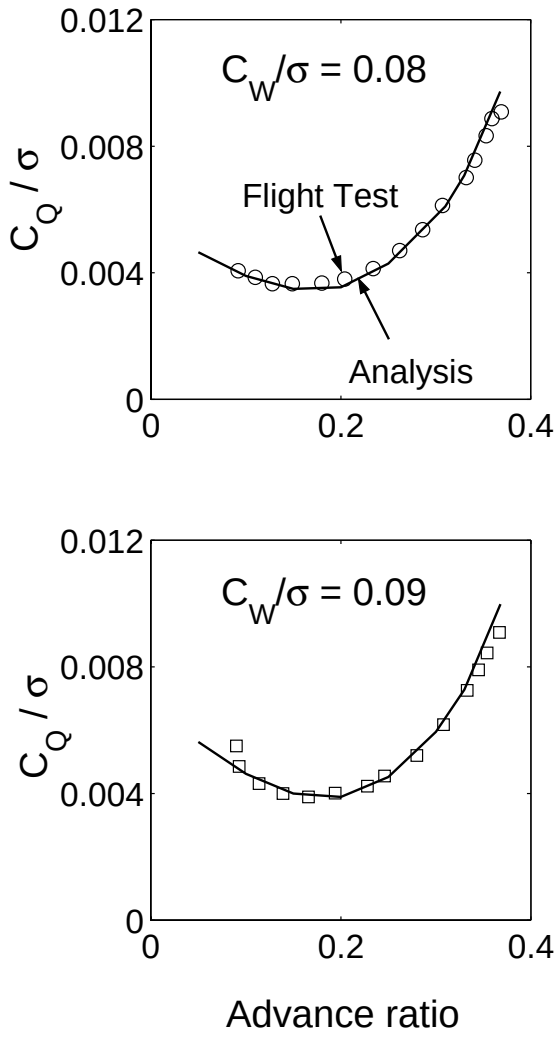

Figure 4.2: **Predicted and measured main rotor power (non-dimensional) in steady level flight for two vehicle weight coefficients**

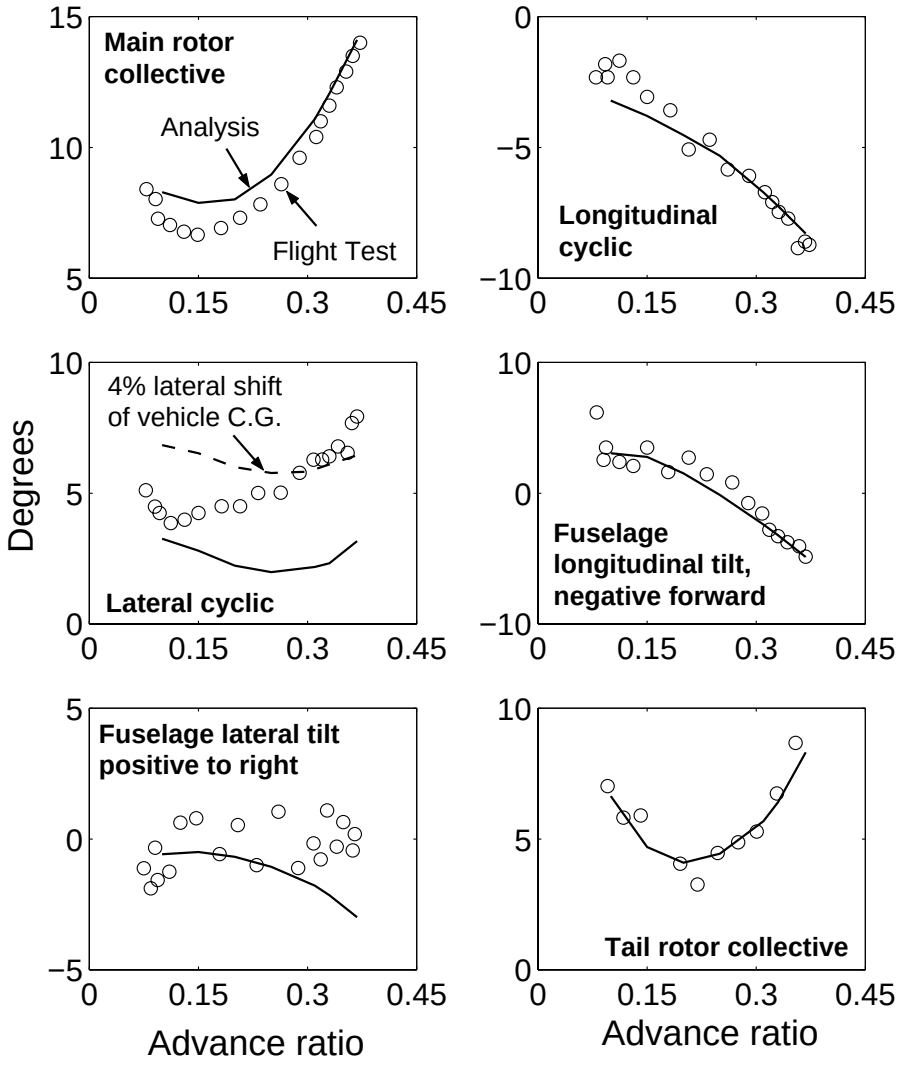

Figure 4.3: **Predicted and measured trim angles at vehicle weight coefficient of $C_W/\sigma = 0.08$**

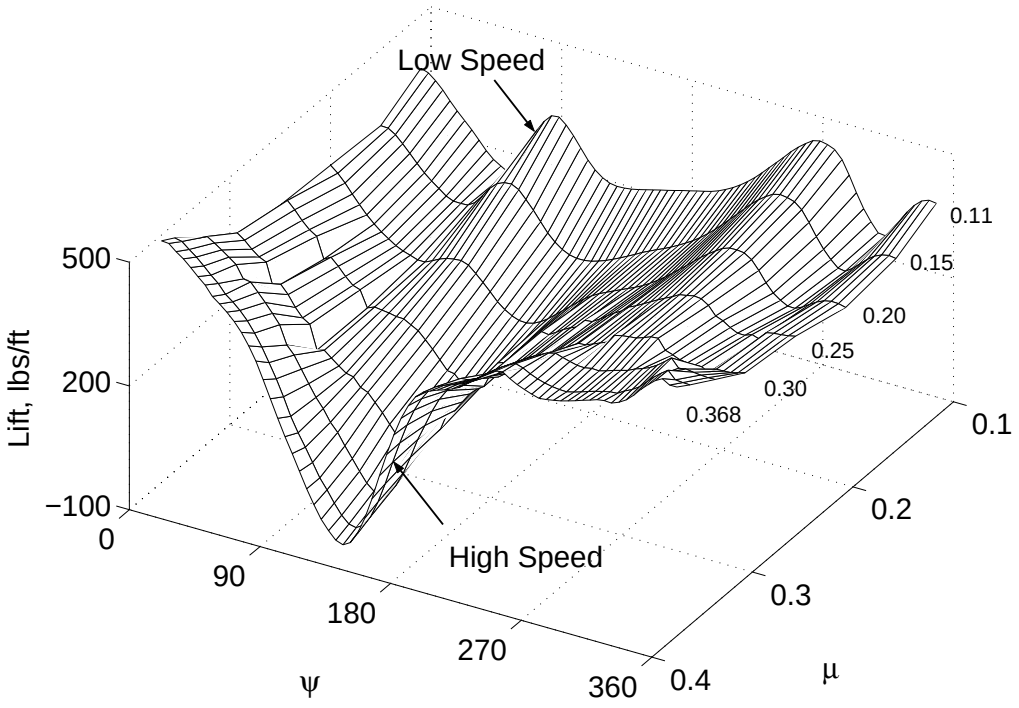

Figure 4.4: **Predicted lift variation near blade tip (96.5% Radius) for a range of forward speeds and azimuth angles (ψ); $C_W/\sigma = 0.0783$**

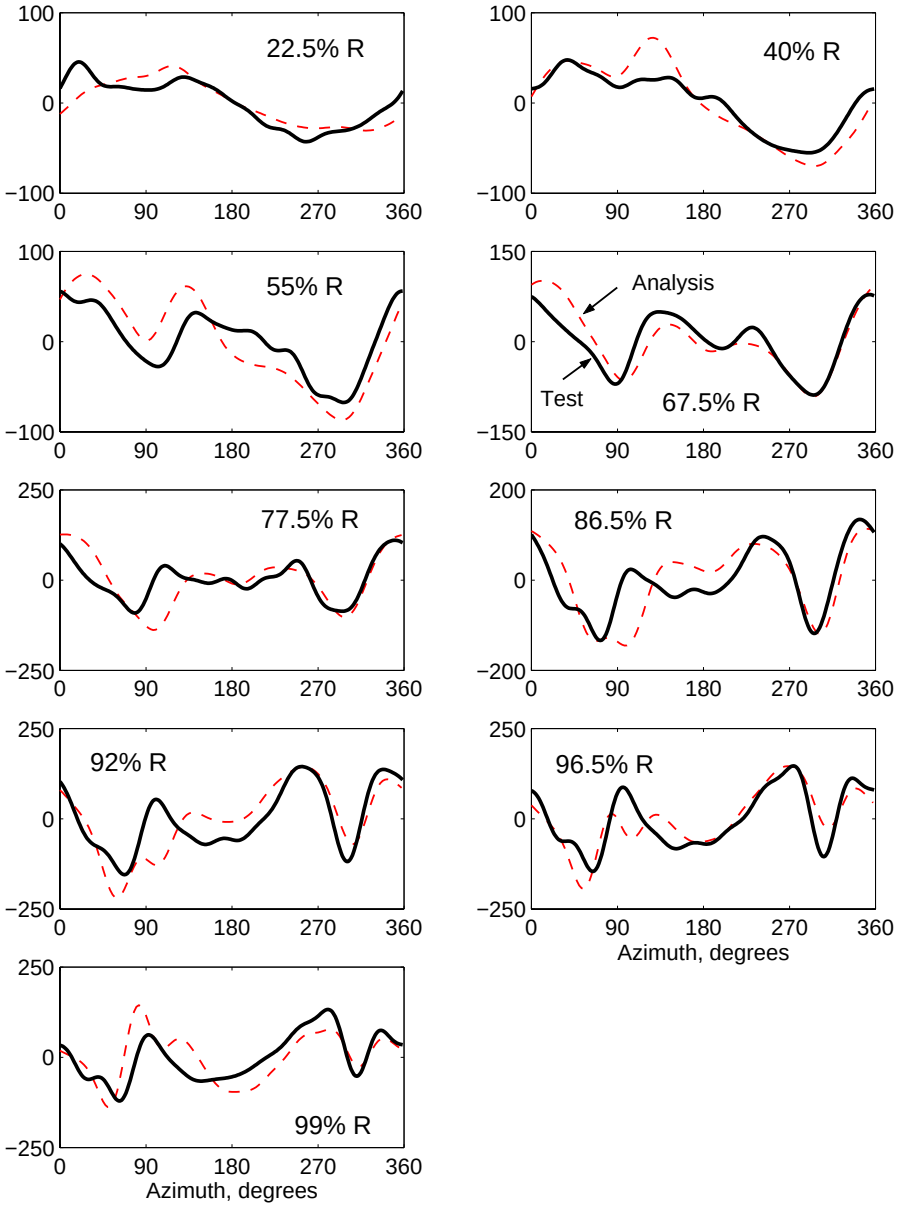

Figure 4.5: **Predicted and measured lift variation at transition speed; $\mu =$ 0.110, $C_W/\sigma =$ 0.0783**

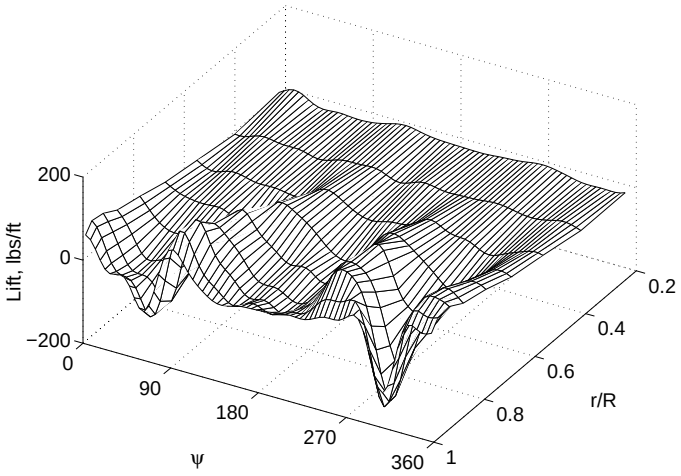

(a) Measured vibratory Lift (3-10/rev) at transition speed; $\mu = 0.110$

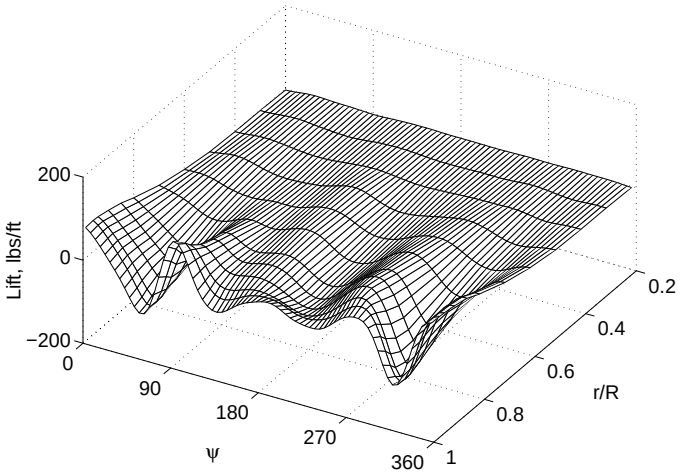

(b) Predicted vibratory Lift (3-10/rev) at transition speed; $\mu = 0.110$

Figure 4.6: **Predicted and measured vibratory lift at transition speed; $\mu =$ 0.110, $C_W/\sigma =$ 0.0783**

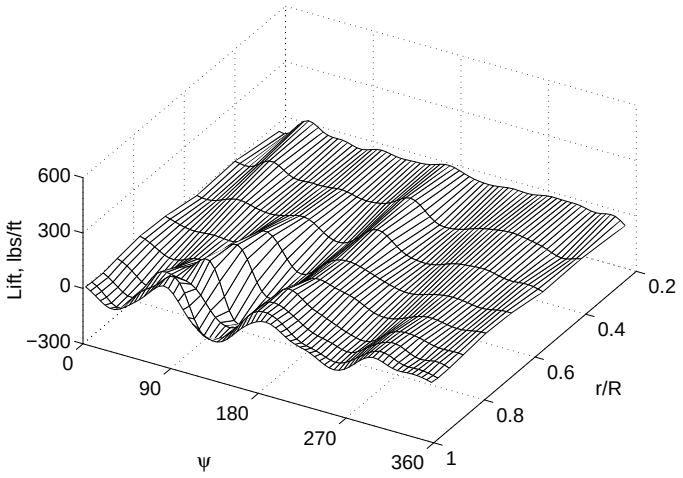

(a) Measured vibratory Lift (3-10/rev) at high speed; μ = 0.368

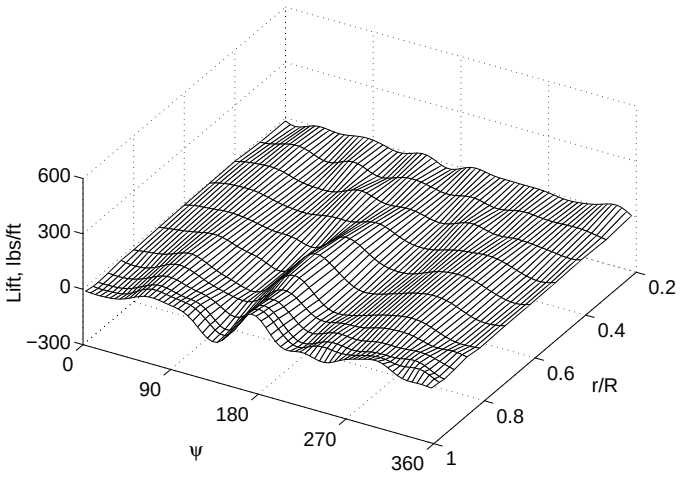

(b) Predicted vibratory Lift (3-10/rev) at high speed; $\mu = 0.368$

Figure 4.7: **Predicted and measured vibratory lift at high speed; $\mu = 0.368$, $C_W/\sigma = 0.0783$**

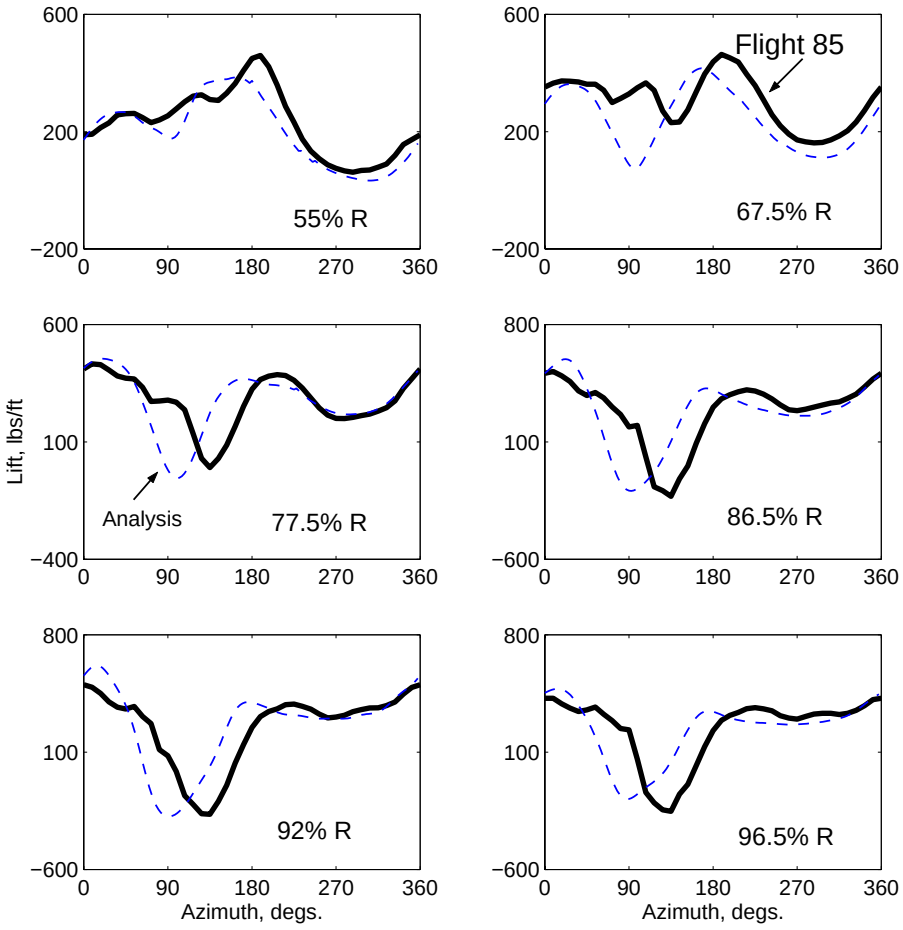

Figure 4.8: **Predicted and measured lift variation at high speed; $\mu = 0.368$, $C_W/\sigma = 0.0783$**

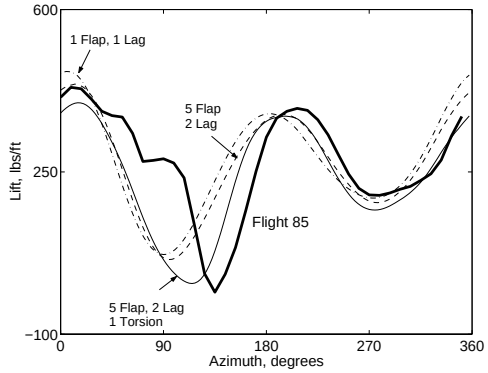

(a) Effect of blade flexibility

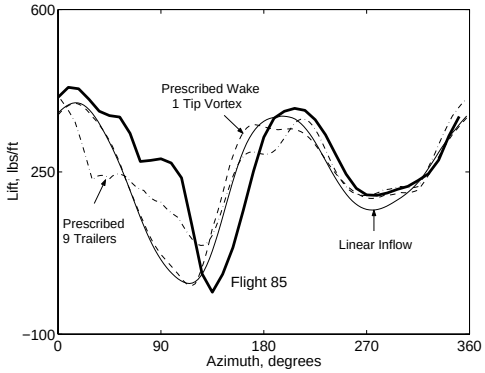

(b) Effect of prescribed wake models

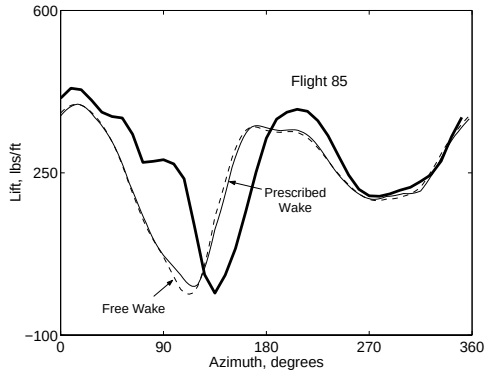

(c) Effect of free wake

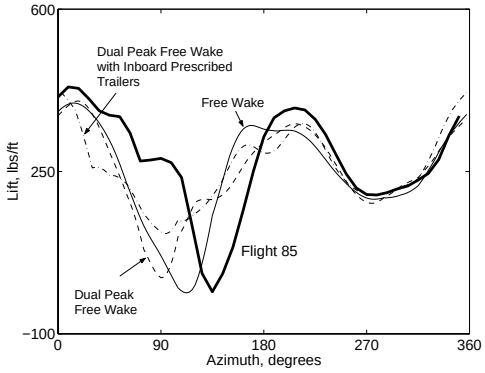

(d) Effect of various free wake models

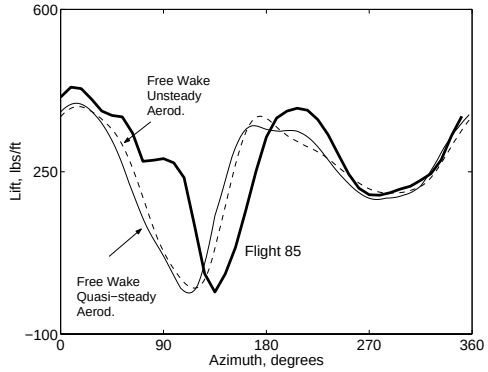

(e) Effect of unsteady aerodynamics

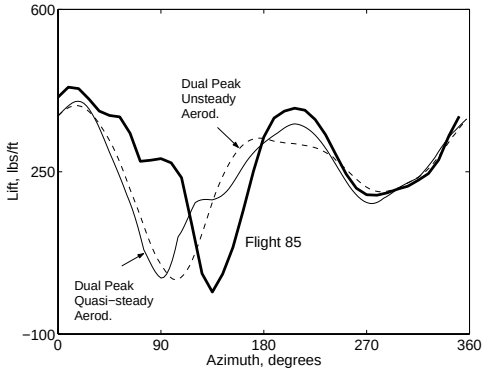

(f) Effect of unsteady aerodynamics

Figure 4.9: **Effect of modeling refinements on high-speed lift prediction at 77.5% Radius; $\mu = 0.368$, $C_W/\sigma = 0.0783$**

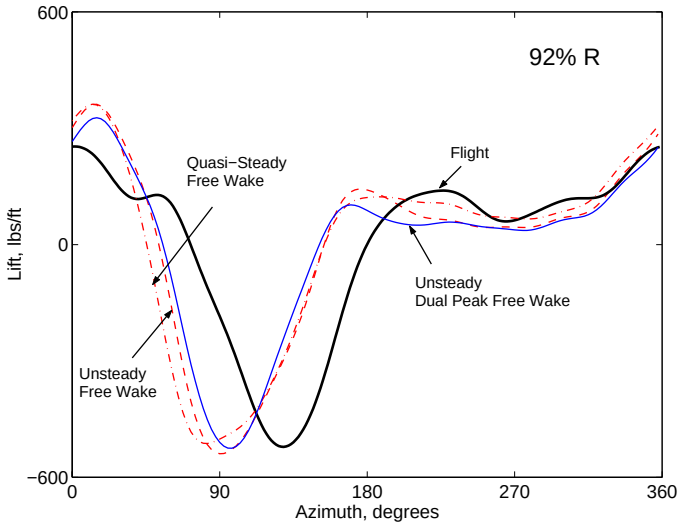

(a) Effect of free wake model at 92% Radius

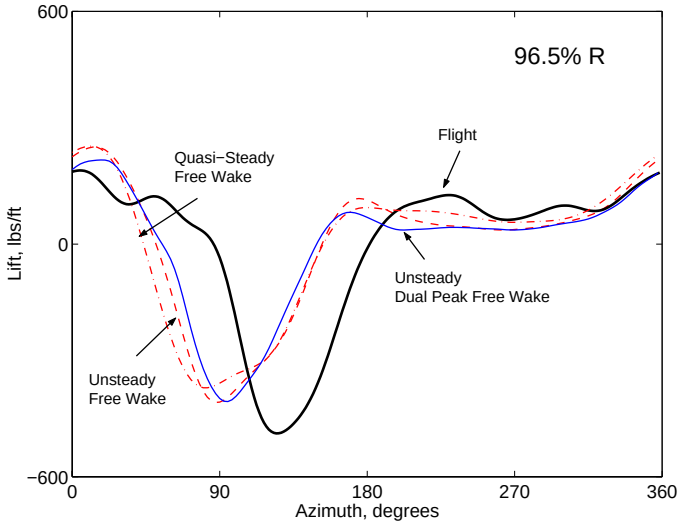

(b) Effect of free wake model at 96.5% Radius

Figure 4.10: **Effect of modeling refinements on high-speed lift prediction at 96.5% Radius; $\mu = 0.368$, $C_W/\sigma = 0.0783$**

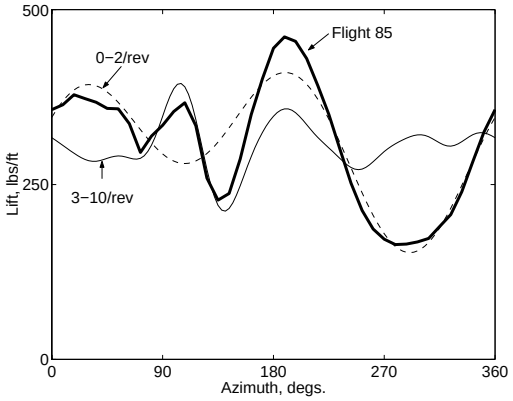

(a) Measured lift separated into non-vibratory (0,1,2/rev) and vibratory (3-10/rev) components

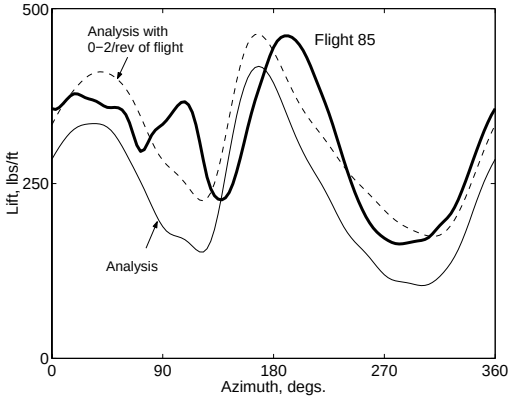

(b) Replacing predicted 0,1,2/rev with measured 0,1,2/rev

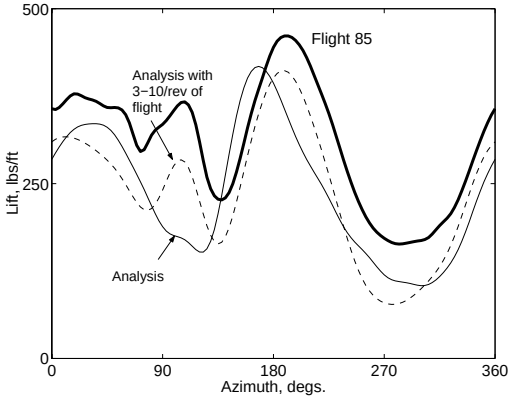

(c) Replacing predicted vibratory lift with measured vibratory lift

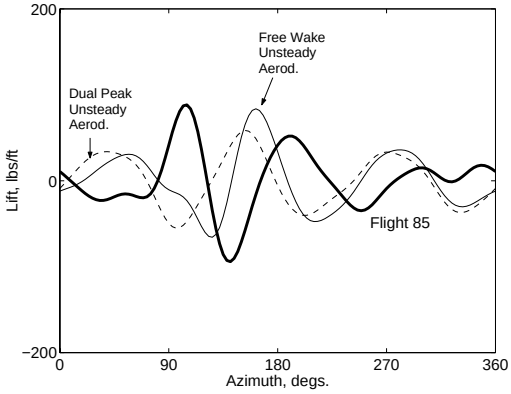

(d) Comparison of predicted and measured vibratory lift

Figure 4.11: **Diagnosis of blade lift at 67.5% R; $\mu = 0.368$, $C_W/\sigma = 0.0783$**

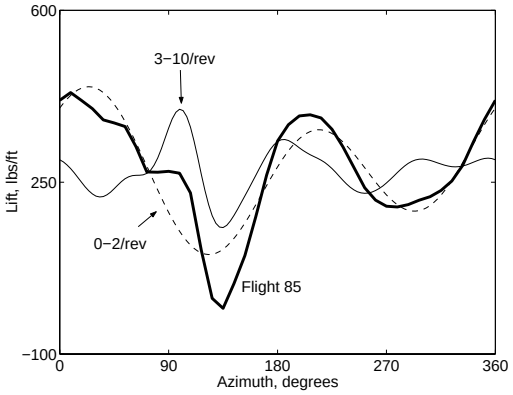

(a) Measured lift separated into non-vibratory (0,1,2/rev) and vibratory (3-10/rev) components

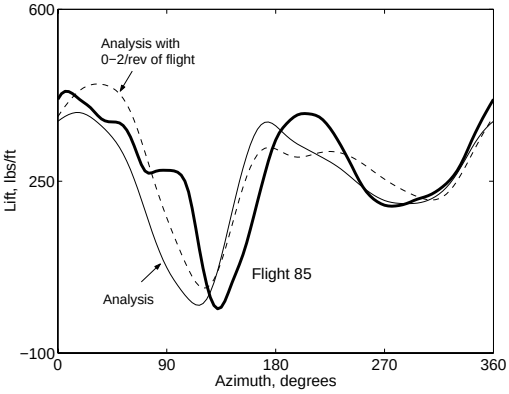

(b) Replacing predicted 0,1,2/rev with measured 0,1,2/rev

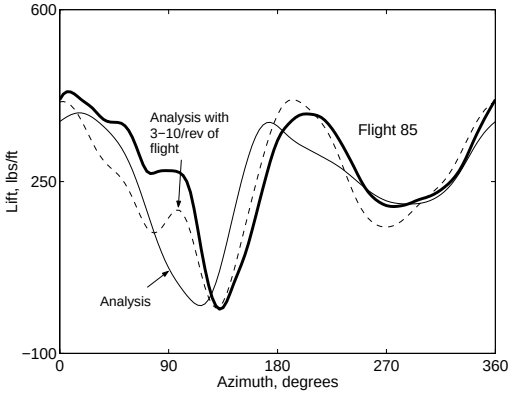

(c) Replacing predicted vibratory lift with measured vibratory lift

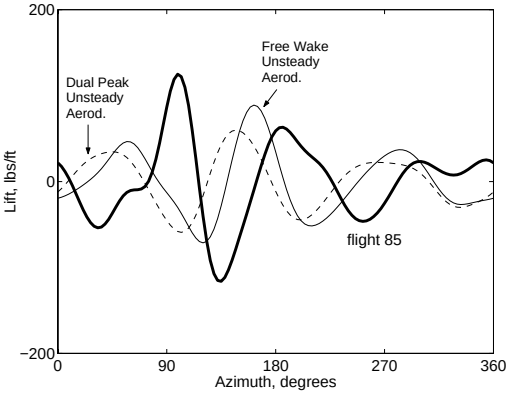

(d) Comparison of predicted and measured vibratory lift

Figure 4.12: **Diagnosis of blade lift at 77.5% R ; $\mu = 0.368$, $C_W/\sigma = 0.0783$**

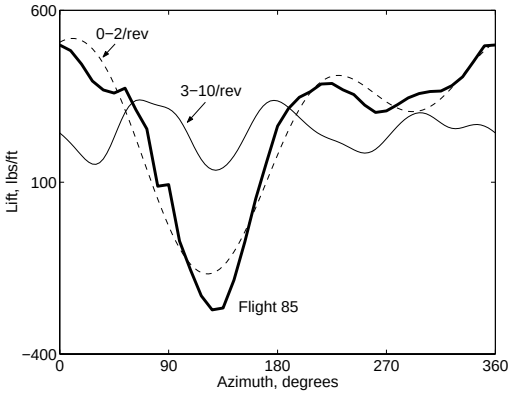

(a) Measured lift separated into non-vibratory (0,1,2/rev) and vibratory (3-10/rev) components

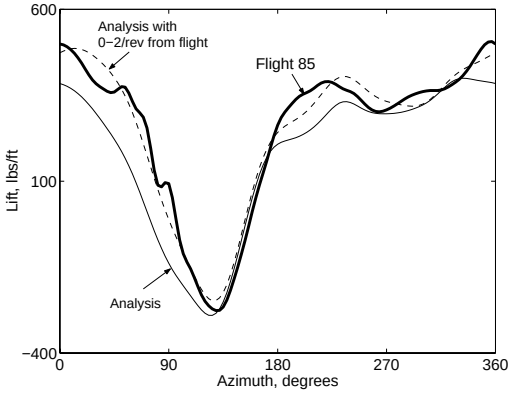

(b) Replacing predicted 0,1,2/rev with measured 0,1,2/rev

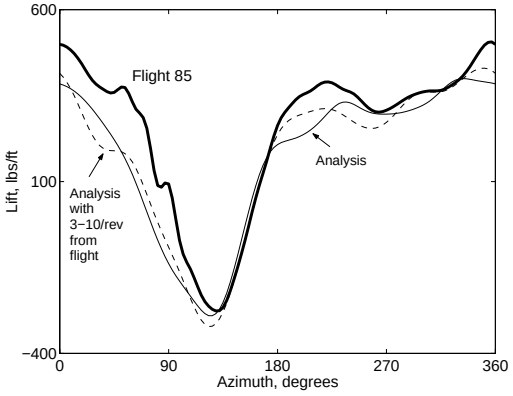

(c) Replacing predicted vibratory lift with measured vibratory lift

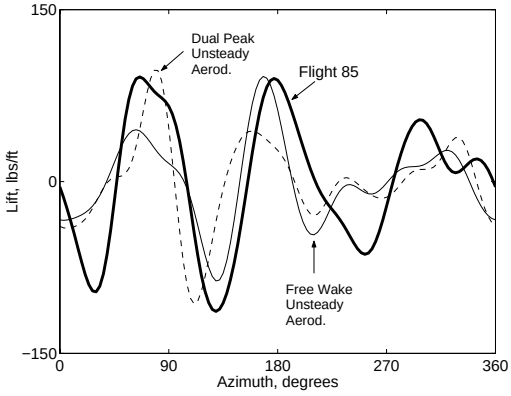

(d) Comparison of predicted and flight test vibratory lift

Figure 4.13: **Diagnosis of blade lift at 92% R; $\mu = 0.368$, $C_W/\sigma = 0.0783$**

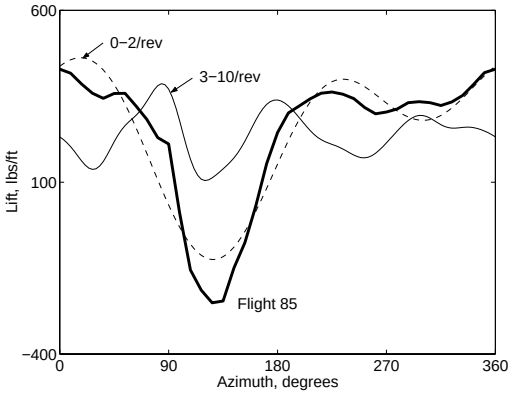

(a) Measured lift separated into non-vibratory (0,1,2/rev) and vibratory (3-10/rev) components

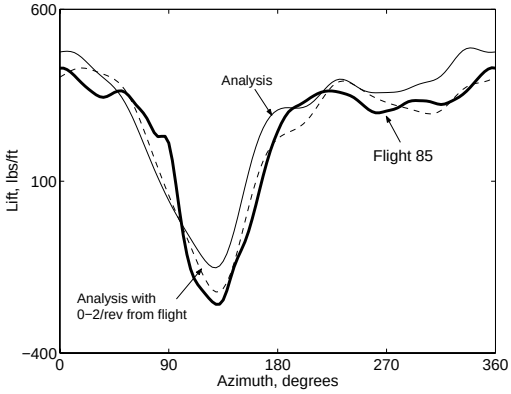

(b) Replacing predicted 0,1,2/rev with measured 0,1,2/rev

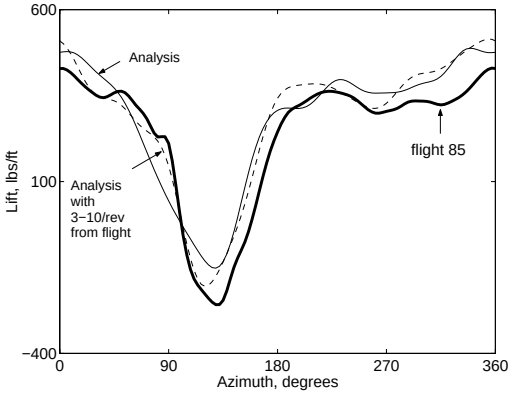

(c) Replacing predicted vibratory lift with measured vibratory lift

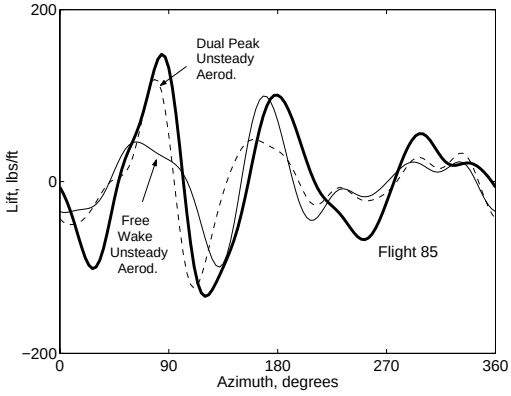

(d) Comparison of predicted and flight test vibratory lift

Figure 4.14: **Diagnosis of blade lift at 96.5% R; $\mu = 0.368$, $C_W/\sigma = 0.0783$**

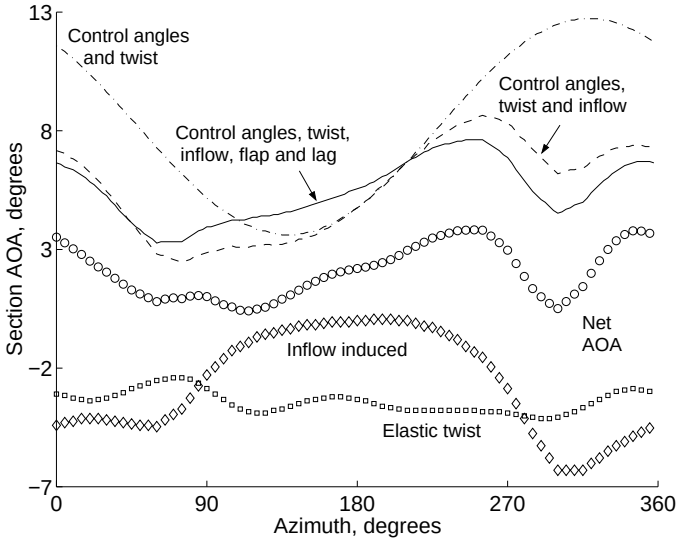

(a) Angle of Attack (AOA) contributions at transition speed

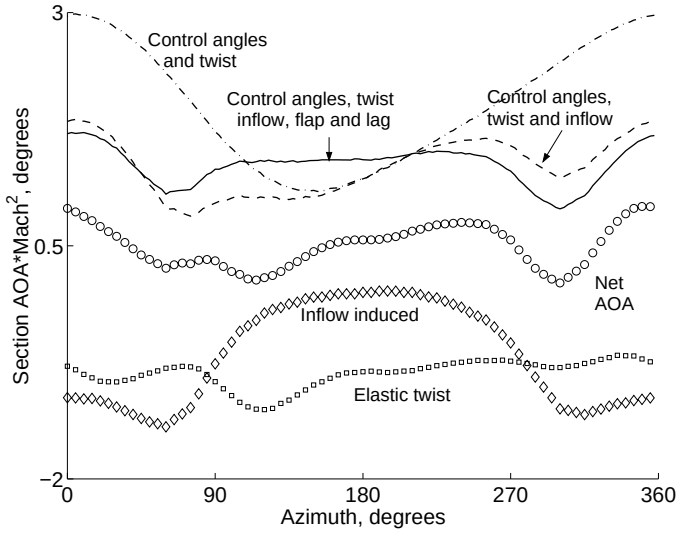

(b) Qualitative lift trends at transition speed

Figure 4.15: **Study of angle of attack distribution at transition speed; μ = 0.110, C_W/σ = 0.0783, 77.5% R**

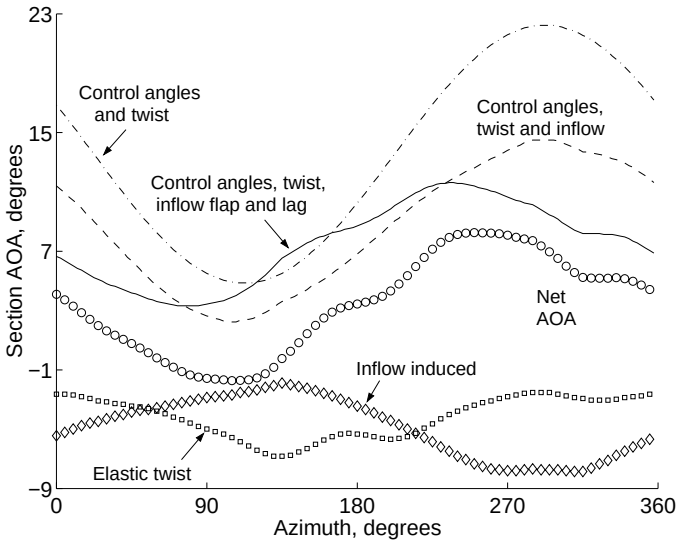

(a) Angle of Attack (AOA) contributions at high speed

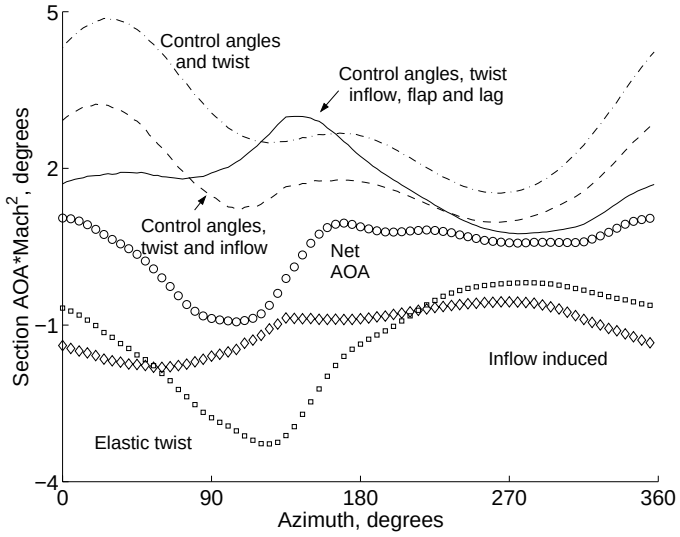

(b) Qualitative lift trends at high speed

Figure 4.16: **Study of angle of attack distribution at high speed; $\mu = 0.368$, $C_W/\sigma = 0.0783$, 77.5% R**

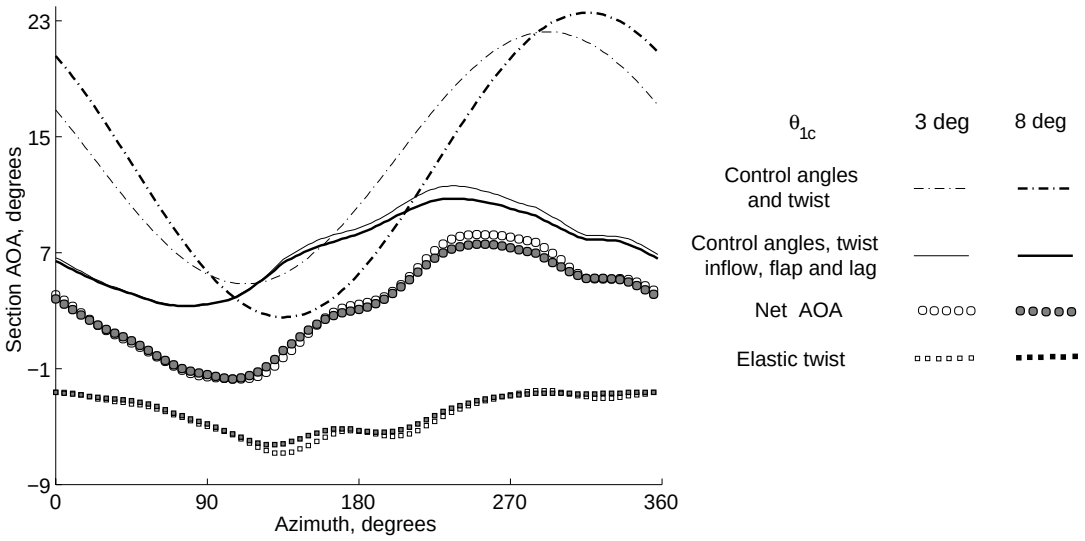

(a) Angle of Attack (AOA) contributions with increased lateral cyclic

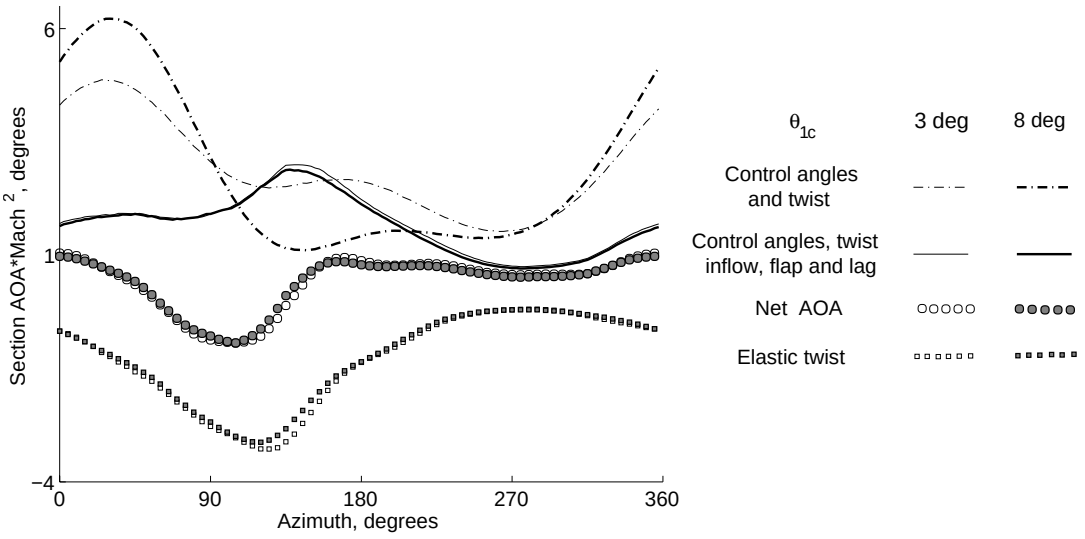

(b) Qualitative lift trends with increased lateral cyclic

Figure 4.17: **Study of angle of attack distribution at high speed with increased lateral cyclic; $\mu = 0.368$, $C_W/\sigma = 0.0783$, 77.5% R**

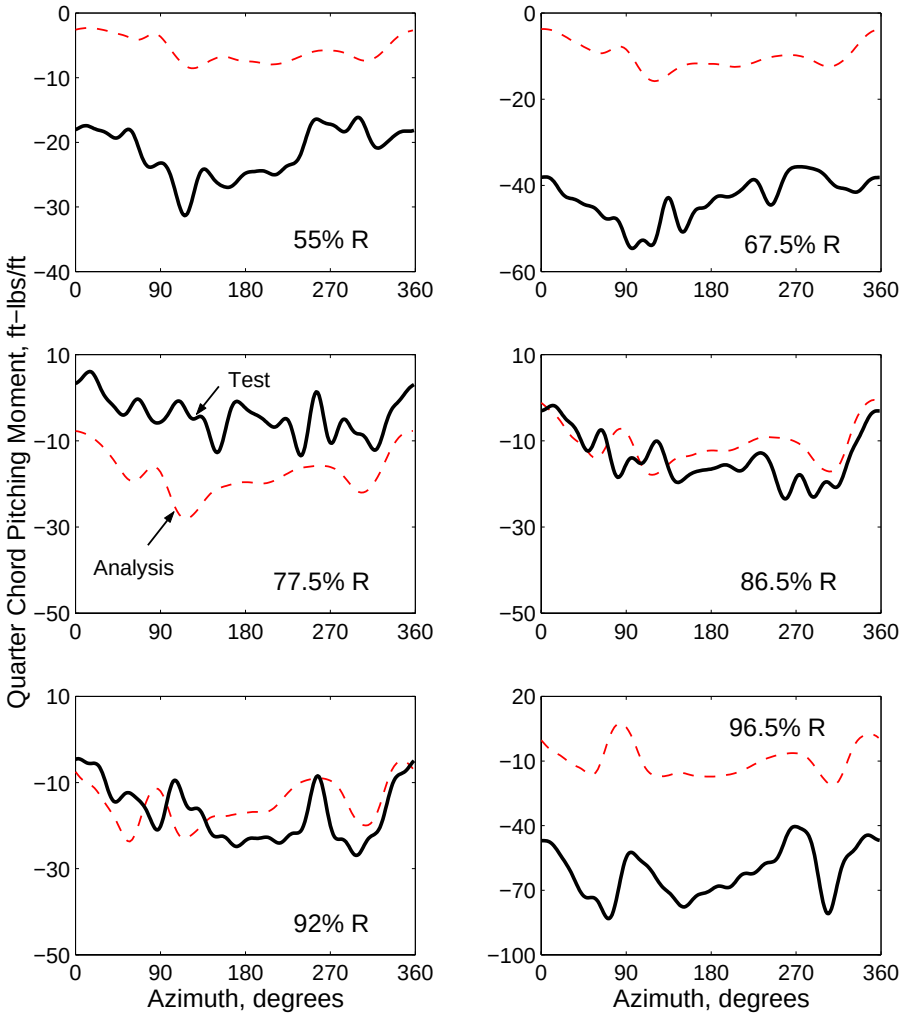

Figure 4.18: **Predicted and measured quarter-chord pitching moment variation at transition speed; $\mu = 0.110$, $C_W/\sigma = 0.0783$**

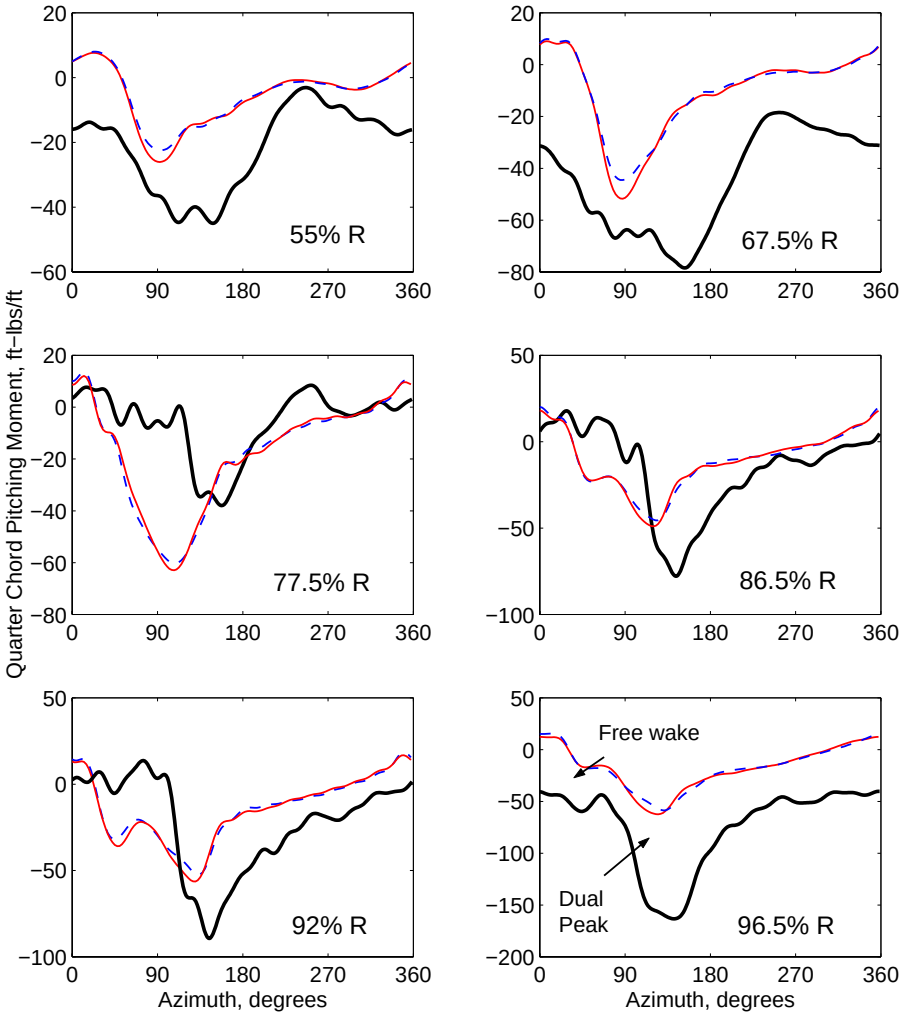

Figure 4.19: **Predicted and measured quarter-chord pitching moment variation at high speed; $\mu = 0.368$, $C_W/\sigma = 0.0783$**

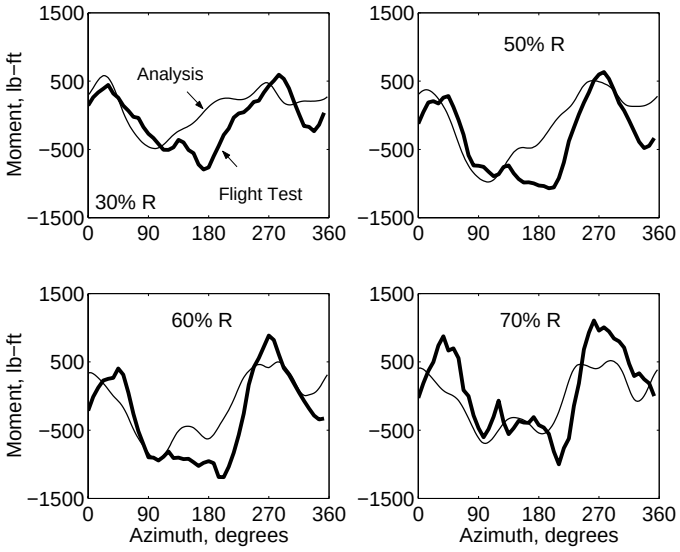

(a) Predicted and measured flap bending moment at high speed

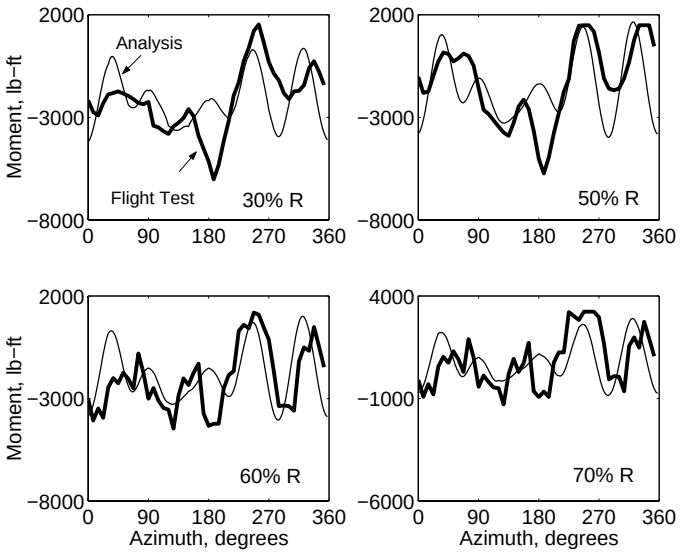

(b) Predicted and measured lag bending moment at high-speed

Figure 4.20: **Flap and Lag bending moments at high speed: Comparison between prediction and flight test ; $\mu = 0.368$, $C_W/\sigma = 0.0783$**

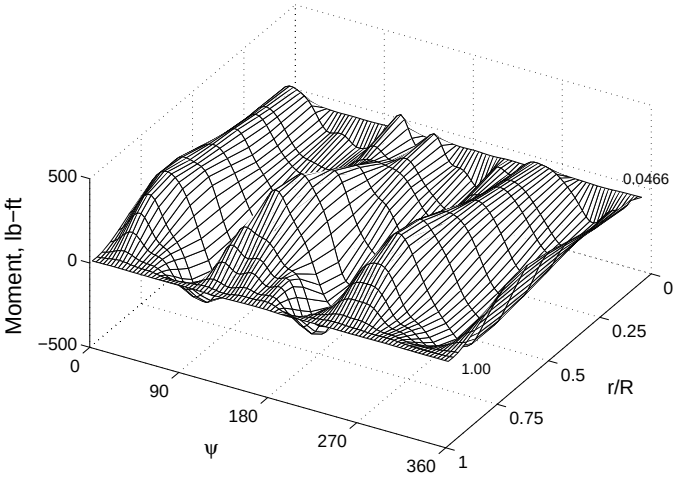

(a) Vibratory flap bending moment (3-24 harmonics) variation with radial station; $\mu = 0.368$

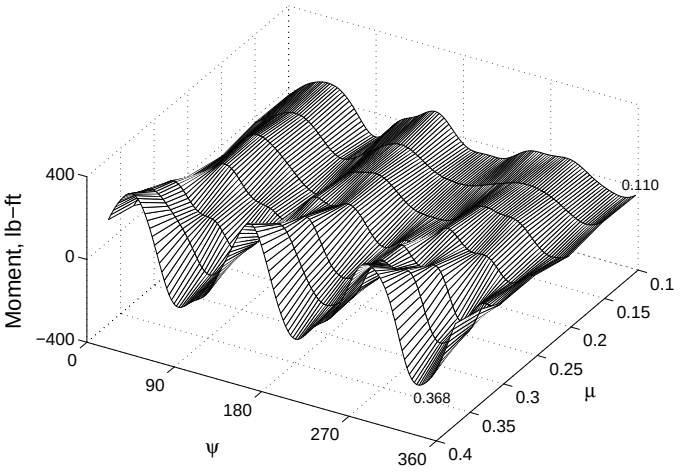

(b) Midspan vibratory flap bending moment (3-24 harmonics) variation with forward speed

Figure 4.21: **Qualitative trends of vibratory flap bending moment predictions Steady level flight; C_W/σ = 0.0783**

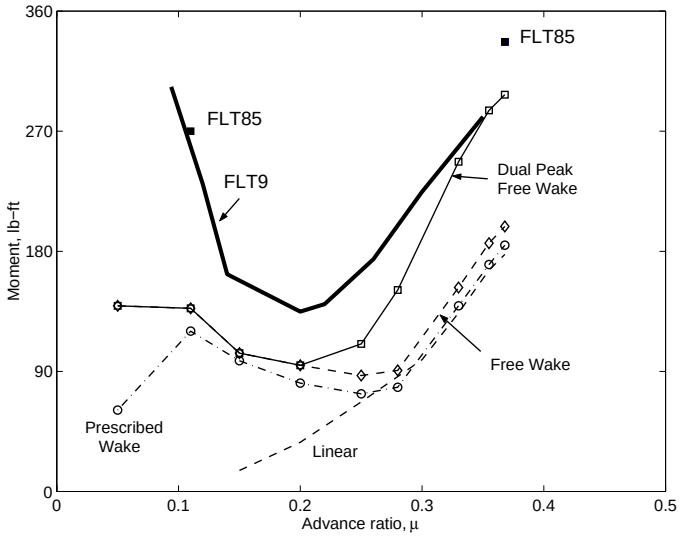

(a) Magnitude of 3/rev flap bending moment at 50% Radius

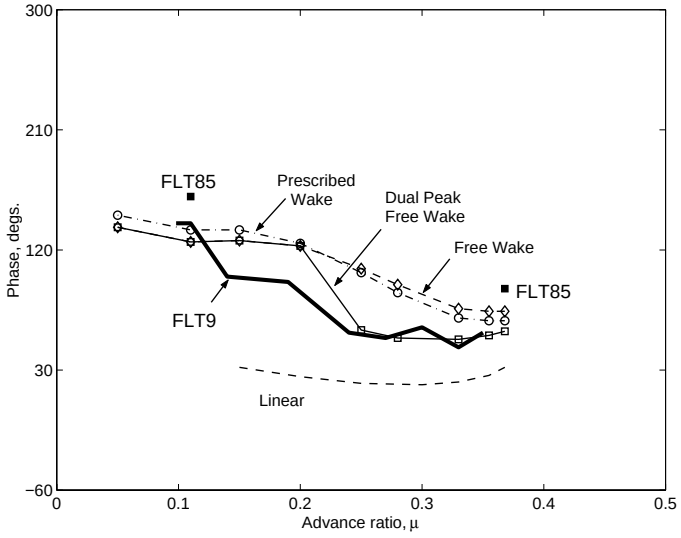

(b) Phase of 3/rev flap bending moment at 50% Radius

Figure 4.22: **3/rev flap bending moment at 50% Radius: Comparison between prediction and flight test 9 ;** C_W/σ **= 0.0783**

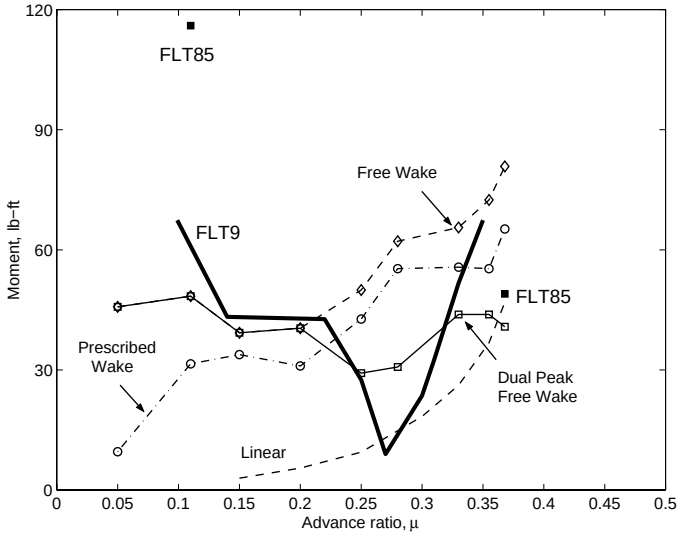

(a) Magnitude of 4/rev flap bending moment at 70% Radius

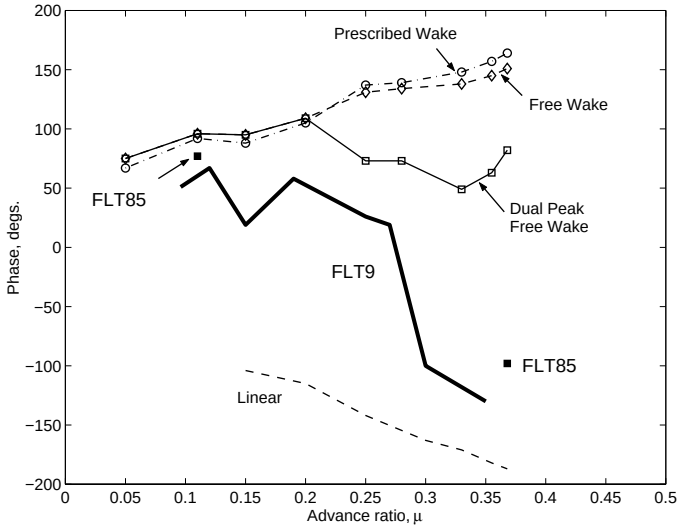

(b) Phase of 4/rev flap bending moment at 70% Radius

Figure 4.23: **4/rev flap bending moment at 70% Radius: Comparison between prediction and flight test 9 ;** C_W/σ **= 0.0783**

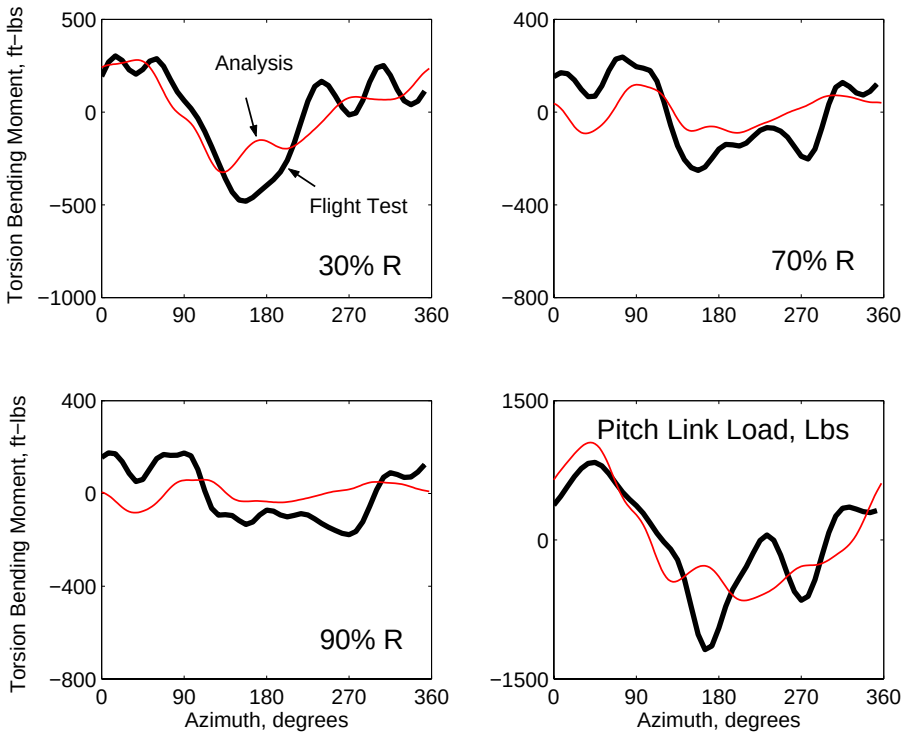

Figure 4.24: **Torsion Bending Moment and Pitch Link load prediction;** $C_W/\sigma = \mathbf{0.0783}$**,** $\mu = \mathbf{0.368}$

Chapter 5

CFD-Comprehensive Analysis

In this chapter, a 3D Navier-Stokes CFD analysis is coupled with the Comprehensive Analysis UMARC to improve prediction of high speed rotor vibration. Chapter 2 validated the UMARC structural model. It was shown that given accurate air loads (measured flight test air loads) the structural model satisfactorily predicts blade dynamic response. Chapter 3 validated lifting-line and 3D CFD models. It was shown that given the correct deformations and same far wake, a 3D CFD model better captured the aerodynamic pitching moments at the outboard stations. Chapter 3, along with chapter 4 established that the vibratory lift in high-speed is dominated by elastic torsion - and that accurate prediction of vibratory lift would resolve the advancing blade lift phase problem. The goal of the present CFD-comprehensive coupling is to improve pitching moment prediction, which would improve elastic

torsion prediction, which would generate improved vibratory lift and resolve the lift phase problem. In addition, it was established in Chapter 3 that the rotor far wake plays a key role in the generation of vibratory lift at the mid span stations (67% R, 77.5% R). This effect was captured by a moving vortex or a dual peak wake but not by a single peak tip vortex wake. The moving vortex wake showed similar predictions as a dual peak wake. In the present CFD coupling study, the effects of both single peak tip vortex wake (baseline) and moving vortex wake are studied. In Chapter 3 air load calculations were performed with a prescribed set of accurate deformations. This chapter presents a fully coupled, comprehensive trim, air loads and blade loads predictions from first principles.

First the role of comprehensive analysis, within the CFD coupling methodology is discussed. Then, the coupling methodology between comprehensive analysis UMARC and CFD analysis TURNS-3D is described. Finally, prediction, convergence and validation of air loads and blade loads are presented.

5.1 Role of Comprehensive Analysis

The CFD loose coupling presented in this study is a coupling between CFD and comprehensive analysis - not a pure structural analysis. The loose coupling methodology involves the transfer of information between an aerodynamic analysis (CFD in this case) and a structural analysis, once for every rotor revolution. Thus, the periodic air loads obtained from the aerodynamic model are imposed on the

structural model to calculate the periodic structural response. The calculation of the structural response is therefore identical to the *mechanical air loads problem* as discussed in Chapter 2. As the structural response equations are solved, the air loads are held constant and do not change with change in blade deformations. This is an ill-posed problem because of the lack of aerodynamic damping. For example, for a teetering rotor with a flap frequency of 1/rev, the 1/rev aerodynamic hinge moment will be identically zero and therefore the 1/rev response of the rotor will be undefined. In practise, numerical errors will give rise to small 1/rev aerodynamic hinge moment which will then drive the response to infinity. In general all conventional rotor systems have some of the natural frequencies close to excitation harmonics - the response solutions of the modes corresponding to these natural frequencies would be inaccurate.

The loose coupling problem becomes well-posed during coupling with a comprehensive analysis. This is because, within the comprehensive analysis, the aerodynamic model supplies the aerodynamic damping terms as discussed in Section 4.1.2, (Chapter 4). These terms are retained. Thus the problem is well-posed. The CFD air loads are incorporated into the coupling iterations as corrections or *deltas* over the air loads calculated by the comprehensive analysis aerodynamic model. The process is described in detail in the next section. The final converged blade response depends entirely on the CFD air loads. They are independant of and unrelated to the aerodynamic model of the comprehensive analysis. The aerodynamic model of the comprehensive analysis only helps to make the methodology well-posed and robust but does not affect the final converged solution. Therefore, a very simple

aerodynamic model can be used, for example, 2D strip theory and uniform inflow, as long as it supplies the air load sensitivity to blade deformations.

In the case of a loose coupling procedure, the steady state periodic airloads are used to calculate the steady state periodic blade response. This is a frequency domain approach. In a tight coupling scheme, on the other hand, air loads calculated at an azimuth location are used to calculated the blade response at the next azimuth location. The response at this azimuth location is then used to calculate air loads at the next azimuth location. Therefore the air loads at one azimuth location are affected by the response at the previous azimuth. Thus aerodynamic damping is accounted for in such a scheme.

In addition to air load sensitivities to blade response, i.e., aerodynamic damping, the UMARC comprehensive analysis provides the following - the structural model, far wake inflow and vehicle trim.

The structural model is identical to that used in Chapter 4 and validated in Chapter 2. As in the case of lifting-line comprehensive analysis used in Chapter 4, a stiff pitch link stiffness of 1090 ft-lbs/deg is used. The measured non-linear lag damper force is not considered. The far wake inflow is calculated using the refined Leishman-Bagai free wake as in Chapter 4. It is incorporated into CFD using the Field Velocity Approach as discussed in Chapter 3. The vehicle trim procedure within the CFD coupling is described in the next section. The trim procedure is a free flight propulsive trim which solves for the three rotor control angles - collective, longitudinal and lateral cyclics, the two vehicle attitudes - longitudinal and lateral fuselage tilts and tail rotor collective based on six force and moment balance about

the vehicle center of gravity.

5.2 CFD coupling methodology

The coupling method adopted, referred to as *loose coupling*, is the method used by *Tung and Johnson* [110]. References [111, 113, 178, 177] have also studied loose coupling schemes. In general, significant convergence problems were noted during pitching moment coupling. A possible source of this problem could be that only the outboard CFD air loads were transfered. A *tight coupling*, though numerically expensive, is a more rigorous approach where the structural and fluid equations are integrated simultaneously at every time step. Reference [108] showed tight coupling results for the UH-60A rotor using measured trim angles. Results showed discrepancies in the high frequency components. Reference [95] shows tight coupling results for the PUMA helicopter. Initial calculations for the UH-60A were unstable due to inaccurate pitching moments. Reference [179] have used tight coupling to produce good correlation of chord-wise pressure data for the ONERA 7A model rotor. Reference [109] studied tight coupling, but the calculations were again performed at prescribed control angles and hence did not ensure the simultaneous convergence of trim and response equations.

In the present study CFD generated normal force, pitching moments and chord force are consistently coupled at all radial stations to obtain stable high-speed solutions for the UH-60A helicopter. The control angles are calculated simultaneously

using the full CFD air loads thereby demonstrating the simultaneous convergence of trim, structural dynamics, fluid dynamics and free wake equations. Loose coupling is employed because of its non-prohibitive computational cost and as a first step for performing coupled rotor aeroelastic analysis.

The coupling methodology is described below. The UMARC comprehensive analysis solution is henceforth referred to as the lifting-line analysis. The UMARC-CFD coupled analysis is referred to as the CFD analysis. The steps are as follows.

1. A lifting-line analysis solution is obtained providing blade deformations, trim angles, free wake and lifting-line air loads.

2. Using the above deformations, free wake and trim angles, 3D CFD air loads are calculated. These air loads are different from and in general improved, compared to the lifting-line air loads.

3. The difference between the CFD air loads obtained in step 2 and lifting-line air loads are the *delta* air loads. The lifting-line comprehensive analysis solution is now re-run with the delta air loads imposed in addition to the intrinsic lifting-line air loads. The delta air loads are held fixed over the trim iterations. The lifting-line air loads change from one coupled trim iteration to another and provide the air load sensitivities required to trim the rotor. In addition, the lifting-line air loads provide aerodynamic damping which makes the procedure stable.

4. Step 2 to Step 3 is one UMARC-TURNS iteration. The UMARC-TURNS

iterations are performed until the delta air loads converge, i.e., become a constant at every radial and azimuthal station.

The final air loads are 3D CFD air loads and equal the lifting-line air loads plus the converged delta air loads. The delta air loads depend on the starting lifting-line air loads and would be different for a different set of starting lifting-line solution. But the sum of the two is equal to the converged CFD air loads and is independent of the starting lifting-line solution.

5.3 Trim solution

The converged trim angles and hub reactions for the lifting-line comprehensive analysis and the CFD comprehensive analysis are shown in Table 5.1. For both analyses, a single tip vortex free wake is used (baseline far wake, as discussed in Chapter 3). The hub roll moment is defined positive to the left. The hub pitch moment is positive nose up. α is the longitudinal shaft tilt angle which includes the 3 degrees of pre-shaft tilt. α is positive nose down. There is no significant difference between the two sets of trim results. This is because the 1/rev normal force distribution is not significantly altered. The higher harmonic normal force predictions show significant differences leading to significant differences in blade loads. *Lift* is used interchangeably with normal force from now on.

Table 5.1: Coupled Trim Values

	Flight	**LL**	**CFD**
Thrust (lbs)	17364	17046	17241
Hub Roll (ft-lbs)	6884	7047	7099
Hub Pitch (ft-lbs)	-2583	-6560	-5623
Coll. (degs.)	13.21	16.16	16.38
Lat. (degs.)	6.56	3.5	2.9
Long. (degs.)	-9.07	-9.7	-9.9
α (degs.)	6.98	8.2	7.67
ϕ (degs.)	0.20	-2.51	-2.25
Tail Coll. (degs.)	8.7	7.22	7.31

5.4 Air Loads

The predicted and measured normal forces are shown in Figure 5.1. Both the lifting-line and CFD analyses use a single tip vortex free wake model (baseline far wake model). Compared to a lifting-line analysis, the CFD analysis shows a marginal improvement in the advancing blade lift phase in the mid-span stations (67.5% R, 77.5% R). As expected, the impulsive behavior at the junction of the first and second quadrant is not captured. This impulse is a dominant source of vibratory harmonics at these radial stations. At the outboard stations (86.5% R - 99% R), the CFD predictions show a significant improvement in the advancing blade. This is due to the accurate prediction of vibratory harmonics at these stations, Figure 5.2.

In general, the vibratory harmonics are improved all across the blade span from 55% R to 99% R.

The evolution of the vibratory harmonics at 92% R is shown in Figure 5.3. The gradual improvement in prediction over UMARC-TURNS iterations is driven by a gradual change in elastic torsion. The evolution of elastic torsion is shown in Figure 5.4. The flap deformations, on the other hand, converge quickly as seen in Figure 5.5. The 1/rev flap, coming from the first flap mode, is relatively unchanged because the trim conditions do not vary significantly with CFD iterations iterations. The 3/rev normal force improves significantly (Figure 5.2) and the effect is seen in increased second mode contribution to the total flap deflection.

The 3/rev lift is the dominant vibratory harmonic at high speed (figure 5.2) and generate the fixed frame (4/rev) hub pitch and roll vibrations. The vertical vibration at the hub depends on the 4/rev air loads. Figure 5.6 shows the 4-10/rev air loads. Once again, lack of the vibratory normal force impulse at the mid-span stations produces an unsatisfactory prediction at 67.5% R and 77.5% R. Near the tip predictions are satisfactory and significantly improved from the lifting-line comprehensive analysis.

Improved elastic torsion results are due to improved pitching moment predictions, Figure 5.7. The advancing blade waveform and peak to peak magnitudes show significant improvements with the CFD analysis. The problem of over-prediction at 77.5% R remains. The peak magnitude is also over-predicted at 92% R (by 30%). In general, there is a phase error between the drop of predicted pitching moments in the advancing blade and the test data. The integrated effect of this phase error will

be seen in torsion bending and pitch link load. The phase error in the pitching moments appears to drive the residual lift phase error of about 15 degrees (figure 5.1) in the advancing blade, via elastic torsion. The vibratory harmonics of the pitching moments are shown in figure 5.8. The blade root shows a large magnitude (20% R), dropping off sharply over the mid span (40% R and 55% R) and then increases uniformly towards the blade tip. This trend is picked up by both the lifting line and CFD analyses. The phase of the vibratory harmonics are significantly improved by CFD.

5.5 CFD vs. Lifting-Line Air loads

Figure 5.1 compared air loads between a lifting-line comprehensive analysis and a CFD comprehensive analysis. The differences in air loads were due to differences in the flow model as well as blade deformations, trim angles and wake.

Blade deformations, control angles and wake from the CFD comprehensive analysis solution are now used to re-calculate air loads using the lifting-line model. Differences in calculated air loads would arise entirely from differences in the flow models. Figure 5.9 compares the lifting-line and CFD normal force predictions. There is no phenomenological difference between the two models. Both models capture the phase of the negative normal force satisfactorily at the outboard stations. Both models consistently miss the phase and normal force impulse at the inboard stations. This is expected as both model use a single tip vortex free wake model.

The greatest discrepancy between the lifting-line and CFD model lies in the pitching moment predictions near the blade tip, figure 5.10. This shows again, that improved lift obtained using CFD analyses is due of improved pitching moment prediction.

5.6 Blade Loads

The predicted torsion bending moments and pitch link load are shown in figures 5.11 (stiff pitch link) and 5.12 (soft pitch link). The torsion loads are not significantly affected by the pitch link stiffness as shown in Figure 5.13. As in the case of measured air loads, predictions in the retreating blade are not satisfactory. The retreating blade waveform of pitch link load and torsion bending moments is affected by the lag damper force. Figure 5.14 shows the effect of using the measured damper force in the UMARC-TURNS analysis. The advancing blade predictions are not affected. However for the stiff pitch link, the damper loads do not show any significant improvement in the retreating blade waveform. The stiff pitch link value is the experimentally measured value and is more reliable. The retreating blade discrepancy in the torsion bending loads is a fundamental discrepancy in the structural model. The peak to peak magnitude and advancing blade waveform of the torsion bending moment and pitch link load is determined by the aerodynamic pitching moments. Improved pitching moment prediction by the CFD analysis therefore improves the torsion loads significantly.

Unlike torsion loads, predicted flap bending moments do not show any improvement over lifting-line comprehensive analysis, Figure 5.15. The possible source of this discrepancy is traced in the following section.

5.7 Flap Bending Moment Investigation

The CFD analysis shows a significant improvement in vibratory normal force prediction (Figures 5.2 and 5.6). Predicted flap bending moments however are not improved (Figure 5.15). Figure 5.16 shows that the flap bending moment is dominated by 1-3/rev harmonics. The 1-3/rev harmonics of predicted normal force show significant discrepancies for both lifting-line and CFD analysis, Figure 5.17. This discrepancy is largest at the mid-span stations (67.5% R and 77.5% R) where neither of the two analyses, captures the vibratory normal force impulse.

The importance of the normal force waveforms at 67.5% R and 77.5% R, on the flap bending moment predictions, can be established by stepwise calculation of flap bending moments using a combination of flight test and CFD normal force. Starting from CFD predicted normal force at all radial stations, flap bending moments are calculated by progressively replacing CFD normal force with flight test measured normal force, from tip inboard - 99%R, 96.5% R to 40% R. Figure 5.18 shows the results from the step wise calculation. The most significant change in the bending moment waveform appears to stem from normal force at 67.5% R and 77.5% R. 8 uncoupled flap modes have been used to calculate the flap bending moments in the

present study, so that the bending moments errors are generated entirely from errors in blade normal force. Clearly, the error in blade normal force prediction at 67.5% R and 77.5% R are significant contributors to error in the flap bending moment waveform.

5.8 Effect of Refined Wake

The baseline single peak free tip vortex wake model is now replaced with a single peak free moving vortex model. The moving vortex model is described in Chapter 3. The free vortex is trailed from the tip at all azimuths except in the regions of negative lift where it moves inboard to the zero circulation cross-over point. The moving vortex model, in presence of accurate blade elastic torsion, was seen to generate the advancing blade lift impulse at the inboard stations.

The dual peak model, which produced a similar effect, is not used in the present study and the CFD analysis at present can incorporate only one free trailer. Figure 5.19 compares CFD air load predictions with the baseline wake and a moving vortex wake. In the outboard stations (86.5% R to 99% R) there is a marginal improvement in blade lift. Predictions at the two inboard stations (67.5% R and 77.5% R) show significant improvement. This is due to improved vibratory harmonics at these two two stations, as shown in figure 5.20. In general, the moving vortex model shows an improvement of the vibratory harmonics at all radial stations. The 4-10/rev harmonics also show improved predictions at the inboard stations with

similar trends outboard.

The improved vibratory harmonics at the two inboard stations (67.5% R and 77.5% R) is a direct effect of the rotor wake. The torsion deformations do not change significantly between the two models because the pitching moment predictions remain the same. Figure 5.22 compare the pitching moments between the two wake models. The moving vortex model shows marginal improvements near the tip (92% R, 96.5% R and 99% R), on the advancing side. This is reflected in the vibratory harmonics as shown in figure 5.23. The phase error inboard (67.5% R and 77.5% R) remain.

Because the inboard lift impulse is better captured, the flap bending moment waveforms show significant improvement as shown in figure 5.24. Both the peak to peak magnitude and the higher harmonic waveform show similar trend as the test data. However, compared to the test data, the predictions appear to show a constant phase shift of 20 to 25 degrees at all radial stations. This is due to the residual phase error in lift prediction coming from phase error in pitching moments. The torsion bending moments and pitch link load are compared in figure 5.25. Both predictions are similar with the refined wake model showing marginal improvements arising from marginal improvement in pitching moments.

To summarize, figure 5.26 compares the CFD analyses flap bending moments with those obtained with measured air loads. The residual error in phase is due to the residual error in lift phase. The residual error in lift phase is due to errors in the pitching moment phase as reflected in the torsion bending plots of figure 5.27.

5.9 Transonic Tip Relief

The greatest discrepancy between the lifting-line and CFD model lies in the pitching moment predictions near the blade tip (Figures 5.9 and 5.10).

Figure 5.28 shows the incident Mach number, angle of attack and pitching moment coefficient distributions at 96.5% R. The pitching moment coefficients are obtained from airfoil tables using the Mach number and angle of attack values. The coefficients obtained from 2D test airfoil tables show the effect of aerodynamic center movement in transonic flow. In the regions of positive angle of attack (around 45 degree azimuth location) high incident Mach number shifts the aerodynamic center behind quarter chord. This generates a high nose down pitching moment. As the angle of attack drops from positive to negative, the normal force, now negative, generates a nose up pitching moment. Unlike a 2D airfoil, a section near the tip of a 3D wing does not undergo the same aerodynamic center movement. The compressibility effects are delayed to a higher Mach number due to a shock relief effect.

To capture the shock relief effect the 2D test airfoil tables are replaced with CFD airfoil tables generated at a section near the blade tip. Fixed wing CFD calculations are performed on a UH-60A blade without twist and sweep. For a set of geometric wing angles of attack (-8,-6 to 10 degrees), airfoil properties are extracted at 97% R.

The 3D wing airfoil characteristics obtained at 97% R (with respect to the geometric angle of attack) are different from 2D airfoil characteristics. In addition to tip effects, the 3D wing airfoil characteristics include the effect of near wake.

Figure 5.29 shows the variation of lift coefficient over wing span for a set of geometric angles of attack. The drop near the tip is due to a reduced effective angle of attack. This reduction is calculated using a lifting-line model (Weissinger-L type) and subtracted from the geometric wing angle. The resulting airfoil characteristics with respect to effective angle of attack do not contain the effect of near wake. The pitching moment properties read from such a tip airfoil table do not show the aerodynamic center movement in the first quadrant (Figure 5.28).

The accuracy of the tip airfoil tables depends on the agreement between CFD and lifting-line fixed-wing near wake. This agreement is not satisfactory for all angles of attack, Figure 5.29. Figure 5.30 shows the calculated pitching moments at 96.5% R. The blade deformations, control angles and wake correspond to the CFD comprehensive analysis. The difference in the steady value is an error in the test data. The tip airfoil extracted with respect to effective angle of attack is used. Compared to the 2D test airfoil table calculations, the waveform in the advancing blade is marginally improved. However there is no change in the peak to peak magnitude.

5.10 Concluding Remarks

Based on the CFD (TURNS-3D) - comprehensive analysis (UMARC) coupling performed in this chapter the following conclusions can be drawn.

1. A CFD-comprehensive analysis coupling improves vibratory lift prediction via

significant improvements in section pitching moments. Improved pitching moment predictions improve torsion bending loads and elastic torsion deformations. Improved elastic torsion deformations improve vibratory normal force prediction at all radial stations. Pitching moment predictions are accurate near the tip (96.5% R) and at the inboard stations (40% - 67.5% R). From 77.5% R to 92% R they are over-predicted in magnitude and shifted in phase in the advancing blade.

2. Improved vibratory normal force prediction, improves the advancing blade waveform and normal force phase at all radial stations. A residual lift phase error at all radial stations stem from phase error in pitching moments.

3. The vibratory normal force impulses at 67.5% R and 77.5% R are captured using a moving vortex model. using a moving vortex model the CFD analyses accurately captures the basic physics of vibratory loading at high speed.

4. The vibratory normal force impulses are important for accurate prediction of flap bending moment waveform. The residual phase error in lift translates to a phase error in the flap bending moment waveform.

5. Pitching moments near the blade tip appear to be affected by steady and unsteady effect of transonic shock relief. They are accurately captured by CFD. CFD based tip airfoil tables can be used to capture the steady transonic effect within a lifting-line model. Improvement in pitching moment waveform is however marginal. The peak magnitudes are not affected.

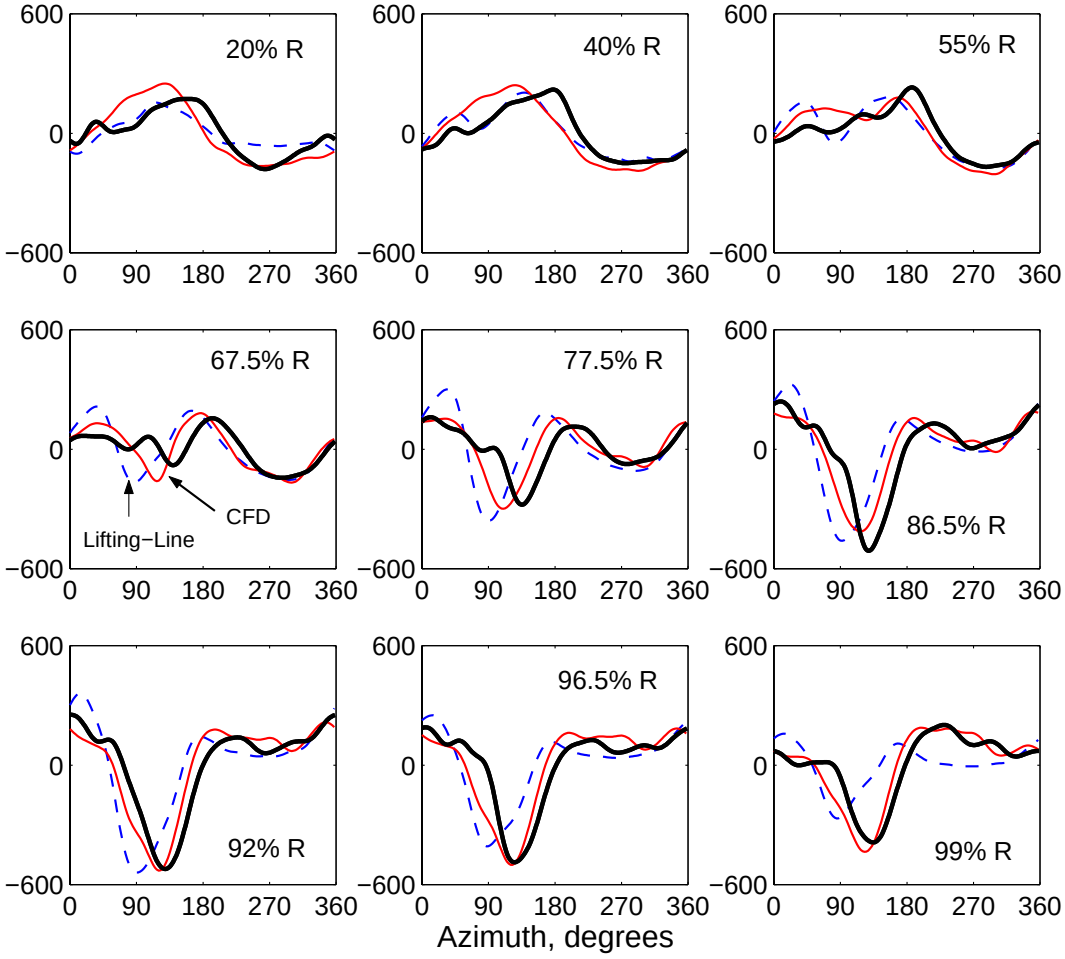

Figure 5.1: **Predicted and measured normal force 0-10/rev; $C_W/\sigma = 0.0783$, high-speed $\mu = 0.368$**

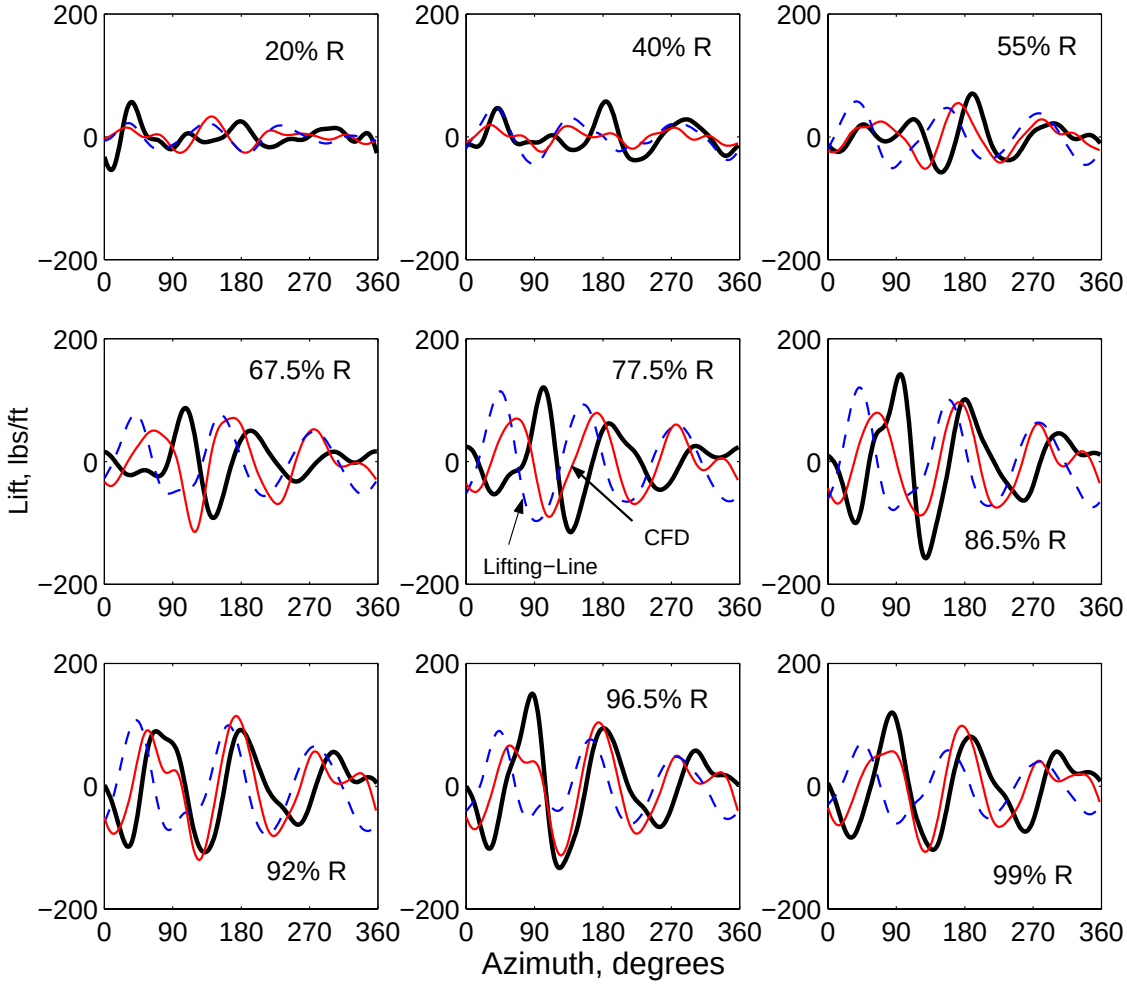

Figure 5.2: **Predicted and measured vibratory normal force 3-10/rev; C_W/σ = 0.0783, high-speed μ = 0.368**

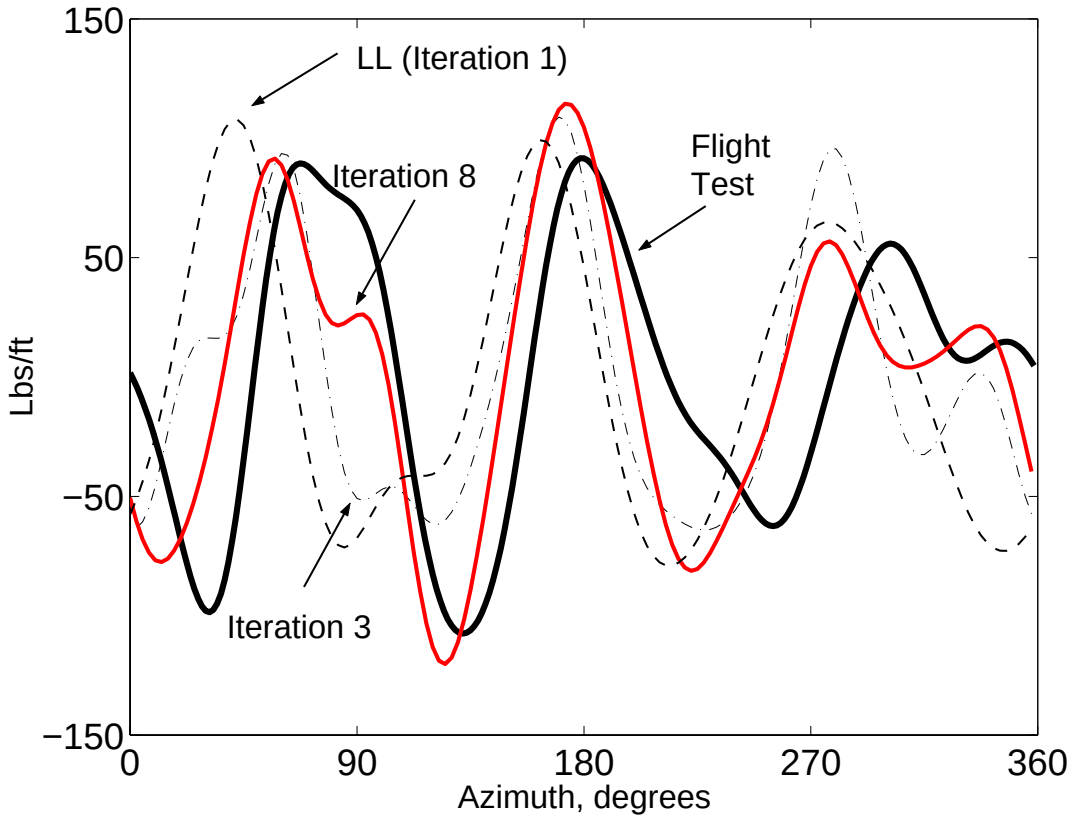

Figure 5.3: **Evolution of predicted vibratory normal force 3-10/rev over UMARC-TURNS coupling iterations; $C_W/\sigma = 0.0783$, high-speed $\mu = 0.368$**

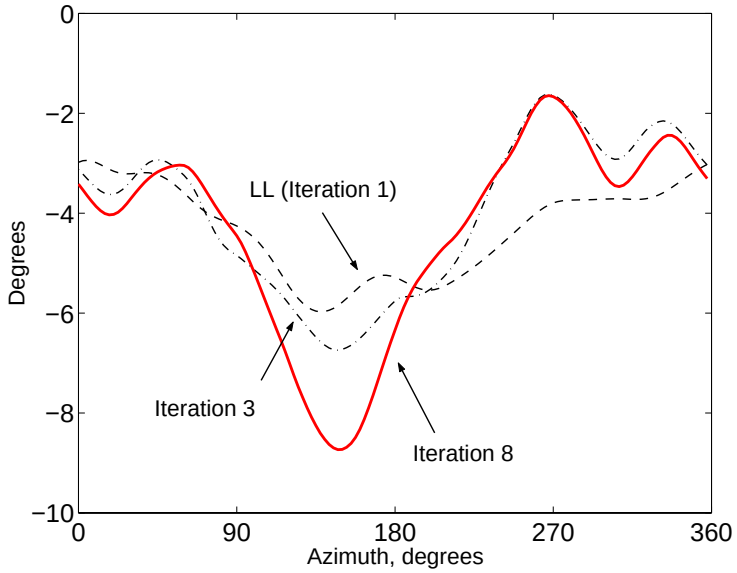

Figure 5.4: **Evolution of predicted elastic torsion over UMARC-TURNS coupling iterations; $C_W/\sigma = 0.0783$, high-speed $\mu = 0.368$**

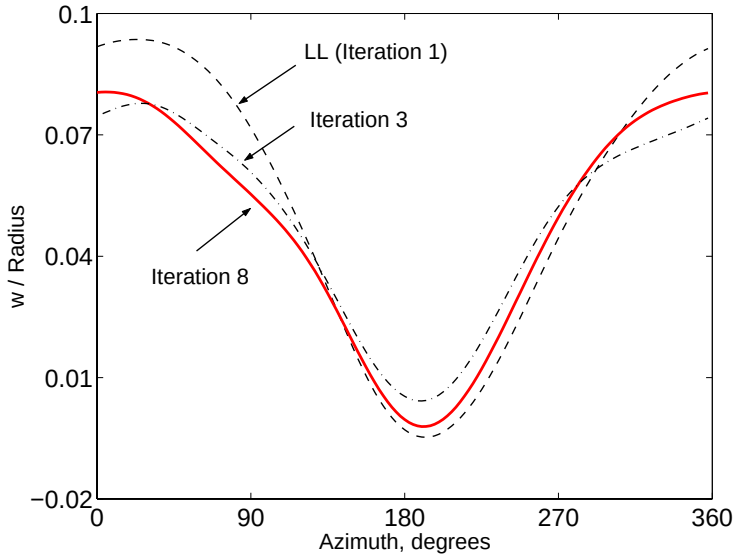

Figure 5.5: **Evolution of predicted flapping over UMARC-TURNS coupling iterations; $C_W/\sigma = 0.0783$, high-speed $\mu = 0.368$**

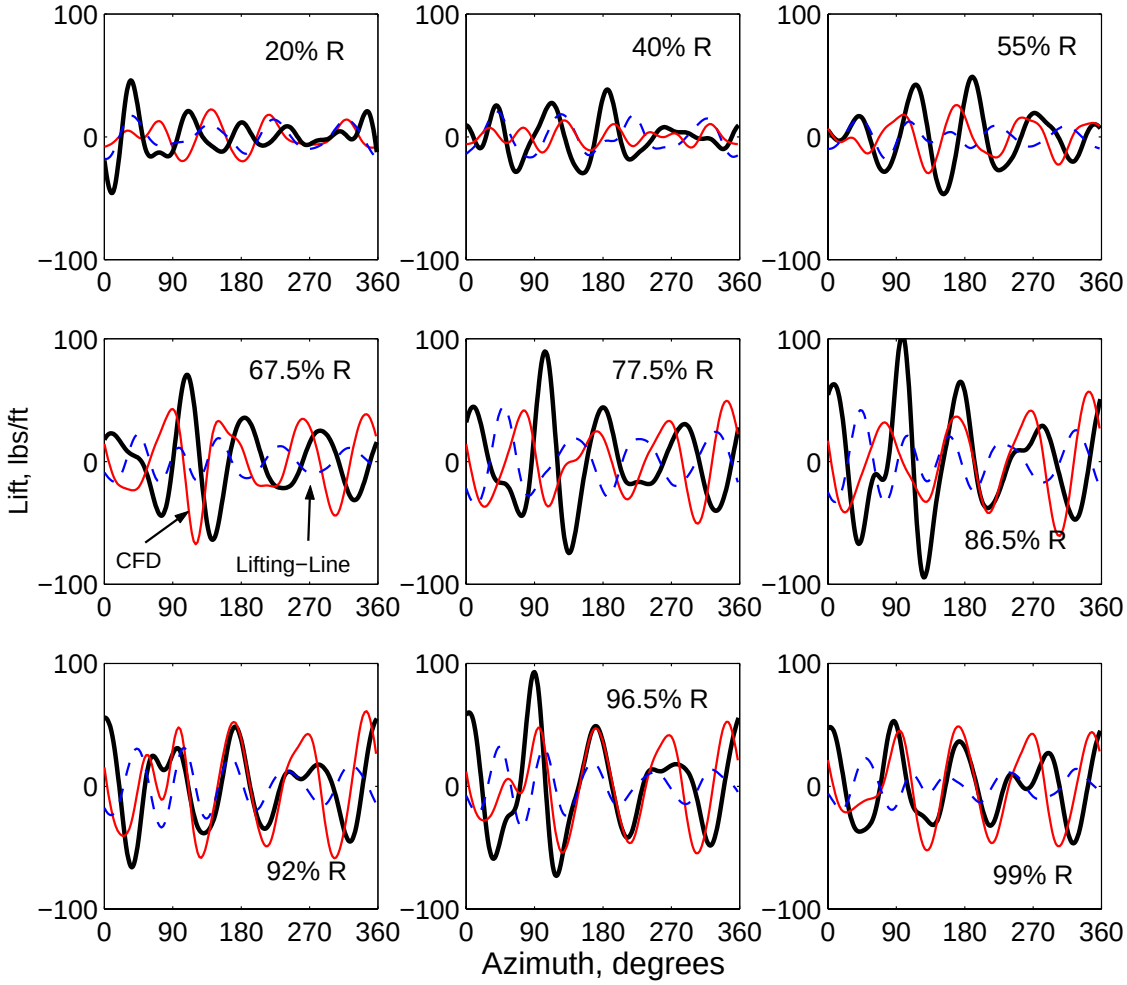

Figure 5.6: **Predicted and measured vibratory normal force 4-10/rev; C_W/σ = 0.0783, high-speed μ = 0.368**

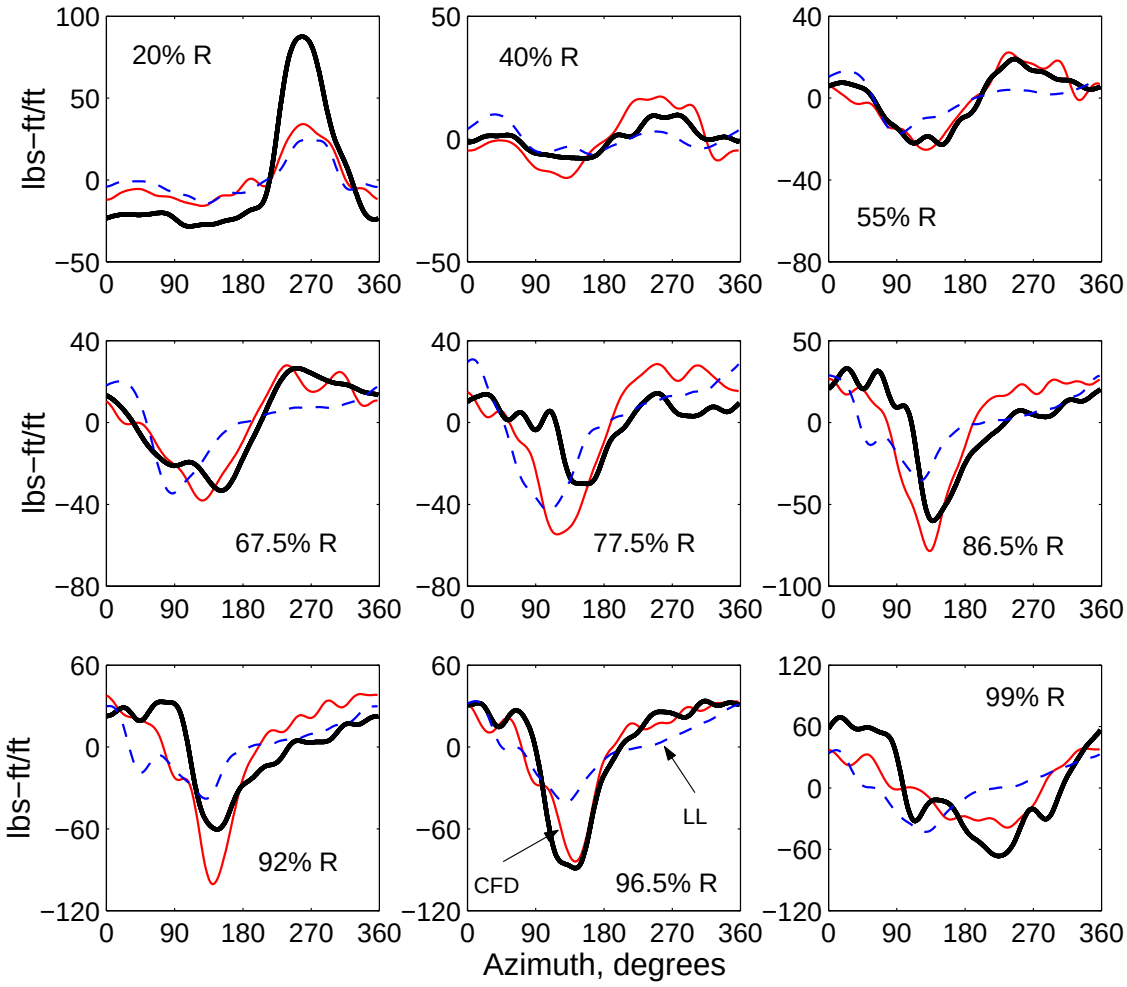

Figure 5.7: **Predicted and measured oscillatory pitching moments (1-10/rev); $C_W/\sigma = 0.0783$, high-speed $\mu = 0.368$**

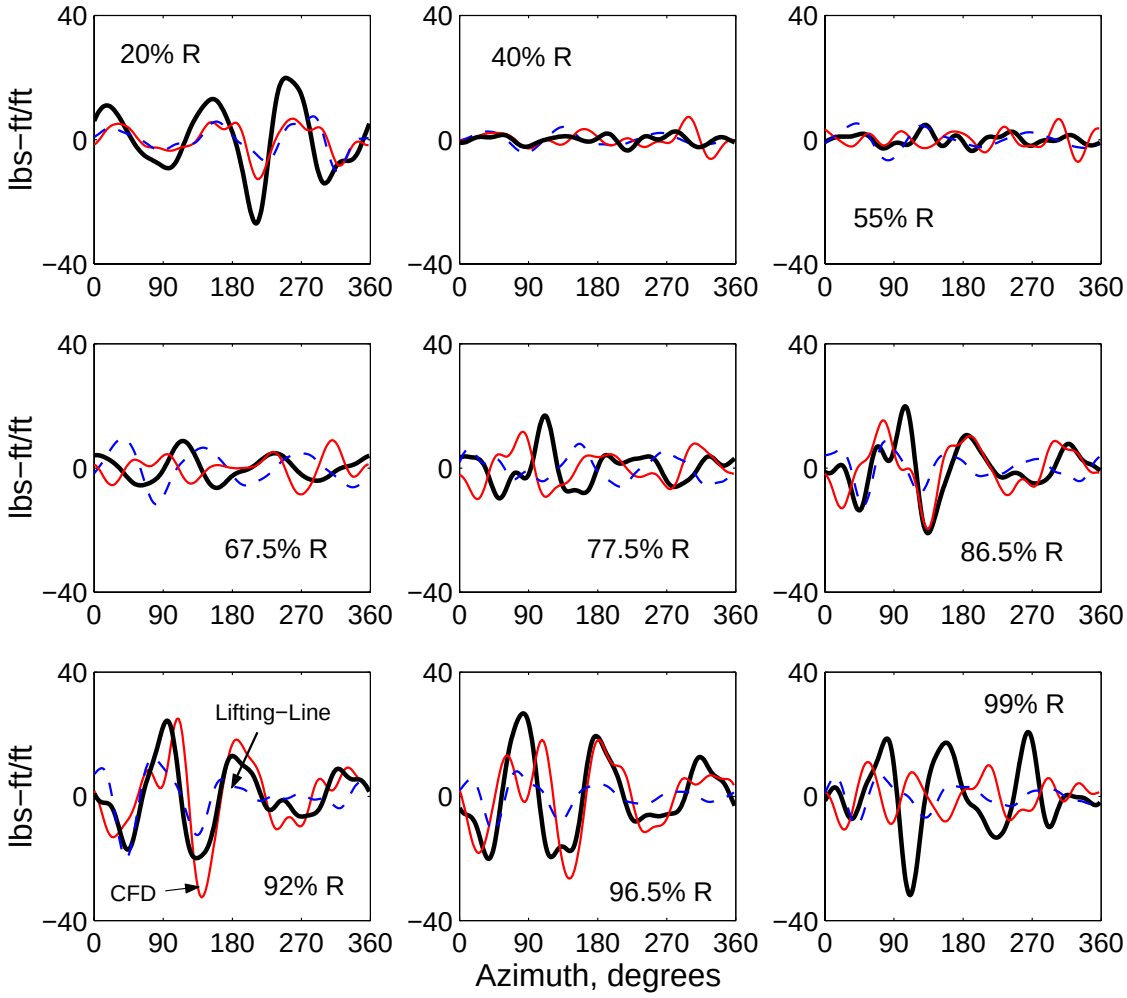

Figure 5.8: **Predicted and measured vibratory (3-10p) pitching moments; $C_W/\sigma = 0.0783$, high-speed $\mu = 0.368$**

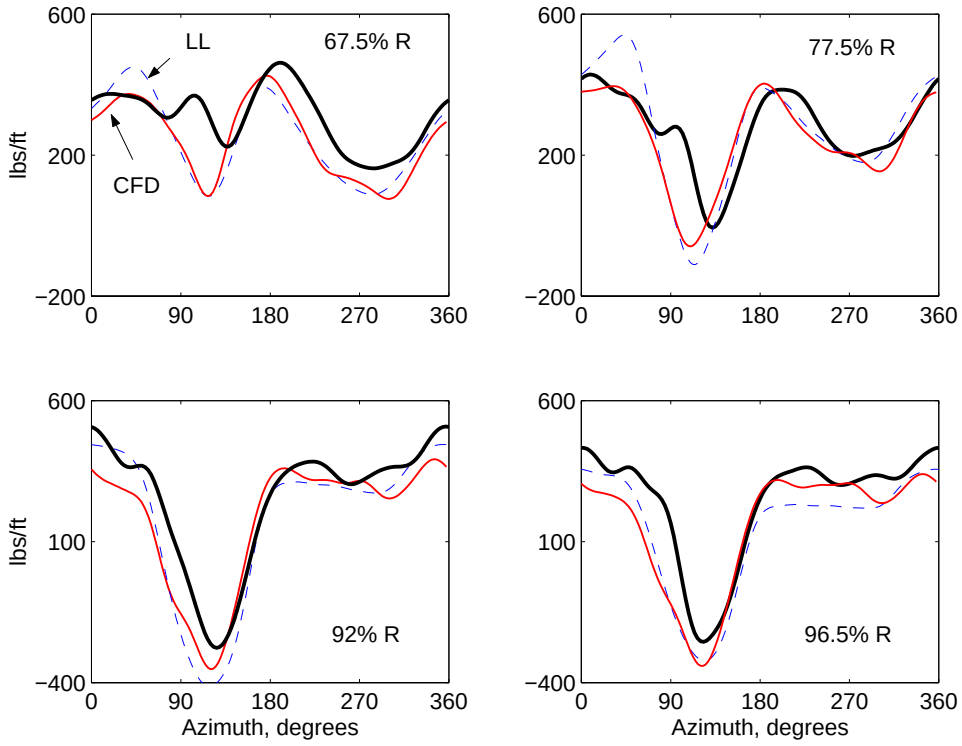

Figure 5.9: **Lifting-line and 3D CFD predicted normal force using same blade deformations, trim angles and inflow; $C_W/\sigma = 0.0783$, high-speed $\mu = 0.368$**

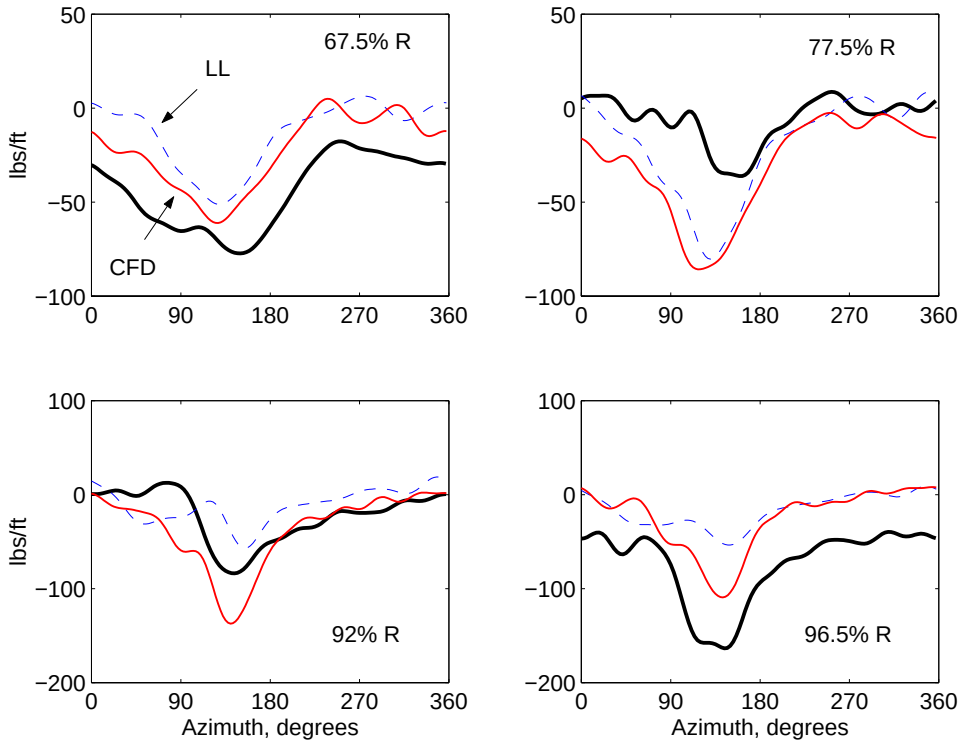

Figure 5.10: **Lifting-line and 3D CFD predicted quarter chord pitching moments using same blade deformations trim angles and inflow; $C_W/\sigma =$ 0.0783, high-speed $\mu = 0.368$**

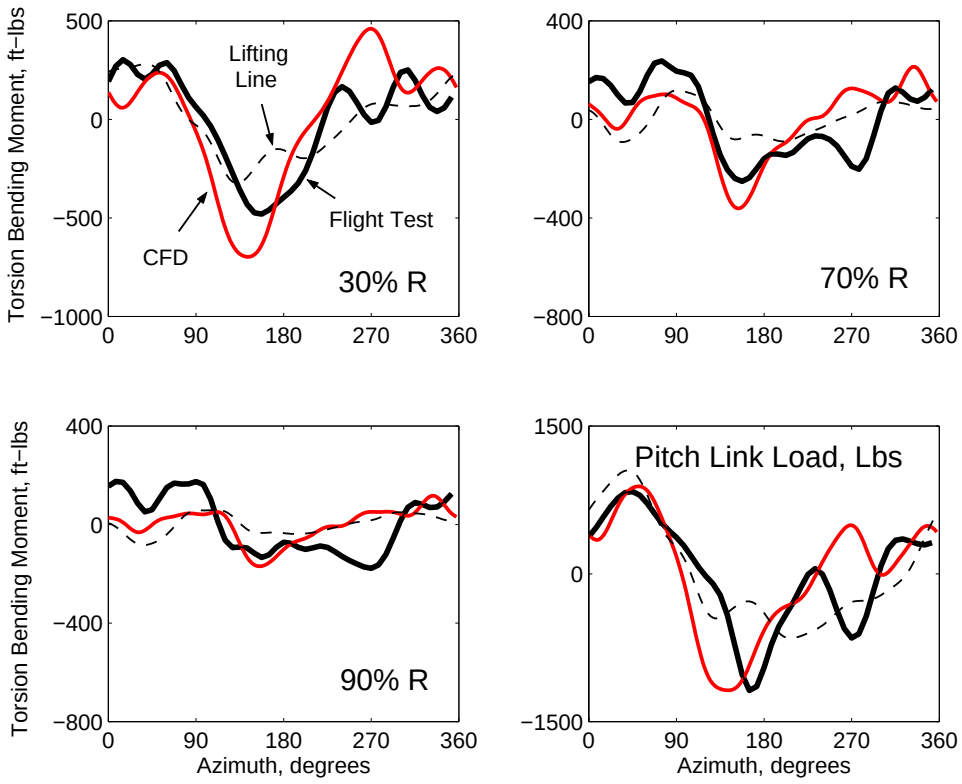

Figure 5.11: **Predicted and Measured Torsion Bending Moments; Stiff Pitch Link, no lag damper; $C_W/\sigma = 0.0783$, high-speed $\mu = 0.368$**

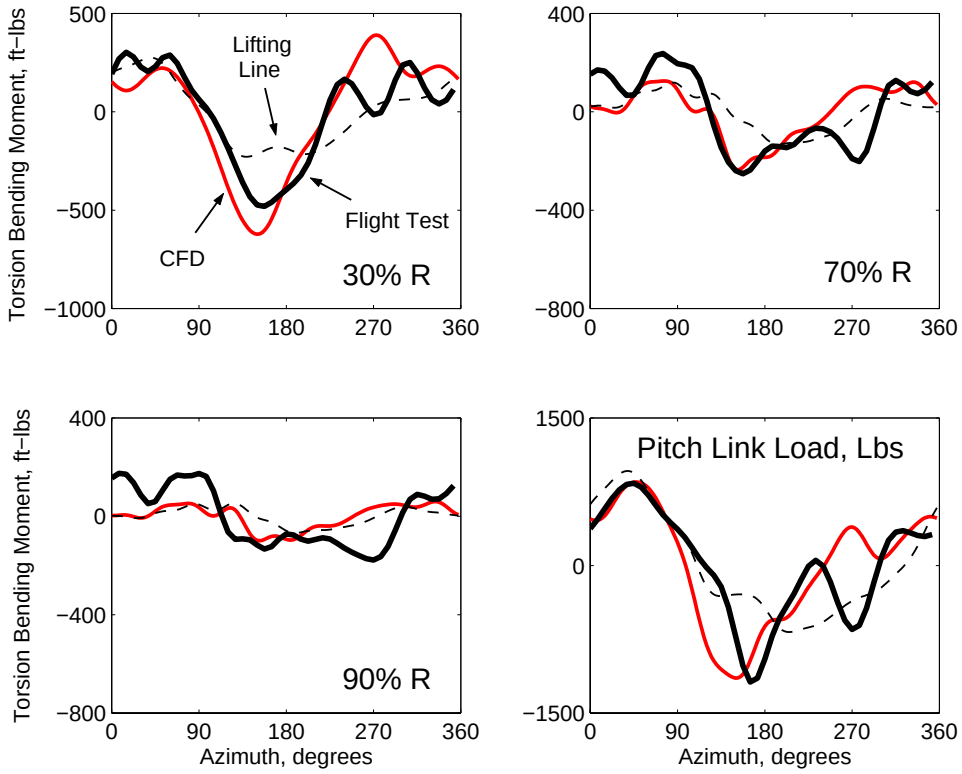

Figure 5.12: **Predicted and Measured Torsion Bending Moments; Soft Pitch Link, no lag damper; $C_W/\sigma = 0.0783$, high-speed $\mu = 0.368$**

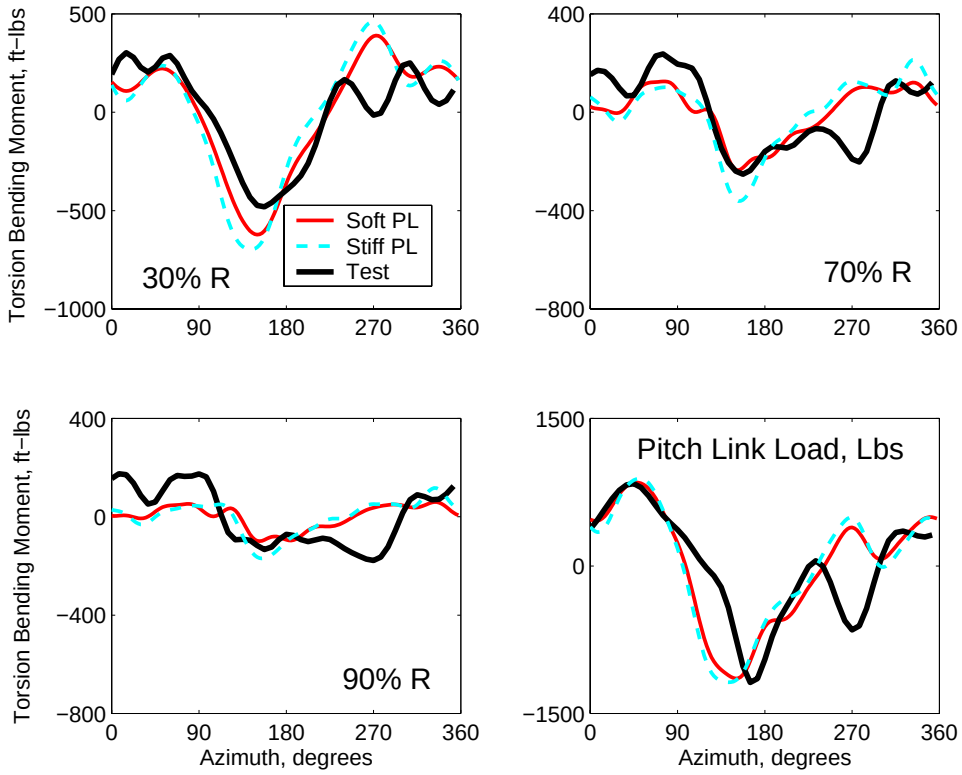

Figure 5.13: **Predicted and Measured Torsion Bending Moments; Effect of Pitch Link Stiffness, no lag damper; $C_W/\sigma = 0.0783$, high-speed $\mu = 0.368$**

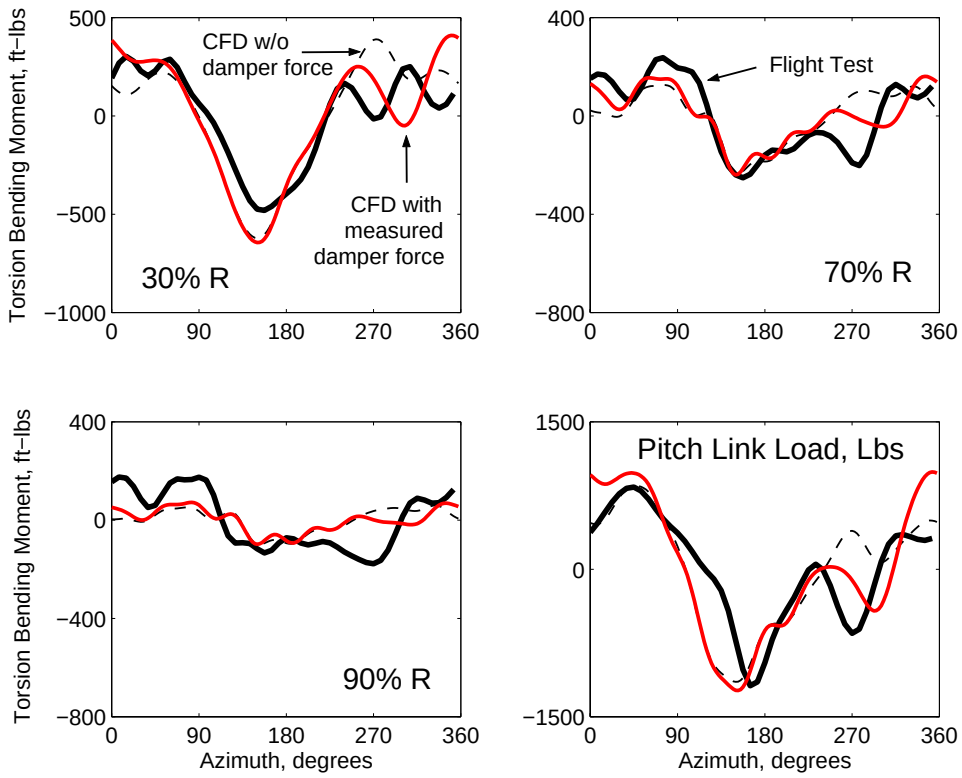

Figure 5.14: **Predicted and Measured Torsion Bending Moments; Soft Pitch Link, measured damper force; C_W/σ = 0.0783, high-speed μ = 0.368**

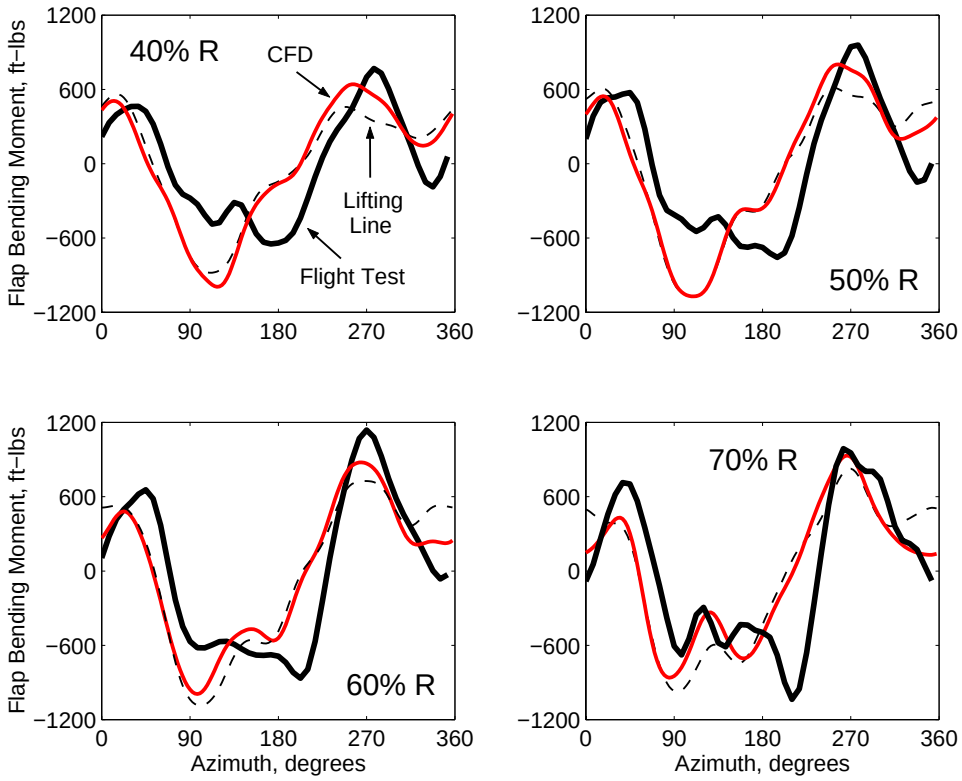

Figure 5.15: **Predicted and Measured Flap Bending Moment; Stiff Pitch Link, no lag damper; $C_W/\sigma = 0.0783$, high-speed $\mu = 0.368$**

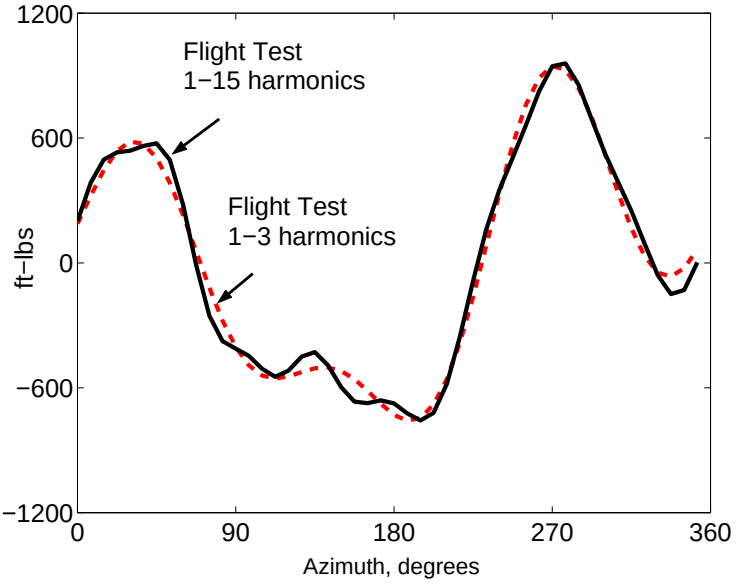

Figure 5.16: **1-3 harmonics of measured flap bending moment at 50% R; C_W/σ = 0.0783, high-speed μ = 0.368**

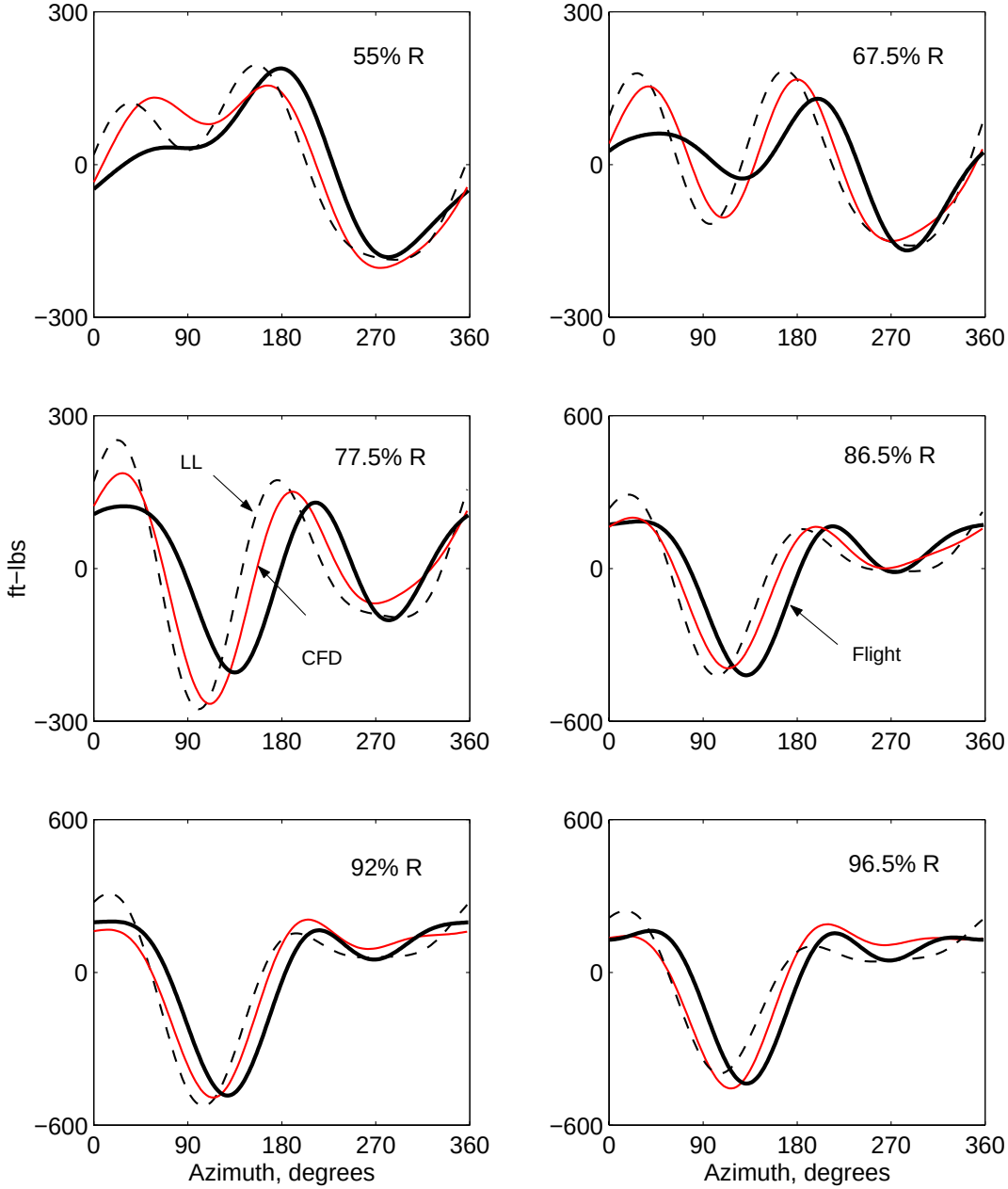

Figure 5.17: **Predicted and measured normal force 1-3/rev; $C_W/\sigma = 0.0783$, high-speed $\mu = 0.368$**

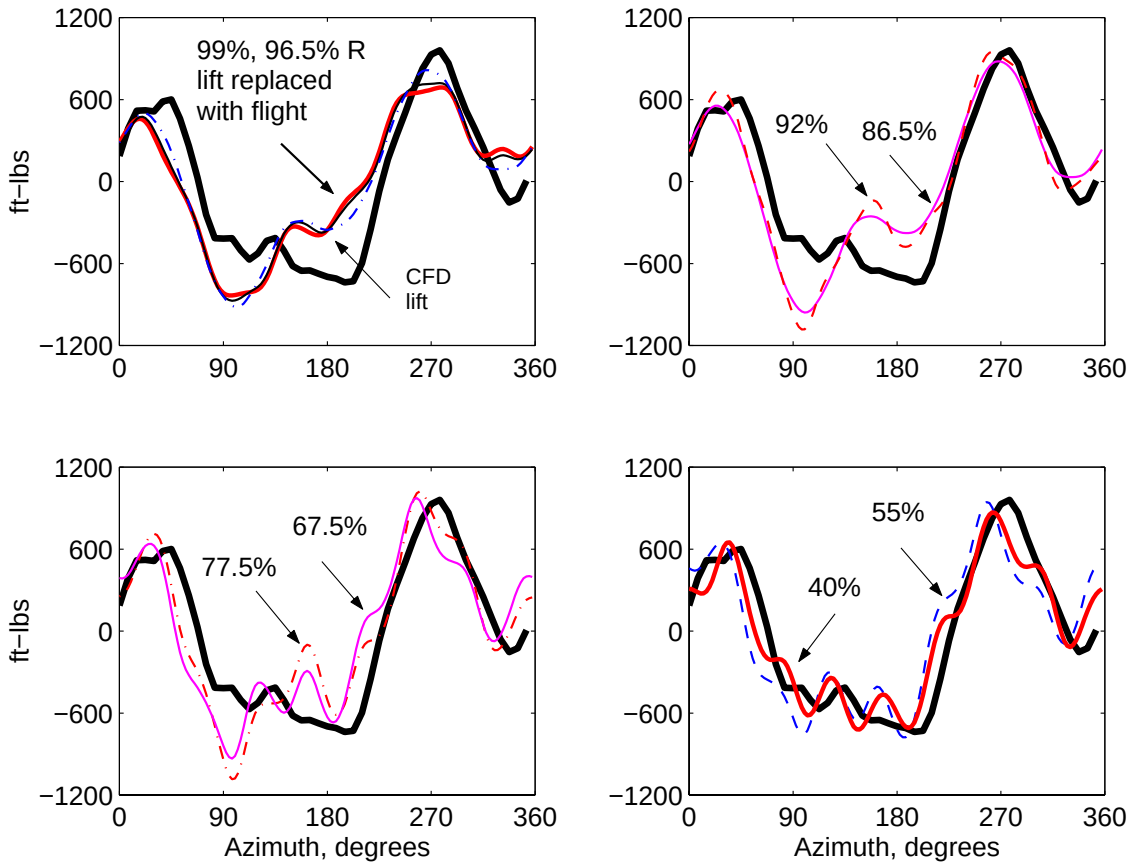

Figure 5.18: **Flap Bending Moment investigation using calculated and measured normal force, eight modes uncoupled solution; 50% R, C_W/σ = 0.0783, high-speed μ = 0.368**

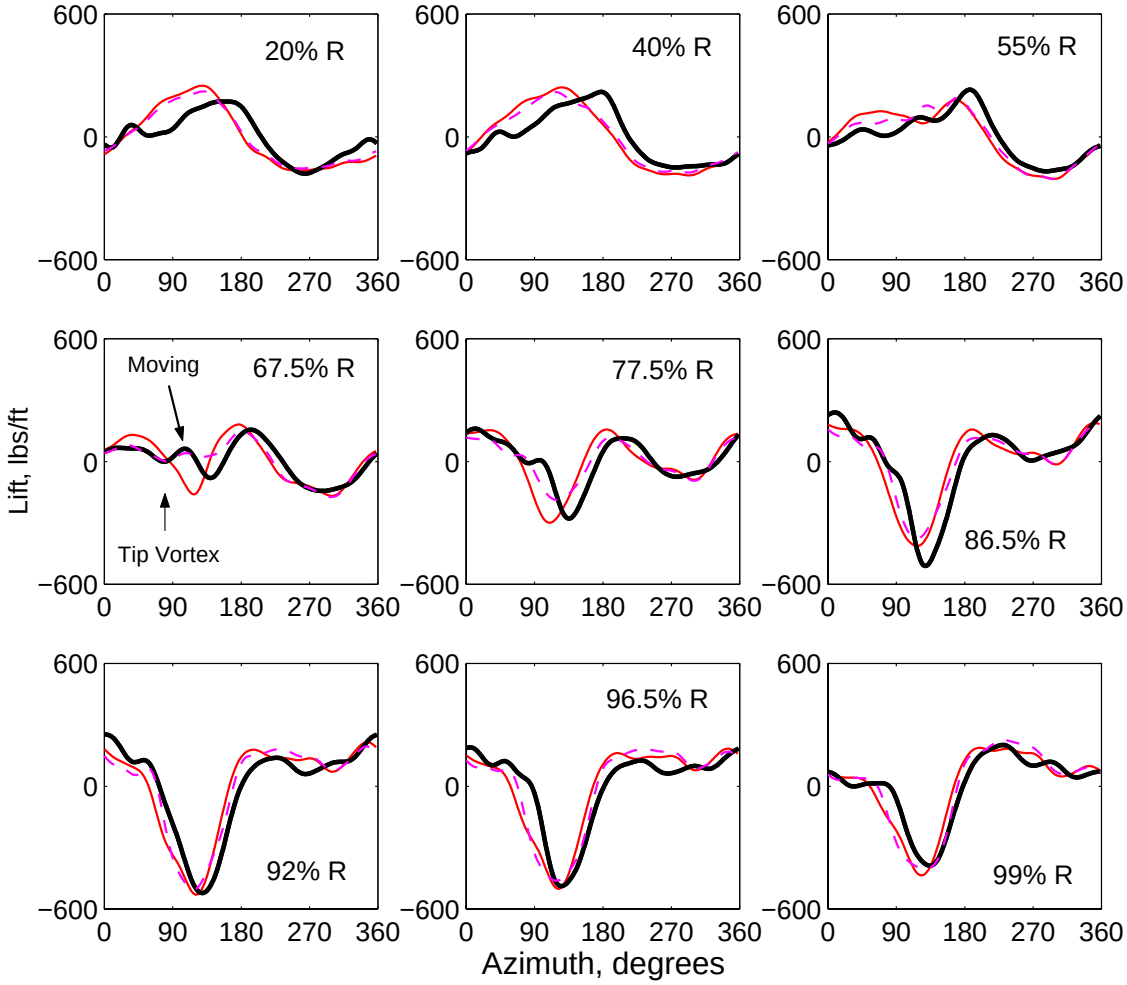

Figure 5.19: **Predicted and measured normal force 0-10/rev; C_W/σ = 0.0783, high-speed μ = 0.368**

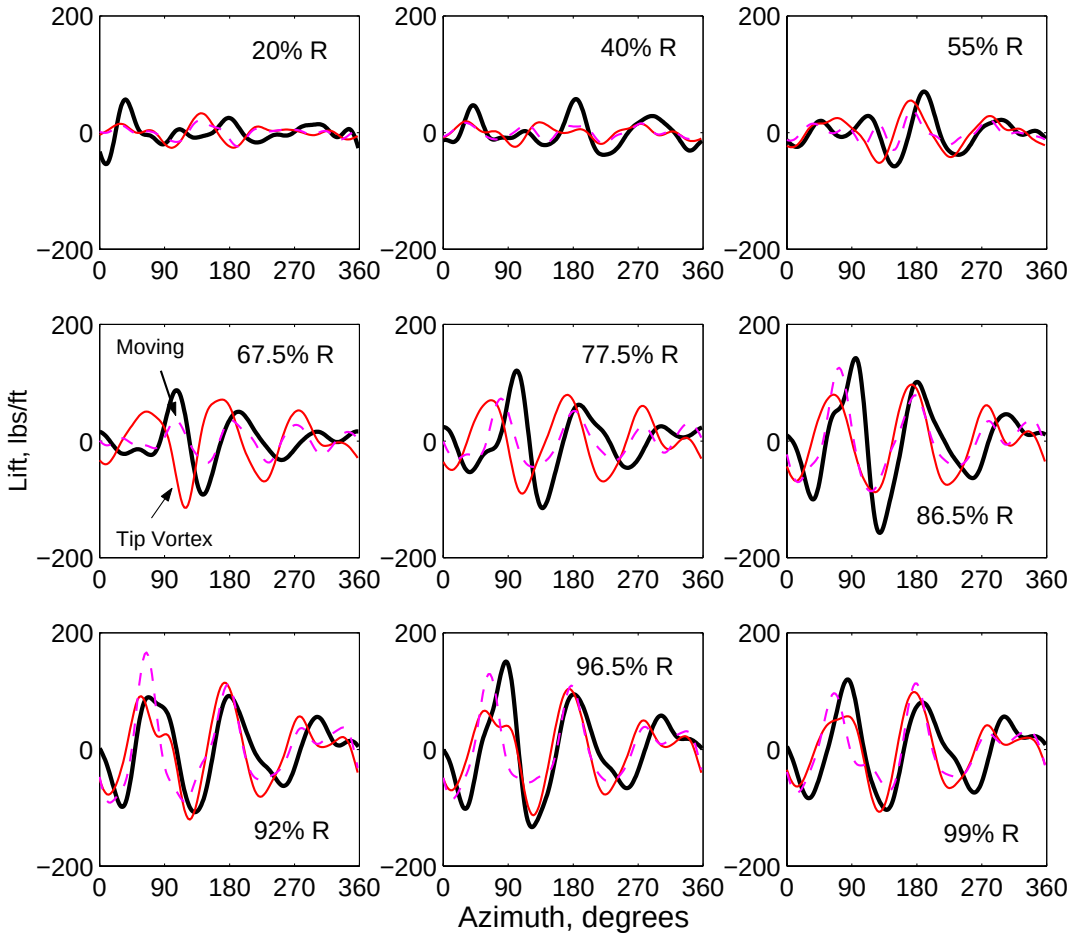

Figure 5.20: **Predicted and measured vibratory normal force 3-10/rev; $C_W/\sigma = 0.0783$, high-speed $\mu = 0.368$**

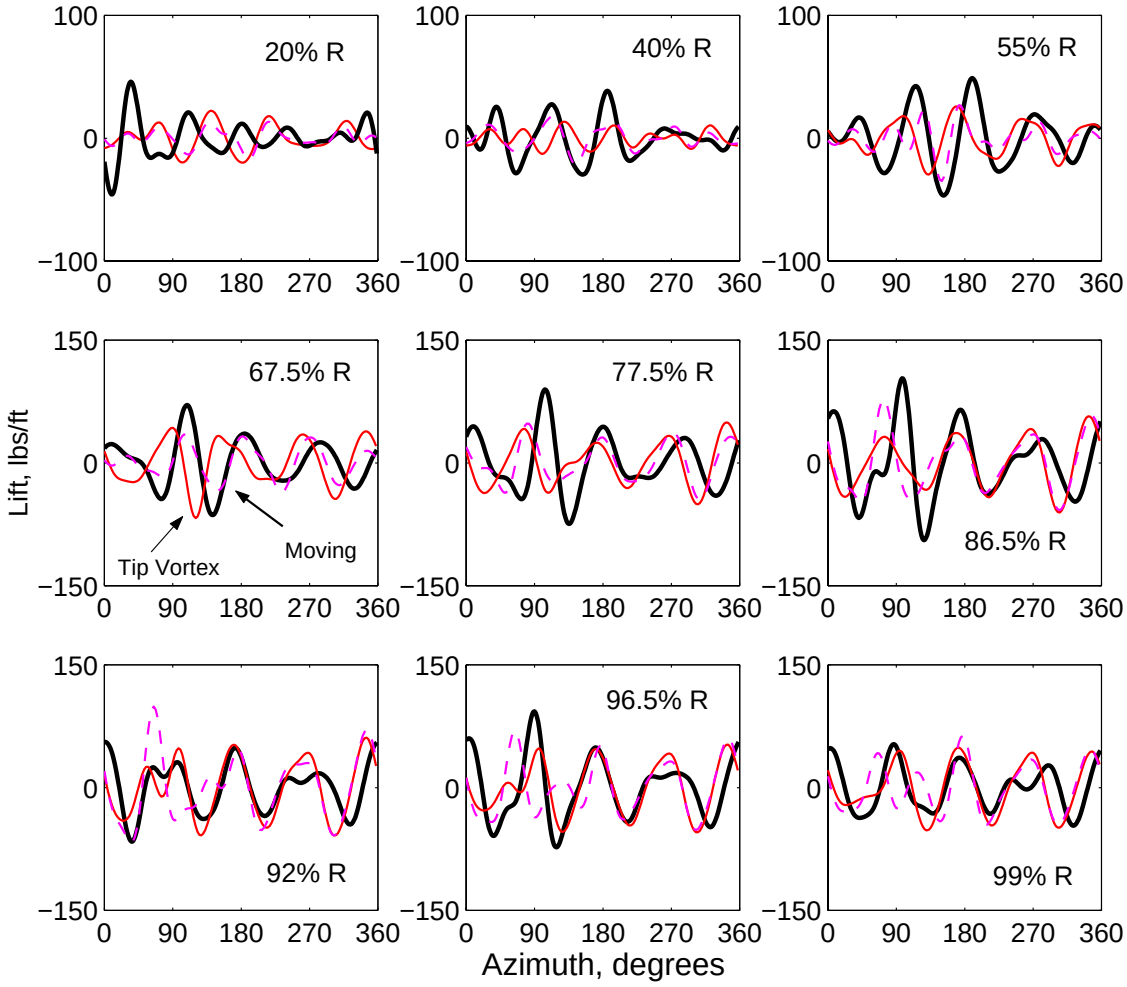

Figure 5.21: **Predicted and measured vibratory normal force 4-10/rev; $C_W/\sigma = 0.0783$, high-speed $\mu = 0.368$**

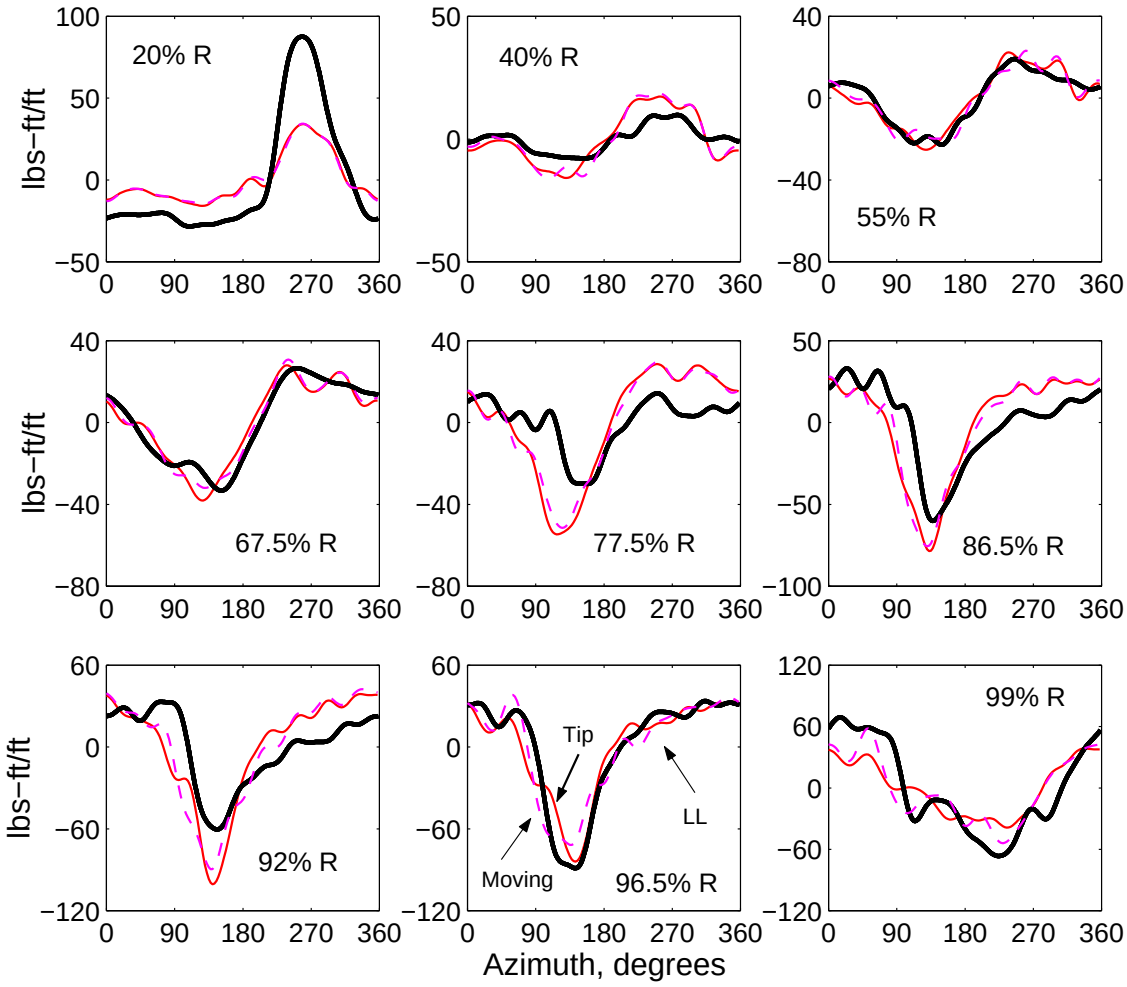

Figure 5.22: **Predicted and measured oscillatory pitching moments (1-10/rev); $C_W/\sigma = 0.0783$, high-speed $\mu = 0.368$**

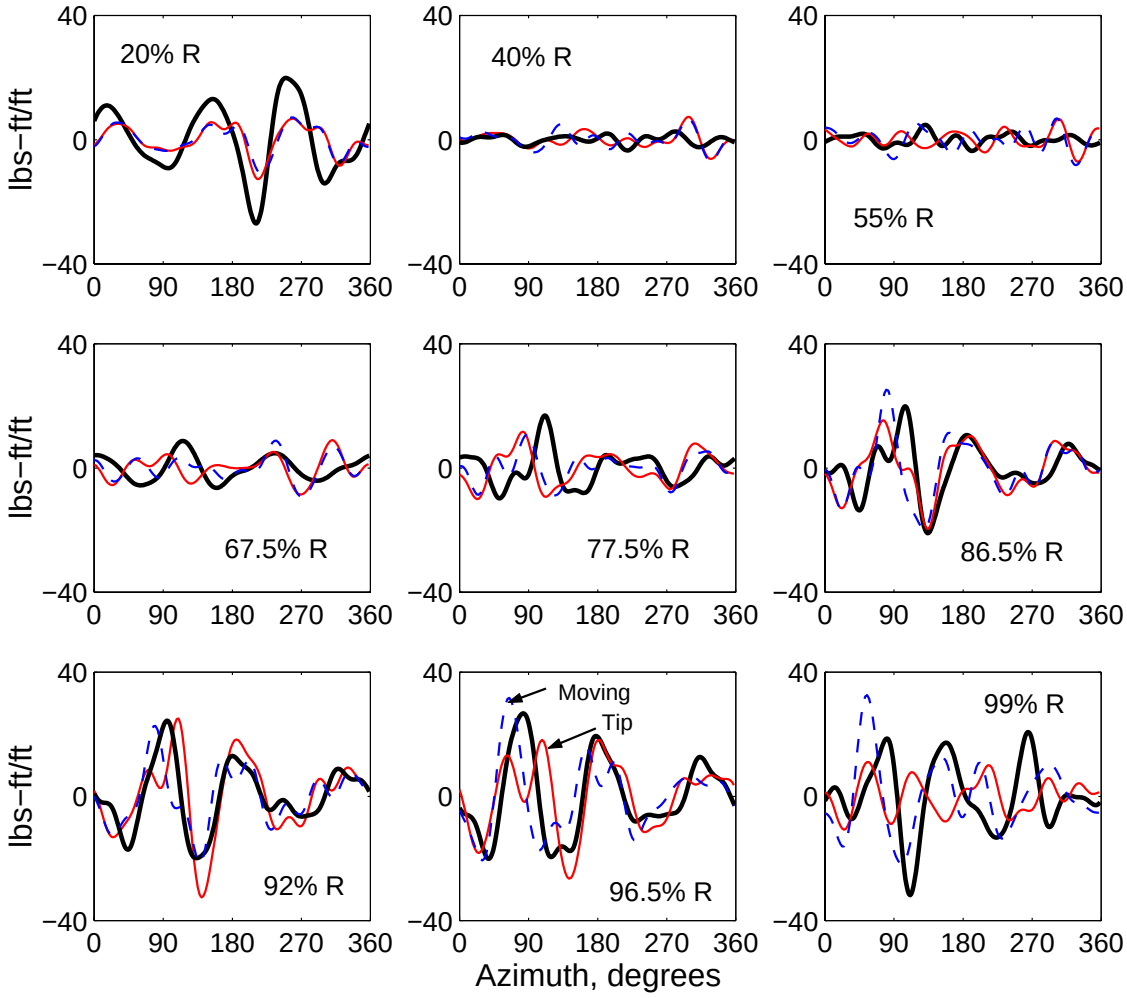

Figure 5.23: **Predicted and measured vibratory pitching moments (3-10/rev); $C_W/\sigma = 0.0783$, high-speed $\mu = 0.368$**

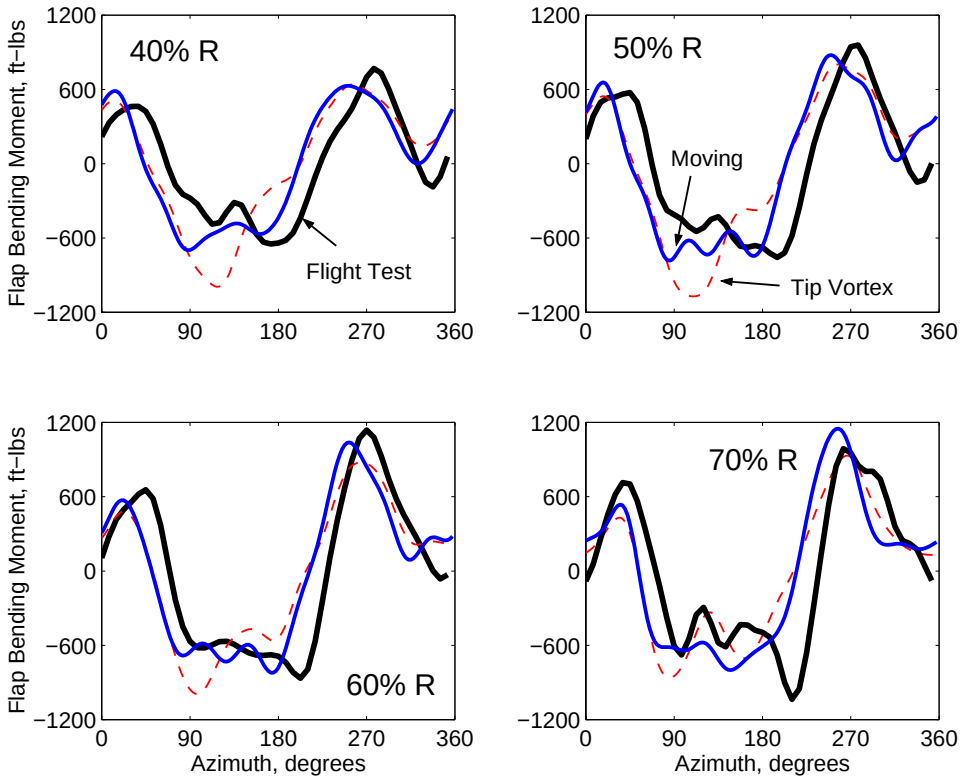

Figure 5.24: **Predicted and Measured Flap Bending Moment; Stiff Pitch Link, no lag damper; $C_W/\sigma = 0.0783$, high-speed $\mu = 0.368$**

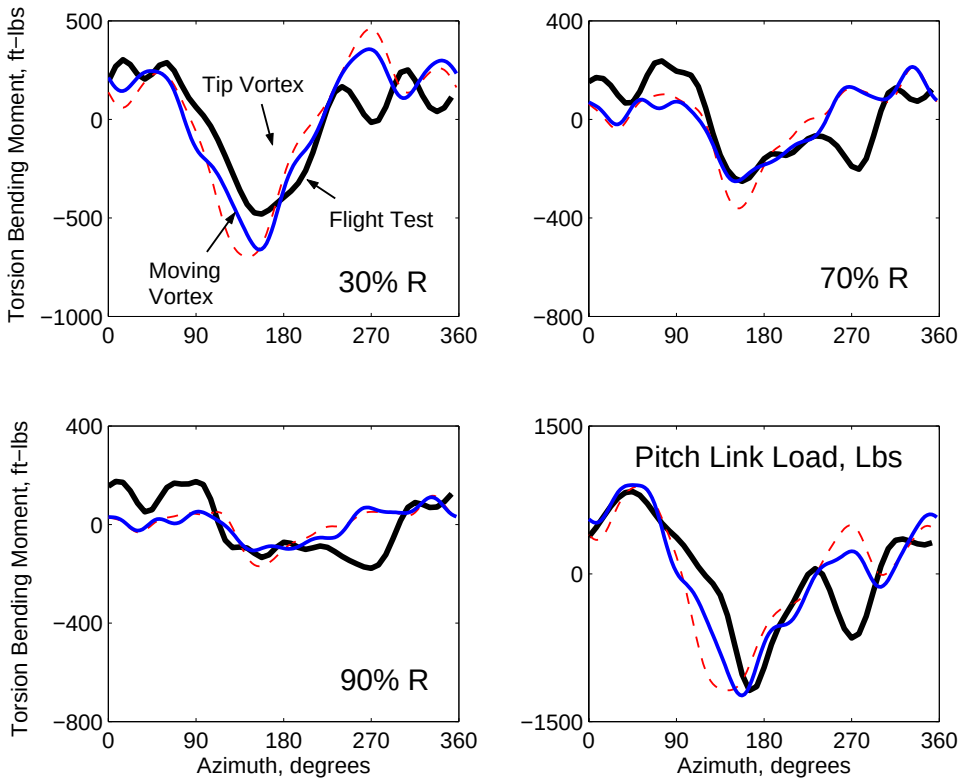

Figure 5.25: **Predicted and Measured Torsion Bending Moment; Stiff Pitch Link, no lag damper; $C_W/\sigma = 0.0783$, high-speed $\mu = 0.368$**

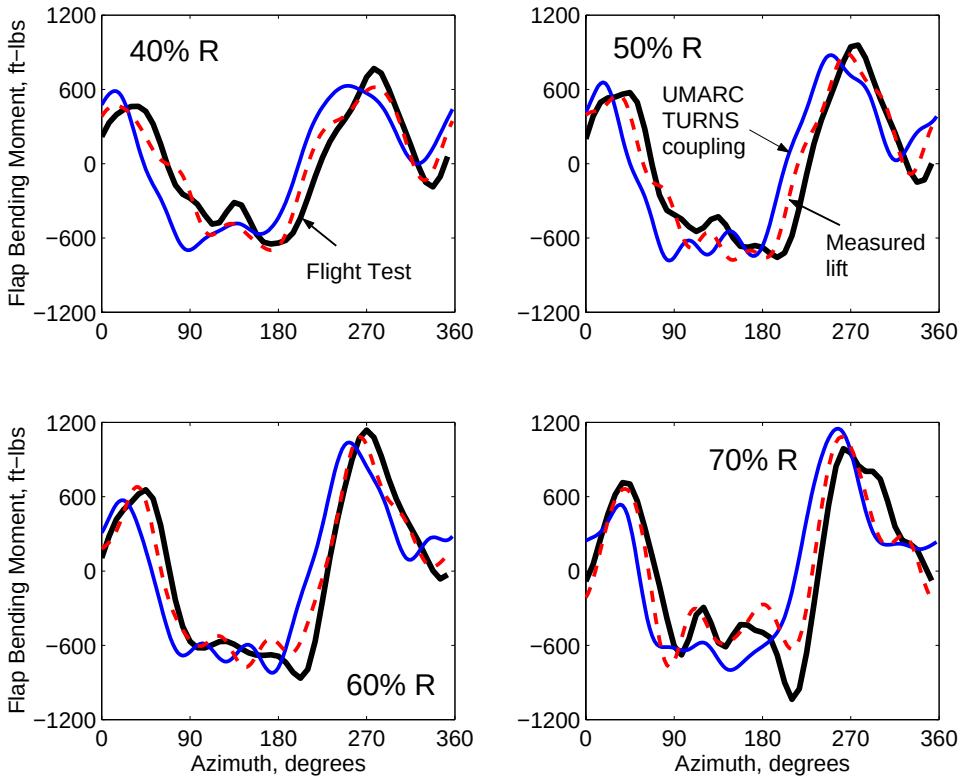

Figure 5.26: **Flap Bending Moment with measured air loads and UMARC-TURNS analysis; $C_W/\sigma = 0.0783$, high-speed $\mu = 0.368$**

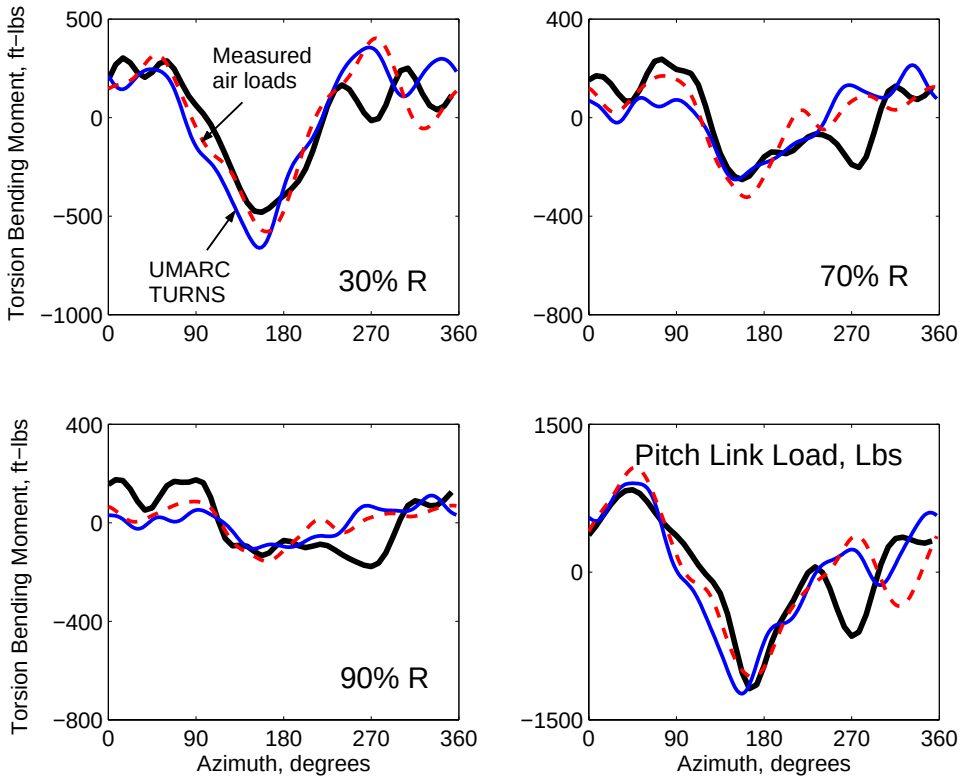

Figure 5.27: **Torsion Bending Moment with measured air loads and UMARC-TURNS analysis; Stiff Pitch Link, no lag damper;** $C_W/\sigma =$ **0.0783, high-speed** $\mu =$ **0.368**

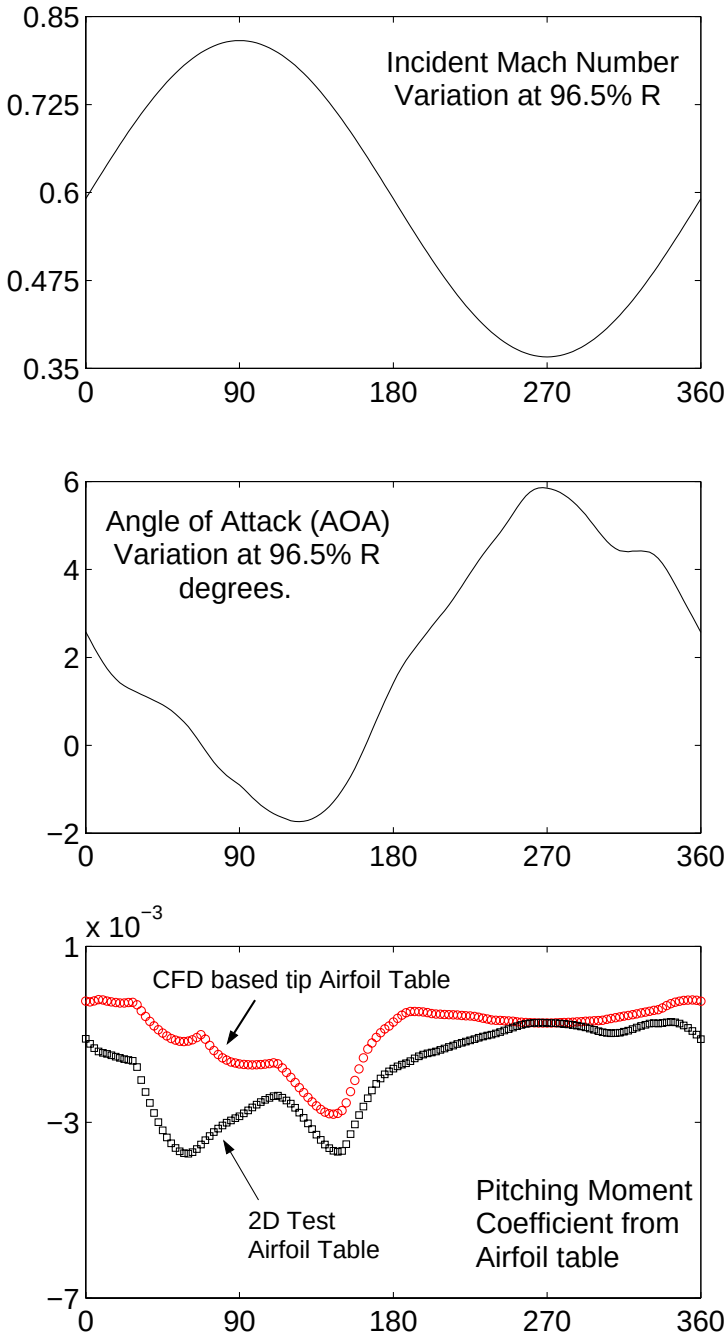

Figure 5.28: **3D Tip Relief Effect on Predicted Pitching Moment Coefficients at 96.5% R; $C_W/\sigma = 0.0783$, high-speed $\mu = 0.368$**

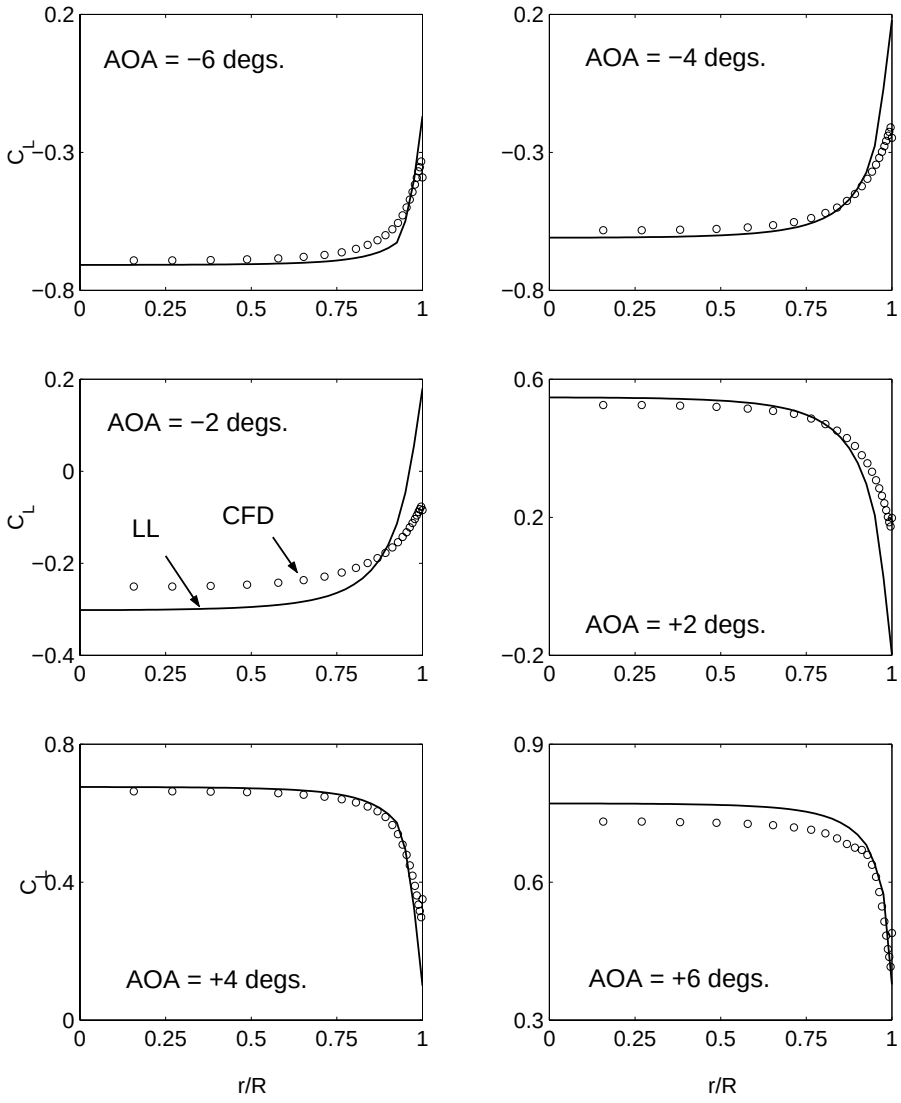

Figure 5.29: **Fixed-wing calculations at Mach 0.8 using CFD and lifting-line models; Span-wise variation of lift on a SC1095 blade of same aspect ratio as an UH-60A blade**

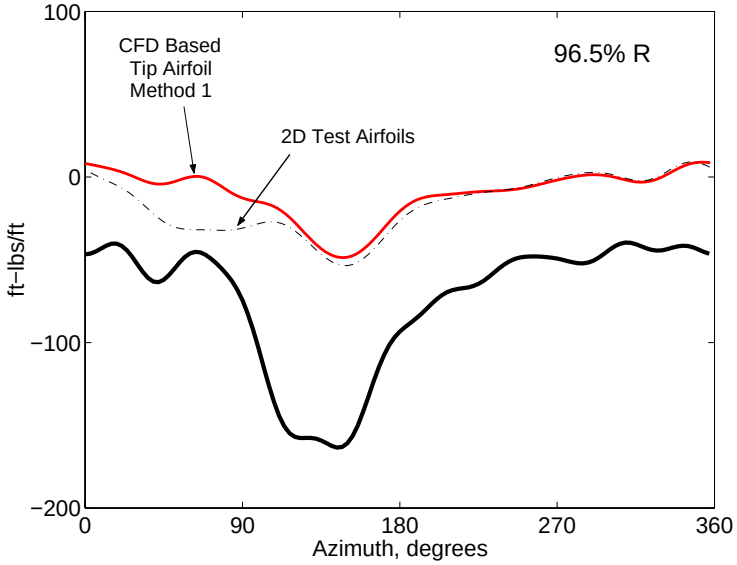

Figure 5.30: **Effect of tip airfoil on pitching moment predictions at 96.5% R; C_W/σ = 0.0783, high-speed μ = 0.368**

Chapter 6

Concluding Remarks

This chapter summarizes the key conclusions of this research work. This research work focussed on the analysis, prediction and validation of high speed rotor vibration. The objective was to understand the fundamental mechanisms behind rotor vibration at high speed and develop a analysis methodology to accurately capture them. The UH-60A Black Hawk was taken as the test bed for prediction and validation of analysis methodology. The UH-60A represents a modern helicopter rotor with high non-linear blade twist (-16 degrees in linear range), tip sweep, sectional center of gravity offsets and large blade deformations in flap, lag and elastic torsion with significant non-linear couplings between the elastic motions. It represented an ideal test case at high speed flight to investigate the consistency of rotor modeling in a systematic manner. Current state of the art analyses meth-

ods showed significant discrepancies in prediction at this flight condition for this helicopter (50% - 100% in magnitude and phase). The prediction deficiency is in general common to all modern rotor systems at high speed. The extensive UH-60A flight test data, repeatable and accurate, ranging from blade loads to air loads to control loads and extensive documentation of the blade and aircraft properties, for the first time opened opportunity for such an investigative work.

This work focussed on the decoupling of the high-speed aeroelastic rotor loads and vibration problem into structural dynamics and aerodynamics. They were studied separately using the UH-60A flight test data. Measured air loads were used to validate, refine and understand the accuracy and limitations of a finite element structural model. Using a reasonably accurate set of blade deformations generated from this study, aerodynamic models were validated and refined. A table look up based unsteady lifting line model was compared with a compressible unsteady Navier-Stokes CFD model. The accuracy and limitations of the lifting-line model and the improvements provided by CFD were understood. The lifting-line model and the CFD model were then coupled to the structural model to obtain comprehensive aeroelastic analysis solutions from first principles.

6.1 Key Conclusions

The detailed conclusions of each segment of the research work have been discussed in detail at the end of each chapter. Here the key ideas are brought together to summarize the end result of the the present research effort.

1. High-speed rotor vibration of the UH-60A at steady level flight (advance ratio $\mu = 0.368$, $C_t/\sigma = 0.0783$) is caused by two phenomenon - 1. large elastic torsion deformations (around -8 to -10 degrees near the tip) driven by blade pitching moments and 2. wake interaction in the advancing blade. The dominant phenomenon at the outboard stations (86.5% R to 99% R) is the elastic torsion. At the inboard stations (67.5% R and 77.5% R) both elastic torsion and wake interactions play key roles.

2. The advancing blade lift phase problem is a manifestation of inaccurate vibratory lift. For accurate lift phase, the vibratory lift must be predicted accurately. For accurate vibratory lift, both elastic torsion and rotor wake interactions must be predicted correctly.

3. Prediction inaccuracy in vibratory lift stem from aerodynamic modeling, not structural dynamic modeling. Trim solution is the not source of error. Comprehensive analyses, in general, predict basic performance and trim accurately at the high speed flight condition. For the UH-60A there is a discrepancy in lateral cyclic (and hub pitch moment) correlation, but this error is not the source of the problem.

4. Error in aerodynamic modeling lies in inaccurate pitching moments. Lifting-line models, with airfoil tables, unsteady aerodynamics, near wake and far wake do not capture the unsteady transonic pitching moments at the outboard stations (86.5% R to 99% R). Without accurate pitching moments, elastic torsion predictions are not accurate and without correct elastic torsion refining

the wake model to capture the wake interactions deteriorates lift prediction, instead of improving it.

5. A CFD analysis captures the pitching moments significantly well. The CFD analysis has to be a 3D analysis which accounts for blade elastic deformations and far wake inflow. Viscosity or turbulence modeling do not appear to be important at this flight condition for lift or pitching moments. It is important for chord forces.

6. Given correct air loads, modern finite element based structural dynamic methods accurately capture the lower harmonics of blade loads. Flap bending moment predictions are accurate, chord bending predictions and torsion loads show significant discrepancies at higher harmonics (4/rev and higher). The lower harmonics, which are well predicted, are the significant contributers to air loads. Therefore predicting the lower harmonics (1 to 3/rev) of the blade deformations are enough to predict the vibratory air loads (up to 5/rev). However, predicting the lower harmonics of structural loads are not enough in terms of vibratory blade loads. Vibratory blade load predictions are not satisfactory for torsion moments and control loads.

7. The dominant behavior of the pitch link load, magnitude and phase of peak to peak up to 3/rev is well predicted using accurate air loads. Prediction errors occur at higher harmonics (4/rev and higher) which lead to a deficiency in the retreating blade prediction. This is an error in the structural model. Possible causes of this error lie in inaccurate details in blade boundary condition and

control system modeling.

8. A lifting-line comprehensive analysis at high speed shows good predictions in performance, satisfactory prediction of peak to peak loads but poor predictions in phase of air loads and blade loads. A CFD comprehensive analysis significantly improves the prediction of phase. The driver behind this improvement is improved pitching moments generating improved elastic torsion via a well developed, accurate structural model.

9. CFD loose coupling with comprehensive analysis is a robust, reliable and fast technique without any convergence problem. The comprehensive analysis provides the structural model, trim model and air loads sensitivity to blade loads during convergence. The final solution depends entirely on the CFD air loads.

6.2 Future Work

In this section future directions of research endeavors are suggested. The causes of rotor vibration at the two vibration critical regimes in steady level flight is now understood. At low speed it is inter-twinning of tip vortices, at high speed it is pitching moment driven elastic torsion and wake. The wake effects and the transonic effects play key roles respectively at these flight conditions.

There is an intermediate flight condition around advance ratio $\mu = 0.25$. This is just high enough to reasonably wash away the low speed wake inter-twinning, but low enough to prevent onset of transonic pitching moments. A high trust condi-

tion at this flight regime is ideal for isolating the effects of dynamic stall induced vibration. The phenomenon of dynamic stall is well understood but prediction capabilities are inaccurate.

Once dynamic stall effects are captured with confidence, the next step is loads and vibration in maneuvers, where all three effects, wake, dynamics stall and transonic flow are important. Beginning with steady maneuvers, the objective would be to move to unsteady maneuvers. Accurately capturing rotor vibration at these level and maneuvering flight conditions will result in aeromechanical analyses being a reliable and well-validated tool for the design of advanced rotor system. It would then adequately compliment, though not entirely replace the need for expensive wind tunnel and flight tests. Some of the broader research areas toward this objective are summarized below.

1. Higher harmonics of blade torsion loads are poor, even with measured air loads. Dynamic stall induced torsion loads are necessarily higher harmonics therefore refinement of structural model will be key to capturing the blade loads. Multi-body formulations of detailed boundary condition and control linkage modeling need to be investigated for possible discrepancies in physics. Multi-body simulations provide the flexibility necessary for full fuselage, tail boom, tail rotor modeling and detailed modeling in general of difficult components required to accurately predict pilot seat and fuselage vibrations.

2. Semi empirical dynamic stall models are well-developed. They are not reliably captured by CFD methods. High fidelity CFD modeling, with detailed vortex

models and Large Eddy Simulations are required. Large Eddy Simulations provide the ability to analyze the effects of large structural motions within turbulence flow. They seek to predict the motion of the larger and most important eddies by isolating them from the smaller ones. They would gradually become essential for a range of aerodynamic problems - from CFD analyses of rotorcraft maneuvering flights to tiny swirls of air shed from micro flapping air vehicles.

3. Rotor fuselage structural and aerodynamic interactions can be handled as a separate and focussed research thrust, leveraging upon the the above two areas. Wake impingement from the main rotor on to the fuselage tail boom is a significant source of 4/rev (for a four bladed rotor) fuselage vibration.

BIBLIOGRAPHY

[1] Crews, S. T., "Rotorcraft Vibration Criteria, A New Perspective," In *Proceedings of the 43rd Annual Forum of the American Helicopter Society*, St. Louis, MO, May 1987.

[2] Schrage, D. P., Peskar, R. E., "Helicopter Vibration Requirements," Proceedings of the 33rd Annual Forum of the American Helicopter Society, May 1977.

[3] William G. Bousman, "Putting the Aero Back Into Aeroelasticity," 8th Annual ARO Workshop on Aeroelasticity of Rotorcraft Systems, University Park, PA, October, 1999.

[4] Roget, B., Chopra, I., "Individual Blade Control Methodology for a Rotor with Dissimilar Blades," *Journal of the American Helicopter Society*, July 2003.

[5] Roget, B., Chopra, I., "Wind Tunnel Testing of an Individual Blade Controller for a Dissimilar Rotor," Presented at the American Helicopter Society 60th Annual Forum, Baltimore, MD, June 7-10, 2004.

[6] Chopra, I., "Status of Application of Smart Structures Technology to Rotorcraft Systems," *Journal of the American Helicopter Society*, Vol. 45, No. 4, October 2000, pp 228-252.

[7] Straub, F. K., "A Feasibility Study of Using Smart Materials for Rotor Control," *Smart Materials and Structures*, Vol. 5, (1), February 1996, pp. 1-10.

[8] Bao, J., Nagaraj, V. T., Chopra, I., Bernhard, A. P. F., "Wind Tunnel Testing of Low Vibration Mach Scale Rotor with Composite Tailored Blades," Presented at the American Helicopter Society 58th Annual Forum, Baltimore, MD, June 7-10, 2004.

[9] Chopra, I., "Review of State of Art of Smart Structures And Integrated Systems," AIAA Journal, Vol. 40, No. 11, November 2002.

[10] Johnson, Wayne, "Recent Developments in the Dynamics of Advanced Rotor Systems," NASA TM 86669, 1985.

[11] Houbolt, J. C. and Brooks, G. W., "Differential Equations of Motion for Combined Flapwise Bending, Chordwise Bending, and Torsion of Twisted Nonuniform Rotor Blades," NACA Report 1346, 1958.

[12] Ormiston, R. A. and Hodges, D. H., "Linear Flap-Lag Dynamics of Hingeless Helicopter Rotor Blades in Hover," *Journal of American Helicopter Society*, Vol. 17, No. 2, April 1972, pp. 2-14.

[13] Hodges, D. H., and Dowell, E. H., "Nonlinear Equations of Motion for the Elastic Bending and Torsion of Twisted Nonuniform Rotor Blades," NASA TN D-7818, December 1974.

[14] Ormiston, R. A., Hodges, D. H., and Peters, D. A., "On the Nonlinear Deformation Geometry of Euler-Bernoulli Beams," NASA Technical Paper 1566, 1980.

[15] Kvaternik, Raymond G., Kaza, Krishna R. V., Nonlinear Curvature Expressions for Combined Flapwise Bending, Chordwise Bending, Torsion, and Extension of Twisted Rotor Blades, NASA TM X-73, 997, 1976.

[16] Rosen, A., Friedmann, P.P., "Nonlinear Equations of Equilibrium for Elastic Helicopter or Wind Turbine Blades Undergoing Moderate Deformation," Report UCLA-ENG 7718, University of California at Los Angeles, June 1977 (also NASA CR-159478, 1978)

[17] Johnson, W., "Aeroelastic Analysis for Rotorcraft in Flight or in a Wind Tunnel," NASA TN D-8515, 1977.

[18] Hodges, D.H., "A Mixed Variational Formulation Based on Exact Intrinsic Equations for Dynamics of Moving Beams," Int. J. Solids Structures, Volume 26, No. 11, 1990.

[19] Bauchau, O.A., Hong, C.H., "Nonlinear Composite Beam Theory," Journal of Applied Mechanics, Vol. 55, No. 1, March 1998.

[20] Smith, E. C., Chopra, I., "Aeroelastic Response, Loads, and Stability of a Composite Rotor in Forward Flight," AIAA Journal, Vol. 31, No. 7, July 1993.

[21] Celi, R., Friedmann, P. P., "Structural Optimization with Aeroelastic Constraints of Rotor Blades with Straight and Swept Tips," *AIAA Journal*, Vol. 28, No. 5, 1992.

[22] Benquet, P., Chopra, I., "Calculated Dynamic Response and Loads for an Advanced Tip Rotor in Forward Flight," Proceedings of the 15the European Rotorcraft Forum, Amsterdam, Netherland, Sep. 1989.

[23] Kim, K. C., Chopra, I., "Aeroelastic Analysis of Helicopter Blades with Advanced Tip Shapes," *Journal of the American Helicopter Society*, Vol. 37, No. 1, Jan 1992.

[24] Bir, G., Chopra, I., "Aeromechanical Stability of Rotorcraft with Advanced Geometry Blades," Presented at the AIAA 34th Structures, Structural Dynamics and Materials Conference, La Jolla, California, April 1993.

[25] Ganguli, R., Chopra, I., "Aeroelastic Optimization of an Advanced Geometry Helicopter Rotor," *Journal of the American Helicopter Society*, Vol. 41, No. 1, January 1996, pp. 18-28.

[26] Yuan, I., Friedmann, P. P., Venkatesan, C., "A New Aeroelastic Model for Composite Rotor Blades with Straight and Swept Tips," Proceedings of the 33rd AIAA/ASME/ASCE/AHS/ASC Structures, Structural Dynamics and Materials Conference, AIAA Paper No. 92-2259, Dallas, Texas, Apr 13-15, 1992.

[27] Ganguli, R., Chopra, I., "Aeroelastic Optimization of an Advanced Geometry Composite Helicopter Rotor," Annual Forum Proceedings of the American Helicopter Society, Vol. 2, 1995, pp. 965-984.

[28] Murthy, V.R., Joshi, A.M., "Free Vibration Characteristics of Multiple Load Path Blades by the Transfer Matrix Method," *Journal of the American Helicopter Society*, Vol. 31, No. 4, October 1986.

[29] Sangha, K. B., Weisenburger, R. K., Straub, F. K., "Rotor/airframe aeroelastic analyses using the transfer matrix approach," Collection of Technical Papers - AIAA/ASME/ASCE/AHS Structures, Structural Dynamics and Materials Conference, 1990, pp. 1712-1726.

[30] Straub, F. K., Friedmann, P. P., "Galerkin type finite element method for rotary-wing aeroelasticity in hover and forward flight," 6th European Rotorcraft and Powered Lift Forum, paper no. 15, Bristol, England, 1980.

[31] Chopra, I., Sivaneri, N. T., "Aeroelastic Stability of Rotor Blades Using Finite Element Analysis," NASA CR 166389, August 1982.

[32] Johnson, W., "Rotorcraft Dynamics Models for a Comprehensive Analysis," 54th Annual Forum of the American Helicopter Society, Washington D.C., May 20-22, 1998.

[33] Saberi, H., Khoshlahjeh, M., Ormiston, R. A., Rutkowski, M. J., "Overview of RCAS and Application to Advanced Rotorcraft Problems," Presented at the AHS 4th Decennial Specialist's Conference on Aeromechanics, San Francisco, California, January 21-23, 2004.

[34] Howlett, J. J., "UH-60A BLACK HAWK Engineering Simulation Program - Vol. 1, Mathematical Model," NASA CR 166309, December 1981.

[35] Bauchau, O. A., Kang, N. K., "A Multibody Formulation for Helicopter Structural Dynamic Analysis," *Journal of the American Helicopter Society*, Vol. 38, No. 2, April 1993.

[36] Ghiringhelli, G. L., Masarati, P., Mantegazza, P., Nixon, M. W., "Multi-Body Analysis of the 1/5 scale Wind Tunnel Model of the V-22 Tiltrotor," 55th Annual Forum of the American Helicopter Society, Montreal, Canada, May 25-27, 1999.

[37] Piziali, R. A., DuWaldt, F., "Computation of Rotary Wing Harmonic Airloads and Comparison with Experimental Results," American Helicopter Society 18th Annual National Forum, Washington DC, 1962.

[38] Piziali, R. A., "A Method for Predicting the Aerodynamic Loads and Dynamic Response of Rotor Blades," *Journal of Sound and Vibration*, Vol. 4, No. 3, 1966, pp 445-489.

[39] Landgrebe, A. J., "An Analytical Method for Predicting Rotor Wake Geometry," *Journal of the American Helicopter Society*, Vol. 14, No. 4, October 1969, pp. 20-32.

[40] Landgrebe, A. J., "The Wake Geometry of a Hovering Rotor and its Influence on Rotor Performance," *Journal of the American Helicopter Society*, Vol. 17, No. 4, October 1972, pp 2-15.

[41] Scully, M. P., "A Method of Computing Helicopter Vortex Wake Distortion," MIT, ASRL TR 138-1, June 1967.

[42] Crimi, P., "Theoretical Prediction of the Flow in the Wake of a Helicopter Rotor," Cornell Aeronautical Laboratory Report BB-1994-5-1, Buffalo NY, September 1965.

[43] Scully, M. P., "Computation of Helicopter Rotor Wake Geometry and Its Influence on Rotor Harmonic Airloads," MIT, ASRL TR 178-1, March 1975.

[44] Kocurek, J. D., and Berkovitz, L. F., "Velocity Coupling : A New Concept or Hover and Axial Flow Wake Analysis and Design," AGARD CP-334, May 1982.

[45] Egolf, T. A., Landgrebe, A. J., "Helicopter Rotor Wake Geometry and its influence in Forward Flight, Vol. 1 - Generalized Wake Geometry and Wake Effects in Rotor Airloads and Performance," NASA CR-3726, October 1983.

[46] Beddoes, T. S., "A Wake Model for High Resolution Airloads," Proceedings of the 2nd International Conference on Basic Rotorcraft Research, Traingle Park, NC, 1985.

[47] Wachspress, D. A., Quackenbush, T. R., Boschitsch, A. H., "First-Principles Free-Vortex Wake Analysis For Helicopters and Tiltrotors," Presented at the American Helicopter Society, 59th Annual Forum, Phoenix, AZ, May 6-8, 2003.

[48] Johnson, W., "A General Free Wake Geometry Calculation For Wings and Rotors," Presented at the American Helicopter Society 51st Annual Forum, Fort Worth, Texas, May 9-11, 1995.

[49] Bagai, A., Leishman, J. G., "The Maryland Free-Wake Analysis - Theory, Implementation and User's Manual," University of Maryland, Department of Aerosp ace Engineering, Technical Report Prepared for NASA Langley Research Center, Aeroacousitics Branch, Fluid Mechanics and Acoustics Division, Contract No. 015-2685, December 1995.

[50] Johnson, W., "Influence of Wake Models on Calculated Tiltrotor Aerodynamics," American Helicopter Society Aerodynamics, Acoustics, and Test and

Evaluation Technical Specialist Meeting Proceedings, San Francisco, CA, January 2002.

[51] Bagai, A., Leisham, J. G., "Free-Wake Analysis of Tandem, Tilt-Rotor and Coaxial Rotor Configurations," *Journal of the American Helicopter Society*, Vol. 41, No. 3, July 1996, pp. 196-207.

[52] Johnson, W. "Wake Model for Helicopter Rotors in High Speed Flight," NASA CR 177507, November 1988.

[53] Clark, D. R. and Leiper, A. C., "The Free Wake Analysis - A Method for Prediction of Helicopter Rotor Hovering Performance," *Journal of the American Helicopter Society*, Vol. 15, No. 1, January 1970, pp. 3-11.

[54] Sadler, S. G., "A Method for Predicting Helicopter Wake Geometry, Wake Induced Inflow and Wake Effects on Blade Airloads," American Helicopter Society 27th Annual National Forum, Washington DC, May 1971.

[55] Egolf, T. A., "Rotor Wake Modeling for High Speed Applications," American Helicopter Society 44th Annual National Forum, Washington D.C., June 16-18 1988.

[56] Baron, A., Boffadosi, M., "Unsteady Free Wake Analysis of Closely Interfering Helicopter Rotors," 19th European Rotorcraft Forum, Cernobbio, Italy, September 14-16, 1993.

[57] Jain, R., Conlisk, A. T., Mahalingam, R., Komerath, N. M., "Interaction of Tip-Vortices in the Wake of a Two-Bladed Rotor," American Helicopter Society 54th Annual National Forum, Washington DC, May 20-22, 1998.

[58] Chung, K. H., Na, S. U., Jeon, W. H., and Lee, D. J., "A Study on Rotor Tip-Vortex Roll-up Phenomenon by Using Time-Marching Free-Wake Method," American Helicopter Society 56th Annual National Forum, Virginia Beach, VA, May 2-4, 2000.

[59] Caradonna, F., Hendley, E., Silva, M., Huang, S., Komerath, N., Reddy, U., Mahalingam, R., Funk, R., Wong, O., Ames, R., Darden, L., Villareal, L., Gregory, J., "Performance Measurement and Wake Characteristics of a Model Rotor in Axial Flight," *Journal of the American Helicopter Society*, Vol. 44, No. 2, 1999, pp. 101-108. (Errata, Vol. 44, No. 3).

[60] Quackenbush, T. R., Keller, J. D., Wachspress, D. A., and Boschitsch, A. H., "Reduced Order Free Wake Modeling for Near Real Time Simulation of Rotorcraft Flight Mechanics," American Helicopter Society 55th Annual Forum Proceedings, Montreal, QC, May 25-27, 1999.

[61] Bhagwat, M. J., and Leishman, J. G., "Stability, Consistency and Convergence of Numerical Algorithms for Time-Marching Free-Vortex Wake Analyses," *Journal of American Helicopter Society*, Vol. 46, No. 1, January 2001, pp. 59-71.

[62] Bhagwat, M. J., Leishman, J. G., "Rotor Aerodynamics During Maneuvering Flight Using a Time-Accurate Free-Vortex Wake," *Journal of American Helicopter Society*, Vol. 48, No. 3, July 2003.

[63] Pitt, D.M., Peters, D.A., "Rotor Dynamic Inflow Derivatives and Time Constants from Various Inflow Models," 9th European Rotorcraft Forum, Stresa, Italy, Sept. 13-15.

[64] Peters, D.A., He, C.J., "Finite State Induced Flow Models Part II : Three Dimensional Rotor Disk," *Journal of Aircraft*, 32(2), pp.323-333.

[65] Morillo, J.A., Peters, D.A., "Velocity field above a rotor disk by a new dynamic inflow model," *Journal of Aircraft*, 39(5), pp.731-738.

[66] Leishman, J. G., *Priciples of Helicopter Aerodynamics*, Cambridge University Press, New York, 2000

[67] Leishman, J.G., "Validation of Approximate Indicial Aerodynamic Functions for Two-Dimensional Subsonic Flow," *Journal of Aircraft*, Vol. 25, No. 1, October 1, 1988.

[68] T.S.Beddoes, "Practical Computation of Unsteady Lift," Proceedings of the 7th European Rotorcraft Forum, Sept. 1982, see also *Vertica*, Vol. 8, No. 1, 1984, pp. 55-71.

[69] Beddoes, T. S., "Representation of Airfoil Behaviours," *Vertica* Vol. 7, No. 2, pp. 183-197, 1983.

[70] Leishman, J. G., Beddoes, T. S., "A Semi-Empirical Model for Dynamic Stall," *Journal of the American Helicopter Society*, July 1989, pp. 3-17.

[71] Leishman, J. G., "Modeling Sweep Effects on Dynamic Stall," *Journal of the American Helicopter Society*, July 1989, pp. 18-29.

[72] Johnson, W., "The Response and Airloading of Helicopter Rotor Blades Due to Dynamic Stall," ASRL TR 130-1, May 1970

[73] Gormont, R. E., "A Mathematical Model of Unsteady Aerodynamics and Radial Flow for Application to Helicopter Rotors," USA AVLABS TR 72-67, May 1970.

[74] Petot, D., "Differential Equation Modeling of Dynamic Stall," La Recherche Aerospatiale, Number 1989-5 (Corrections dated October 1990).

[75] Truong, V. K., "A 2-D Dynamic Stall Model Based on a Hopf Bifurcation," Nineteenth European Rotorcraft Forum, Marseiles, France, September, 1998.

[76] Johnson, W., "Rotorcraft Aerodynamics Models for a Comprehensive Analysis," 54th Annual Forum of the American Helicopter Society, Washington DC, May 20-22, 1998.

[77] Johnson, W., "Recent Developments in Rotary-Wing Aerodynamic Theory," *AIAA Journal*, Vol. 24, No. 8, August 1986, pp. 1219-1245.

[78] Desopper, A., "Study of Unsteady Transonic Flow on Rotor Blade with Different Tip Shapes," *Vertica*, Vol. 9, No. 3, July 1985.

[79] Desopper, A., Lafon, P., Ceroni, P., and Phillipe, J. J., "10 Years of Rotor Flow Studies at ONERA - State of the Art and Future Studies," 42nd Annual Forum of the American Helicopter Society, Washington D.C., June 1986.

[80] Philippe, J. J., Vuillet, A., "Aerodynamic Designs of Advanced Rotors with New Tip Shapes," 39th Annual Forum of the American Helicopter Society, St. Louis, Missouri, May 1983.

[81] Tarzanin, F. J., Vlaminck, R. R., "Investigation of the Effects of Blade Sweep on Rotor Vibratory Loads," NASA CR-166526, Oct. 1983.

[82] Chopra, I., "Perspectives in Aeromechanical Stability of Helicopter Rotors," *Vertica*, v 14, n 4, 1990, pp. 457

[83] Vellaichamy, S., Chopra, I., "Effect of Modeling Techniques in the Coupled Rotor-Body Vibration Analysis," In Proceedings of the 34th Structures, Structural Dynamics and Materials Conference and Adaptive Structures Forum, La Jolla, CA, April 1993.

[84] Chiu, T., Friedmann, P. P., "A Coupled Helicopter Rotor/Fuselage Aeroelastic Response Model for ACSR," In Proceedings of the 36th Structures, Structural Dynamics and Materials Conference and Adaptive Structures Forum, New Orleans, LA, April 1993.

[85] Yeo, H., Chopra, I., "Coupled Rotor/Fuselage Vibration Analysis Using Detailed 3-D Airframe Models," *Mathematical and Computer Modelling* 33 (2001) pp. 1035-1054.

[86] Wachspress, D. A., Quackenbush, T. R., Boschitsch, A. H., "Rotorcraft Interactional Aerodynamics with Fast Vortex/Fast Panel Methods," *Journal of the American Helicopter Society*, Vol. 48, No. 4, October 2003.

[87] Leishman, J. G., Bi, N., "Aerodynamic Interactions Between a Rotor and a Fuselage in Forward Flight," *Journal of the American Helicopter Society*, Vol. 35, No. 3, July 1990.

[88] Zori, L. A. J., Mathur, S. R., Rajagopalan, R. G., "Three Dimensional Calculations of Rotor-Airframe Interaction in Forward Flight," American Helicopter Society 52nd Annual Forum Proceedings, Washington D.C., June 1992.

[89] Bettschart, N., "Rotor Fuselage Interaction : Euler and Navier-Stokes Computations with an Actuator Disk," American Helicopter Society 55th Annual Forum Proceedings, Montreal, Canada, May 1999.

[90] Johnson, W, "A Comprehensive Analytical Model of Rotorcraft Aerodynamics and Dynamics, Part I : Analysis Development," NASA TM-81182, June 1980.

[91] Johnson, W., *Helicopter Theory*, Princeton University Press, Princeton, New Jersey, 1980.

[92] Dugundji, J., Wendell, H., "Some Analysis Methods for Rotating Systems with Periodic Coefficients," *AIAA Journal*, Vol. 21, No. 6, June 1983.

[93] Panda, B., Chopra, I., "Dynamics of Composite Rotor Blades in Forward Flight," *VERTICA*, Vol. 11, No. 1/2, January 1987.

[94] Panda, B., Chopra, I., "Flap-Lag-Torsion Stability in Forward Flight," *Journal of the American Helicopter Society*, Vol. 29, No. 4, October 1985.

[95] Ormiston, R. A., Rutkowski, M. J., Ruzicka, G. C., Saberi, H., Jung, Y., "Comprehensive Aeromechanics Analysis of Complex Rotorcraft using 2GCHAS," Presented at the American Helicopter Society Aeromechanics Specialists Conference, San Francisco, California, January 19-21, 1994.

[96] Bir, G., Chopra, I., Nguyen, K., "Development of UMARC (University of Maryland Advanced Rotor Code)," American Helicopter Society 46th Annual Forum Proceedings, Washington, D.C., May 1990.

[97] Bousman, Young, C., Toulmay, F., Gilbert, N. E., Strawn, R. C., Miller, J. V., Maier, T. H., Costes, M. and Beaumier P., "A Comparison of Lifting-Line and CFD Methods with Flight Test Data from a Research Puma Helicopter," NASA TM 110421, October 1996.

[98] Yen, J. G., Corrigan, J. J., Schillings, J. J., Hsieh, P. Y., "Comprehensive Analysis Methodology at Bell Helicoper : COPTER," American Helicopter Society Aeromechanics Specialists Conference, San Francisco, CA, January 1994.

[99] William G. Bousman, T. Maier, "An Investigation of Helicopter Rotor Blade Flap Vibratory Loads," American Helicopter Society 48th Annual Forum Proceedings, Washington D.C., June 1992.

[100] Lim, J. W., Anastassiades, T., "Correlation of 2GCHAS Analysis with Experimental Data," *Journal of the American Helicopter Society*, Vol.40, No. 4, October 1995, pp. 18-33.

[101] Yeo, H., Johnson, W., "Assessment of Comprehensive Analysis Calculation of Airloads on Helicopter Rotors," Presented at the American Helicopter Society 4th Decennial Specialist's Conference on Aeromechanics, San Francisco, CA, January 21-23, 2004.

[102] Datta, A., Chopra, I., "Validation and Understanding of UH-60A Vibratory Loads in Steady Level Flight," 58th Annual Forum of the American Helicopter Society, Montreal, Canada, June 2001.

[103] Wang, J. M., "Challanges in Rotor Dynamics Correlation," Presented at the 54th Annual Forum of the American Helicopter Society, Washington D.C., May 20-22, 1998.

[104] Sopher, R., Duh, J. E., "Prediction of Control System Loads in Level Flight and Maneuvers," Presented at the AHS 50th Annual Forum, Washington D.C., May 11-13, 1994.

[105] Vinokur, M., "An Analysis of Finite-Difference and Finite-Volume Formulations for Conservation Laws," *Journal of Computational Physics*, Vol.81, No.2, March 1989, pp. 1-52.

[106] Paramesvaran, V. and Baeder, J. D., "Indicial Aerodynamics in Compressible Flow - Direct Computational Fluid Dynamic Calculations," *Journal of Aircraft*, Vol. 34, No. 1, January 1997, pp. 131-133.

[107] Altmikus, A. R. M., Wagner, S., Beaumier, P., and Servera, G., "A Comparison : Weak versus Strong Modular Coupling for Trimmed Aeroelastic Rotor Simulation," American Helicopter Society 58th Annual Forum, Montreal, Quebec, June 2002.

[108] Bauchau, O., A. and Ahmad, J., U., " Advanced CFD and CSD Methods for Multidisciplinary Applications of Rotorcraft Problems," AIAA 6th Symposium on Multidisciplinary Analysis and Optimization, Seattle, WA, September 1996.

[109] Pomin, H. and Wagner, S. "Navier-Stokes Analysis of Helicopter Rotor Aerodynamics in Hover and Forward Flight," AIAA 2001-0998, Reno, NV January 2001.

[110] Tung, C., Caradonna, F., X. and Johnson, W., "Conservative Full Potential Model for Unsteady Transonic Rotor Flows," *AIAA Journal*, Vol. 25, No. 2, 1987 p 193-198.

[111] Strawn, R., C., Desopper, A., Miller, J., Jones, A., "Correlation of Puma Airloads - Evaluation of CFD Prediction Methods," Paper No. 14, 15th European Rotorcraft Forum, September 1989.

[112] Strawn, R. C., Bridgeman, J. O., "An Improved Three-Dimensional Aerodynamics Model for Helicopter Airloads Prediction," AIAA Paper 91-0767, AIAA 29th Aerospace Sciences Meeting and Exhibit, Reno, NV, January 1991.

[113] Kim, K. C., Desopper, A. and Chopra, I.,"Blade Response Calculations Using Three-Dimensional Aerodynamic Modeling," *Journal of American Helicopter Society*, Vol. 36, No. 1, p. 68-77, January 1991.

[114] G. Servera, P. Beaumier, M. Costes, "A Weak Coupling Method between the Dynamics Code Host and the 3D Unsteady Euler Code Waves," 26th European Rotorcraft Forum, The Hague, Netherlands, Sept 2000.

[115] Pahlke, K. and Van Der Wall, B., "Calculation of Multibladed Rotors in High-Speed Forward Flight with Weak Fluid-Structure-Coupling," 27th European Rotorcraft Forum, Moscow, Russia, September 2001.

[116] Sitaraman, J., Baeder, J. D., and Chopra, I., "Validation of UH-60 Rotor Blade Aerodynamic Characteristics using CFD," 59th Annual Forum of the American Helicopter Society, Phoenix, AZ, May 6-8, 2003.

[117] Sitaraman, J., Datta, A., Baeder, J. D., and Chopra, I., "Fundamental Understanding and Prediction of Rotor Vibratory Loads in High-Speed Forward Flight," 29th European Rotorcraft Forum, Friedrichshafen, Germany, Sep 16-18, 2003.

[118] Datta, A., Sitaraman, J., Chopra., I, and Baeder, J., "Analysis Refinements for Prediction of Rotor Vibratory Loads in High-Speed Forward Flight," American Helicopter Society 60th Annual Forum, Baltimore, MD, June 2004.

[119] Potsdam, M., Yeo, Hyeonsoo, Johnson, Wayne, "Rotor Airloads Prediction Using Loose Aerodynamic/Structural Coupling," Presented at the American Helicopter Society 60th Annual Forum, Baltimore, MD, June 7-10, 2004.

[120] W.E.Hooper, "The Vibratory Airloading of Helicopter Rotors," Paper No.46, 9th European Rotorcraft Forum, Stresa, Italy, September, 1983.

[121] W.G.Bousman, "Response of Helicopter Rotors to Vibratory Airloads," *Journal of the American Helicopter Society*, Vol. 35, No. 4, Oct, 1990, pp. 53-62.

[122] Rabbot, J. P., Churchill, G. B., "Experimental Investigation of the Aerodynamic Loading on a Helicopter Rotor Blade in Forward Flight," NACA RM L56107, Oct. 1956.

[123] Bell Helicopter, "Measurement of Dynamic Air Loads on a Full-Scale Semi-Rigid Rotor," TCREC TR 62-42. Dec. 1962.

[124] Scheiman, J., "A Tabulation of Helicopter Rotor-Blade Differential Pressures, Stresses, and Motions as Measured in Flight," NASA TM X-952, March 1964.

[125] Rabbott, J. P., Lizak, A. A., Paglino, V. M., "A Presentation of Measured and Calculated Full-Scale Rotor Blade Aerodynamic and Structural Loads", USAAVLABS TR66-31, July 1966.

[126] Pruyn, R. R., "In-Flight Measurement of Rotor Blade Airloads, Bending Moments, and Motions, Together with Rotor Shaft Loads and Fuselage Vibration, on a Tandem Rotor Helicopter," USAAVLABS TR 67-9A,B,C and D, Nov. 1967.

[127] Bartsch, E. A., "In-Flight Measurement and Correlation with Theory of Blade Airloads and Resources in the XH-51A Compound Helicopter Rotor," USAAVLABS TR 68-22A, May 1968.

[128] Fenaughty, R., Beno, E., "NH-3A Vibratory Airloads and Vibratory Rotor Loads," Department of the Navy SER 611493, Jan. 1970.

[129] Beno, E., "CH-53A Main Rotor and Stabilizer Vibratory Airloads and Forces," Department of the Navy SER 65593. June 1970.

[130] Shockey, G. A., Cox, C. Z., Williams, J. W., "AH-1G Helicopter Aerodynamic and Structural Load Survey," USAAMRDL TR-76-39.

[131] Shockey, G. A., et al, "AH-1G Tip Aero-Acoustic Test," NASA.

[132] Johnson, W., "Performance and Loads Data on a Full-Scale Rotor with Four Tip Planforms," NASA TM 81229, 1980.

[133] Cross, J. L., Watts, M. E., "Tip Aerodynamics and Acoustics Test," NASA RP 1179, Dec. 1988.

[134] Heffernan, R., Gaubert, M., "Structural and Aerodynamic Loads and Performance Measurements of an SA 349/2 Helicopter with an Advanced Geometry Rotor," NASA TM 88370, Nov. 1986.

[135] Lau, B. H., Louie, A. W., Sotiriou, C. P., Griffiths, N., "Correlation of the Lynx-XZ170 Flight-Test Results Up To and Beyond the Stall Boundary," American Helicopter Society Forum. May 1993.

[136] Nguyen, K., Lauzon, D., Anand V., "Computation of Loads on the McDonnell Douglas Advanced Bearingless Rotor," American Helicopter Society Forum, May 1994.

[137] Isaacs, N. C. G., Harrison R. J., "Identification of Retreating Blade Stall Mechanisms Using Flight Test Pressure Measurements," American Helicopter Society 45th Annual Forum, Boston, MA, May 1989.

[138] Caradonna, F. X., Tung, G., "Experimental and Analytical Studies of a Model Helicopter Rotor in Hover," NASA TM 81232, USAAVRADCOM TR-81-A-23, 1980.

[139] Dadone, L., Dawson, S., Boxwell, D., Ekquist, D., "Model 360 Rotor Test at DNW - Review of Performance and Blade Airload Data," American Helicopter Society 43rd Annual Forum, St. Louis, MO, May 1987.

[140] Dawson, S., Jordan, D., Smith, S., Ekins, J., Silverton, L., Tuttle, B., "HARP Model Rotor Test at the DNW," American Helicopter Society 45th Annual Forum, Boston, MA, May 1989.

[141] Yu, Y. H., Liu, S. R., Landgrebe, A. J., Lorber, P. F., Pollack, M. J., Martin, R. M., Jordan, D., "Aerodynamic and Acoustic Test of a United Technologies Model Scale Rotor at DNW," American Helicopter Society 46th Annual Forum, Washington D.C., May 1990.

[142] Peter F. Lorber, "Aerodynamic Results of a Pressure-Instrumented Model Rotor Test at the DNW," *Journal of the American Helicopter Society*, Vol. 38, No. 3, July 1993, pp. 26-34.

[143] Yung, H. Y., et al, "The HART-II Test : Rotor Wakes and Aerocoustics with Higher-Harmonic Pitch Control (HHC) Inputs - The Joint German/French/Dutch/US Project," American Helicopter Society 58th Annual Forum, Montreal, Canada, June 11-13, 2002.

[144] Kufeld, R. M., Balough, D., Cross, J. L., Studebaker, K. F., Jennison, C. D., Bousman, W. G., "Flight Testing the UH-60A Airloads Aircraft," American Helicopter Society 50th Annual Forum Proceedings, Washington, D.C., May, 1994.

[145] Specialists Meeting on Helicopter Rotor Loads Prediction Methods, AGARC Conference Proceedings No. 122, North Atlantic Treaty Organization, Milan, Italy, 30-31 March 1973.

[146] Loewy, R. G. "Summary Analysis," AGARD Conference Proceedings No. 122, March 1973

[147] Piziali, R. A., "Rotor Aeroelastic Simulation - A Review," AGARD Conference Proceedings No. 122, March 1973.

[148] Hansford, R. E., Vorwald J., "Dynamics Workshop On Rotor Vibratory Loads Prediction," *Journal of the American Helicopter Society*, Vol. 43, (1), January 1998, pp 76-87.

[149] Elliot, J. W., Althoff, S. L., Sailey, R. H., "Inflow Measurements made with a Laser Velocimeter on a Helicopter Model in Forward Flight," Vols. I and II, Rectangular Blades - Advance Ratios of 0.23 and 0.30, NASA TM 100542, 100543, April 1988.

[150] Miller, R. H., Ellis, S. C., Dadone, L., "Effects of Wake Migration during Roll-up on Blade Air Loads," *Vertica*, Vol. 30, No. 1, 1989, pp. 1-15.

[151] Joon W. Lim, "Analytical Investigation of UH-60A Flight Blade Airloads and Loads Data," American Helicopter Society 51st Annual Forum Proceedings, Forth Worth, Texas, May, 1995.

[152] Bousman, W. G., "A Note on Torsional Dynamic Scaling," *Journal of the American Helicopter Society*, Vol. 43, No. 2, April 1998, pp. 172-175.

[153] Torok, M. S. and Goodman, R. K., "Analysis of Rotor Blade Dynamics Using Model Scale UH-60A Airloads," *Journal of the American Helicopter Society*, Vol.39, No. 1, January 1994, pp. 63-69.

[154] Torok, Michael S. and Berezin, Charles R., "Aerodynamic and Wake Methodology Evaluation Using Model UH-60A Experimental Data," *Journal of the American Helicopter Society*, Vol.39, No. 2, April 1994, pp. 21-29.

[155] Andrew Z. Lemnios, "Rotary Wing Design Methodology," AGARD Specialists Meeting on Helicopter Rotor Loads and Prediction Methods, Seine, France, 1973.

[156] Lim, J., "RC Airload Workshop," Presented at Boeing, Philadelphia, First NRTC Black Hawk Loads Workshop, August 28, 2001.

[157] Esculier, J. and Bousman, G., "Calculated and Measured Blade Structural Response on a Full-Scale Rotor," *Journal of the American Helicopter Society*, Vol.33, No. 1, January 1988, pp. 3-16.

[158] Love, A. E. H., *A Treatise on the Mathematical Theory of Elasticity*, Fourth Ed. Dover Publications, New York, 1944, pp. 381-400

[159] Lanczos, C., *The Variational Principles of Mechanics*, Dover Publications, Inc., New York, NY, 1970.

[160] Shanley, J. P., "Application of the Comprehensive Analytical Model of Rotorcraft Aerodynamics and Dynamics to the UH-60A Aircraft," SER-72126, February 1986.

[161] Kufeld, R. M., Johnson, W. "The Effects of Control System Stiffness Models on the Dynamic Stall Behavior of a Helicopter," American Helicopter Society 54nd Annual Forum Proceedings, Washington, D.C., May 20-22.

[162] Bagai, A., Leishman, J.G., "Rotor Free-Wake Modeling using a Pseudo-Implicit Technique - Including Comparisons with Experiment," *Journal of the American Helicopter Society*, Vol. 40, No. 3, July 1995, pp. 29-41.

[163] Colin P. Coleman and William G. Bousman, "Aerodynamic Limitations of the UH-60A Rotor," AHS Aeromechanics Specialists Conference, San Francisco, California, January 19-21, 1994.

[164] J. Weissinger, "The Lift Distribution of Swept-Back Wings," National Advisory Committee for Aeronautics, Technical Memorandum No. 1120, 1942

[165] Bhagwat, M. J., "Transient Dynamics of Helicopter Rotor Wakes Using a Time-Accurate Free-Vortex Method," Ph. D. Thesis, University of Maryland, College Park, 2001.

[166] De Young, J., and Harper, C. W., "Theoritical Symmetric Span Loading at Subsonic Speeds for Wings Having Arbitrary Plan Form," NACA Report 9210, 1948

[167] Johnson, W., "Recent Developments in Rotary-Wing Aerodynamic Theory," *AIAA Journal*, Vol. 24, No. 8, August 1986, pp. 1219-1245.

[168] Lomax, H., Heaslet, M.A., Fuller, F.B., and Sluder, L., "Two and Three Dimensional Unsteady Lift Problems in High Speed Flight," NACA Rept. 1077, 1952.

[169] Ballhaus, W. F. and Goorjan, P. M., "Computation of Unsteady Transonic Flows by the Indicial Method," *AIAA Journal*, Vol. 15, Feb. 1978, pp. 117-124.

[170] Srinivasan, G.R. and Baeder, J.D., "TURNS: A Free Wake Euler/ Navier-Stokes Numerical Method for Helicopter Rotors," *AIAA Journal*, Vol. 31 No. 5, May 1993, p 959-962.

[171] Srinivasan, G. R., Baeder, J., D., Obayashi, S., McCroskey, W., J., "Flowfield of a Lifting Rotor in Hover: A Navier-Stokes Simulation," *AIAA Journal*, Vol 30., No. 10, Oct 1992, p 2371-2378.

[172] Roe, P. L., "Approximate Riemann Solvers, Parametric Vectors, and Difference Schemes," *Journal of Computational Physics*, Vol. 43, No. 3, 1981, pp. 357-372.

[173] Vatsa, V. N., Thomas, J. L., and Wedan, B. W., "Navier-Stokes Computations of Prolate Spheroids at Angle of Attack," AIAA Paper 87-2627, August 1987.

[174] Jameson, A., and Yoon, S., "Lower-Upper Implicit Schemes with Multiple Grids for the Euler Equations," *AIAA Journal*, Vol. 25, No. 7, July 1987, pp. 929-935.

[175] Sitaraman, J., Baeder, J. D., and Iyengar, V., "On the Field Velocity Approach and Geometric Conservation Law for Unsteady Flow Simulations," AIAA paper 2003-3835, Orlando, FL, June 2003.

[176] Yeo, H., Bousman, W. G., Johnson, W., "Performance Analysis of a Utility Helicopter with Standard and Advanced Rotors," AHS International Technical Specialists Meeting on Aerodynamics, Acoustics, and Test and Evaluation, San Francisco, January 23-25, 2002.

[177] Strawn, R.C. and Tung, C., "Prediction of Unsteady Transonic Rotor Loads with a Full-Potential Rotor Code," American Helicopter Society, 43rd Annual Forum, St. Louis, MO, May 18-20, 1987.

[178] Yamauchi, G. K., Heffernan, R. M., and Gaubert, M., "Correlation of SA349/2 Helicopter Flight Test Data with a Comprehensive Rotorcraft Model," *Journal of American Helicopter Society*, Vol. 33, (2), April 1988, p 31-42.

[179] Buchtala, B., Wehr, D. and Wagner, S., "Coupling of Aerodynamic and Dynamic Methods for Calculation of Helicopter Rotors in Forward Flight," Proceedings of 23rd European Rotorcraft Forum, pp. 5.1-5.12, Dresden/ Germany, September 1997.